Analysis of the microscopic structure of pedestrian bottleneck flow based on experiments and simulations

UNIVERSITÄT ZU KÖLN

INSTITUTE FOR THEORETICAL PHYSICS

FORSCHUNGSZENTRUM JÜLICH

INSTITUTE FOR ADVANCED SIMULATION

INAUGURAL-DISSERTATION
zur Erlangung des Doktorgrades
der Mathematisch-Naturwissenschaftlichen Fakultät
der Universität zu Köln

Vorgelegt von:
JONAS RZEZONKA

aus Bergisch Gladbach

2023

Berichterstatter:
Prof. Dr. Andreas Schadschneider
Prof. Dr. Joachim Krug

Tag der mündlichen Prüfung: 02.02.2023

Abstract

Improving the understanding of pedestrian crowd dynamics is a growing field with essential contributions from many areas of science utilizing empirical data and mathematical models. Simulations of pedestrian systems are an important method for empirically investigating many scenarios that would be difficult or unethical to study. They can improve the understanding of the pedestrians' interactions with other pedestrians and their environment by focusing on minimal models that can reproduce observed phenomena. Especially the observation of self-organization effects is of interest in that regard. Many of these phenomena in pedestrian dynamics are not unique to the system and are observed in related fields like granular materials, colloids, and active matter. Microscopic phenomena in pedestrian dynamics are partially analyzed by utilizing measures from these related fields. The presented work introduces methods from solid-state physics and granular matter to quantify the spatial order of pedestrian systems. The focus is on bottleneck flow when a crowd has to pass a spatially restricted area (e.g., a door leading to a hall), a crucial scenario in pedestrian dynamics and the flow of granular matter. Several collective effects are observed in this simple scenario. However, the dynamics are not well understood. This can lead to controversies about the origin of observed phenomena, especially in an interdisciplinary field. In a situation where the corridor width leading to the bottleneck is variable, empirical studies found a surprising behavior. The density in narrower corridors decreases, even though a wider corridor allows for more space where pedestrians could distribute. Additionally, lane formation emerges in narrow corridors. It was argued that this is an example of social norms influencing the dynamics of pedestrians. However, the hypothesis is missing convincing evidence. From a physical standpoint, this thesis investigates the phenomenon using a microscopic velocity-based model using simple interactions. To obtain a better understanding of the models' interactions, the scenario of a bottleneck with a wide area in front is further analyzed regarding the spatial order, utilizing the measures and methods used in the study of granular materials. Experimental data and agent-based simulations are analyzed using velocity-based and force-based models. The comparison of the experimental data to the simulations shows that the simulated systems have a higher degree of spatial order, while the experimental data behaves closer to a fluid. A further investigation of simulated systems with a large number of agents and variation in the interactions reveals a rich behavior in the modeled systems, exhibiting increased spatial order, partial jamming, influencing the clogging probability, and a general transformation of the bulk shape in front of the bottleneck.

Kurzzusammenfassung

Die Dynamik von Fußgängerströmen ist von zunehmendem Interesse, mit neuen Beiträgen aus verschiedenen Bereichen der Wissenschaft, wie der Physik, den Ingenieurswissenschaften und der Sozialpsychologie. Die Beiträge basieren auf empirischen Daten sowie mathematischer Modelle und numerische Simulationen. Insbesondere Simulationen von Fußgängersystemen sind wichtig zur Untersuchung von Situationen, deren experimentelle Umsetzung schwierig oder unethisch wären. Zusätzlich können Modelle helfen, das Verständnis von Fußgängerinteraktionen mit anderen Fußgängern und ihrer Umwelt zu verbessern, indem sie sich auf minimale Wechselwirkungen fokussieren, die die beobachteten Phänomene reproduzieren können. Besonders interessant sind Beobachtung von emergenten Selbstorganisations-Effekten. Fußgängersysteme zeigen eine Reihe dieser Effekte, welche jedoch nicht zwingend systemimmanent sind und auch in anderen Bereichen wie granularer Materie, Kolloiden und aktiver Materie beobachtet werden. Messgrößen, die im Bereich der Fußgängergynamik zum Einsatz kommen, um mikroskopische Phänomene zu analysieren, stammen teils aus diesen verwandten Bereichen. Die vorliegende Arbeit führt Methoden aus den Bereichen Festkörperphysik und granularer Materie ein, um die räumliche Ordnung von Fußgängersystemen zu quantifizieren und analysieren. Der Fokus liegt hierbei auf der Bewegung von Fußgängerströmen durch einen Engpass (sogenannte Bottlenecks), wenn eine Menschenmenge sich durch einen räumlich begrenzen Bereich bewegen muss (z.B. der Eingang in eine Eventhalle). Bottlenecks sind ein wichtiges Szenario im Bereich der Fußgängerdynamik und granularer Materie. In diesem relativ einfachen System können mehrere kollektive Effekte beobachtet werden, die Dynamik ist jedoch noch nicht gut verstanden. Ein tieferes Verständnis der Ursachen ist insbesondere bei Anwendungen in interdisziplinären Fragestellung wichtig. In Experimenten, bei denen die Breite des zum Engpass führenden Korridors variiert wurde, wurden überraschende Phänomene beobachtet. In schmalen Korridoren, die zu dem Bottleneck führen, ist die Dichte geringer im

Vergleich zu einem weiten Korridor, obwohl dort mehr Platz in der Nähe des Bottlenecks ist, auf dem sich Fußgänger verteilen könnten. Zusätzlich kommt es in den schmalen Korridoren zu einer Spurenbildung (sogenannte lane formation). In vorangegangenen Studien wurde argumentiert, dass dies ein Beispiel für den Einfluss sozialer Normen auf die Dynamik von Fußgängern ist, jedoch fehlen der Hypothese überzeugende Beweise. Um den Ursprung der beobachteten Phänomene besser zu verstehen, wird in der vorliegenden Arbeit die Situation aus physikalischer Sicht, anhand eines mikroskopischen, geschwindigkeitsbasierten Modells mit einfachen Interaktionen untersucht. Damit Wechselwirkungen in Modellen besser verstanden werden können, wird im weiteren Verlauf der Arbeit das Bottleneck-Szenario in der Hinsicht auf die räumliche Ordnung der Fußgänger in experimentellen Daten und geschwindigkeits- und kraft basierten Modellen untersucht. Dabei werden vor allem Methoden zur Untersuchung der räumlichen Struktur granularer Materie verwendet. Der Vergleich von Modellen und experimentellen Daten zeigt, dass sich in den Modellen eine höhere Ordnung der simulierten Fußgänger bildet, während sich die experimentellen Daten ähnlich zu einer Flüssigkeit verhalten. Zur Untersuchung, welchen Einfluss die Wechselwirkungen in den Modellen auf die Struktur haben, werden Bottlenecksysteme mit einer großen Anzahl an Agenten simuliert, um Randeffekte zu minimieren. Die Ergebnisse zeigen, dass verschiedene Wechselwirkungen die räumliche Struktur und Dynamik des Systems maßgeblich verändern. Zusätzlich wird die Wahrscheinlichkeit für Blockaden im System (sogenannte Clogs) beeinflusst und die allgemeine Form der Ansammlung von simulierten Fußgängern.

Contents

Chapter 1

Introduction

Pedestrian dynamics is a vastly interdisciplinary subject with research interest from many fields, such as social psychology, engineering, and physics. The field is relatively accessible even for a layman because it is straightforward to explain the fundamental ideas, and almost everyone can imagine the investigated scenarios since nearly everyone has experienced similar situations. Most people are also aware of the occurrence of crowd disasters when in a large group of people, the density increases due to the crowd's dynamics to a point where the pressure on individuals can cause serious bodily harm and death (e.g., the Love Parade disaster in Duisburg, Germany 2010, the Hillsborough disaster in Sheffield, England 1989, Meron crowd crush in Mount Meron 2021, Seoul Halloween crowd crush in Korea 2022 etc.). Especially critical are situations where a large crowd has to traverse through a so-called *bottleneck*, describing areas of restricted flow, like an entrance to a building. In emergency situations, like an evacuation, bottlenecks can exhibit high densities and temporary flow arrest in extreme cases [1, 2]. A misconception that is still widespread is the emergence of panic in a crowd as the cause of a disaster. The idea that the individuals in a crowd turn from a rational and social state to an irrational and anti-social state is unproven [3] (See Section 1.3). The field's interdisciplinary nature yields various approaches to the design of experiments and the mathematical modeling of this system. It is straightforward from an engineering perspective to strive for accurate and high-fidelity models that can accurately describe complex environments. This is useful in traffic and city planning to ensure efficient transportation.

A question often posed is: what is the relation between pedestrian systems and physics? From a perspective of statistical mechanics, pedestrians can be described as particles analogous to a gas or a liquid. Especially descriptions similar to granular materials can be applied in which case the macroscopic-sized particle dynamics (i.e., thermal noise is not relevant) are determined by external forces. In contrast to granular particles, humans are self-driven and have multiple individual characteristics, e.g., individual walking speeds can vary depending on individual targets [4, 5]. Popular models, therefore, treat pedestrians as individual self-driven agents, usually with relatively simple interactions and often homogenous parameters for the agent's behavior [6–8].

There is research that puts forward the idea that human behaviour improves the realism of models [9–13], which partly criticize the simplicity of physical models, where pedestrians are treated as individuals, while social groups [11] and the influence of social norms are neglected [13]. Nevertheless, the physical approach aiming to reduce models to simple interactions successfully describes multiple collective phenomena observed in laboratory and field studies [14, 15]. These phenomena are characterized by macroscopic effects in crowds which stem from the microscopic interactions of pedestrians without needing external forcing in the system. Simple models of self-driven agents can reproduce these self-organization using basic and homogeneous interactions in discrete or continuous time and space [8, 16–20]. Including clogging at bottlenecks, lane formation in counter flow, stop-and-go waves and counter flow at bottlenecks. Popular models build on Newtonian dynamics [16] or use discrete cellular automata with specific transition rules [19] but many other approaches exist [6, 8]. Velocity-based models gained popularity in recent years, which neglect the inertia of pedestrians [18, 21, 22].

Other many-particle systems apart from pedestrian dynamics exhibit similar behavior. For example the faster-is-slower effect [23] at bottlenecks sometimes observed in pedestrian systems [1, 2, 24] (see [15] for the controversies surrounding this matter) can also be observed in sheep herds [25], granular matter [26] and colloidal systems [27]. The formation of lanes in counter flow [14, 28] can be observed in driven colloidal media [29, 30]. This illustrates how the pedestrian system can be partially treated analogously to physical granular, colloidal and active matter systems. Simple self-driven systems can also exhibit self-ordered motion analogous to flocking behavior divided by a phase transition [31] using simple rules.

One problem in the discussion of the origin of emergent phenomena is the challenge of distinguishing physical effects from social psychological effects. The first part of this thesis investigates one claim, wherein a bottleneck scenario with varying geometries, the density near the entrance is affected, and lane formation in the corridors is observed [13, 32]. The analysis in Chapter 3 investigates this claim using a simple model of self-driven particles similar to [18], which illustrates the difficulty to distinguish self-organization phenomena caused by physical interactions from phenomena caused by social norms. The results from this chapter have been published in [33].

In the analysis of pedestrian systems, useful quantities from a physics and engineering perspective to describe the dynamics are density, velocity, and flow. Often studies focus on the macroscopic properties, taking the mean of the quantities over space and time [8, 34]. Microscopic phenomena like lane formation [28, 35], correlations in the velocity of pedestrians [2, 36] and position of the nearest neighbor [37] in unidirectional flow have been investigated. Also sophisticated measures are introduced that focus on microscopic interactions [38]. However, there is still potential to utilize simple measures from solid-state physics and granular matter that characterize the spatial structure of the system. These measures are introduced to analyze the spatial structure of bottleneck flow scenarios of the two-dimensional system. Especially important are the bond orientation factor Ψ_6 4.17, the shape factor 4.20 and the coordination number N_n in Section 4. First strives in this direction have been made [39] analysing a force based model, though a more general analysis of spatial structure in experimental data and an investigation of the way model parameters affect the structure in the system have not been conducted until now. The analysis shows that the model class, isotropy of interactions, noise in the direction, and the strength of the interactions influence the dynamics and structure in a bottleneck scenario. Even simple interactions of agents lead to rich behavior in two-dimensional phase space and surprising ordering phenomena. The following section introduces the observables commonly used in pedestrian dynamics more thoroughly and discusses the mentioned emergent phenomena in more detail.

1.1 Pedestrian dynamics: empirical observations and observables

There are multiple sources that give comprehensive reviews of pedestrian dynamics [7, 8, 15, 34, 40]. Empirical observations in experiments or field studies in pedestrian dynamics have gained popularity during the last 30 years. The development of efficient image processing and readily available hardware like camera systems make it possible to analyze large groups of pedestrians in field studies and controlled experiments efficiently. Though the study of pedestrian dynamics is far older, the first experiments are over 100 years old [41]. The systems can be examined in field studies or controlled experiments using volunteers as participants. Experimental studies have the advantage of being able to control the parameters and to avoid outside influences. The recent introduction of sophisticated sensors makes it also possible to track the three-dimensional movement of the body [42] and the pressure acting on the doors in an evacuation scenario [2]. However, it is not easy to estimate if people behave differently in experimental setups compared to real-life situations. This is the advantage of field studies where pedestrians are observed in a natural environment (e.g., at train stations or large-scale events). With the measured trajectories, quantitative analysis of the pedestrian dynamics becomes possible. Three crucial quantities studied are the pedestrian density ρ, velocity $\mathbf{v}$, and the flow $\mathbf{J}$. These can be measured and calculated in multiple ways. The methods used to determine the density ρ are discussed in detail in Chapter 3. A straightforward approach to measure the flow is to set a boundary in the observed system and measure the time gap $\Delta t = t_{i+1} - t_i$ of consecutive pedestrians i and $i+1$ passing the boundary. The flow of N pedestrians passing the boundary is then defined by

$$J = \frac{1}{\langle \Delta t \rangle}, \tag{1.1}$$

with $\langle \Delta t \rangle = \frac{t_{N+1} - t_1}{N} = \frac{\Delta t}{N}$. It is usually defined as a scalar quantity in relation to the normal vector of the linear boundary. Analogously to fluid dynamics, the flow can also be defined using the average speed v and density ρ of a pedestrian stream passing through a corridor with width b

$$J = \rho v b = J_s b, \tag{1.2}$$

where $J_s = \rho v$ is the hydrodynamic relation describing the specific flow of pedestrians per unit time and unit length. The relations between the quantities J, ρ, and v are called the *fundamental diagram.* Its name already points to its importance and can be equivalently described as $J_s(\rho)$, $v(J_s)$, and $v(\rho)$ because of the hydrodynamic relation. The fundamental diagram is used to design facilities in civil engineering [43–45] and in the context of modelling used to benchmark and fit parameters [46, 47]. Measured fundamental diagrams vary widely, suggesting that cultural norms and population differences [48–50], gender [51], the specific situation (e.g., uni- and multidirectional flow)[52, 53], short-range fluctuations [53] etc. could have significant influence on the relation. There is a consensus that the speed of the pedestrian decreases with increasing density and that there exists a density where J_s is maximal, which, together with the width b, defines the facility's maximum capacity. The density ρ where the capacity is reached is called the "critical density," though the term critical does not necessarily refer to its understanding in physics. Below the critical density, the system is free-flowing, where pedestrians can move with their desired velocity. Above the critical density, the system is in a congested state, where the flow decreases with increasing density.

In a bottleneck in the free-flowing state, the incoming and outgoing flow are equal. When the incoming flow exceeds the capacity, the system transitions into the congested state, where the density in front of the bottleneck increases and is higher compared to inside the bottleneck [54, 55]. The situation is illustrated in Figure 1.1. One important question, especially in building design, is how the bottlenecks' capacity increases with increasing width w. When discussing this, it is crucial to distinguish the pedestrians' behavior in systems. Especially in dense situations, it is important whether the pedestrians in the bottleneck are competitive or cooperative. In a competitive scenario, pushing could be a strategy that some people use to move quickly to their target, influencing the overall dynamics. Considering scenarios where this is not the case, older building codes assumed that the capacity of a bottleneck increases step-wise when the width is sufficient for additional lanes to form [56]. This was also supported by empirical studies [54, 57]. However, studies investigating a larger number of bottleneck widths found that this is not the case, and the capacity increases linearly with the width [58–60]. Other factors that can influence the flow of a bottleneck is the length of the bottleneck, where the flow decreases with increasing length [61, 62], obstacles in front of the bottleneck influence the evacuation time of sheep [25] but not pedestrians [1, 2]. The influence of the bottleneck's geometry is also minor [63], while an initial increased density can increase the flow [64].

1.2 Self-organization in pedestrian dynamics

From a physics standpoint, the most interesting observations in pedestrian dynamics are collective self-organization phenomena. These describe macroscopic phenomena

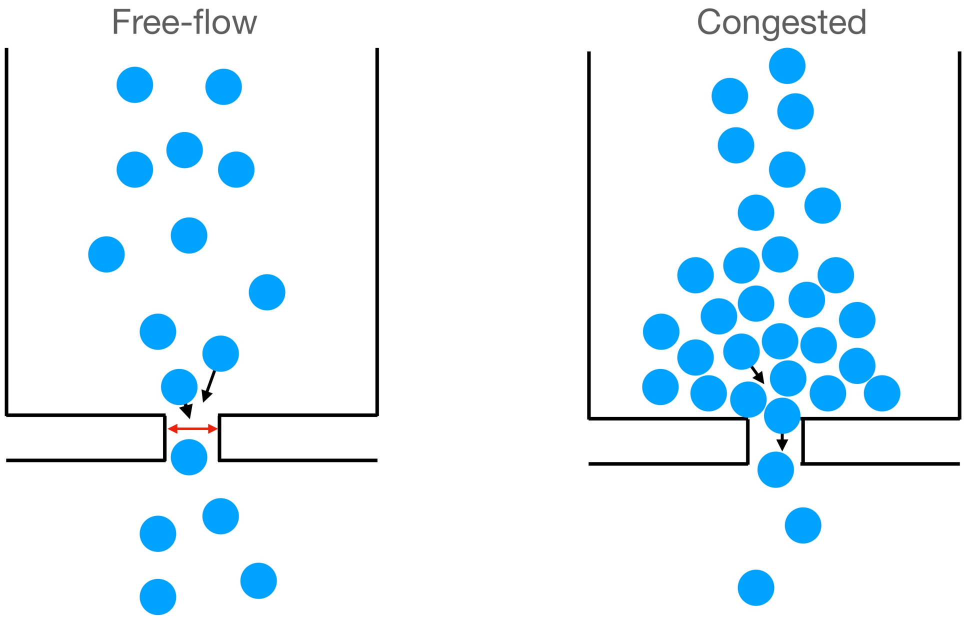

Figure 1.1: Illustration of a free-flowing and congested bottleneck. The red arrows mark the bottleneck width w.

caused by microscopic interactions in the system [40]. It should not be confused with aggregated behavior [40] since collective motion emerges from spatial or temporal synchronization of the system. Important phenomena in pedestrian dynamics that were observed until now are summarized in this section.

Lane formation

Lane formation is an example of a microscopic ordering phenomenon in pedestrian dynamics. In counterflow, when pedestrians move in opposite directions of each other, lanes form, which are elongated clusters moving in the same direction [28, 35, 65]. Under certain conditions, it can also be observed in unidirectional flow towards a bottleneck [13, 32]. Figure 1.2 illustrates this phenomenon in a counterflow experiment. In this scenario, lanes form dynamically where new ones appear, and existing lanes disappear over time (see [66]). However, there are also cases where static lanes can form, e.g., half of a corridor moves in one direction, and the other half in the opposite direction [35]. In counterflow lanes form because they reduce interactions with oncoming pedestrians, producing a more comfortable walking environment and increasing walking speed [35]. The phenomenon does not depend on cultural preferences to move on one side but is influenced by it. The effect can also be observed in situations where no preference for a walking side exists. Cultural influences affect the kind of lanes formed and the order thereof.

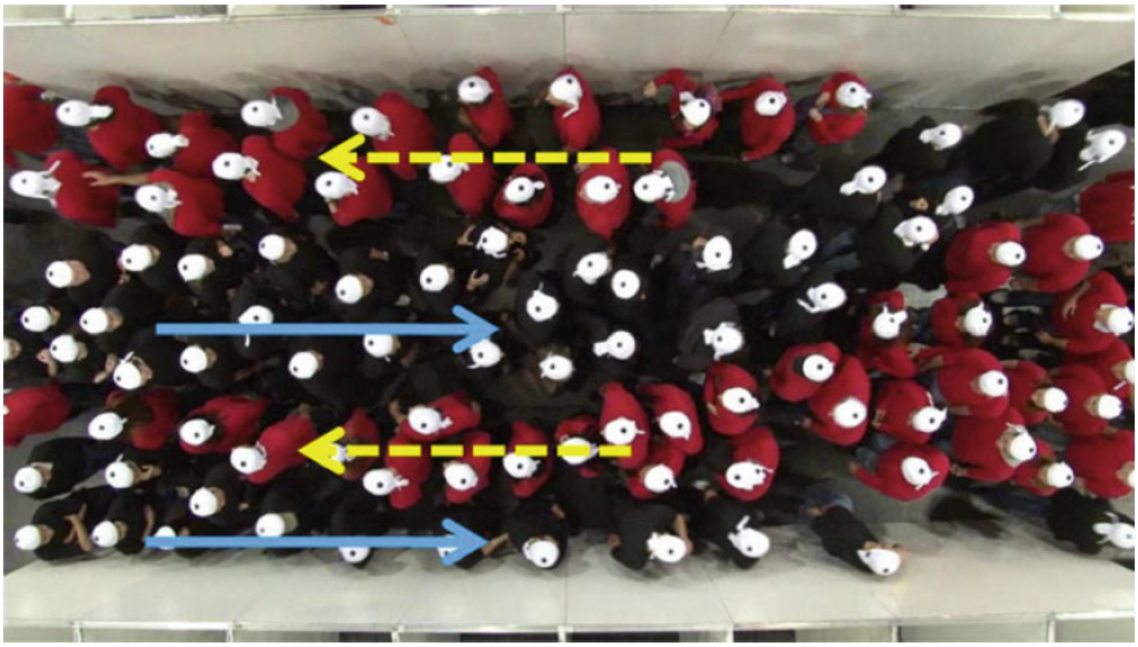

Figure 1.2: Lane formation in a counter flow experiment. Screenshot from [35, 66].

The effect can be quantified using different methods. One way is to use the band index introduced by Yamori [67], which calculates the ratio of pedestrians in lanes and the total number of pedestrians. Transversal velocity profiles at fixed positions were introduced by Burstedde et al. in 2001 [68]. In Zhang et al. [35], the Voronoi method to distinguish lanes is introduced. From colloidal systems driven by an external field where this effect is also observed, the idea of the order parameter $\phi = \langle \sum_{j=1}^{N} \phi_j \rangle$ [30, 69, 70] has been transferred to pedestrian dynamics. The variable $\phi_j = 1$ when the lateral distance to all other particles of the other type (i.e., moving in the opposite direction) is larger than a certain length scale, depending on the density. Otherwise $\phi_j = 0$. When the lanes are separated in an ideal AB configuration, where A and B define the opposing movement directions, $\phi = 1$ and in a mixed state with no lanes $\phi = 0$. Theoretical models predict a jamming transition [71], where the counter flow stops in a gridlock. However, this is not observed in any empirical study. The reason could be that the necessary densities are not reached in experiments, from [72] it is known that the lower density limit for the occurrence is larger than 3.5 m^{-2}.

Similarly to counterflow, a multitude of collective patterns are observed at intersections. For example, short-lived roundabouts can emerge. These are small detours in the path that make the overall movement more time-efficient and "smoother" [34].

Stop-and-go waves

Stop-and-go waves are connected to density waves that describe the phenomenon of quasiperiodic variations in the density in space and time. They can be observed in dense corridors in experiments [73, 74] and in field studies of subway stations [73]. The phenomenon describes a periodic phase of stop-and-go motion, hence the name. It is similar to stop-and-go waves in vehicular traffic, where in single-file motion, the density fluctuations move opposite to the movement direction. In vehicular traffic, there is phase separation in standing, and fast-moving vehicles (with a narrow transition layer), caused by the slow-to-start behavior of automobiles [75]. In contrast, in pedestrian motion, the phases are separated by standing and slow-moving pedestrians, indicating a fundamental difference that is not yet understood.

Emergent phenomena at bottlenecks

The focus of this thesis lies on emergent phenomena at bottlenecks. As discussed above, pedestrian movement through a bottleneck can be free-flowing below the bottleneck's capacity and in a congested state above the capacity. In the congested state, multiple emergent phenomena are observed. Crucially, especially in emergency situations, the emergence of **jamming** and **clogging** affects the dynamics. In the congested state, because of the volume exclusion principle and the desire of pedestrians to move through the exit, stable arches can appear that clog the system. This phenomenon appears in a multitude of system, like granular matter [76], sheep herds [25, 77], and colloidal systems [78]. Figure 1.3 illustrates clogging in an experimental pedestrian study [79] and a granular system, they are studied in multiple experiments [1, 2, 24, 59, 80, 81]. Arches that cause the clogging are self-stabilizing structures when the forces come from one direction (e.g. granular flow through a hopper under gravity). In this case, the flow can arrest indefinitely. Changing the direction of the force can break an arch apart. In pedestrian systems, people can break the arch through body movement and fluctuating forces, which leads to temporal clogs. The same phenomena can be achieved in shaken granular matter [82, 83]. It is especially relevant in evacuation situations where pedestrians are competitive and highly motivated to leave a certain area. This can lead to the

faster-is-slower effect, where the overall evacuation time increases with the urgency of the pedestrians to leave the area (e.g., leaving an area quickly because the fire alarm rings vs. leaving the area when fire and smoke are perceived). The effect was first predicted theoretically [17]. It can be observed in experiments [1, 2, 24], but the exact circumstances are not understood since there are empirical studies where it is not observed [15, 84]. Its occurrence also depends on the calibration of the model [85]. Though the effect exists in other systems as mentioned above [25–27].

Another important phenomenon is the so-called **zipper-effect**. Hoogendoorn and Daamen experimentally observed lane formation in a spatially enlarged bottleneck [86] illustrated in Figure 1.4. The effect occurs in narrow bottlenecks where two separate lanes are impossible to form because of the shoulder width. In this case, a pedestrian in one lane overlaps with the neighboring lane, where two consecutive pedestrians partially occupy the longitudinal gap in adjacent lanes, similar to a zipper. Increasing the width of the bottleneck increases the lateral distance and decreases the longitudinal gap. This configuration allows higher densities and results in a linear increase of the capacity in contrast to a gradual increase if the lanes do not overlap [87]. The zipper-effect is responsible for the linear increase of the bottleneck's capacity with width discussed in the introduction of this chapter.

In counterflow at a bottleneck where from both sides pedestrians try to pass (e.g., people exiting and entering a train station), oscillatory behavior can be observed in high-density situations [7, 16, 34, 88]. The situation is illustrated in Figure 1.4. When one pedestrian is able to pass the bottleneck, other pedestrians that want to pass in the same direction can follow, causing a stream of pedestrians that walk through the bottleneck. After some time, the pressure from the other side increases to the point that holds the stream of pedestrians, and the same phenomenon occurs the other way around. In Figure 1.4 the string of pedestrians passing the bottleneck belonging to either group A or B would, for example, look like "$BBBBBBAAAAAAAABBBBBAAA$....". The effect can be replicated in models of pedestrian dynamics [16, 18].

1.3 The role of psychology

When discussing psychological effects in pedestrian crowds, the notion of "panic" is widely known and perceived as the cause of crowd disasters. Though there is no

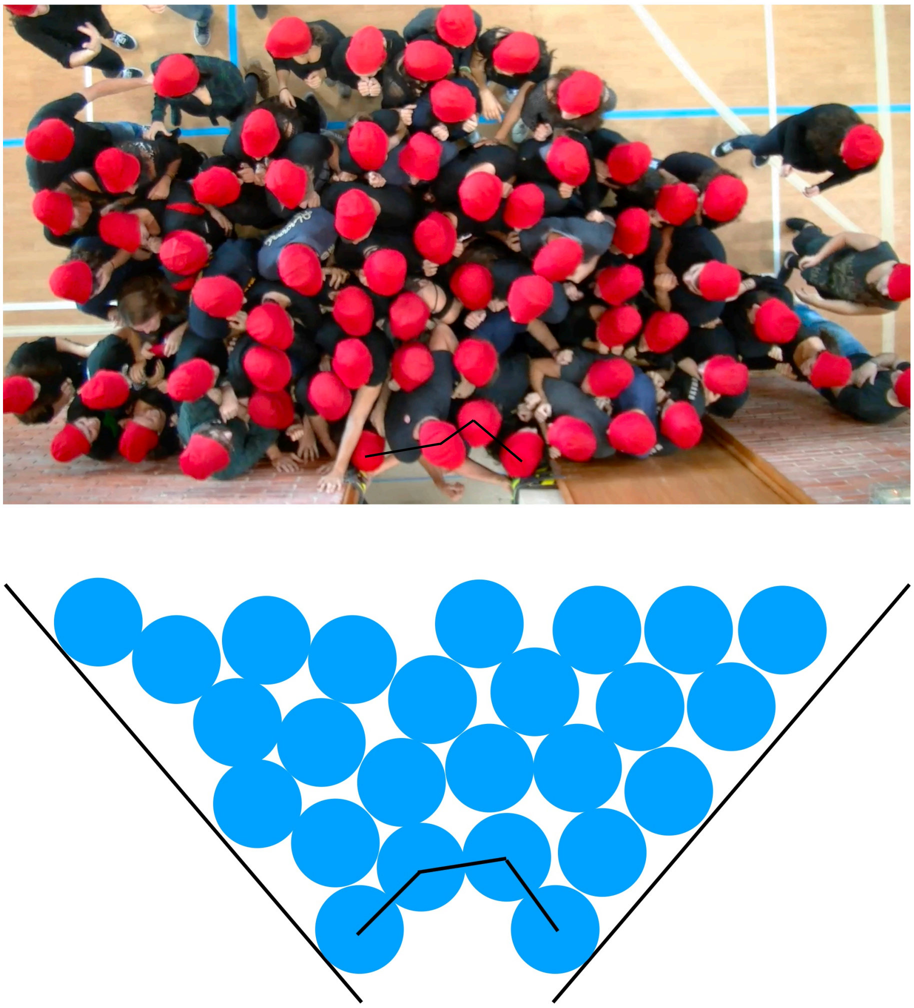

Figure 1.3: Top: Clog near the exit in an evacuation experiment [79]. **Bottom:** Illustration of a granular clog in a hopper stabilized through the friction with the hopper walls.

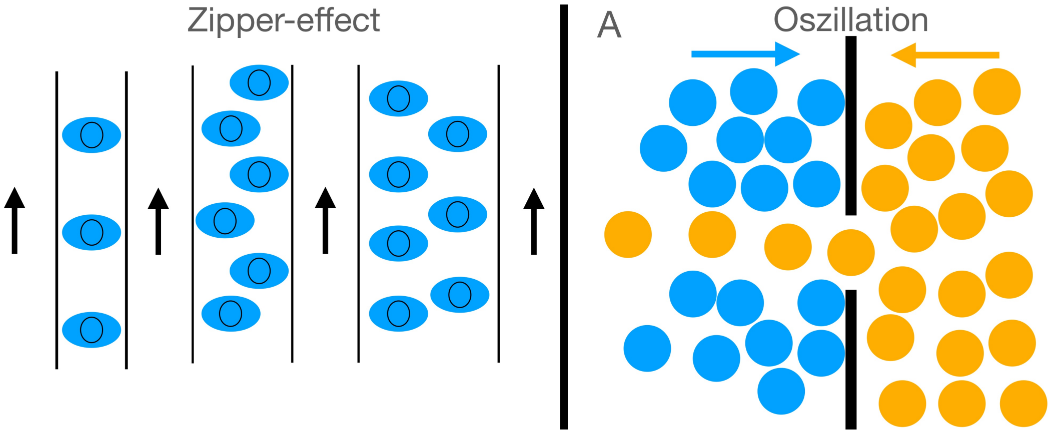

Figure 1.4: Left: Illustration of the zipper-effect. The errors show the movement direction. **Right:** Illustration of oscillations at a bottleneck with counterflow. Group A, shown in blue, wants to move to the right, indicated by the blue arrow. Group B wants to move to the left.

clear definition of "panic" in the literature, the idea behind the term is usually an occurrence of irrational and asocial behavior when humans are confronted with a dangerous, potentially life-threatening situation [3, 40, 89]. The widely held idea is that the crowd turns from a rational state into a panicking state that causes disaster, potential injuries and causalities. However, there is little evidence of "panic" in crowd disasters [3, 89, 90], and the idea has been thoroughly challenged as it is seldom observed [3]. Therefore, it is recommended to dispense with the term in the context of crowd disasters as it is not factual and puts the blame on the victims. The role of psychology in pedestrian dynamics is a point of discussion, especially at the interface where physics base studies and studies based on social psychology meet.

From a physics perspective, a crowd of pedestrians describe a collection of people walking in the same space simultaneously that can be treated as self-driving interacting particles. However, humans are intelligent beings with complex stimulus-response mechanisms, perceiving their environment and reacting to it accordingly. In social identity theory, the idea of the 'psychological' crowd exists [11], which describes a subgroup of the 'physical' crowd where people in this group perceived themselves as part of the group and distinguish between members and outsiders. Studies show that this categorisation influences the dynamics of pedestrians [9–11]. An important psychological factor in pedestrian dynamics is the motivation and competitiveness of pedestrians. Especially evacuation experiments with bottlenecks show in some instances the faster-is-slower effect when pushing of other participants is allowed [1, 2] but can not be reproduced in other experiments [32, 84], where pushing is not allowed. This points to the possibility that cooperative behavior vs. competitive behavior could influence the dynamics of evacuations. Some studies argue that social psychological aspects are important to describe natural walking behavior [10, 12, 13] though there is few concrete empirical evidence distinguishing situations where physics-based models are sufficient to explain empirical phenomena and where they are not. In [13], it is claimed that certain observations near bottlenecks with geometrical restrictions can not be explained without social psychology. This claim is the subject of Chapter 3 of this thesis. Before discussing this matter, the modeling of pedestrian system is introduced in detail.

Chapter 2

Modelling of self-driven agents

Modeling pedestrian dynamics is a diverse field using various approaches with individual advantages and disadvantages. The reason behind modeling pedestrian systems is manifold. For engineering purposes, it is useful to simulate a wide variety of scenarios where empirical studies would not be feasible or ethically too dangerous. Models that capture a wide spectrum of interactions are useful for investigating these scenarios in pedestrianized spaces' design. From a physics perspective, apart from the feasibility, modeling is useful to understand better the interactions in pedestrian systems that lead to the emergent phenomena described in the previous section. In this case, simple models are often interesting to investigate, to see what kind of interactions can replicate empirically observed emergent phenomena. The choice of a useful model depends on the situation and aim of the scenario studied. Over the years a large variety of models, model classes and subclasses have been introduced [6–8, 40]. The characteristics of pedestrian dynamics are usually divided into three categories.

The *strategic level* contains the activities a pedestrian would like to perform and the order thereof. On the *tactical level*, the short-term decision-making of pedestrians, e.g., the schedule of the activities, route choice, taking obstacles into account and densities, etc., is accounted for. The third level is the *operational level*, which describes the inner workings of the walking behavior of pedestrians. This contains the real-time decisions pedestrians make to avoid collisions with obstacles or other pedestrians. While the first two categories are considered extrinsic and need the description of sociological and psychological principles, the operational category can be described through physical granular models, usually treating pedestrians as self-driven interacting particles similar to active matter. In this context the "particles" are referred to as agents [40]. An agent is usually a two-dimensional representation of a pedestrian by vertical projection onto the plane in which they move (e.g., as a disc, ellipse, or occupying a discretized space). They interact with other agents nearby and their environment and can inhibit internal states that characterize their behavior. The agents' interactions with their environment or other agents are usually "simple" because few basic mechanisms are utilized to describe them. An extension to "intelligent" agents are called *multi-agent systems* [91, 92].

Agent models are a *microscopic* description of pedestrian dynamics, as they represent every individual separately and are straightforward in introducing heterogeneities in the agent behavior. Models that forego the individual agent ansatz are *macroscopic models*, where instead of the individual description of pedestrians by agents, the system is characterized by space and time averages of the observables of interest, like the velocity, density, and flow analogous to fluid dynamics in physics. Examples are [93–99] which are developed using principles from hydrodynamics and gas-kinetic theory, and led to the introduction of a fluid-dynamics theory of pedestrian flow [94]. Even though microscopic models are more popular because of their precision (at the cost of computational expanse), macroscopic models are still an active area of research [98, 100, 101], especially in applied mathematics

Between macroscopic and microscopic models, mesoscopic models describe agents individually but use the macroscopic averages to model the interactions. They try to combine the computational lower cost of macroscopic models while still inhibiting the heterogeneity of pedestrian interactions [102].

Another categorization is *discrete* vs. *continuous* models. The former comprises models that discretize the basic variables (space, time, and state variables like velocity). In a discrete model, the space can be divided into cells that can be empty or inhibited by one or more agents or an obstacle like a wall. The velocity allows the agent to move a certain amount of the discrete cell in a discrete-time step that can be realized by moving all agents simultaneously. This approach can be realized using cellular automata [7]. In the continuous approach, the basic variables are real numbers where the change in time, space, and state variables can be arbitrarily small.

Both macroscopic and microscopic models can be discrete [19, 101, 103], continuous [16, 18, 93, 98]. Continuous and discrete models are not mutually exclusive as a mixture of both properties can be used in a model [20]

The dynamics of the models can be either *deterministic* or *stochastic*. In determin-

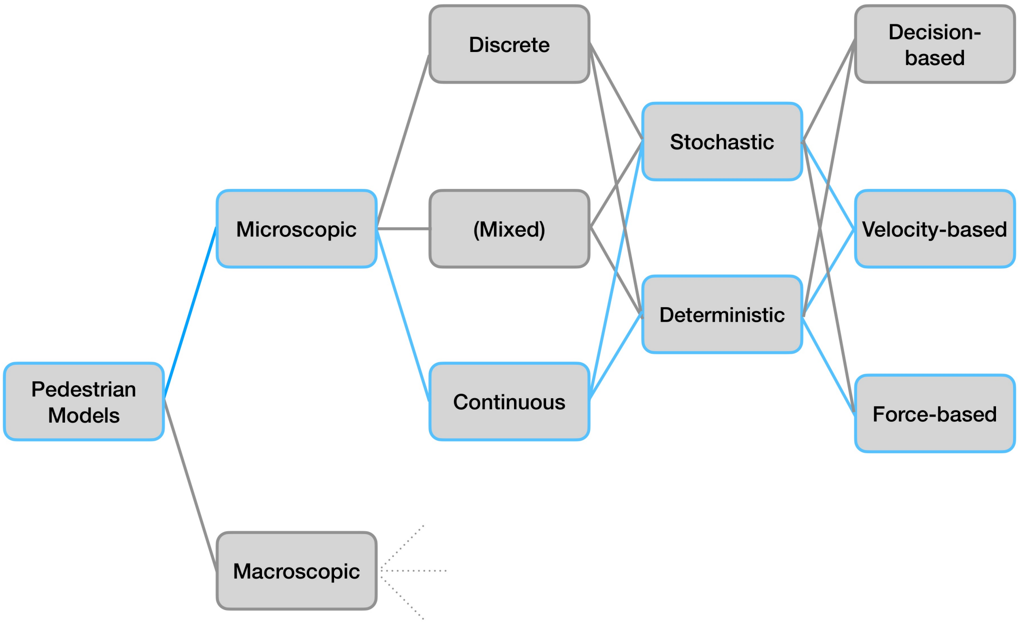

Figure 2.1: Illustration of the different model categories and how they relate to each other. Categories marked by the blue path are especially relevant to this thesis.

istic models, the system's future states are uniquely determined by the present. In stochastic models, on the other hand, the future is characterized by a probability distribution, i.e., the agent's behavior can differ in identical configurations. Usually, the probabilities for a certain action depend on the current state of the system (e.g., position of neighbors, density, etc.), which represents the uncertainties in pedestrian motion. Stochastic models are often more realistic than their deterministic counterparts. This kind of stochasticity is referred to as intrinsic, not to be confused with external "noise" that can be added onto a deterministic system's variables, e.g., onto the trajectories. Adding noise can circumvent the formation of undesirable and unrealistic configurations, like completely blocked states. The added noise does not change the overall behavior significantly, while for models with intrinsic stochasticity, the dynamics vary largely from the deterministic limit.

The above discussion of the microscopic models has already pointed out many different design approaches. These can be mainly categorized into three different model types. In *rule-based* or *decision-based models*, the dynamics of the agents are determined by a set of rules which determine the agent's behavior under certain conditions, e.g., the position of neighbors and obstacles, the desired direction of motion, etc. The rules of the model characterize the intrinsic properties of pedestrians, which can be justified by psychology. The other two categories are distinguished from the rule-based model but are related. *Force-* or *velocity*-based models determine the motion of the agent through the integration of the present state variable (acceleration or velocity, respectively); they are characterized by second-order and first-order differential equations. Especially force-based models are popular since they utilize Newtonian physics and are seen as a close analogy to other complex many-particle systems, like granular or colloidal matter. The interactions in these models are determined by forces exerted by surrounding agents or obstacles. These can be classical contact forces like friction and compression and virtual forces that deter agents from moving too close to each other, modeling the desire for personal space. Interactions in velocity-based models usually adjust the speed of the agents directly without the need to accelerate in relation to their environment. In a simple model, the speed can increase linearly with the distance to other agents or obstacles in the way. To find a way around obstacles in their path, the agent's direction can be influenced by their presence, aiming to optimize the trajectory to their target regarding their speed and the distance of the path. In contrast to the rule-based models, which emphasize the intrinsic decision-making of the agents, velocity- and force-based models emphasize the effect of extrinsic properties. An important property of the model types inhibit is the concept of *volume exclusion.* This is the concept that two pedestrians cannot inhibit the same space simultaneously. The models can be build *heuristically* or via *first principles.* The model inhibits several variables in a heuristic approach to describe the agents' interactions. The variables are fitted to empirical data, while the dynamics are derived from fundamental postulates in first-principle models. The approaches are often not clearly distinguished. An overview of the different concepts and how they relate to each other is illustrated in Figure 2.1. The blue boxes mark model categories that are especially important in the research of this work.

In the following, the model classes are discussed in more detail, and specific models related to the work in the dissertation are highlighted to give an overview of the subject.

2.1 Force-based models

Force-based models (also called acceleration-based) describe the dynamics of pedestrian motion via the superposition of external forces acting on the agent. Mathematically they constitute ordinary second-order differential equations. These can be solved numerically in computer simulations using e.g., the Euler or Runge-Kutta method. Force-based models are very popular because of their intuitive description from a physics perspective, where especially methods from molecular dynamics can be utilized to describe the complex dynamics of pedestrian crowds. The dynamics are determined by multiple forces acting on the agent; most importantly, the force accelerating the agent toward its desired direction and the repulsion force exerted by other agents and the environment to avoid collisions. The acceleration towards the target usually takes an exponential form, while the repulsion decreases with increasing distance to be object or agent exerting it. The repulsion acts as a soft form of volume exclusion. It is still possible for agents to overlap in contrast to decision-based models (see Section 2.2). The first force-based model was introduced in 1975 by Hirai [104]. Other examples of the model are the general centrifugal force model [105], and most famously, the social force model [16].

Social Force Model

The social force model is one of pedestrian dynamics' most studied operational models. Using a second-order differential equation, the model inhibits three forces to describe the dynamics and interactions on an agent i in the system.

$$\frac{d^2\mathbf{r}_i(t)}{dt^2} = \mathbf{f}_i^{driv} + \mathbf{f}_i^{soc} + \mathbf{f}_i^{phys}. \tag{2.1}$$

The force $\mathbf{f}_i^{driv}$ is the agent driving force responsible for the desire of the agent to move to a specific target location. The so-called social force $\mathbf{f}_i^{soc}$ describes the desire of humans to not be too close to other humans through repulsion but can also be attractive when describing grouping behavior. The physical forces $\mathbf{f}_i^{phys}$ are contact forces from physics like friction and restoring force when an agent is compressed. According to [106], the velocity increases exponentially towards a desired velocity. This behavior is described by the following force:

$$\mathbf{f}_i^{driv} = m_i \frac{\mathbf{v}_i^0 - \mathbf{v}_i}{\tau_i}, \tag{2.2}$$

where $\mathbf{v}_i^0 = v_i^0 \hat{\mathbf{e}}_i^0$ is the desired velocity. It can be decomposed into the desired speed v_i^0 and the desired direction $\hat{\mathbf{e}}_i^0 = (\mathbf{r}^0 - \mathbf{r}_i)/|\mathbf{r}^0 - \mathbf{r}_i|$ with $\mathbf{r}^0$ the target location. The factor τ is the relaxation time of an agent to reach its desired velocity. The social force $\mathbf{f}_i^{soc}$ can be decomposed into the social interaction of agent i with agent j, $\mathbf{f}_{i,j}$

and agent i with the wall or other obstacles w, $\mathbf{f}_{i,w}$. Here, the case of a disc-shaped agent with radius r_i and repulsive interaction

$$\mathbf{f}_{i,j} = -\nabla_{\mathbf{r}_{i,j}} V(\Delta r_{i,j}), \tag{2.3a}$$

$$\mathbf{f}_{i,w} = -\nabla_{\mathbf{r}_{i,w}} U(\Delta r_{i,w}) \tag{2.3b}$$

is discussed, where $\Delta r_{i,j} = |\mathbf{r}_i - \mathbf{r}_i|$ and $d_{i,j} = r_i + r_j$. Analogous $\Delta r_{i,w} = |\mathbf{r}_i - \mathbf{r}_w|$, with $V(r)$ and $U(r)$ monotonic decreasing potential functions. In the work of Helbing, Farkas, and Vicsek concerning evacuation dynamics [23] exponential repulsion functions realize the interaction forces

$$\mathbf{f}_{i,j} = -A_i \exp\left((\Delta r_{i,j} - d_{i,j})/B_i\right) \hat{\mathbf{e}}_{i,j}, \tag{2.4a}$$

$$\mathbf{f}_{i,w} = -C_i \exp\left((\Delta r_{i,w} - r_i)/D_i\right) \hat{\mathbf{e}}_{i,w}. \tag{2.4b}$$

The parameters A_i and C_i describe the interaction strength of agent i with agent j and a wall or obstacle, respectively. B_i and D_i quantify the interaction length, and the vector $\hat{\mathbf{e}}_{i,k} = (\mathbf{r}_i - \mathbf{r}_k)/|\mathbf{r}_i - \mathbf{r}_k|$. In the case of a continuous wall, the point $\mathbf{r}_w$ is the closest point to the agent. The physical forces $\mathbf{f}_i^{phys}$ are treated similarly. The social force can be direction-dependent, considering the field of view of an agent. Neighboring agents that are outside the field of view angle 2ϕ have a weaker influence in terms of the social force by multiplying the force with a weight

$$\omega(\hat{\mathbf{e}}, \mathbf{f}) = \begin{cases} 1 & \text{if} \quad \hat{\mathbf{e}} \cdot \mathbf{f} \geq |\mathbf{f}| \cos\phi \\ c & \text{if} \quad \text{otherwise,} \end{cases} \tag{2.5}$$

with $0 \leq c \leq 1$ and $\cdot$ the scalar product, which can be factorized onto the respective forces

$$\mathbf{f}_i^{soc} = \omega \mathbf{f}_{i,0}^{soc}. \tag{2.6}$$

The physical forces that influence the dynamics, namely friction and the restoring force, are contact forces, i.e., they only occur when agents overlap. These forces are introduced to avoid overlap of agents in high-density situations and give stricter restrictions to ensure volume exclusion [17, 23]. The restoring force is also called "*body force*" and defined as $k\Theta(\Delta r_{i,j} - d_{i,j})\hat{\mathbf{e}}_{i,j}$, which is simply Hooke's Law with the spring constant k and the step function $\Theta(x) = 1$ for $x < 0$ and nill otherwise.

The second physical force is the "*sliding friction force*" $\kappa\Theta(\Delta r_{i,j} - d_{i,j})\Delta v^t_{j,i}\hat{\mathbf{e}}^t_{i,j}$ acting on the relative tangential motion if pedestrian i and j are in contact. The tangential vector is defined as $\hat{\mathbf{e}}^t_{i,j} = (-\hat{e}^2_{i,j}, \hat{e}^1_{i,j})$, the tangential velocity difference as $\Delta v^t_{j,i} = (\mathbf{v}_j - \mathbf{v}_i)\hat{\mathbf{e}}^t_{i,j}$ and the friction coefficient κ. Combining the social force with the physical forces for the agent-agent and agent-wall interactions yields

$$\mathbf{f}_{i,j} = \left[A_i \exp\left((\Delta r_{i,j} - d_{i,j})/B_i\right) + k\Theta(\Delta r_{i,j} - d_{i,j})\right]\hat{\mathbf{e}}_{i,j} + \kappa\Theta(\Delta r_{i,j} - d_{i,j})\Delta v^t_{j,i}\hat{\mathbf{e}}^t_{i,j}, \tag{2.7a}$$

$$\mathbf{f}_{i,w} = \left[C_i \exp\left((\Delta r_{i,w} - d_{i,w})/D_i\right) + k\Theta(\Delta r_{i,w} - d_{i,w})\right]\hat{\mathbf{e}}_{i,w} + \kappa\Theta(\Delta r_{i,w} - d_{i,w})\Delta v^t_{w,i}\hat{\mathbf{e}}^t_{i,w}. \tag{2.7b}$$

The differential equation of the social force model (SFM) (2.1) can be rewritten to

$$m_i \frac{d^2\mathbf{r}_i}{dt^2} = m_i \frac{\mathbf{v}^0_i - \mathbf{v}_i}{\tau_i} + \sum_{j\neq i} \omega(\hat{\mathbf{e}}_{i,j}, \mathbf{f}_{i,j})\mathbf{f}_{i,j} + \sum_{w} \omega(\hat{\mathbf{e}}_{i,w}, \mathbf{f}_{i,w})\mathbf{f}_{i,w}. \tag{2.8}$$

The original model [16] (with no physical interaction) is successful in qualitatively describing lane formation and oscillation in counterflow at bottlenecks. In high density evacuation simulations the version containing physical forces [23] predicts the faster-is-slower effect. Over the years, several alternatives and extended versions of the SFM have been introduced. A recent comprehensive summary by Chen et al. can be found in [107].

Shortcomings of force-based models

Force-based models and especially the SFM have several shortcomings inherent to the approach that produce undesirable and unrealistic behavior. One crucial feature a model should inhibit is that it should fit the fundamental diagram [62]. The SFM, in its standard form described above, seems unable to reproduce the fundamental diagram in a corridor with the unidirectional flow and single file motion [108–110]. Only with adjustments and new concepts to the model can it reproduce realistic results [108, 109, 111]. However, this is not a problem unique to the SFM since it is generally challenging for models to reproduce fundamental diagrams and many models need to be modified [112–114]. Other issues unique to the force-based approach stem from the Newtonian treatment of the system. An agent's inherent inertia is not well suited to model a pedestrian. Pedestrian motion can be non-smooth in space due to the high friction with the ground while walking. They can stop almost instantly, which does not fit the description of a particle with inertia. Additionally, Newton's third law does not apply to pedestrian dynamics. Especially for the social force, the assumption that the pedestrians exert an equal force in the opposite direction is unrealistic, as a pedestrian only has limited capability to sense other pedestrians outside their field of view. Though this can be adjusted through the weight, ω (2.5), the general assumption of Newton's third law is still unrealistic. The fitted parameters in the SFM [17] are unrealistic. For example the effective range of the social force in equation (2.4a) is rather short with $B_i = 0.08\,\mathrm{m}$. In [115] the parameters are set to more realistic values which lead to additional modifications of the model to produce realistic behaviour. One of the major problems, again due to inertia, is oscillation and backward motion of the agents. In this case oscillating describes forward and backswords motion in respect to the desired moving direction when approaching other agents [116]. The issue of oscillation is inherent to the model in single file motion [117, 118]. It can be mitigated by reducing the repulsive force, but this leads to overlapping of the agents, violating the volume exclusion principle. In [105], it is shown that there is a narrow parameter space where both effects can be minor but non-zero. Other studies try to fix these problems by introducing new concepts to the model that restrict the agents' motion either through collision detection [119] or not allowing oscillation by setting the velocity to zero [16, 120]. However, these ideas add extra complexity to the model known for its simplicity. The superposition of the different forces (driving force, social force and physical) can lead to excessively high velocities or backwards motion away from the target area, especially in high density situations [121]. But even in low density situations where a pedestrian desire is comprised of multiple targets, the superposition of the forces could inhibit the agent to reach any of its goals. A closer analysis of the numerical properties of the SFM done by Köster et al. [122] revealed that there are inherent numerical problems in the model that can only be overcome by further alterations, which led to the introduction of the mollified SFM. It successfully improves the dynamics by mitigating oscillation and collision while avoiding numerical discontinuities. The problems in force-based models like oscillation, overlap and superposition of forces are inherent to the approach. Numerical problems like instabilities and the high computational cost add to it. Overall the numerous issues of force-based models led to the development of new continuous models using a non-force-based Ansatz, like velocity-based models discussed below.

2.2 Cellular automata models

Cellular Automata Models (CA) are a popular and widely studied class of decision-based models, discrete in time, space, and state variables. They are studied not only in the context of pedestrian dynamics but in general for transport phenomena, for example, in biology [123] or vehicular traffic [75, 124]. The origin of CA stems from statistical mechanics where the one-dimensional ASEP [7] is an important model system to study non-equilibrium phenomena and phase transitions. In vehicular traffic, the Nagel-Schreckenberg model for Autobahn traffic [124] gained wide popularity even outside the scientific community because of its ability to produce stop-and-go waves ("traffic jam out of nowhere"). The advantages of this modeling approach are that they are computationally inexpensive, and straight forward to implement rules into the system that are intuitive an clear to define in the discrete system, which makes them naturally decision-based. CA in pedestrian dynamics is a two-dimensional extension of the ASEP. The general principle of a CA is to discretize the space by separating it into cells, usually represented as squares (see Figure 2.2 A and B), but other patterns like hexagonal cells are also used (see Figure 2.2 C). The cell size is derived from the maximal density a pedestrian system exhibits and is usually set to 0.4×0.4 m for square cells. An agent can occupy a cell on the grid and traverse to neighboring cells in discrete time steps. Which cells are traversable by a pedestrian depends on the definition of the neighborhood. In the Moore neighborhood, an agent can move to all neighboring cells that share an edge or a corner (Figure 2.2 A). In the more popular Von-Neumann neighborhood, only the neighbors that share in edge are accessible (Figure 2.2 B). The definition of traversable neighboring cells in the hexagonal neighborhood is straightforward since all neighbors share an edge and are equidistant (Figure 2.2 C). The volume exclusion principle is imposed by making a cell occupied by an agent inaccessible to other agents. CA are usually intrinsically stochastic. The cell an agent at time t traverses to in the time step $t+1$ is chosen from a probability distribution (Figure 2.2 B). The rules of the model determine the probability for a target cell. Important factors are the *desired direction*, *interactions* with other agents and the environment (walls, obstacles, doors, etc.). In the deterministic limit of a CA, only one neighboring cell is accessible with probability $p = 1$ if it is unoccupied. The discrete-time dynamics are realized by a *parallel* or *synchronous* update, where all agents move simultaneously or *random sequential update*, where a randomly chosen subset of agents move. The movement of an Agent is not necessarily restricted to the nearest neighbors. The integer velocity of the agent can, in some models, determine the number of cells an agent can jump. For example, in the first pedestrian CA model by Blue and Adler, this is the case [125]. The model is a variation of the Nagel-Schreckenberg model using a multilane structure as its geometry. The rules of the model determine the preference of the lane an agent takes, the desire to change lanes, and the agent's velocity.

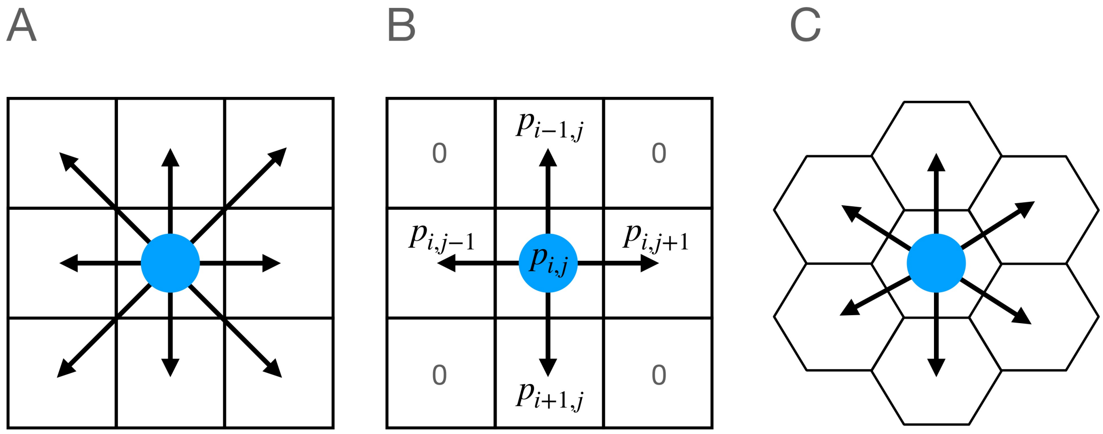

Figure 2.2: (**A**) Moore neighborhood, (**B**) Von-Neumann neighborhood, (**C**) Hexagonal neighborhood.

Floor Field Model

A more sophisticated and popular version of a CA in pedestrian dynamics is the Floor Field Model [19, 68, 126] especially for evacuation dynamics [127, 128]. The model is built on a square lattice using a Von-Neumann or Moore neighborhood. It introduces a dynamical field that determines the transition probabilities of the cells, which contrasts previous approaches with fixed transition probabilities. The dynamical field encodes interactions between agents using the bio-concept of chemotaxis [129]. The idea is that, similar to some insects (like ants) who use chemotaxis as means to communicate paths to resources (e.g., food, water, building material), pedestrians leave a virtual trace. The virtual trace represents an abstract concept externalizing the path a pedestrian has in their mind. In praxis, an agent in the model creates a virtual particle ("pheromone") at the formerly occupied cell (i, j) when traversing to a new cell. Other agents can detect the "pheromones" and react accordingly (e.g., be attracted to it, modeling an approach where agents follow each other). The advantage of this approach is that the interactions grow linearly with the number of agents in the system and can be calculated locally, which makes it computable with few resources. The number of virtual particles are stored in the dynamical floor-field $D_{i,j}$, which decay over time. Additional to the dynamic floor-field, a static floor-field $S_{i,j}$ determines the interaction of the agents with their environment (walls, obstacles, etc.) and the desired direction. The sense of direction is realized by increasing the field with distance r to the target area. Walls and other obstacles could have a repulsive effect. As the name suggests, the static floor-field is time-independent and does not depend on the number or spatial distribution of the agents. Using the concepts of the dynamic floor-field, the static floor-field, and volume exclusion, the transition probability is defined as

$$p_{i,j} = N \exp\left(k_D D_{i,j}\right) \exp\left(k_S S_{i,j}\right) (1 - n_{i,j}) \xi_{i,j}, \tag{2.9}$$

where N is a normalization constant so that $\sum_{\langle i,j \rangle} p_{i,j} = 1$. The factor $n_{i,j} = 0, 1$ counts the number of agents in a cell. Because of the exclusion principle, the number is limited to one. This is ensured by the factor $(1 - n_{i,j})$. The factor $\xi_{i,j}$ determines if an obstacle fills a cell. When $\xi_{i,j} = 0$, The cell is occupied by an obstacle like a wall and excluded from the available cells. If the cell is available for agents than $\xi_{i,j} = 1$. The coupling constant of the dynamical floor-field k_D and the static floor-field k_S determines the relative influence of the respective field. The coupling has a major influence on the dynamics, and the respective strengths of the coupling make it possible to simulate different situations. When the coupling k_S to the static field is strong, agents will prefer the shortest path to the exit. This is the preferred behavior in non-emergency situations. In emergencies, pedestrians follow other pedestrians to the exit, which corresponds in the model to strong coupling to the dynamic field k_D. The model has multiple further extensions and variations [46, 126, 128, 130–133]. One extension that is important for evacuation dynamics is the idea of a friction parameter [128]. Because of the parallel update, situations exist where multiple agents try to enter the same cell simultaneously. In the basic model, this is solved by choosing one agent randomly according to their relative probability of entering the cell. This problem can be avoided by using sequential instead of parallel updates, but this introduces the problem of ambiguity in the time scale of the model. To circumvent this and embrace the conflict as an important part of the dynamics [134], the friction parameter $\mu \in [0, 1]$ is introduced. It defines the probability that no agent is allowed to enter the cell when a conflict arises (see Figure 2.3). Especially in evacuation dynamics at bottlenecks, the friction parameter can reproduce clogging. It can be interpreted as the willingness of the agents to cooperate. Most conflicts can be resolved if μ is small and the dynamics are not inhibited. When μ is large, conflicts are often unresolved, inhibiting the dynamics and increasing the probability of clogs near a bottleneck, where conflicts are common. This local interaction influences macroscopic measures, like the flow and evacuation time [128].

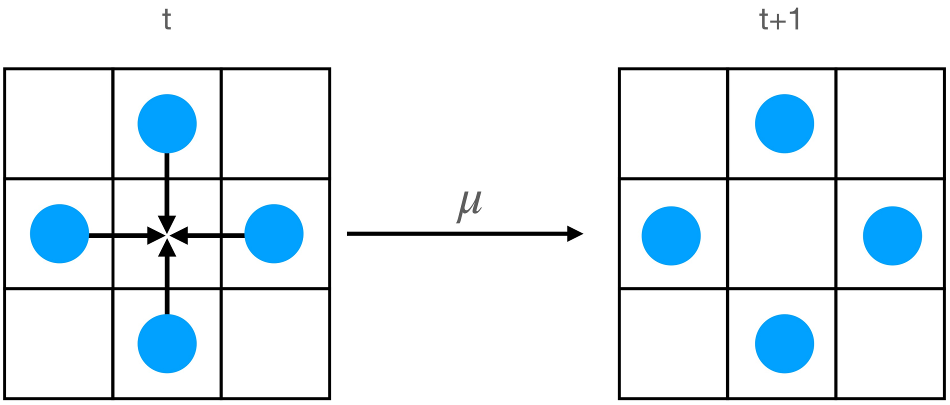

Figure 2.3: Illustration of the effect of the friction parameter μ.

2.3 Velocity-based models

A recently more popular approach is velocity-based models (VB). These models are inspired by robotics and techniques from video games, where the change in velocity is instant, neglecting the effects of inertia prominent in force-based models and the influence of an implicit reaction time. This is useful in robotics since light robots can almost instantly change their velocity and direction with sufficient friction. The same assumption can be made about pedestrians since a person can stop their motion in one step when moving at average walking speeds. In the work of Maury et al. [135], a framework for VB models, they include volume exclusion and collision-free properties through constraints in the velocity. The concept of the VB approach is to model pedestrians as agents with a visual input interacting locally with neighboring agents. This is described mathematically by a first order differential equation

$$\frac{d\mathbf{r}_i}{dt} = \mathbf{V}((\mathbf{r}_j - \mathbf{r}_i, \mathbf{v}_j), j \in N_i), \tag{2.10}$$

expressing the dynamics of agent i via the velocity function $\mathbf{V}(.)$ and its arguments, the relative position $\mathbf{r}_j - \mathbf{r}_i$ and the neighbors velocities $\mathbf{v}_j$ in the set of interacting agents N_j. The first VB models are *velocity obstacle models* [136]. The agents in the model minimize the deviation from their desired velocity $\mathbf{v}_0$ under the condition of collision avoidance. This is reached by excluding the space represented by *velocity cones $VO(i)$* from the space of allowed velocities, which would lead to a collision, assuming the velocity of all agents in the system stays constant. This describes an optimization problem, where the velocity of agent i is determined by

$$\mathbf{V}_i = \arg \min_{\mathbf{v} \notin VO(i)} |\mathbf{v} - \mathbf{v}_0|. \tag{2.11}$$

One problem of velocity obstacle models is oscillations in the velocity direction called the ping pong effect. This effect occurs when for two neighboring pedestrians i and j, the velocity of pedestrian i depends on j and the velocity of j on i. The reciprocal *velocity obstacle model* (RVO) suppresses this problem by taking the reciprocal relationship of velocity optimization into account (i.e., agent i knows that agent j optimizes the velocity in the same way and vice versa) [137]. The extension to the model poses a new problem because hardcore volume exclusion can be violated. The most popular variant of this model is called the *optimal reciprocal collision avoidance* (ORCA), which extends the model to ensure volume exclusion and collision avoidance [138].

Another kind of VB decomposes the velocity vector into its speed V and direction $\hat{\mathbf{e}}$ component

$$\frac{d\mathbf{r}_i}{dt} = V((\mathbf{r}_j - \mathbf{r}_i, \mathbf{v}_j), j \in N_i)\, \hat{\mathbf{e}}((\mathbf{r}_j - \mathbf{r}_i, \mathbf{v}_j), j \in N_i). \tag{2.12}$$

On example is the *synthetic-vision-based steering* model [139]. The model central in this thesis is the collision-free speed model [18] explained in detail in the following section.

Collision-free speed model (CSM)

The collision-free speed model (CSM) introduced by Tordeux et al. [18] is a velocity-based model without overlapping agents (therefore collision-free). It is introduced as a model with minimal interactions that can reproduce several emergent phenomena observed in empirical studies, such as lane formation in counterflow and intermittent bottleneck flow. The model does not exhibit the problems encountered in its force-based counterparts, such as oscillation and agent overlap. Its success led to several studies extending the model to successfully describe a broader range of scenarios, like the jamming transition at bottleneck flow, the density near a bottleneck, and better fits to the fundamental diagram in 1D and 2D motion [21, 22, 140].
The model has two main components, the optimal speed function $V(s_i(\mathbf{x}_i, \mathbf{x}_j, ...))$ and the movement direction of the agent $\hat{\mathbf{e}}_i(\mathbf{x}_i, \mathbf{x}_j, ...)$, with $\mathbf{x}_i$ the position of agent i. The velocity of agent i is then calculated

$$\mathbf{v}_i = V(s_i(\mathbf{x}_i, \mathbf{x}_j, ...)) \cdot \hat{\mathbf{e}}_i. \tag{2.13}$$

The function $V(s_i)$ is defined as

$$V(s_i) = \min\{v_0, \max\{0, (s_i - l)/T\}\}\,. \tag{2.14}$$

The velocity of the agent i is determined by the diameter of the agent l, the minimum spacing s_i, the desired velocity v_0 and the gradient factor T. The minimum spacing is defined as

$$s_i = \min_{j \in J_i} s_{i,j}. \tag{2.15}$$

The set J_i contains all agents in the headway of agent i

$$J_i = \{j, \mathbf{e}_i \cdot \mathbf{e}_{i,j} \leq 0 \wedge |\mathbf{e}_i^{\perp} \cdot \mathbf{e}_{i,j}| < l/s_{i,j}\}. \tag{2.16}$$

The vector $\mathbf{e}_i^{\perp}$ is perpendicular to $\mathbf{e}_i$. Figure 2.4 A illustrates the set J_i.

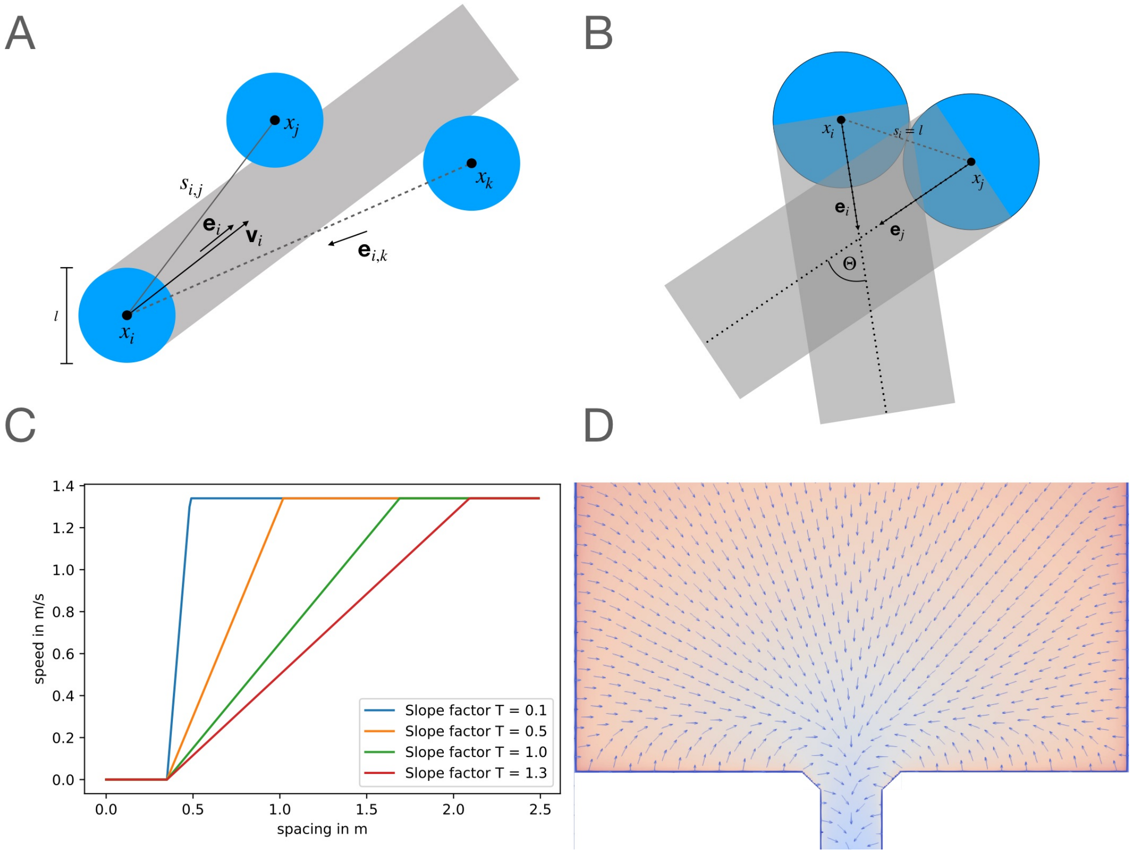

Figure 2.4: (**A**) Illustration of the CSM. Agents that overlap with the grey area are in the set J_i. (**B**) Example of a deadlock situation and the interaction angle Θ. (**C**) Examples for the speed function (2.14) for different slope factors T in s. **D** Illustration of the floor-field $F(\mathbf{x})$ with wall avoidance.

The direction $\mathbf{e}_i$ is determined by two components, the desired direction $\mathbf{e}_0$ of agent i and an exponential repulsive interaction of agent i with all neighbors

$$\hat{\mathbf{e}}_i(\mathbf{x}_i, \mathbf{x}_j, ...) = \frac{\hat{\mathbf{e}}_0 + \sum_{j \neq i} R(s_{i,j}) \hat{\mathbf{e}}_{i,j}}{N} \tag{2.17}$$

with repulsive function $R(s) = a_i \ \exp((l - s)/d_i)$ and N a normalization constant setting $|\hat{\mathbf{e}}_i| = 1$. The repulsion function is calibrated by the repulsion strength $a_i \geq 0$ and the repulsion length $d_i > 0$. The desired direction $\hat{\mathbf{e}}_0$ is determined by a strategy that the agents apply to reach their target. There are a multitude of strategies. In this work the desired direction is determined by a floor field [126]. In this case the continuous floor field consists of two parts which are implemented into JuPedSim.

The quickest way to the exit is determined by the "Eikonal equation" [95]

$$|\nabla c(\mathbf{x})| = F(\mathbf{x}), \quad \mathbf{x} \in \Omega, \quad c|_{\delta\Omega} = 0. \tag{2.18}$$

It solved on the spatial domain Ω, with $\delta\Omega$ the target domain.
The speed of a particle $v = 1/F(\mathbf{x})$ is determined by the slowness field $F(\mathbf{x})$. The time-cost to the target domain is determined by the function $c(\mathbf{x})$. Near the walls, the slowness field decreases linearly with distance, so agents move away from the wall at proximity. The minimal value of the wall avoidance is 0 and the wall avoidance distance d_w is set to 0.25 m. For more details see [141, 142]. An example of a floor field is illustrated in Figure 2.4 D. It can happen that the wall avoidance is not sufficient to hinder the agents from leaving the geometry through a wall. In this case, if an agent crosses a wall in the next time step, it is blocked from doing so by not allowing it to take the step. The resolution of the floor field is set to $\Delta h = 0.01\,\text{m}$.

Stochastic collision-free speed model (SCSM)

A stochastic version of the collision-free speed model (SCSM) is deployed in parts of this thesis. When considering the parameters of the exponential repulsion (2.17), because of the collision-free property of the model [18], agents can get into a deadlock, setting their speed to 0 (Figure 2.4 B). This problem can be solved by adding a white noise term to the desired direction, which also captures the imperfect choice of direction:

$$\hat{\mathbf{e}}_i = \frac{\hat{\mathbf{e}}_0 + \zeta}{N}\,. \tag{2.19}$$

$\hat{\mathbf{e}}_0$ the direction of the floor field and ζ a random direction vector. Both components of ζ are determined by a normal distribution with zero mean and standard deviation σ. The factor N normalizes the vector $\hat{\mathbf{e}}_i$.

Motivation in CSM and SCSM

The motivation is an important factor in pedestrian dynamics especially in the context of bottlenecks, where depending on the motivation the dynamics can significantly differ [1, 2, 32, 80]. In both the CSM and SCSM, the slope factor T_i is an essential parameter to model the effect of motivation. In the simulations conducted for this work, all agents are implemented with a homogeneous slope factor $T_i = T$

for all agents i. This assumption is reasonable for a comparison with empirical data, since the experiments are conducted with a rather homogenous group of participants (e.g. students or soldiers). The general notion is that highly motivated pedestrians jostle into any available gap in their way to try to minimize their distance to the bottleneck as quickly as possible. This corresponds to a smaller value of T, while pedestrians with low motivation keep more distant and leave gaps open, realized by a larger value for T. Figure 2.4 C represents the speed function (2.14) for several values of T. The slope factor T controls at what distance agent i responds to the nearest neighbor in its path (i.e. a neighbor agent j that satisfies (2.15)) and changes the speed as a function of the distance between agent i and j, with a constant slope that depends on the value of T. In the limit $T \to 0$, the speed function reduces simply to volume exclusion, with an agent moving at its desired speed even if the distance to its neighbor is small. In the event of an imminent collision with an agent, the velocity is instantly set to 0. Additionally in the CSM the the Repulsion $R(s)$ is considered. It affects the direction of an agent depending on the surrounding agents (6.1), which should be discussed concerning the effects of motivation on a system. In this case the idea is that highly motivated agents will react at a shorter distance from their neighbors to adjust their path. In turn a higher motivation corresponds to a lower value of the repulsion length d_i, while a low motivation is modelled by a larger value of d_i, which is again homogenous $d_i = d$ for all agents i. The consequence is that a highly motivated agent continue its desired path longer in presence of other agents to minimize the distance to its destination. The exponential repulsion $R(s)$ also directly affects the system's density. This fact is discussed in detail in Section 6.1.

2.4 Self-organization in models

To summarize the successful description of the self-organization phenomena discussed in Section 1.2 in theoretical models: multiple models can reproduce lane formation in counterflow e.g. the floor-field model [143], SFM [144], CSM [18, 22] and other models [20, 144], However the phenomenon is not fully understood. The lanes formed in models are usually rather static compared with dynamical lane formation in empirical studies [16, 126]. The systems also jam at rather low densities. This can be improved upon when including anticipation of the agents to interacting with neighbors in the system [22, 131, 145]. In these models, the agents predict the movement of other agents and adapt their behavior accordingly. At bottlenecks, lattice gas models predict a phase transition between the free-flowing and congested state [146]. The faster-is-slower effect occurs in the SFM [17] and the Floor-Field model [128] with friction. Counterflow at the bottleneck is reproduced in the SFM [16] and the CSM [18]. Stop and go waves are not observed in the SFM [110, 147, 148]. Adjustments to the velocity [110, 149, 150] or the addition of inhomogeneities [151, 152] need to be considered to reproduce this effect. Other examples that can reproduce this phenomenon are a stochastic velocity-based model [153], a semi-continuous and discrete model [20], macroscopic models [154]. A general problem in pedestrian simulations is the tendency to jam, as mentioned above, in bi-directional flow but also at a bottleneck [140]. Especially deterministic models can reach unrealistic jammed or frozen states where the system stays indefinitely [126, 131, 140]. Adding noise on the direction an agent chooses can reduce this problem (see Chapter 6). However, in bi-derectional flow this increased noise can freeze the system [155].

Chapter 3

Pedestrian bottleneck: self-organization phenomena

In Section 1.2, multiple self-organization phenomena at bottlenecks are discussed. This section continues the analysis of a specific self-organization phenomenon observed in recent studies [13, 32]. To reiterate, bottlenecks are one of the most important scenarios in crowd motion. They occur in a wide range of spaces and are impossible to avoid altogether. For example, the entrance to venues needs to be controlled, which can only be achieved by locally restricting the flow into it. These restrictions cause increased densities near the entrance when the motivation in the crowd is high to enter as fast as possible (e.g., when there is a restricted number of spaces close to the stage). The motivation in this scenario is a crucial factor as the dynamics differ significantly between low motivation in a crowd (e.g., students entering a lecture hall on a Monday morning) or high motivation in the scenario of a popular concert. In bottleneck experiments with an unrestricted space in front of a corridor, the density in high-motivation runs increases significantly, and a collective swaying motion perpendicular to the desired direction towards the bottleneck can be observed [1]. The safety in these situations can be improved by using specific geometrical restrictions that are sometimes employed in the entrance area [13]. In 2013 experiments were performed where the space leading to the bottleneck was altered between two different geometries. The study [13] investigates the data gained in the context of social norms and rules of conduct humans follow in this scenario, depending on their environment. The two different geometries were a wide corridor with no restrictions for the participants and a narrow corridor with a 90° turn leading into the bottleneck. The situation is illustrated in Figure 3.1. In the

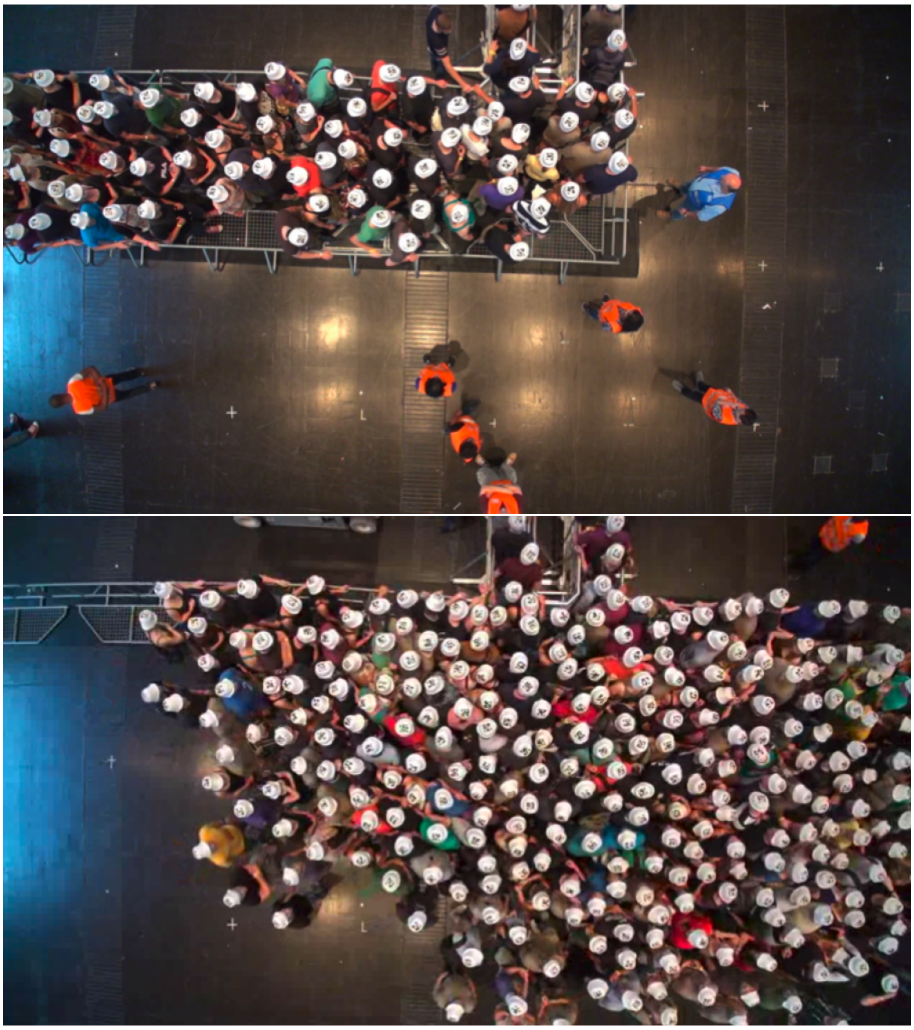

Figure 3.1: Photo of the experiment modified from [13]. On the **top** is the corridor setup, while on the **bottom**, the unrestricted setup is presented.

experiment, the participants were told to enter a venue through a bottleneck with high motivation because they want to have a good view, and the number of places are restricted. Initially, they were distributed loosely to ensure a low density at the start of the experiment.

Surprisingly the narrow corridor setup has a significantly lower density near the bottleneck compared to the wide area, even though in the wider setup, the pedestrians have more space to distribute. This fact is illustrated in Figure 3.2 A and B. Panel A shows the trajectories of every participant and the measurement area for the density in the red square. In the wide corridor, the participants form a semicircle in front of the bottleneck. The density for the unrestricted setup and the corridor in the measurement area are depicted in panel B. In the unrestricted setup, the density ρ [1] is consistently higher by a factor of about 1.8. In this case, participants fill gaps quickly, leading to pushing behavior, which is less observed in the corridor.

The hypothesis in the study [13] is that social norms affect the behavior of the participants in different environments. The idea is that the narrow corridor triggers a different behavior in the participants that leads to them queuing up to the entrance, which would also cause the lane formation observed in Panel A of Figure 3.2 in the narrow corridor. However, the data from the experiment is insufficient to make a definite statement about this claim.

A new experimental setup with a simplified geometry of a variable straight corridor (see Figure 3.2 C) was conducted in 2018 [32]. Additional to the simplified geometry, motivation was introduced as a variable. It was modulated by describing different scenarios. In the low motivation runs, the participants were told that enough spaces are in the venue for a good view. In the high-motivation runs, they were told that only a restricted number of places have a good view, and they want to get one of those. The influence of the corridor width was investigated by varying it between $b = 1.2\,\mathrm{m}$ to $b = 5.6\,\mathrm{m}$ in $\Delta b = 1.1\,\mathrm{m}$ steps. For the analysis, the density and flow are measured in the area specified in Figure 3.2 C. The main results from the experiments are discussed in detail below. For a short summary: the increase in corridor width increases the density in the measurement area monotonously for both motivations. High-motivation runs have a consistently higher density than low-motivation runs. The participants were asked to fill out a questionnaire to investigate the influence of social norms. The results cast doubt on the relevance of social norms to explain the increase in density for a given motivation since social behavior, like queuing norms,

---

[1] The density ρ is calculated via the Voronoi method defined in Section 3.1.

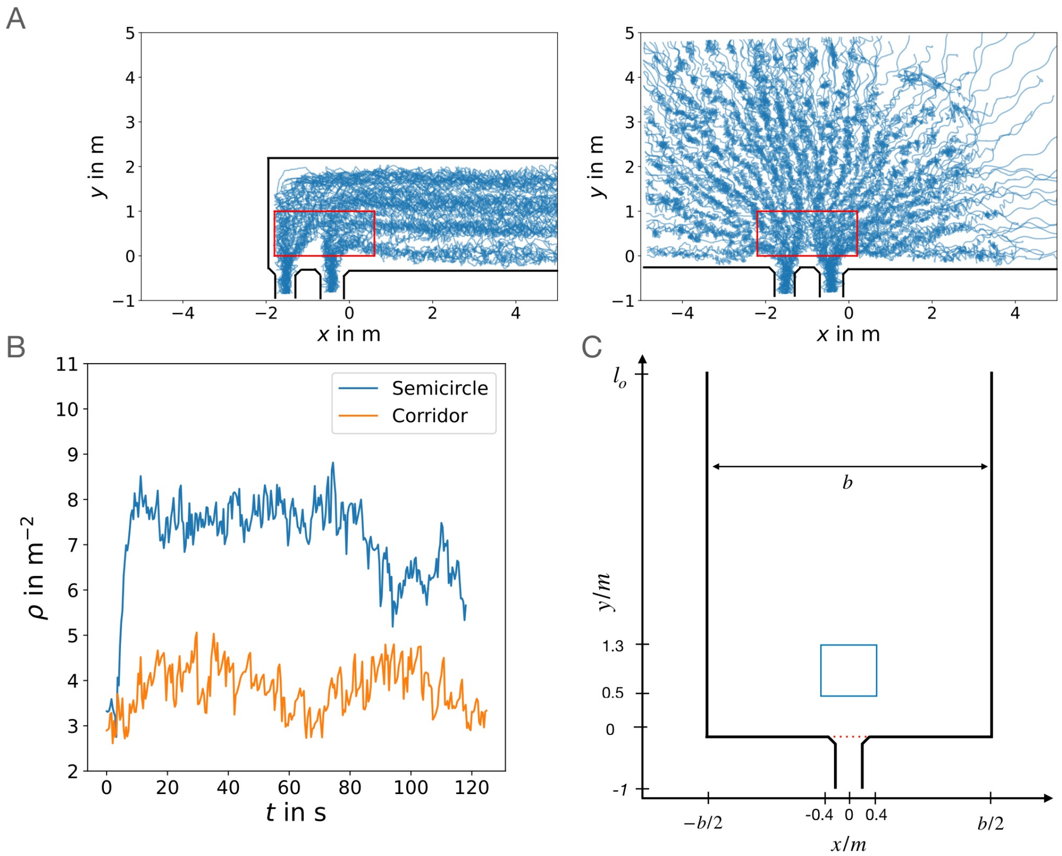

Figure 3.2: (**A**) Cumulative trajectories from the experiments [13] for both corridor geometries. (**B**) The pedestrian density measured in the area marked by the red rectangle in A. (**C**) The geometry analogous to the experiments [32] used in the simulations with the area to measure the density ρ marked by the blue square and the border to measure the flow j marked by the red line. Panel A and B are adapted from [13].

could not be detected. However, a theoretical study utilizing simulations of a cellular automata model hints at a physical explanation for the density increase [101]. The cellular automata model has limited spatial resolution due to its discrete nature. In the following, the stochastic collision-free speed model (SCSM, see Section 2.3) is employed to simulate the situation investigated in [32] with varying corridor width using the geometry in Figure 3.2 C.

The SCSM's simple interactions and continuous nature make it a suitable candidate to investigate the scenario. Recreating the observed effects of density increase and lane formation in such a basic model is a strong indicator that social norms are not necessary to explain these effects in the presented situation. However, it should be stated that this approach is not to diminish the role of social psychology but to highlight the challenge of properly distinguishing social psychological effects in pedestrian dynamics from emergent physical phenomena. In the following, the experimental data [32] is discussed in more detail, introducing the specific methods to compute the density and flow of the system [2].

3.1 Experimental data and observables

To be able to discuss the experimental [32] and simulation data [33, 156], the methods to measure the observables need to be introduced. The focus of this investigation is mainly on the density and flow. The method to calculate the density from the experimental and simulated trajectories in a set measurement area relies on the concept of the Voronoi diagram.

3.1.1 Voronoi diagram

A Voronoi diagram [157] partitions a plane into subdivisions closest to a defined set of objects. In the context of this thesis the two-dimensional plane $\mathbf{X}$ is relevant, where the objects are either pedestrians in an experiment or agents in a simulations with defined central points. In this case $\mathbf{X}$ is divided into subregions called Voronoi cells. The positions of the N agents $\mathbf{r}_i, i \in \{1, N\}$ at a given time act as vertices of the Voronoi diagram. A point in space belongs to the Voronoi cell R_i of agent i if the euclidean distance $d(\mathbf{r}_i, \mathbf{x}) = |\mathbf{r}_i - \mathbf{x}|$ to agent i is minimal compared to all other agents. The set R_k is defined as

$$R_k = \{\mathbf{x} \in \mathbf{X} \mid d(\mathbf{x}, \mathbf{r}_i) \leq d(\mathbf{x}, \mathbf{r}_j) \, \forall \, j \neq i\} \,. \tag{3.1}$$

The Voronoi diagram of a random set of points is illustrated in Figure 3.3.

3.1.2 Density

The main focus in this section is on the mean density in front of a bottleneck. The simplest method to measure the density ρ is to divide the number of pedestrians N by the size of the measurement area $|A|$, $\rho = N/|A|$. This method has two drawbacks. The first problem is that there needs to be an arbitrary decision about

---

[2] The results of this chapter are published in two journals [33, 156]. The presented analysis and text base on [33].

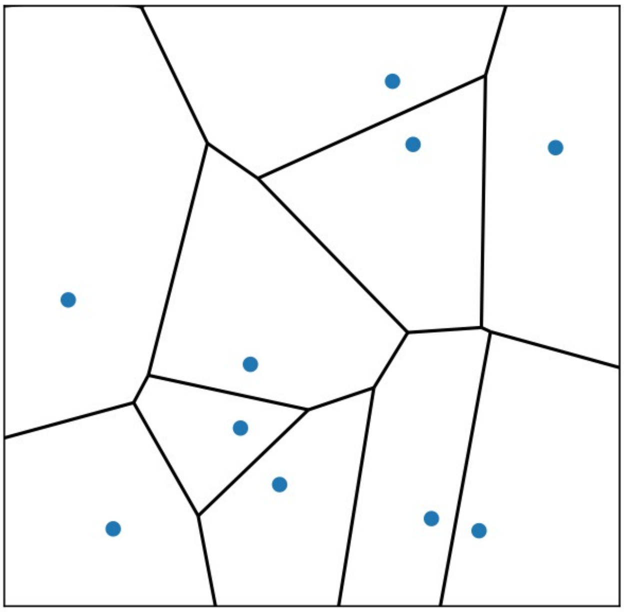

Figure 3.3: Illustration of a Voronoi diagram.

which agent is inside the measurement area and which is outside since pedestrians are not point particles. The second problem is that since only an integer numbers of pedestrians can be inside the measurement area, a pedestrian leaving or entering the area produces discontinuous density measurements. Three different measures for the density are used in this thesis to solve the issues. To be consistent with [32], the mean density in the measurement area is measured using the Voronoi method introduced in [158] since it produces smooth density curves. The computational procedure is as follows: given a set of trajectories at time t of N pedestrians with position $\mathbf{X} = \{\mathbf{x}_0(t), \mathbf{x}_1(t), \mathbf{x}_2(t)...\mathbf{x}_N(t)\}$ on the two-dimensional plane. Use $\mathbf{X}$ to compute the Voronoi diagram introduced above, which defines the cell A_i for each pedestrian i. At last calculate the size $|A_i| = \int_{A_i} d\mathbf{x}$ with which the density distribution $\rho_i(\mathbf{x})$ of pedestrian i can be defined as

$$\rho_i(\mathbf{x}) = \begin{cases} 1/|A_i| & \mathbf{x} \in A_i \\ 0 & \text{else} \end{cases} \quad \text{and} \quad \rho(\mathbf{x}) = \sum_i \rho_i(\mathbf{x}) \tag{3.2}$$

The mean Voronoi density in a measurement area A is then defined as

$$\rho_0 = \frac{\int_A \rho(\mathbf{x}) d\mathbf{x}}{|A|}. \tag{3.3}$$

A second approach to calculate the density field over the whole corridor area is used to get detailed density maps with homogeneous shapes of agents. In this case, the local density ρ in the system can be defined as

$$\rho(\mathbf{r}; \mathbf{X}) = \sum_{i=1}^{N} \delta(\mathbf{x}_i - \mathbf{x}), \quad \rho(\mathbf{x}) = \langle \rho(\mathbf{x}; \mathbf{X}) \rangle, \tag{3.4}$$

where the mean is taken over the realisation $\mathbf{X}$ of the system. In a computation with finite resolution the Dirac delta-function $\delta(x)$ can be approximated by a Gaussian

$$\delta(x) = \frac{1}{\sqrt{\pi} a} \exp[-x^2/a^2] \tag{3.5}$$

but other functional representations are possible e.g., a cylinder (see [2]). The local density of an agent is defined via the area A_i of the Voronoi cell.

$$\rho_n = 1/|A_i| \tag{3.6}$$

Due to the volume exclusion and the densest packing of circles, the maximal local density a circular particle can have is defined by the area of the hexagon with diameter l. The area of this hexagon is $A_{hex} = \sqrt{3}/2\, l^2$ and the resulting maximal density is

$$\rho_{max} = A_{hex}^{-1} = 2/\sqrt{3}\, l^{-2}. \tag{3.7}$$

3.2 Density of the experimental trajectories

The experimental data [32, 159] is reanalyzed in this study to allow a better comparison to the simulations. The geometry of the corridor is illustrated in Figure 3.2 C. The exit has a width of 0.5 m. The corridor width is varied between five values, $b \in \{1.2, 2.3, 3.4, 4.5, 5.6\}$ m. Measurements for the mean density are made in a rectangular area between $x = \{-0.4, 0.4\}$ m and $y = \{0.5, 1.3\}$ m. The outflow and exit times are measured at the $y = 0$ m line by counting the number of participants

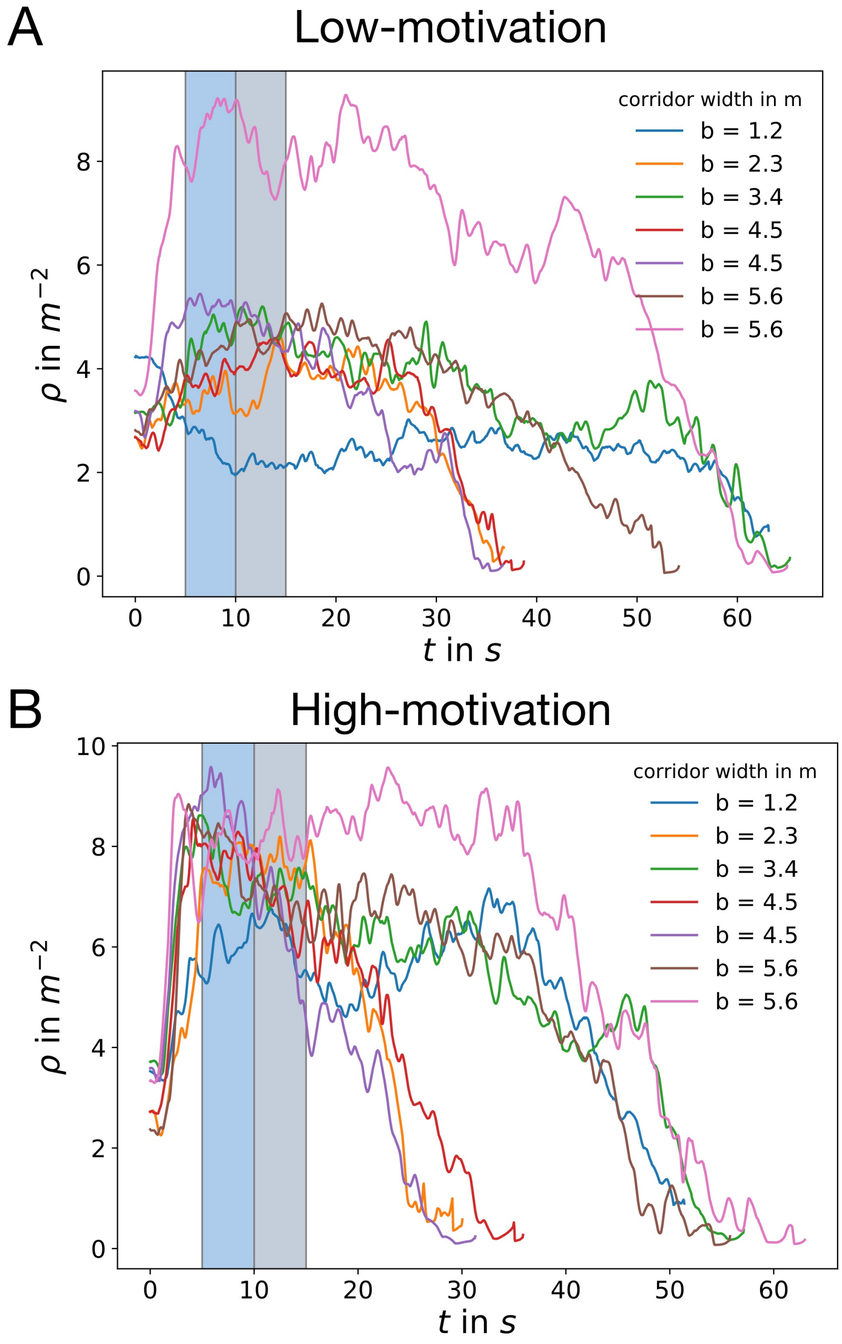

Figure 3.4: Voronoi density time series from the experiments [32] for low-motivation (**A**) and high-motivation (**B**). The blue and grey areas mark the region between 5 and 10 s and 10 and 15 s. The measurement of the density is conducted in the area presented in Figure 2.4 B.

that cross the line in the time interval Δt. The mean density time series for the different experimental runs are shown in Figure 3.4 both for the experiments with low and high motivation. These are all runs considered in this study. Runs with fewer than 42 participants (i.e., 20 - 25 participants) have been discarded in this study since it is unclear whether a consistent, steady state is reached. In the experimental study, the measurement time interval for the mean density is from 5 s to 10 s to have comparable conditions, considering the varying and limited number of participants. In this study, the interval between 10 s and 15 s is measured to be closer to a steady state, as can be observed for most runs in Figure 3.4. Only the runs for $b = 4.5$ m in the high motivational case (Figure 3.4 B) do not reach a consistent steady-state as the mean density quickly peaks between 5 s and 10 s and decreases from there on. The mean values for the experiments in the 5-10 s and 10-15 s interval are shown in Figure 3.6 A.

3.3 Simulation of the experiment

To analyze the situation from a theoretical standpoint, the SCSM is implemented numerically using the geometry shown in Figure 3.2 C. Before discussing the results, the initial conditions have to be defined. The experiments used motivation as a variable, which is discussed in the context of the SCSM in Section 2.3. The theoretical study aims to distinguish the social psychological effects from emergent physical effects in the specific scenario described above. The following discusses the connection between social psychology and variables in a mathematical model of pedestrian dynamics.

Psychology and model parameters

The parameters in the SCSM and CSM are connected with fundamental diagrams (see Section 1.1). The speed function 2.14 is a special representation of the fundamental diagram showing the linear speed and distance relationship in a certain interval [160]. The relationship depends on the desired speed v_0, the slope factor T, and the diameter of the disc-shaped agents l. These parameters in the model can be described as a set of individual properties $P = \{P_1, P_2, ...\}$ that depend on factors like gender, culture, body height, or motivation [48, 74, 161–164]. Additionally, environmental factors $E = \{E_1, E_2, ...\}$ have to be considered as an influence.

For example, background music and rhythms can influence the behavior of pedestrians [165, 166], as is visible in [167]. Psychological influences in the model would translate to a dependence of the parameters on these factors, e.g., agent i has the parameter $T_i = f_i(P, E)$, and $v_{0,i} = g_i(P, E)$ determined by the unknown functions g_i and f_i. A simple example in this thesis is the assumption that the motivation (see Section 2.3) influences the slope factor T, decreasing it with increasing motivation. In its current state, pedestrian research is not capable of estimating the functional form of these influences or identifying the major influences. To distinguish between the physical and social psychological effects, the SCSM is implemented with mostly static and homogeneous parameters for all agents, except for the variation of the slope factor T as a consequence of a change in motivation as an initial condition (which is estimated to first order). The only environmental variable is the corridor width, which has no influence on the parameters of the model.

Parameters and initial conditions

The desired speed is set to $v_0 = 1.34$ m/s, which corresponds to the empirically estimated mean walking speed for unobstructed pedestrians [168]. The other free model parameters are estimated from experimental data [32]. Non-deformable disks represent agents with fixed diameter l. The exclusion property of the model then provides an upper bound on the density. To estimate the agent diameter from the experimental data, the maximum density $\rho_{\max}$, which is slightly above 9 m^2 for highly motivated runs, is taken as the pivot point (see Figure 3.4). Assuming that this maximum density corresponds to a (hexagonal) dense packing of disks, one finds that $r_a = 0.175$ m corresponds to a maximum density of $\rho \approx 9.4\,\mathrm{m}^2$. Simulations with this value give good results; see Appendix A.1 for more details.

Initial density and population size

The influence of the initial density ρ_i on the mean density ρ in the measurement area needs to be discussed. Figure 3.5 A shows the mean value of the density between 10 s and 15 s, with the initial density ρ_i on the x-axis. The initial density has a non-negligible influence on the density. This is particularly pronounced for narrow corridors ($b < 3.4$m) and reduces in wider corridors ($b > 3.4$m) with $\rho_i > 2\mathrm{m}^{-2}$. The initial Voronoi densities ρ_i in the experiments are approximately identical between $1.5 - 3.0\ \mathrm{m}^{-2}$ (see Figure 3.5 C). To meet this criterion, the corridor length l_c is

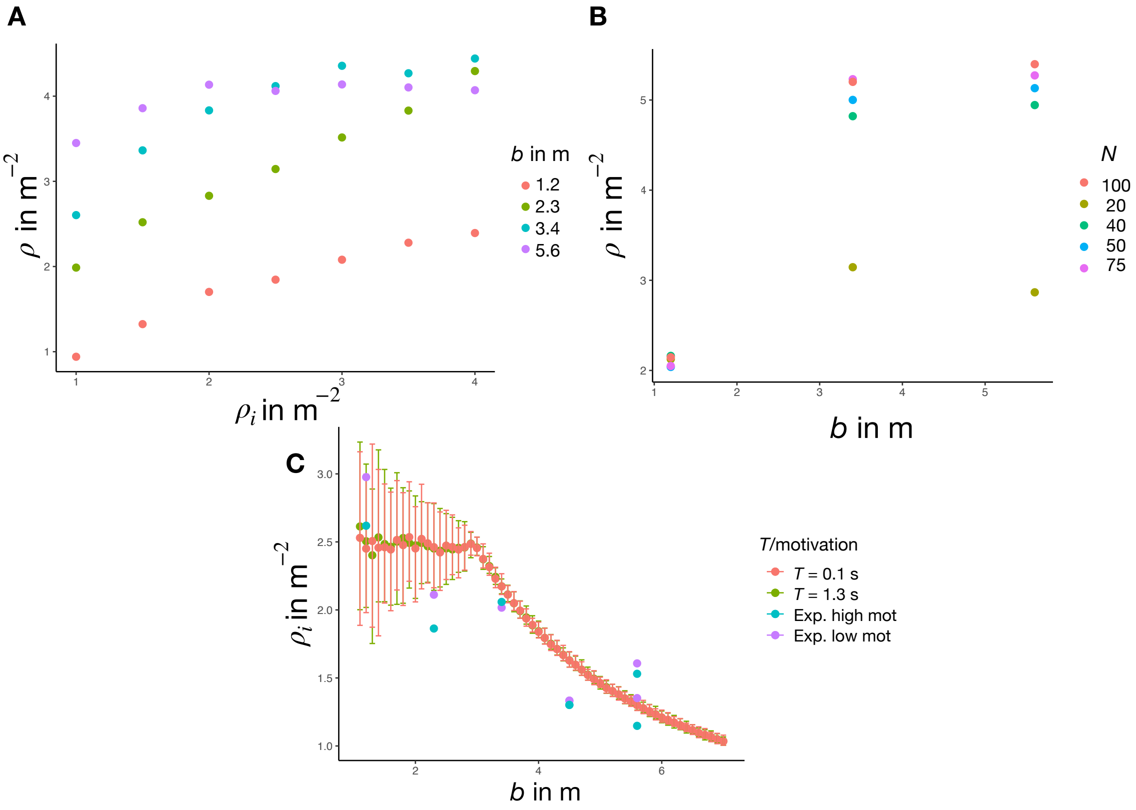

Figure 3.5: (A) Mean density after 10 s with respect to the initial density ρ_i in the corridor for different corridor width b. **(B)** Mean density after 10 s in respect to the corridor width b for a different number of agents N. **(C)** Mean Voronoi density for different initial densities ρ_i in the whole corridor from $y_{min} = 0\,m$ to $y_{\max} = 7.0$ m. Comparison between experimental (Exp.) and simulation densities for high and low motivation.

adjusted so that the agents are evenly distributed over the corridor area and can satisfy the initial conditions. The length is set to $l_c = N/b\rho_i$ until the corridor length is less than 7 m (the corridor length used in [32]). From there, the corridor length stays constant. The initial density ρ_i is chosen randomly from a uniform distribution $\mathcal{U}(2.0, 3.0)$. Figure 3.5 C shows the initial experimental densities in comparison to the simulation. For corridors with $b < 3.4$ m, the corridor length $l_c < 7$ m and thus have a wider range of values. As mentioned, runs with fewer than 42 participants are excluded from the experiment. Figure 3.5 B shows that in the model for $N > 40$, the number of agents has a limited but not negligible influence on the mean density. To obtain comparable results for the mean Voronoi density with respect to the corridor width, the number of agents in the simulation is set

Parameter	Variable	Value
Slope factor (motivation)	T	$\{0.1, 1.3\}$ s
Desired velocity	v_0	1.34 m/s
Agent size (hardcore exclusion)	l	0.35 m
Noise standard deviation	σ	0.7
Population	N	55
Floor field resolution	Δh	0.01 m
Wall avoidance distance	d_w	0.25 m
Corridor width	b	$[0.8, 7.0]$ m
Bottleneck width	w	0.5 m

Table 3.1: Summary of model parameters and their values.

constant at $N = 55$ in the center of the participant range. The simulation runs are calculated in a range of $b = [0.8, 7.0]$ m in 0.1 m steps. For each value of b, 500 simulation runs are performed with random initial conditions. This results in 31000 for each motivation $T = \{0.1, 1.3\}$ s and a total of 62000 simulations for the main analysis. The model parameters are summarised in table 3.1.

3.4 Comparing the SCSM with experimental data

For the experimental data, the measurement interval for the mean density is between 5 s and 10 s. This interval was chosen to obtain comparable results because the number of participants varies between runs and, as described above, affects the mean density. Since the simulations control the number of agents, it is also interesting to consider a second interval and compare it to the experimental data. Here the interval of 10 s to 15 s is chosen. Figure 3.6 A compares the simulation results with the experimental data. The error bars show the 95% interval of the 500 runs performed. The simulations reproduce the increase in density with corridor width b without adjusting any other parameter for a particular motivation. The increase in density from a low to a high motivation can be reproduced by adjusting the slope factor T. The mean density measured between 10 and 15 s shows a monotonically increasing behavior until it saturates at about $b = 3.2$ m. At low motivation ($T = 1.3$ s), the density is not monotonic. The experimental data are mostly within the 95% interval, with 19 of the 28 points being inside, while the points outside are closely spaced. In particular, the runs for $b < 4.5$ m are in good agreement with the experimental data.

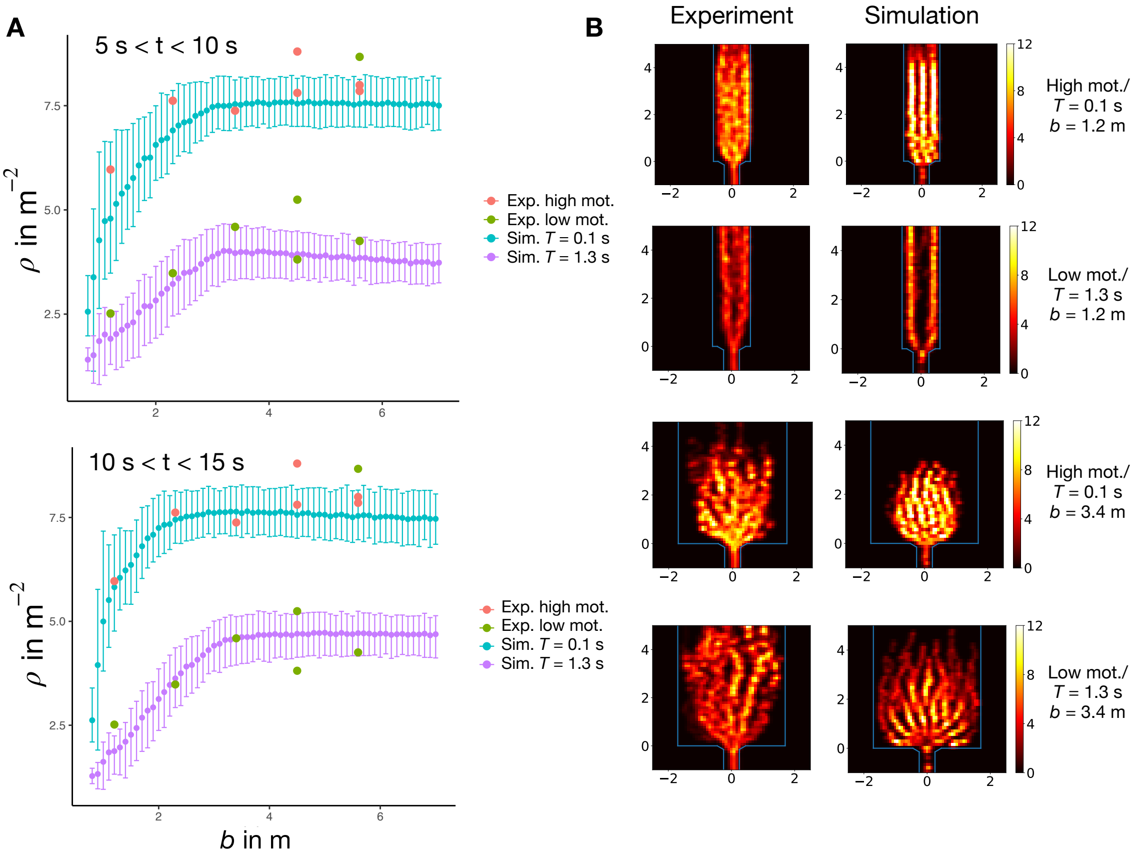

Figure 3.6: (**A**) **Top:** Mean density in the measurement area calculated with the Voronoi method from $5-10$ s for different values of the slope factor T (Sim.) and motivations in the experimental data (Exp.). The simulation runs were conducted 500 times for each corridor width b. The error bars show where 95 % range of the mean. **Bottom:** The same as above from $10-15$ s. (**B**) Density fields for different motivations and corridor width b. **left column** depicts the experimental data while the **right column** shows the simulation results. From top to bottom, the motivation alternates between high motivation ($T=0.1$ s) and low motivation ($T=1.3$ s). The corridor width is $b=1.2$ m in the top panels and $b=3.4$ m in the bottom panels.

The runs for $b=4.5$m show the largest deviation from the simulation results for high motivation. As explained in the previous section, the experimental runs for $b=4.5$m do not reach a steady state at high motivation. In the low motivation data, there is an outlier for $b=5.6$ m, where the density is comparable to the high motivation scenario. This is the largest run with $N=75$ participants. Figure 3.5 B shows the density for low motivation and a different number of participants. However, the increased number of agents cannot explain the high value of the measured density.

To better understand the overall dynamics in the corridor, the density field of a

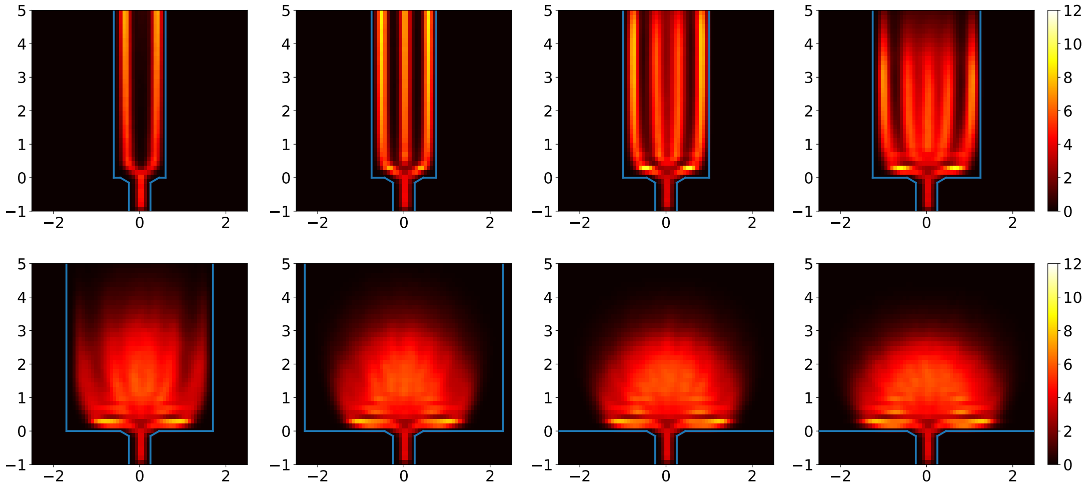

Figure 3.7: Mean density fields (m^{-2}) on the x-y plane (m) for all 500 runs from 10 to 30 s for $T = 1.3$ s. The top row shows the runs with corridor width $b = \{1.2, 1.5, 2.0, 2.5\}$ m. The bottom row shows values for $b = \{3.4, 4.6, 5.8, 7.0\}$ m.

single run is calculated according to the equation (3.4). Figure 3.6 B depicts the density fields for $b = 1.2$ m and $b = 3.4$ m from the experiments and simulations. At low motivation and $b = 1.2$ m, two equally lanes form in both the experiments and the simulations, which merge near the exit. In the high motivation case, three lanes form in the simulation and the total density increases. In the experiments, the total density increases, but there are no clearly identifiable lanes. In the case of low motivation with $b = 3.4$ m, clear lane formation can also be observed in both the experiments and the simulation. One noticeable difference is that the agents in the simulation near the $y = 0$ line are broadly distributed over the entire corridor, whereas the distribution of participants near the exit is wedge-shaped. One possible reason for this is the experiment's barricades, which have metal grids (see Figure 3.11 C). These seem to be avoided by the experiment participants, especially during the low-motivated runs, and could therefore be an obstacle. This becomes clearer when looking at the videos of the experiments, which are available at [169]. In the simulations, this circumstance was not taken into account in order to keep the geometry simple, as the wedge shape reduces or disappears altogether in the high motivation case (Figure 3.11 D). In this case the experimental participants and the simulation agents are more compressed than in the low motivation case. Distinct trajectories can be observed for both motivations. The wedge shape in the density profile is still recognisable, but less pronounced in the experimental data.

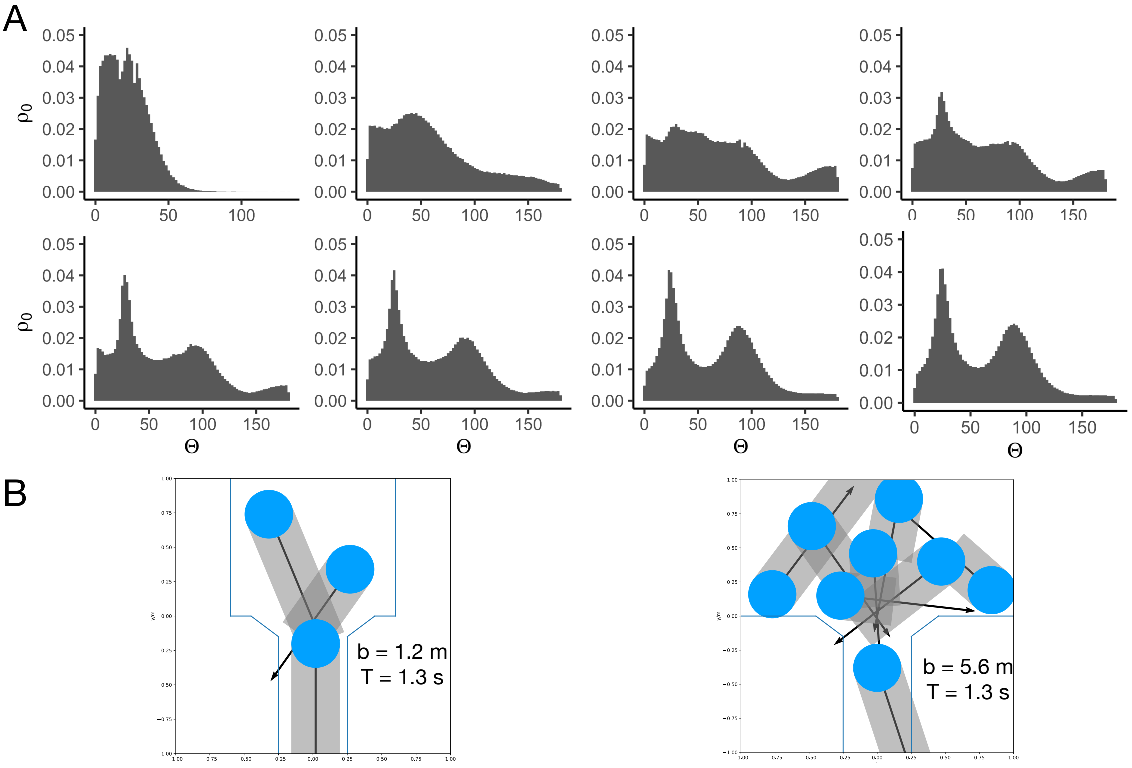

Figure 3.8: (**A**) Interaction angle distribution for all 500 Simulations from 10 s for $T = 1.3\,\mathrm{s}$. The top row shows the runs with corridor width $b = \{0.9, 1.4, 1.7, 1.8\}$ m. The bottom row shows values for $b = \{2.0, 2.3, 3.0, 4.5\}$ m. (**B**) Configuration in front of the bottleneck from a simulation with $b = 1.2$ m and $b = 5.6$ m.

The dynamics of the systems in the region of b with saturated density compared to the region where the density increases become clearer in Figure 3.7, where the mean density field of selected corridor widths is shown for all 500 runs. The top row shows runs with $b < 3.2\,\mathrm{m}$, while the bottom row shows runs with $b > 3.2\,\mathrm{m}$. The widening of the corridor impacts the dynamics of the evacuation process. As b increases, new lanes form, and the interaction angle at the merge point between the desired direction of the agents and the bottleneck steepens. Because of this the potential for conflicts increases and therefore the density. For $b > 3.2$ m, the influence of the corridor width is small, as the formation of new lanes has little influence on the situation near the bottleneck. Figure S3 shows an analogous comparison for simulations with high motivation, with similar behavior. The distribution of the interaction angle, as defined in Figure 2.4 B is depicted in Figure 3.8 A for varying b in a radius of $r = 1$ m around the point $\mathbf{r} = \mathbf{0}$. The area is chosen because there the lanes merge (see Figure 3.7). The interaction angle is defined as the angle between the noiseless desired direction of an agent and the noiseless direction of the agent with which it interacts (i.e., the agent that satisfies the conditions given by equations (2.15) and (2.16)). Noiseless means that the noise defined in equation (2.19) in the SCFM is ignored, and the interactions are calculated according to the desired direction determined by the eikonal equation (2.18). This corresponds to the expected interaction angle for the specific configuration between two agents. The situation is illustrated in Figure 3.8 B for a wide and a narrow corridor.

The transition of the distribution in panel A shows an interesting behavior where existing peaks with smaller b disappear as b gets wider, and new peaks appear until the distribution stabilizes with a bimodal distribution. In general, the probability of larger interaction angles increases with b. The shape of the distribution can be divided into three regimes. When b is small ($b < 1.4$ m), the probability of interaction angle is highest at small angles $\Theta < 50°$ and decreases monotonically at larger angles. For $b > 1.4$ m and $b < 1.8$ m, the distribution widens with a higher probability for large interaction angles up to 180°. For $b = 1.7$m, no pronounced peak is observed. Widening b further causes a new peak to emerge at about 30°, making the distribution uni-modal. Further widening the corridor turns the distribution bimodal with a narrow peak around $\Theta = 30°$ and a broader peak at $\Theta = 90°$. This structure is stable for large $b > 3$ m. Interactions at larger angles have a higher potential for conflict because the noise is not as sufficient in resolving these conflicts compared to smaller angles where pedestrians follow each other. At high motivation ($T = 0.1$ s, Appendix A.1 Figure S5) the behaviour is similar, but the transitions occur at smaller b. The distribution converges to a bimodal shape but with a more pronounced peak at a smaller angle and a smaller peak at a large angle.

An additional observable that was measured in the studies of Adrian et al. and Garcimartin et al. [2, 32] is the waiting time T_w of the pedestrians with respect to the distance to the door r at time t. In the study of Garcimartin et al. [2], participants are not constrained by a corridor, i.e., the corridor can be assumed to be infinitely wide. The study argues that the evacuation time should follow a power law distribution $T_w \propto r^\alpha$ with $\alpha = 2$ in the case of a wide corridor. The evacuation time for a single pedestrian leaving the area scales linearly with r. In a crowded scenario, pedestrians interact. Assuming that the movement of the pedestrians can be approximated as a fluid with laminar flow, the velocity scales with $1/r$ due to the continuity. Therefore, the evacuation time scales with r^2. In a narrow corridor

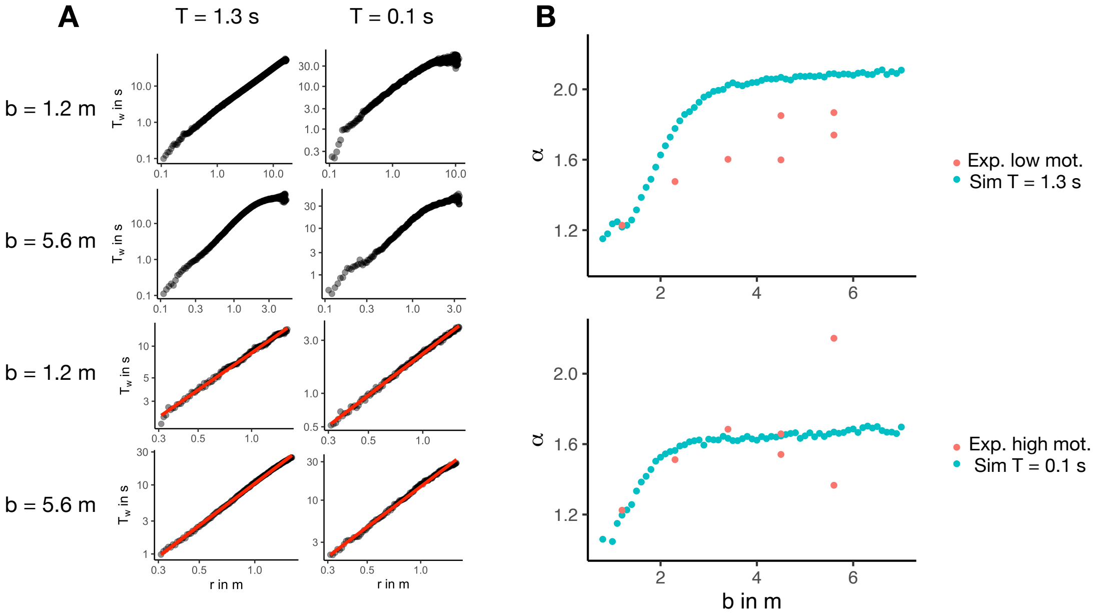

Figure 3.9: (**A**) Waiting time to target T_w in respect to the distance r from the target between 10 and 20 s with all 500 runs pooled together. The left column depicts runs with $T = 1.3$ s, while the right column depicts runs with $T = 0.1$ s. The alternating order from top to bottom shows the results for $b = \{1.2, 5.6\}$ m for different cut-off distances of the data (no cut-off for the top two values and 1.5 m for the bottom). (**B**) The power law exponent for the waiting times for low motivation and $T = 1.3$ s in the top panel and high motivation and $T = 0.1$ s in the bottom panel.

the flow is close to single file motion, where the evacuation time should only depend on the distance to the bottleneck and scales linearly with $\alpha = 1$

This relationship is tested by taking the evacuation time for all runs, measured between 10 s and 20 s. The euclidian distance to the exit is measured from the point $\mathbf{r} = \mathbf{0}$. At every timestep with $\Delta t = 0.5$ s, the evacuation time T_w is calculated for each agent. The timestep Δt is chosen so that the position of each agent changes sufficiently. The log-log plot of T_w with respect to r is depicted in Figure 3.9 A. The evacuation time for all distances is shown in the top four panels. The power law relationship is true between $r = 0.3$ m to about $r = 1.6$ m. Figure 3.9 B shows α as a function of b for both motivations. For $b = 0.8$ m, the exponent is close to one. As expected for low motivation, α increases and saturates around $\alpha = 2$. Though the exponent α calculated from the experimental data [32] is only close to the simulation data for $b = 1.2$ m.

For high motivation, the exponent converges to a value of about $\alpha = 1.7$, which is in close agreement with the values for α calculated from the experimental data. For $b = 5.6$ m, α is scattered widely. These runs differ significantly in the number of participants. The smaller value was performed with $N = 57$ participants, while the larger value comes from the run with 75 participants. Figure 3.11 A shows α for simulations with different N, $b = 5.6$ m and $T = 0.1$ s. The number of agents affects α, which increases to $\alpha = 2$ for $N \approx 100$. The smaller exponent could be due to the lack of a complete semicircle in the analyzed region because of the compact clustering of pedestrians (see Figure S3). In general, the runs with high motivation fluctuate more than those with low motivation. The deviation of the simulation from the empirical data calculated values for low motivation could be a consequence of the already mentioned wedge-shaped, as this influences the geometry near the bottleneck. To check this, simulations are run with a different geometry. Instead of a horizontal lower wall, as shown in Figure 2.4 C, The wall has a 45° angle up to the intersection with the vertical wall (Figure 3.11 C). Figure 3.11 B depicts the results for varying values of b. The simulations are repeated 50 times. The value for α saturates around $\alpha = 1.8$ and is closer to the values calculated from the experiment.

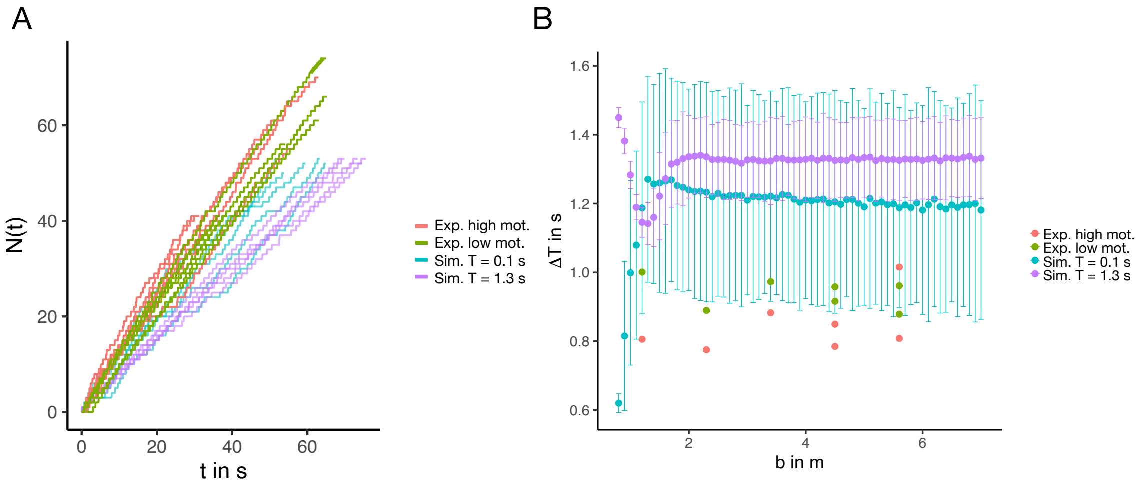

Figure 3.10: (**A**) N-t diagram for the experimental data (vibrant colors) with high motivation (red) and low motivation (blue). Analogous exemplary simulation data (pale colors) for the same corridor width b as in the experiments using one run per width. (**B**) Simulation and experimental results for the exit-time differences ΔT. The error bars show the 95 % Interval of the simulation data for 500 runs.

The N-t-diagram and the intermediate timegap ΔT are depicted in panels A and B of Figure 3.10. The timegap ΔT is the time between the successive crossing of

agents over the $y = 0\,\mathrm{m}$ line.
The time interval is proportional to the reciprocal flow $\Delta T \propto J^{-1}$. The results show that the agents in the model are less efficient in exiting through the bottleneck than participants in the experiments. The mean timegap increase when widening the corridor while b is narrow but reach a plateau at about $b = 1.8\,\mathrm{m}$. The experimental data do not exhibit this behavior. The faster-is-slower effect [17] can be observed neither in the model nor in the experiments. This agrees with the experiments of Haghani et al. [84], where aggressive pushing was forbidden, and with recent numerical studies using the SFM [85]. The spread between the data points of the different runs is larger for $T = 0.1$ s than for the runs with $T = 1.2$ s. This is due to the increased occurrence of clogs in the system, which are evident in the N-t diagram (Figure 3.9 D). Similar behavior is observed in the experimental data, where the initial slope of the curve is larger. Still, clogging may interrupt the flow for a long time. More data are needed to make a more conclusive statement, but a higher probability of larger ΔT is reported in [1]. Agents in the SCFM only react to the presence of other agents in their path. However, they cannot communicate their intentions to their environment or anticipate the behavior of other agents. This could indicate that the absence of a cooperation and negotiation mechanism [86] in the model as a reason, supported by the increase in ΔT with increasing b as conflicts become more frequent.

3.5 Summary

To summarize, the SCSM is able to reproduce the empirical observed phenomena of density increase and lane formation in the narrow corridor using a minimal number of variables in the low and high motivation scenario. The effect of the motivation on the density can be modeled by adjusting the slope factor T, while for the density increase, no other variable is altered except for the corridor width b. The simplicity of the model implies that the effects studied do not stem from social behaviour.

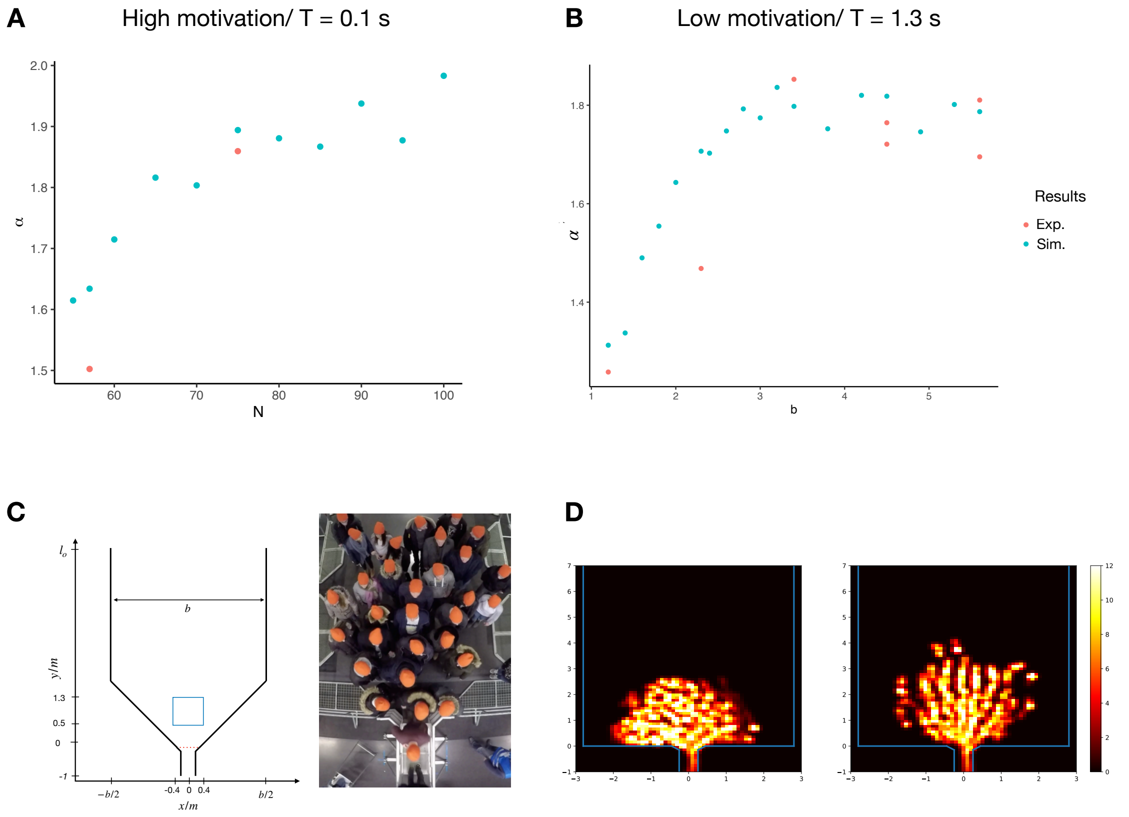

Figure 3.11: **(A)** Simulation results for α in respect to the number of agents N for $b = 5.6$ m between 10 and 20 s. Every data point is the mean of 50 simulations. **(B)** Exponents α of the power law for the waiting times for low motivation using the hopper-shaped geometry for $T = 1.3$ s shown in panel C. **(C)** Illustration of the geometry with hopper shape walls and a Snapshot from an experimental run [32] with low motivation. **(D)** Heat maps for the experimental runs with high motivation (left) and low motivation (right) with a corridor width of $b = 4.5$ m.

Chapter 4

Structure in atomic and granular materials

The previous section illustrated that a better understanding of microscopic interactions of pedestrian dynamics is necessary to distinguish better the human characteristics of pedestrian and crowd dynamics and their granular physical features. Generally, the granular approach to pedestrian dynamics is popular, and especially in bottleneck flow, these approaches are closely studied alongside granular realizations of analogous systems [1, 22, 76, 170–176]. The studies of bottleneck flow apart from pedestrian dynamics are not constricted to granular particles falling under the influence of gravity. Studies of self-driven 'hex bugs' are gaining popularity as a simplified setting for pedestrian bottleneck experiments [177–179]. A crowd traversing through a narrow bottleneck and granular materials falling through a vibrated hopper or active particles share several features. The survival function of stable clogs in high motivation experiments displays a power law tail $P(t_c > t) \propto t_c^{-\alpha}$ [82]. This feature is especially noteworthy because for an exponent $\alpha < 2$, the mean timegap t_c of two consecutive pedestrians passing the bottleneck diverges, and the flow rate vanishes for large systems. The burst size of pedestrians exiting the bottleneck is exponentially distributed [174] and the faster is slower effect can be observed in both kinds of systems (on the controversies of this, see Section 1.2). In granular systems, the faster is slower effect can be achieved by increasing the slope of the hopper or turning up the drive that is responsible for the movement of active particles [27, 82]. Most studies analyze macroscopic features of the system, like the flow J or the density ρ of the system. There are also studies analyzing microscopic features of the bottleneck flow, mostly the structure of the clogging arches in pedestrian models and granular systems [22, 76, 172, 173, 180]. Recently several studies consider the spatial structure of pedestrian systems in bottleneck flow [39] and in more general setting [37, 181–183]. This takes the analogy between granular matter and pedestrian systems further considering granular dens packing [184]. These ideas lead back to the discussion of human psychology and the ability of humans to make decisions. In situations where, because of the volume exclusion principle, the possibility to make decisions could become restricted to the point where the difference between granular matter and active particles vs. humans becomes insignificant. To further the analogy between granular matter and pedestrians, it is interesting to not only consider macroscopic features but to utilize measures from solid-state physics and granular physics that characterize the structure and order of a system. To build a coherent framework for this analysis, the following section is a brief excurse into basic concepts of solid state and granular physics in the context of defining order and structure in media.

4.1 Crystal structure, amorphous solids and order

This short introduction into crystalline structures and order is mainly based on [185]. Crystalline structures are a central topic in condensed matter physics. They exhibit periodic recurring atomic structures (e.g., silicon crystals). This is not only true for atomic structures but also colloidal and granular materials can exhibit crystalline patterns in equilibrium [186, 187] and non-equilibrium [188, 189]. An ideal crystal can be defined as a group of particles referred to as the *basis*, which is connected via a series of points that build a *lattice* that extends infinitely in all directions of the space. In the two-dimensional euclidean space, the lattice is defined as

$$\mathbf{r}' = \mathbf{r} + u_1\mathbf{a}_1 + u_2\mathbf{a}_2, \tag{4.1}$$

where $\mathbf{r}$ and $\mathbf{r}'$ are points on the lattice, $\mathbf{a}_i$ refers to the translation vectors and $u_i \in \mathbf{Z}$. With the definition of the translation vectors $\mathbf{a}_i$, the lattice looks identical at the point $\mathbf{r}$ and $\mathbf{r}'$ in the two-dimensional space. An example is depicted in Figure 4.1 A.

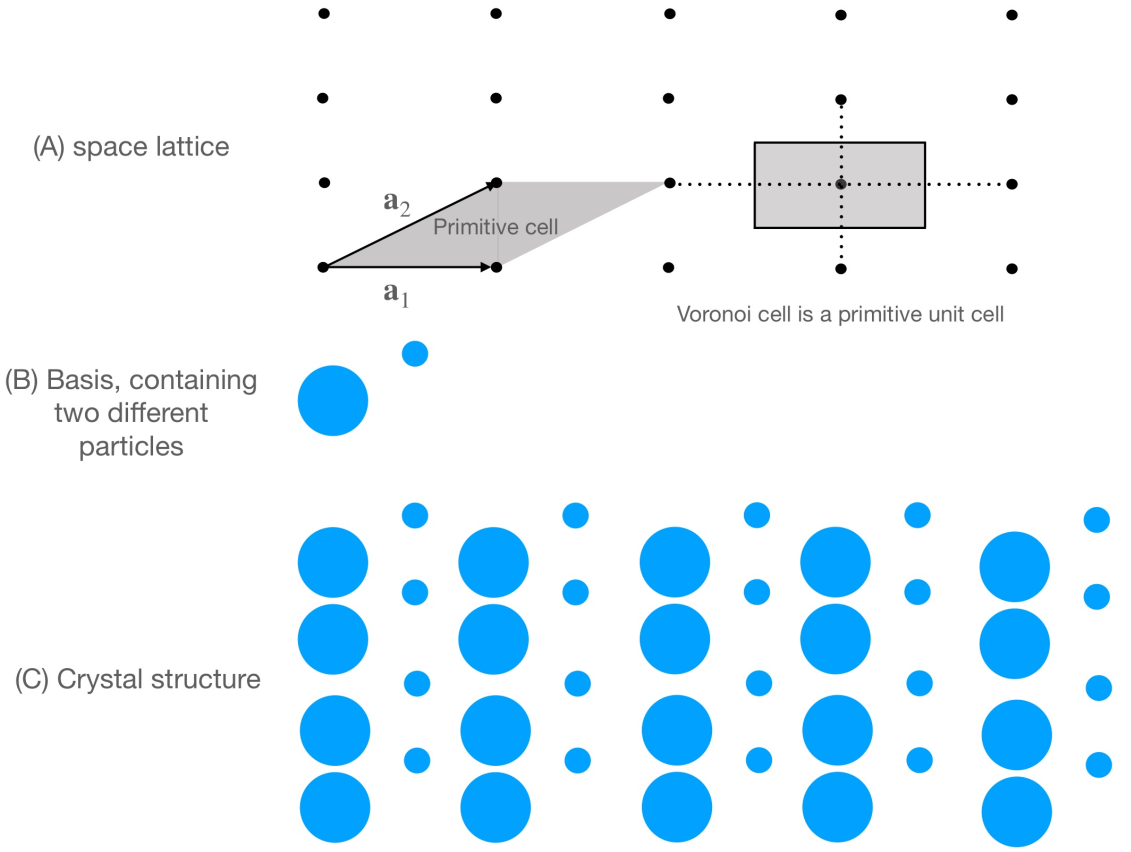

Figure 4.1: Figure adapted from [185]. (**A**) Example of a rectangular lattice with the translation vectors $\mathbf{a}_i$. (**B**) A basis with two different particles. (**C**) The lattice and basis together build the crystal structure.

A lattice where every point $\mathbf{r}$ in space satisfies equation (4.1) for a set of u_i is called *primitive*. In turn, the translation vectors $\mathbf{a}_i$ of these lattices with the minimal area of the parallelogram $A = |\mathbf{a}_1 \times \mathbf{a}_2|$ are the *primitive translation vectors*. They usually define the *crystal axis*. The parallelogram A of the *primitive translation vectors* is called the *primitive cell* (see Figure 4.1 A). It is the minimum area cell, which can fill up the entire two-dimensional space without overlap or gaps by a suitable translation. The *primitive cell* and *primitive translation vectors* are not unique for a certain lattice. The Voronoi cell (3.1) of the lattice (in condensed matter physics called Wigner-Seitz cell) is one solution to choose a primitive cell (see Figure 4.1 A). The lattice points build the underlying structure of a crystal on which the so-called basis can be translated to produce the crystal structure (see Figure 4.1 B and C). The basis can consist of multiple particles that are repeated via translation on the lattice.

An important characteristic that distinguishes different types of lattices is the set of operations that transform the lattice into itself. The translation vectors are one example. Another symmetry operation is the set of rotation angles that rotate the lattice into itself. Lattices can have one-, two-, three-, four-, and sixfold rotation axes, with the corresponding rotation angles being 2π, $2\pi/2$, $2\pi/3$, $2\pi/4$ and $2\pi/6$. There are no lattices with five- or sevenfold rotation symmetry.

Lattice types in two-dimension

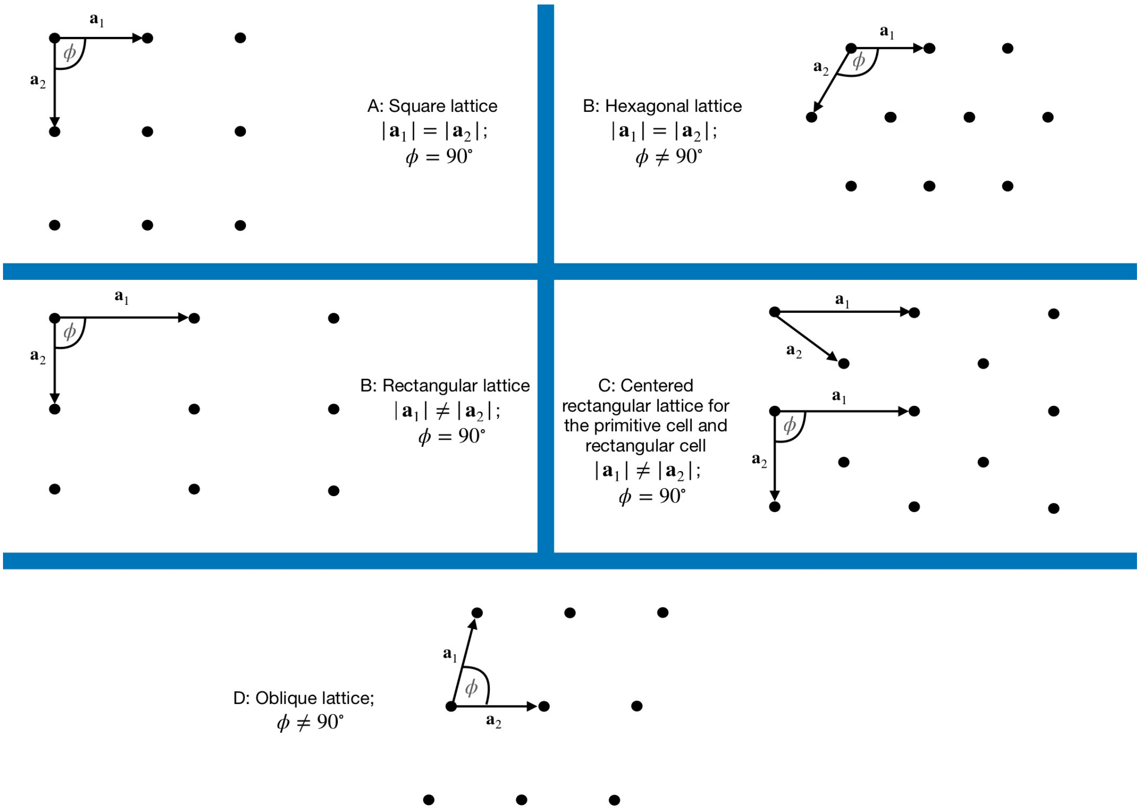

Figure 4.2: Figure adapted from [185]. Illustration of the five two-dimensional lattice types.

In two dimensions, there are five distinct lattice types. The general lattice drawn by two arbitrary vectors $\mathbf{a}_1$ and $\mathbf{a}_2$ is called the *oblique lattice* that is invariant only for rotations of π and 2π. There are four lattice types that inhibit invariance under one or more rotation angles of $2\pi/3$, $2\pi/4$, or $2\pi/6$, or mirror reflection. These four are the *special lattice types* illustrated in Figure 4.2 together with an example of an *oblique lattice*. They are referred to as a *Bravais lattice*; thus, there are five Bravais lattices in the two-dimensional case. The **hexagonal lattice** is of special interest in this work. For systems of circular two-dimensional agents, the *hexagonal packing* is the densest configuration. Taking a hexagon with side length D and discs with diameter D the area of the hexagon is $A_H = \frac{3\sqrt{3}}{2}D^2$ and for the disc $A_C = \frac{\pi}{4}D^2$. The area of the hexagon A_H can cover three times the area A_C (see Appendix A.1, Figure S1), therefore the covered area is defined as $A_{HC} = 3A_C = \frac{3\pi}{4}D^2$ and the packing fraction is defined as

$$\eta = A_{HC}/A_H = \frac{\pi\sqrt{3}}{2} \approx 0.9069. \tag{4.2}$$

The packing fraction is defined via the local density ρ_n (see equation (3.6)) as the ratio between the local density and the maximal possible density in the system

$$\phi = \frac{\rho_n}{\rho_{max}}\eta, \tag{4.3}$$

with $\rho_{max} = 1/(\frac{\sqrt{3}}{2}l^{-2})$, with l the particle diameter, since the closest packed Voronoi cell has the area of a hexagon (See Section 3).

Amorphous solid

Amorphous solids (also referred to as glasses) are an active topic of research [190–192]. In contrast to the perfect crystal described above, the amorphous solids are disordered materials. In the real world, a perfect crystal structure does not exist, as these are always finite and possess some imperfections. The kind of disorder that constitutes an amorphous solid is different. These exhibit no *long-range* order, i.e., there exists no set of translation vectors (4.1) that can reproduce the structure of the material (see Figure 4.3 for an illustration). The amorphous solid therefore is described by *topological disorder*. The emphasis on amorphous solids not exhibiting any long-range order is important because the degree of disorder in them can differ. Some exhibit short-range order, others do not, but non exhibit long-range order.

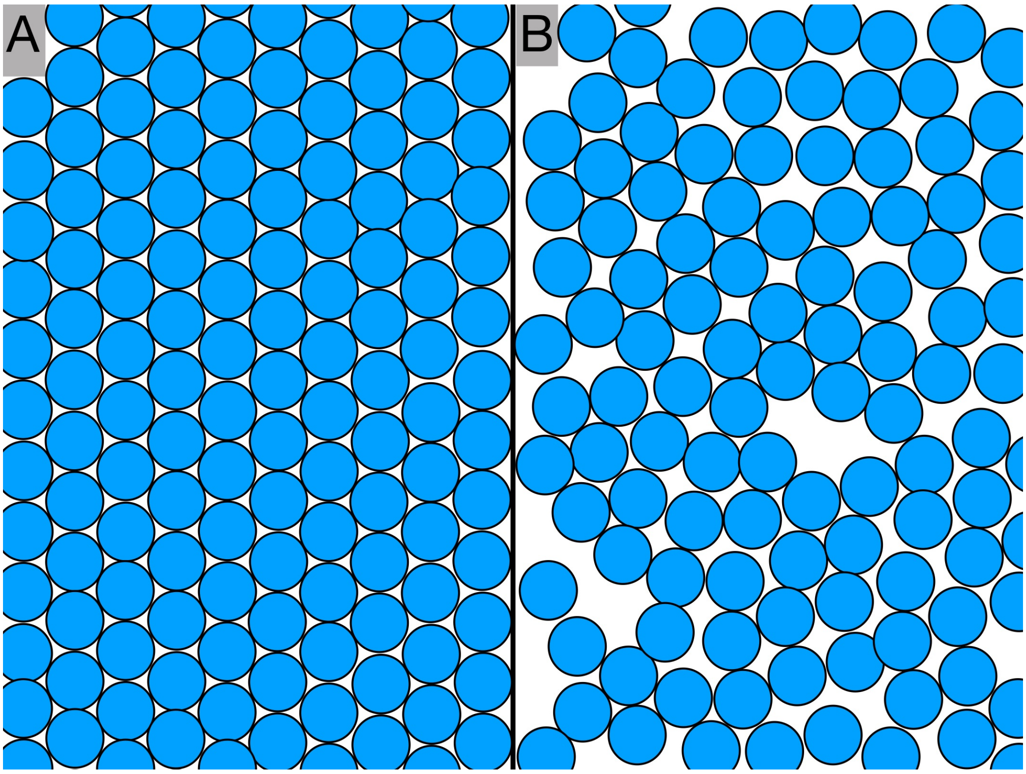

Figure 4.3: (**A**) Illustration of hexagonal crystal structure. (**B**) Illustration of an two-dimensional amorphous structure.

4.2 Structure in granular matter

The introduction of crystalline and amorphous solids stems from studying atomic solids affected by thermal noise and quantum-mechanical effects. Systems closer to pedestrian dynamics are also studied regarding their structural properties, especially granular materials, colloids, and active particles [186, 188, 189, 193–206]. As an analogous system to pedestrians, quasi-two-dimensional driven systems are especially interesting [186, 188, 189, 194, 195, 205, 207, 208]. The important difference between driven granular and colloidal systems versus thermodynamic gases, liquids, and solids is that they are not affected by thermal noise and are of a mesoscopic size. Computer-simulated systems of granular materials are usually in equilibrium, but experimental systems are far from it because they are constantly driven, and energy dissipates in them. Still, many empirical systems show the same behavior as the equilibrium simulations [186–189, 195].

The driven two-dimensional granular matter exhibit interesting phase behavior e.g., crystallization [188, 200, 201, 205, 207] and two-step melting via the hexatic fluid phase [189, 208]. Commonly six-fold symmetries are observed in crystalline granular matter [186, 188, 189, 199] but also fourfold symmetries (square lattice) can be observed [199, 205]. In colloidal media, driven monodisperse colloids [194] show crystallization and sixfold symmetry. Polydispers colloids and granular hard discs exhibit formation of grain boundaries [195, 197, 203, 206]. In recent years, persistent homology methods [209] gained popularity in the structure analysis of hard sphere force networks, enabling new means to characterize the topological structure of the systems [198, 204]. Granular two-dimensional systems are also studied in glass formation (amorphous solids). These exhibit interesting structures of crystalline clusters in an otherwise disordered assembly [191, 210, 211]. An active field of study in the study of granular and colloidal glasses is the jamming transition of a granular medium, where a compressed system arrests in a disordered [190, 212, 213]. The jammed state is also referred to as fragile matter, which constitutes a new type of solid-state systems. A jammed state is reached by externally driving the system, for example, in traffic jams, evacuations of pedestrians, or granular silos. The fragility stems from the fact that these systems are solid under applied stress that drives them into the state. Changing the direction of the stress can break the jam apart and brings the system back to a flowing state. With this, a new phase diagram of the glass and jammed state is proposed [190].

In the following, methods to analyze the microscopic structure in granular and colloidal materials are discussed in detail. These are used to quantify the structure of pedestrian experiments and simulations.

4.3 Two-point correlation function

The microscopic state of a classical system can be described as a point in the *phases pace.*

$$(\mathbf{r}_1, \mathbf{r}_2, ..., \mathbf{r}_n, \mathbf{p}_1, \mathbf{p}_2, ..., \mathbf{p}_n) = (r^n, p^n), \tag{4.4}$$

where $\mathbf{r}_i$ is the position of particle i and $\mathbf{p}_i$ its momentum. Let $f(r^N, p^N) dr^N dp^N$ be the probability of the system being at the phase space point (r^N, p^N). Because of the factorization of the Hamiltonian $H(r^N, p^N) = T(p^N) + U(r^N)$ the probability $f(r^N, p^N)$ factorizes

$$f(r^n, p^n) = \Phi(p^N) P(r^N). \tag{4.5}$$

The probability of observing the system at momentum point p^N is given by $\Phi(p^N)$, and the probability of finding the system at the configurational space point r^N is provided by $P(r^N)$. Focusing on the configurational space, looking at the distribution function for a small subset of particles can be useful by integrating $P(r^N)$ over all coordinates except the ones of interest

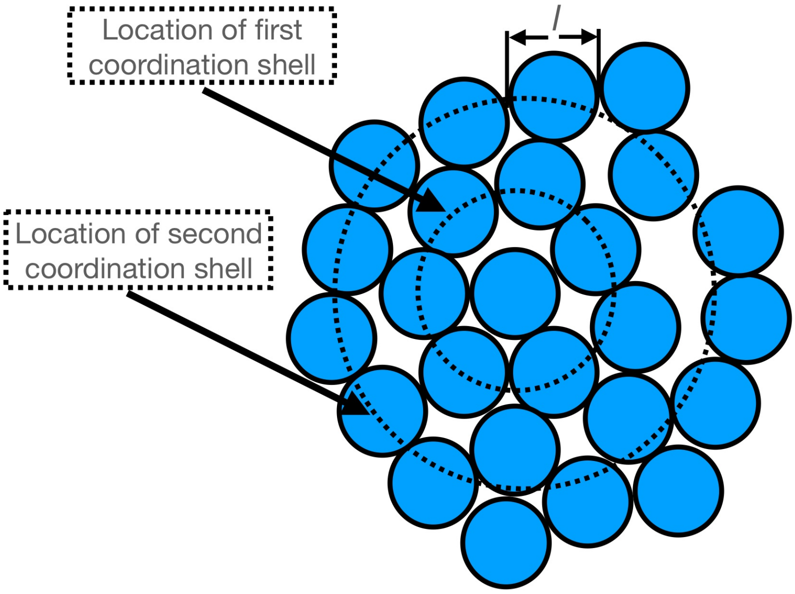

Figure 4.4: Illustration of a simple liquid and the position of the first two coordination shells. Graphic adapted from [185].

$$P^{2/N}(\mathbf{r}_1, \mathbf{r}_2) = \int d\mathbf{r}_3 \int d\mathbf{r}_4 ... \int d\mathbf{r}_N P(r^N), \tag{4.6}$$

which is the joint probability distribution of finding particle 1 at $\mathbf{r}_1$ and particle 2 at $\mathbf{r}_2$. This is the so-called specific probability distribution because of the specificity that the particle at 1 and 2 have to be at $\mathbf{r}_1$ and $\mathbf{r}_2$. In atomic and some granular or colloidal systems, particles are usually indistinguishable. In pedestrian dynamics, humans are, of course, very much distinguishable. Still, to analyze the structure, it is not of interest if participant Alice in an experiment is at position $\mathbf{r}_1$ and Bob at $\mathbf{r}_2$ but if there is any person at these two positions. It is, therefore, useful to treat the participants as indistinguishable particles, which leads to the introduction of the distribution

$$\rho^{2/N} = N(N-1)P^{(2/N)}(\mathbf{r}_1\mathbf{r}_2). \tag{4.7}$$

The factor $N(N-1)$ comes from the fact that there are N possible ways to pick the first particle and $N-1$ for the second. Analogously this can be generalized to $\rho^{n/N} = \frac{N!}{(N-n)!}P^{(n/N)}(\mathbf{r}_1, \mathbf{r}_2, ..., \mathbf{r}_n)$. Simple examples are the probability of an isotropic fluid

$$\rho^{1/N} = \rho = N/V \tag{4.8}$$

and in case of an ideal gas.

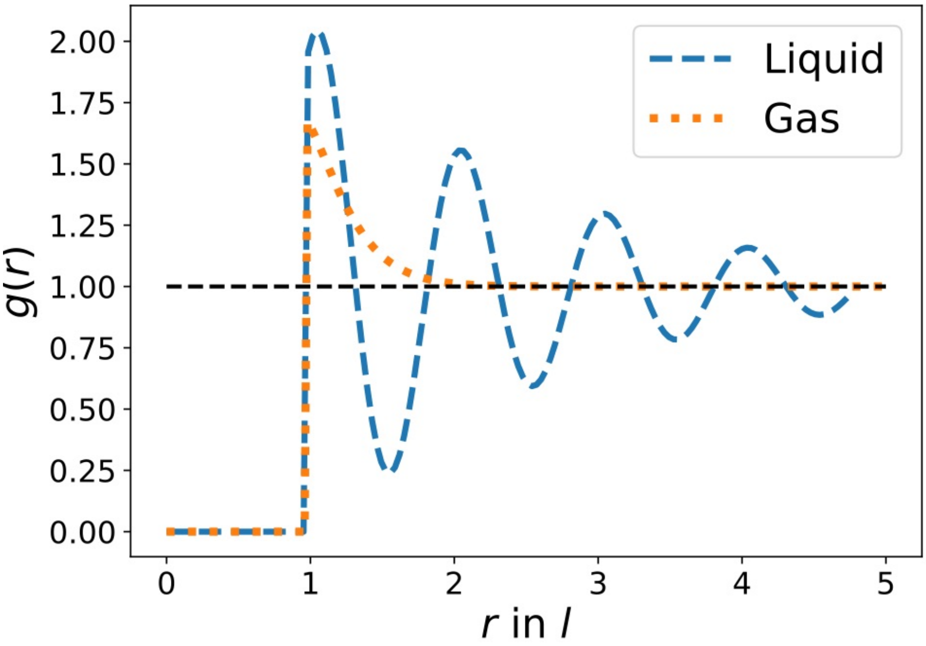

Figure 4.5: Example of the two-point correlation function $g(r)$ for a liquid and a gas in units of the particle diameter l.

$$\rho^{2/N} = N(N-1)/V = \rho^2(1-N^{-1}) \approx \rho^2, \tag{4.9}$$

in the thermodynamic limit. With this foundation the *two-particle-correlation function*

$$g(\mathbf{r}_1, \mathbf{r}_2) = \rho^{2/N}(\mathbf{r}_1, \mathbf{r}_2)/\rho^2 \tag{4.10}$$

can be introduced. In the case of an isotropic fluid the function only depends on $|\mathbf{r}_1 - \mathbf{r}_2| = r$ and the correlation function reduces to $g(r)$ which is the so-called *radial distribution function.* For a uniform system (see above) $\rho^{1/N}(\mathbf{r}_1) = \rho$ and therefore

$$\rho^{2/N}(0, \mathbf{r})\rho = \rho g(r), \tag{4.11}$$

which is the conditional probability that a particle is found at r, given there is a particle at the origin. To analyze the structure of agents, it is useful to treat them similarly to an isotropic fluid. With the density definition (3.4) $\rho(\mathbf{r}; \mathbf{X}) = \sum_{i=1}^{N} \delta(\mathbf{r}_i - \mathbf{r})$, $\rho(\mathbf{r}) = \langle \rho(\mathbf{r}; \mathbf{X}) \rangle$, and the mean density of an isotropic fluid $\langle \rho(\mathbf{r}; \mathbf{X}) \rangle = \rho = N/V$. At a point $\mathbf{r}$ of the fluid, the density fluctuates around its mean value. The density fluctuation is quantified by

$$\delta\rho(\mathbf{r}) = \rho(\mathbf{r}) - \rho. \tag{4.12}$$

The two-point density fluctuations is defined as

$$G(\mathbf{r}, \mathbf{r}') = \langle \delta\rho(\mathbf{r}) \delta(\mathbf{r}') \rangle = \rho\delta(\mathbf{r} - \mathbf{r}') + \rho^2 g(\mathbf{r}, \mathbf{r}') - \rho^2 \tag{4.13}$$

and $g(\mathbf{r}, \mathbf{r}')$ is calculated via

$$g(\mathbf{r}, \mathbf{r}') = \frac{\langle \delta\rho(\mathbf{r}) \delta(\mathbf{r}') \rangle - \rho\delta(\mathbf{r} - \mathbf{r}')}{\rho^2}. \tag{4.14}$$

In the case of pedestrian flowing through a bottleneck the assumption of the isotropic fluid that $\langle \rho(\mathbf{r}; \mathbf{X}) \rangle = \rho = N/V$ is not valid and equation (4.14) has to be altered to

$$g(\mathbf{r}, \mathbf{r}') = \frac{\langle \delta\rho(\mathbf{r}) \delta(\mathbf{r}') \rangle - \rho\delta(\mathbf{r} - \mathbf{r}')}{\rho(\mathbf{r})\rho(\mathbf{r}')} \tag{4.15}$$

Using data from simulations or experiments the Dirac function can be approximated using (3.5), $\delta(x) = \frac{1}{\sqrt{\pi}a} \exp[-x^2/a^2]$. The two-point correlation function $g(r)$ is then calculated by

$$g(r) = \frac{\langle \int \rho(\mathbf{r} - \mathbf{r}')\rho(\mathbf{r}') d\mathbf{r} \rangle - \langle \int \rho(\mathbf{r}')\rho(\mathbf{r} - \mathbf{r}') d\mathbf{r}' \rangle}{\int \rho(\mathbf{r}) d\mathbf{r} \int \rho(\mathbf{r}') d\mathbf{r}'} \tag{4.16}$$

The two-point correlation function is useful in the analysis of the structure of a system. The shape and decay of the function reveal if the system is in a liquid, crystalline, or gas state. It is illustrated in Figure 4.5 for a gas and a liquid. The function is zero in the exclusion zone of the particles. In the liquid stage, the different shells of particles illustrated in Figure 4.4 are visible, while in the gas stage, this is only true for the first shell of particles near the exclusion zone. In both cases, the maxima of the correlation function decay exponentially $g(r) \propto \exp(-r/\xi)$. This distinguishes the liquid and gas from the crystalline phase, where $g(r) \propto r^{-\eta}$ is quasi-long-range and decays with a power law. In a crystalline solid, the position of the peaks contains information on the structure of the solid. For a hexagonal structure, the peaks are at $r/l = \{1, \sqrt{3}, 2...\}$.

4.4 Delaunay triangulation

Delaunay triangulation (also Delaunay graph), introduced by Boris Delaunay [214], is a method to triangulate $DT(\mathbf{X})$ of a set of discrete points $\mathbf{X}$ on the two-dimensional plane such that no point in $\mathbf{X}$ lies inside the circumcircle of any triangle in $DR(\mathbf{X})$. Delaunay triangulation is the construction of a graph that maximizes the minimal angle of the triangles. It is closely related to the Voronoi diagram (3.1) and can be constructed in the following way (illustrated in Figure 4.6):

- From the Voronoi diagram constructed according to (3.1) take each point in $\mathbf{X}$ (blue points in Figure 4.6 A) as a vertex v_s.
- Connect each vertex v_i and v_j that share an edge in the Voronoi diagram by an arc (Figure 4.6 B), which constructs the graph $G(\mathbf{X})$.
- Straighten all the lines to produce the Delaunay graph $DT(\mathbf{X})$ (Figure 4.6 C)

Delaunay triangulation is utilized to define the nearest neighbor of a particle. With that, the coordination number (or the number of nearest neighbors) N_n, the mean neighbor distance $\langle d_N \rangle$, and the angle between neighboring bonds θ_{ij} can be calculated.

4.5 Orientational order parameter

The bond orientation order parameter is defined by the local director field of a particle. The particle i at position $\mathbf{r}_i$ has N_n nearest neighbors determined by the Delaunay triangulation. The angle θ_{ij} (see Figure 4.7 C) of a bond to a neighboring particle and an arbitrary axis is used to calculate the sixfold space, normalized by

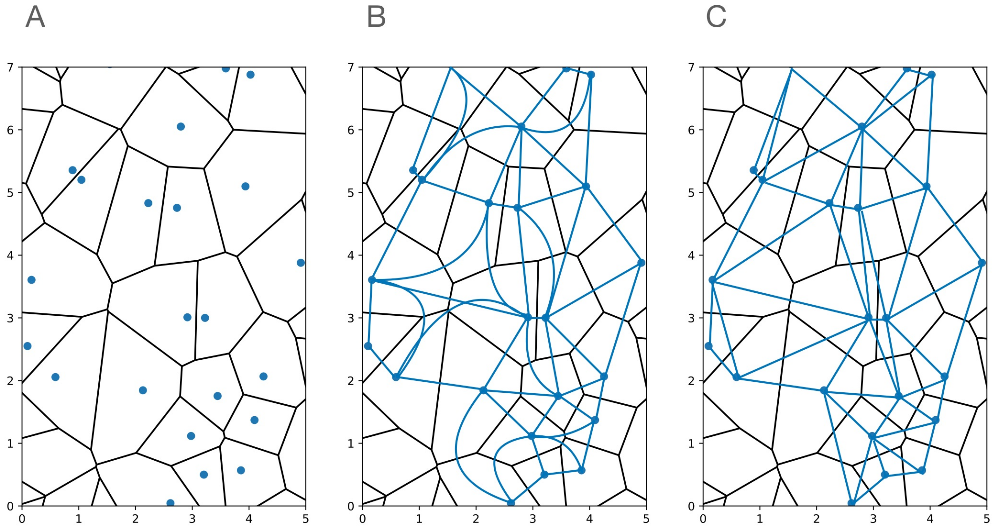

Figure 4.6: Illustration of the Delaunay graph construction. The points outside the plot range are ignored for simplicity.

the coordination number:

$$\Psi_6(\mathbf{r}_i) = 1/N_n \sum_{j=1}^{N_n} \exp(i6\theta_{ij}). \tag{4.17}$$

It takes complex values and is bounded by $|\Psi_6(\mathbf{r}_i)| \leq 1$, where $|\Psi_6| = 1$ a perfect hexagon. The real part of the function can take values of $\psi_6 = \mathrm{Re}(\Psi_6) \in [-1, 1]$ and can be written as

$$\psi_6(\mathbf{r}_i) = 1/N_n \sum_{j=1}^{N_n} \cos(6\theta_{ij}), \tag{4.18}$$

which is also 1 for perfect hexagonal order and $\langle \psi_6 \rangle \approx 1/N$ for a random gas with N particles [198]. Figure 4.7 A illustrates ψ_6 for systems with different amount of hexagonal order. On the left, a perfect hexagonal crystal is illustrated, which can be seen by the shape of the Voronoi cells. Onto the hexagonal lattice with position $\mathbf{r}_i$ defined by the translation vectors (4.1), random noise is added by adding i.i.d uniform random variable onto the position $\mathbf{r}_i' = \mathbf{r}_i + \mu U(0, 1)$ with μ the noise strength. In Figure 4.7 B $\langle\psi_6\rangle$ for a system of $N = 300$ lattice points is shown with respect to the noise strength μ. The parameter reacts non-linear on the noise added to the system and goes to $\langle\psi_6\rangle \approx 0$ for $\mu > 1.0$. The orientational order for the whole space, averaged over multiple realizations of the systems, is defined as

$$\langle\Psi_6\rangle = 1/N \sum_{j=1}^{N} |\Psi_6(\mathbf{r}_i)|, \tag{4.19}$$

and analogously for ψ_6, with N the total number of particles. In this thesis, the bond orientation is calculated individually for each particle. The axis to define the angle is set arbitrarily to one of the bonds. In two-dimensional systems, it can also be

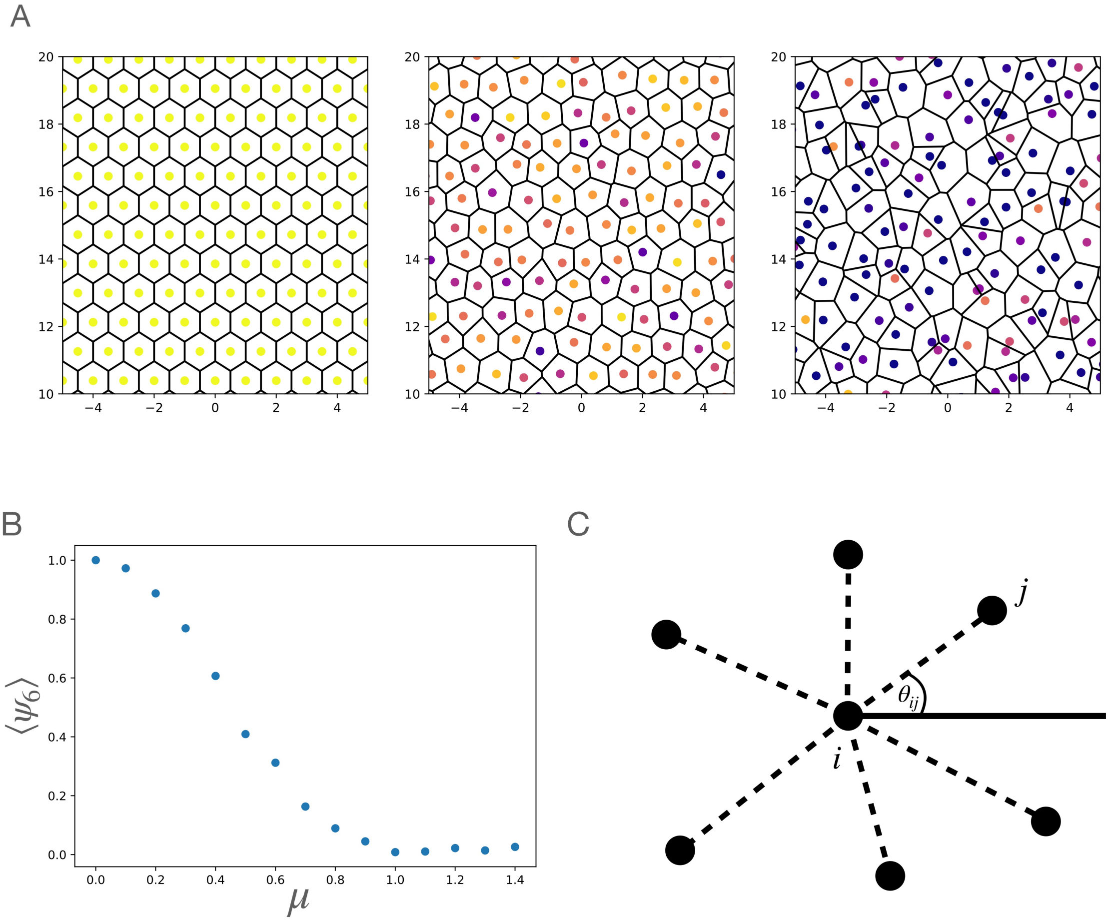

Figure 4.7: (**A**) Illustration of the bond orientation parameter Ψ_6 for a perfect hexagonal crystal with increasing noise from left to right. The noise level is $\mu = \{0.0, 0.4, 1\}$. (**B**) The mean bond orientation measure $\langle\Psi_6\rangle$ with respect to the noise level μ. (**C**) Illustration of the bond angle between particle i and j.

useful to fix the axis for the entire system to calculate the orientational-correlation function analogous to the two-point-correlation for the position (see Section 4.3) $g_6(r) = \langle \Psi_6(\mathbf{r})\Psi_6(\mathbf{r}-\mathbf{r}')\rangle / g(r)$ and $\Psi_6(\mathbf{r}) = \sum_i \Psi_6(\mathbf{r}_i)\delta(\mathbf{r}-\mathbf{r}_i)$. The orientation correlation is useful to detect a phase unique to two-dimensional systems called the *hexatic phase.* It is characterized by a short-range translational order $g(r) \propto \exp(-r/\xi)$ similar to a liquid and long-range orientational order $g_6(r) \propto r^{-\eta_g}$. In contrast a liquid exhibits short-range orientational order. The difference between the hexatic phase and the liquid phase stems from the kind of defects they inhibit (see Section 4.6). The hexatic phase emerges in the melting of a two-dimensional system as described in the KTHNY theory [215–217]. In this work, either the absolute value of Ψ_6 is used or the real value ψ_6. As a simplification, the absolute value of $|\Psi_6| \equiv \Psi_6$ from here on.

4.6 Defects in two dimensions

In real systems, the perfect crystal does not exist. First of all, the system is finite, but it also exhibits several possible different defects. This section discusses two important kinds of defects, grain boundaries and dislocations/disclinations. Ordered crystalline structures can grow separately in proximity to each other. These small crystals are referred to as grains (not to be confused with the grains of granular matter) and can vary in size from macroscopic structures to microscopic crystals in e.g., metals. When two-grain crystals meet, they usually have different crystal orientations. The area between the separate granular crystals is referred to as the *grain boundary.* In two dimensions, the grain boundary is a one-dimensional defect. It is common in granular crystals with polydisperse particle size [197, 203, 218]. An example of a grain boundary in a two-dimensional Lennard-Jones fluid with low-temperature [219, 220] is illustrated as a Voronoi plot in Figure 4.8. Panel A depicts the particles with $\Psi_6 > 0.7$ in yellow and $\Psi_6 \leq 0.7$ in blue. The threshold is set so that the grain boundary becomes visible. Panel B in Figure 4.8 shows the coordination number $N_n \neq 6$ in red ($N_n = 5$) and green ($N_n = 7$). Along the grain boundary is a chain of alternating 5- and 7-fold *dislocations* (A bounded 5-fold and 7-fold particle pair is called a dislocation).

A dislocation is a topological defect characterized as an additional half-row of particles in the crystal structure. A topological defect is a defect that cannot be created without cutting the crystal up to infinity (i.e., there is no affine transformation that

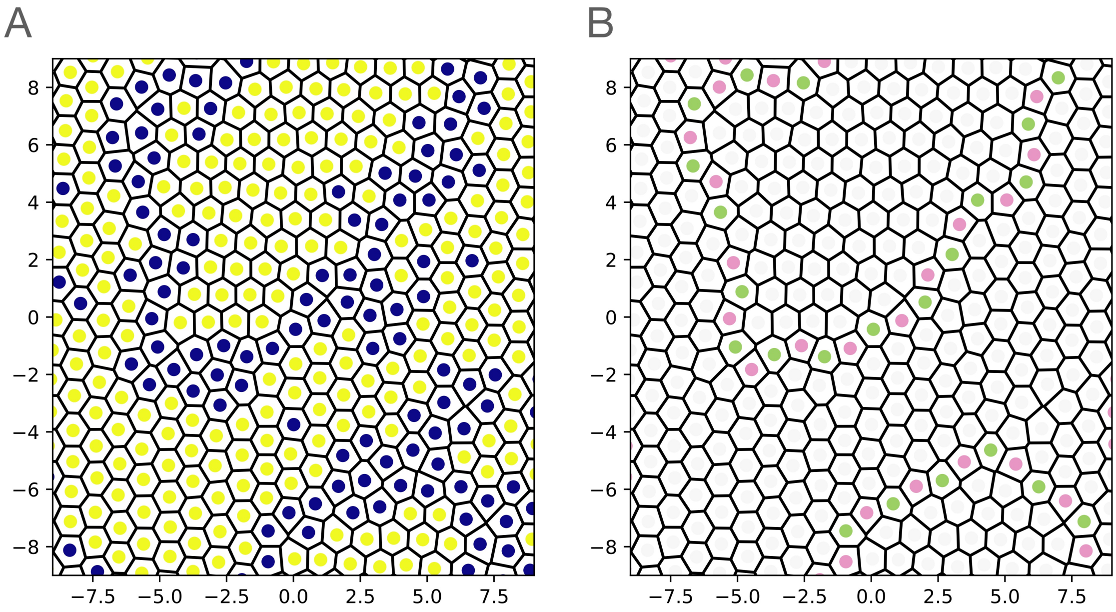

Figure 4.8: (**A**) Grain boundaries (blue) between grain crystals (yellow) in a two-dimensional Lennard-Jones simulation. The yellow particles have an order parameter $\Psi_6 > 0.7$, and the blue particles $\Psi_6 \leq 0.7$. (**B**) Analogous to panel A, the plot of the coordination number $N_n \neq 6$. Particles with $N_n = 5$ are in pink, and particles with $N_n = 7$ are in green.

isolates the defect). Figure 4.9 B and E show a single dislocation in a hexagonal crystal structure for the Voronoi and Delaunay plots. In panel E, the extra row of particles is visible when counting the horizontal edges of the Delaunay triangulation. The defect is usually defined by the Burgers vector [185]. When traversing on a hexagonal circuit with step length a (the length of the hexagonal translation vector), the trajectory forms a closed loop. Traversing around a dislocation in the same manner will produce an open geometric figure. The Burgers vector is then the vector closing this figure marked as yellow in Panel E. Dislocations in the structure disrupt translational order in the system (causing $g(r)$ to decay exponentially). In contrast, the orientational order is retained (quasi long range with $g_6(r)$ decaying as a power law, see Figure 4.9 B). A bound pair of dislocations illustrated in Figure 4.9 A and B retain both translational and orientational order and do not disrupt the topology of the crystal (See Panel A). Another kind of topological defect is the 5- or 7-fold disclination illustrated in Figure 4.9 C and F. This defect destroys translational and orientational order (i.e., $g(r)$ and $g_6(r)$ both decay exponentially), illustrated in Figure 4.9 C. Dislocations and disclinations are important in the melting of two-dimensional crystals. Starting from a hexagonal crystal, they are created in pairs because these are topological defects. When heating a two-dimensional crystal, dislocation pairs appear in it. In the melting process, these dissociate into 5-7 fold dislocations. This is the hexatic phase. Further into the melting process, the dislocations dissociate into disclinations, constituting the two-dimensional system's liquid phase. This two-step melting process unique to two-dimensional crystals is described in the KTHNY-theory [215–217].

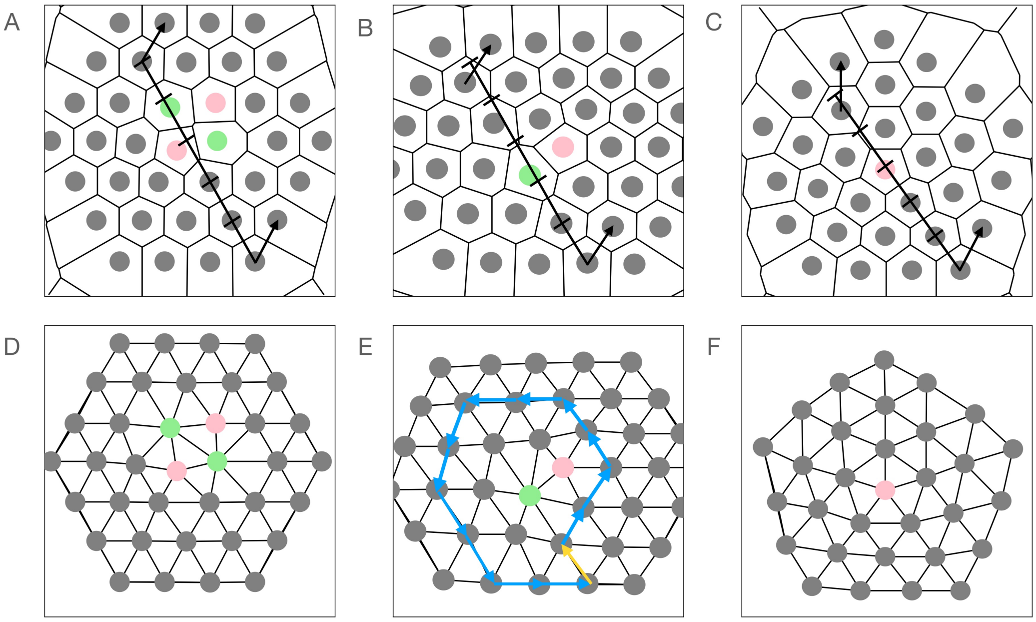

Figure 4.9: Illustration of the different kinds of defects in the Voronoi plot (**A-C**) and Delaunay plot (**D-E**). Panels **A&D** show a 5-7-fold dislocation pair in a solid, panels **B&E** a 5-7-fold dislocation in a hexatic fluid, and panels **C&D** a 5-fold disclination in a liquid. Panel **E** shows the Burgers vector[185] for a dislocation. Figure adapted from[221].

4.7 Shape factor

With the use of the Voronoi cell (3.1), each particle has a clearly defined polygon associated with it. The shape of the polygons contains information on the structure of the whole system. In Figure 4.8 B and 4.9 A-C, the different shapes from 5 to 7-fold polygons can be clearly distinguished. The Voronoi cell of particles with $N_n = 6$ are mostly close to regular hexagons, and the cells of particles with $N_n = 5$ are close to regular pentagons. Particles with $N_n = 7$ are quite irregular in contrast. The shapes of the polygons have distinct ratios between their area and perimeter, which makes it possible to distinguish the shapes of the Voronoi diagram quantitatively. In the study of quasi-two-dimensional granular fluids, the shape factor was introduced [186, 188]. It is defined as

$$\zeta_i = \frac{C_i^2}{4\pi S_i}, \tag{4.20}$$

with C_i the perimeter of the Voronoi cell and S_i the area. The values of ζ are unique for regular polygons. For a circle, the value of $\zeta_i = 1$. For all other shapes $\zeta_i > 1$. For a square $\zeta = 4/\pi \approx 1.273$, for a regular hexagon $\zeta_i = 6/\sqrt{3\pi^2} \approx 1.103$, for a pentagon the value of $\zeta_i = \pi/5\tan(\pi/5) \approx 1.156$, and for regular heptagons $\zeta_i = 7\tan(\pi/7)/\pi \approx 1.073$. The advantage of the shape factor in comparison to other measures like the bond orientation factor Ψ_6 (see Section 4.5) is that it can clearly detect the structuring of the system into various shapes, without a bias about the expected ordering of the system.

4.8 Detection of clusters on a grid

In the analysis of the structure in a system, it is interesting to look for ordered clusters (granular crystals as described in Section 4.6). One efficient method to separate and label a discrete dataset into clusters is the Hoshen-Koppelman Algorithm [222]. The algorithm can be used on a grid of either occupied or unoccupied cells analogous to cellular automata (Section 2.2). An example is illustrated in Figure 4.10 A, where blue cells are occupied and grey cells are not. The algorithm performs a raster scan line by line from left to right. Its target is to assign a label to each occupied cell corresponding to the cluster it belongs to. The labels are natural numbers between 1 and N. It checks for neighbors on the left and above on a Von-Neumann neighborhood (see Figure 2.2). The algorithm performs the following steps:

- If the cell is unoccupied: continue.
- If the cell is occupied with no label and no occupied and labled neighbors: assign an unused label to it.
- If the cell is occupied and has one occupied and labeled neighbor, assign its neighbor's label to it (they belong two the same cluster).

- If the cell is occupied with two occupied and labeled neighbors, assign the smaller label to it and note that the two clusters the neighbors belong to must be merged.

Neighboring cells share an edge (i.e., $N_n = 4$ for all cells except the boundary). The merging of two equivalent clusters, described in the last step, is performed using a Union-Find algorithm [223]. To merge the clusters, a function $union(x, y)$ specifies that items x and y belong to the same cluster (i.e., they are assigned the same label). Since all cells that belong to cluster x also belong to cluster y, the function $find(x)$ is called to take all cells in cluster x and assign them the correct label of cluster y. The process is illustrated in Figure 4.11 according to the steps explained above, and the functions $union(x, y)$ and $find(x)$. Figure 4.10 B illustrates the resulting clustering of the cells. A good summary of implantations for $union(x, y)$ and $find(x)$ can be found at [224].

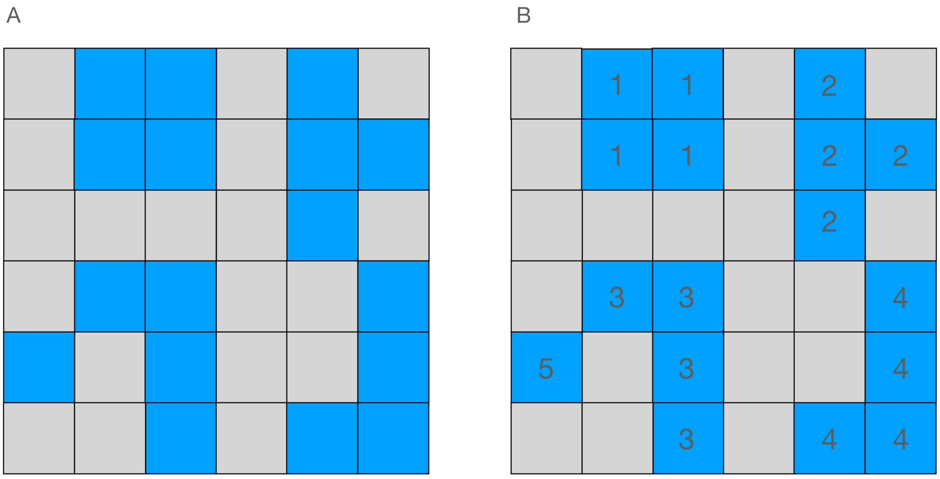

Figure 4.10: (**A**) Illustration of a grid with occupied (blue) and unoccupied (grey) cells. (**B**) Clustering of the grid according to the Hoshen-Koppelmann algorithm with labels 1 to 5.

The data from the simulations analyzed in this thesis are from continuous models on which the grid approach of the Hoshen-Koppelman algorithm is not applicable. To circumvent this problem, the data is processed and set onto a grid. In the simulated data of the continuous speed and force-based models (see Chapter 2.3 and 2.1) is a set of discrete points in a continuous space that evolves over time. The position of the N agents in the simulation at time t is $\mathbf{r}_i(t)$ with $i \in \{1, ..., N\}$. Each agent is also assigned the local order measures like the shape factor $\zeta(\mathbf{r}_i(t))$ or the orientational order $\Psi_6(\mathbf{r}_i(t))$ (see Section 4.5 and 4.7). To analyze the clustering of an arbitrary order measure $\Omega(\mathbf{r}_i(t))$, it is convenient first to transform it into a continuous field

$$\Omega(\mathbf{r}(t)) = \frac{\sum_i \Omega(\mathbf{r}_i)\delta(\mathbf{r}_i - \mathbf{r})}{\sum_i \delta(\mathbf{r}_i - \mathbf{r})}, \tag{4.21}$$

with the smoothed delta function (3.5) and then put a fine grid over the field to utilize the Hoshen-Koppelman algorithm. The discretization of the grid comes automatically while computing the field since the resolution of the computation is finite. The algorithm works on binary data. Therefore a threshold ϵ is defined on the order parameter. The condition for cell i being either occupied or unoccupied is

$$i = \begin{cases} \text{occpuied} & \text{if} \quad \Omega_i > \epsilon \\ \text{unoccpuied} & \text{if} \quad \Omega_i \leq \epsilon. \end{cases} \tag{4.22}$$

With this, a discrete binary grid is produced on which the algorithm can cluster the data depending on the arbitrary threshold of the measure of interest.

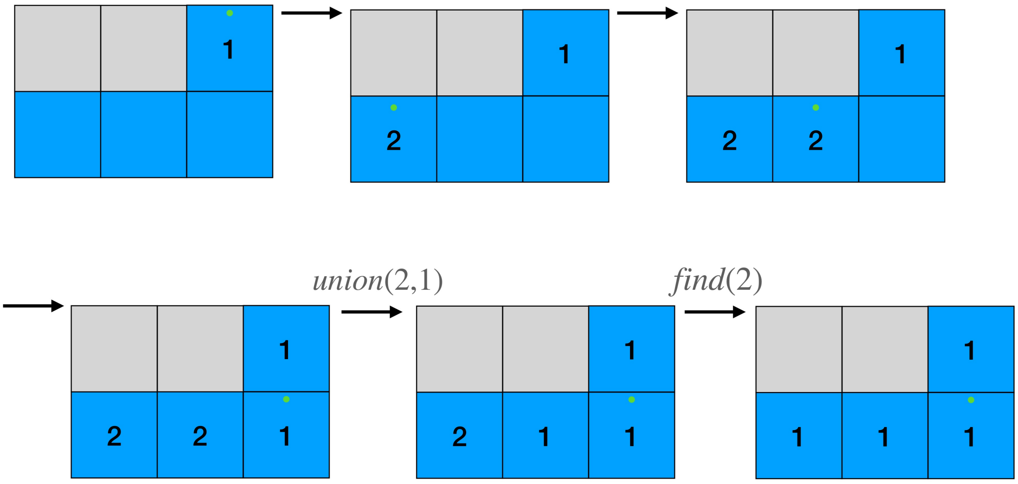

Figure 4.11: Illustration of the Hoshen-Koppelman algorithm with the functions $union(x, y)$ and $find(x)$. The green dot marks the cell that is currently scanned. The process in the illustration starts at the first occupied cell.

Chapter 5

Structure in pedestrian bottleneck experiments

In this Chapter, part of the methods introduced in Chapter 4 are applied to pedestrian bottleneck experiments and compared to simulations. It should be noted that though there are some analogies to the granular systems, there are also differences. The granular systems are not self-driven, and the experiments that investigate the structure of shaken granular matter have no net flow. The particles in these systems interact by collisions and are in non-equilibrium because of energy dissipation and injection by shaking [188, 195]. In comparison, the pedestrian system has more complex interactions via either the stimulus-response system. In high-density situations, it can come to pushing behavior, which leads to body-body interactions, though because of the self-driving mechanism of pedestrians, this is different from collisions in granular media. The experiments analyzed are from the University of Navarra and are compared to simulated models. The data stems from a set of experiments conducted with 180 soldiers in the America 66 regiment of the Spanish army [1]. The trajectory files and videos are freely available online [225]. The design of the experiments aimed to examine the influence of an obstacle near a bottleneck (realized by a column) on the evacuation dynamics in respect of flow and density. The experiments are part of a larger set of experiments that examined the "column effect" [1, 2, 79]. Here the runs with an obstacle are omitted, and the scenario of a simple evacuation through a bottleneck is in focus with no restrictions on the corridor width. The particular set is most suitable to analyze the structure because of the larger number of participants ($N = 180$ vs. $N = 90$ in [79]). In the experiments, the participants were told to evacuate quickly through a bottleneck realized by a

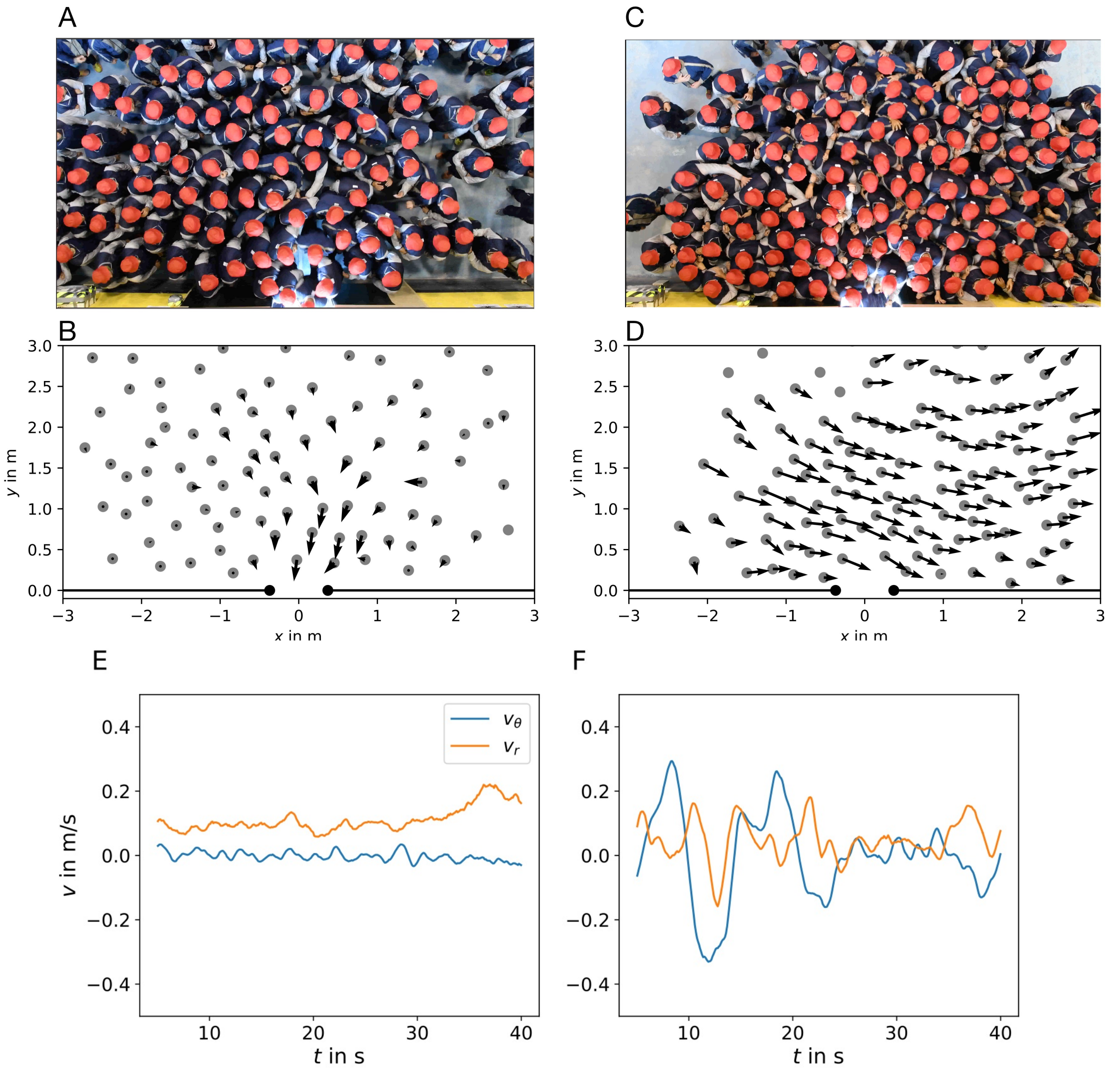

Figure 5.1: (**A**)&(**C**) Snapshot of the camera system of the experiment (**A**) with low motivation and (**C**) with high motivation. Panels (**B**) and(**D**) show the scatter plot of the trajectory data captured from the camera approximately at the same time with the velocity vectors. (**E**)&(**F**) Mean absolute value of the radial velocity v_r and angular velocity v_θ of the whole system for a typical run. (**E**) shows low motivation and (**F**) high motivation. Figure adapted from [1].

75 cm wide door in a large hall. They were conducted with two motivation levels. In the low-motivation runs, the participants were told not to push but to leave the perimeter quickly. In the high-motivation runs, pushing was allowed. There are three runs of the experiment with low motivation and no obstacle and seven runs with high motivation and no obstacle. The experiments were tracked with an optical camera system in 4k high resolution. An imaging software is applied to extract the trajectory data (see [1, 80]). A snapshot is illustrated in Figure 5.1 A and C for low and high motivation, respectively. Part of the analysis in [1] is the collective motion of the pedestrians. The dynamics of low and high motivation differ significantly. A surprising observation is the emergence of a collective transversal motion in runs with high motivation. While pushing each other to evacuate the room, the participants collectively start to sway perpendicular to the direction of the exit. This phenomenon is illustrated in Figure 5.1 B and D. In the low motivation experiment (panel B), the movement is "laminar" towards the exit. In contrast, for high motivation, the collective motion perpendicular to the exit direction becomes visible (panel D). The velocities of the participants are measured in cylindrical coordinates, with the exit being the origin of the coordinate system. In [1], the swaying is visualized by decomposing the velocity into the components of polar coordinates. The origin of the system is the center of the exit. The radial velocity v_r is positively defined towards the origin, and the angular velocity v_θ is defined clockwise. In Figure 5.1 E-F, the velocity components are visualized. To illustrate the swaying motion, the angular velocity v_θ is a good indicator. For the low motivation run (Panel E in Figure 5.1), v_θ oscillates closely around 0. The oscillation comes mainly from the swaying motion of the participants while walking. As expected, they walk in a mostly straight line toward the target. In the run with high motivation (panel F), strong oscillation of v_θ illustrates the collective swaying motion the crowed exhibits. The reason for this phenomenon is still unknown. The effect shows that the dynamics differ significantly depending on the motivation. The next step is to analyze the system's spatial structure using the methods introduced in Section 4.4 - 4.7. The experimental datasets are rather small to calculate correlation functions, so the focus lies on the measure of hexagonal bond orientation ψ_6 (4.18), the shape factor ζ (4.20) and the coordination number N_n. Figure 5.2 depicts the Voronoi-scatter plot of a snapshot of the trajectory data at $t = 15$ s after the start of the experiments (i.e., when the first participant exits the room) for low motivation in the left column and high motivation in the right column. The panels show from

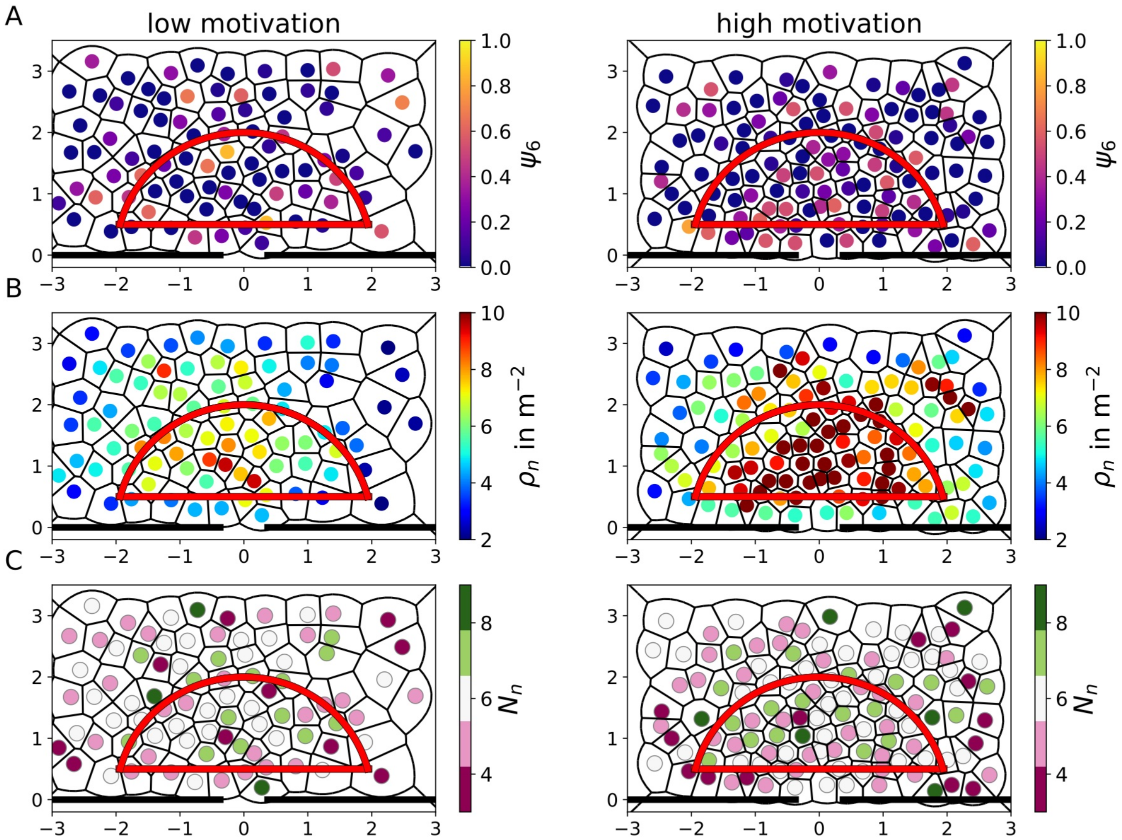

Figure 5.2: Scatter plot at $t = 15\,\mathrm{s}$ with low motivation (left column) and high motivation (right column). (**A**) hexagonal orientation factor ψ_6 (purple low ψ_6, yellow high ψ_6). (**B**) Local density ρ_n. (**C**) Coordination number (white: $N_n = 6$, light green: $N_n = 7$, light pink: $N_n = 5$). The measurement area depicted as the red half circle has the conditions $r < 2\,\mathrm{m}$ and $y > 0.5\,\mathrm{m}$.

top to bottom the local real value of the bond orientation measure ψ_6), the local density ρ_n (3.6), and the coordination number N_n. The bond orientation measure is consistently low and far from the hexagonal order. The disorder is also reflected in the shape of the Voronoi cells, which exhibit no particular pattern in the snapshot. This is consistent over the experiments for both motivations, which can also be seen in the video of this plot "*StructureNavarra.mp4*" in the supplementary video files [226]. The structure of low and high-motivation experiments does not seem to differ much. It is irregular in both cases, comparable to a fluid (see Section 4.5). The measure ρ_n shows the local density of the participants. The snapshot illustrates the difference between the lower density in the low-motivation experiment and the high density in the high-motivation experiment. The highest density of the experiment is inside the red half circle. This defines the measurement area for further analysis of the data. It is chosen to have a distance to the boundaries to lessen the impact of boundary effects. The last two panels show defects in the system. The system has an abundance of 5-7 fold dislocations and disclinations in both high and low motivation, characterizing the measured trajectories as fluid-like. The coordination number N_n of the participants changes rapidly during the experiments. This dynamical change can be seen in the video and can also be illustrated when plotting the individual participant's coordination number over time. Figure 5.3 shows in panels A and B the coordination number with the same color code as in Figure 5.2. The y-axis encodes the individuals *id* that identify them during an experimental run. The trajectories are taken between 10 s and 20 s. The individuals were chosen from the upper boundary of the red measurement area (between $1.5\,\mathrm{m} < r < 2\,\mathrm{m}$). Because of the higher density, more trajectories are shown in the high-motivation experiment. The plot illustrates how each individual's coordination number changes dynamically in short periods. Most participants' coordination number is between $N_n = 5$ and $N_n = 7$, and most participants have each coordination number at some point in time. Even though the dynamics of high motivation runs differ significantly, the coordination number dynamics are qualitatively similar. In the same manner, the dynamics of the shape factor ζ is plotted (Figure 5.3 C and D). The time series shows that the shape factor changes dynamically over various values for individual trajectories. Small changes in ζ describe significant differences in the shape (see Section 4.7). Analogous to the dynamics of the coordination number, the shape factor dynamics are qualitatively similar for both high and low motivation in the change of the shape factor over time and the variation of shapes an individual inhibits.

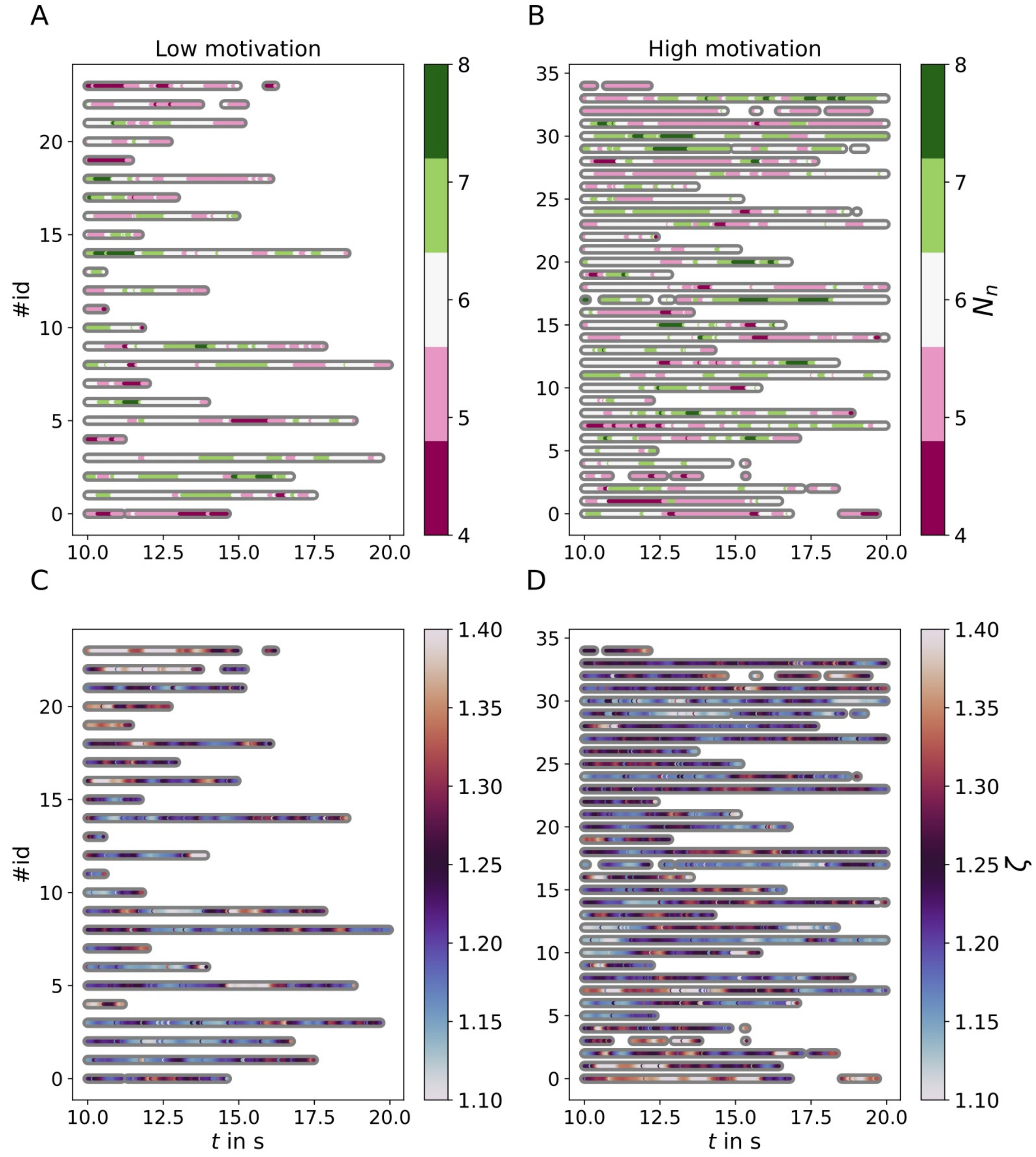

Figure 5.3: (**A**)&(**B**) A time series plot of the coordination number N_n with respect to the time t of a single run in the measurement area from $10\,\mathrm{s} < t < 20\,\mathrm{s}$. The y-axis shows the identification number of the agents. (**C**)&(**D**) Analogous to A and B for the shape factor ζ. Panels A&C show low motivation, and panels B&D high motivation.

The coordination number N_n can be utilized to analyze the lifespan of the different neighbor configurations from 5-fold to 7-fold. Because of the discrete nature, it is straightforward to define a lifespan t_c of a coordination number for a certain individual as the consecutive time an individual has N_n number of neighbors. The lifespan is the length of each color in Figure 5.3 A and B. The change from one coordination number to the next at time t is the time of birth t_b of the new coordination number and the time of death t_d of the other. The time t_b is then the null point from which the lifespan is calculated. With this definition, the survival function is defined as $S(t) = P(t_d > t)$, which is the probability that the coordination number is still alive at time t. The survival of the coordination numbers is measured in the measurement area and time interval of $10\,\mathrm{s} < t < 20\,\mathrm{s}$. Because of the starting time and new individuals entering the measurement area, the data is left censored [1], meaning that the birth t_b of individuals entering the measurement area is unknown. To account for this, the first birth of a coordination number of an individual is the first time the coordination number changes in the measurement area. This introduces a new bias against individuals with very stable coordination numbers. Still, since these are few, and the aim is to analyze the general dynamics of the system, it only influences the tail of the survival curve. When individuals leave the measurement area, the death of the last coordination number is also unknown, and the data is right censored. This circumstance is accounted for in the Kaplan-Meier estimator [227], a non-parametric estimator used to calculate the survival function of empirical data. The estimator is defined as

$$\hat{S}(t) = \prod_{i:t_i \leq t} \frac{1 - d_i}{n_i}. \tag{5.1}$$

In the estimator, t_i is the time where at least one death happened, d_i is the number of deaths at time t_i, and n_i is the number of individuals still at risk (e.g., are not dead or censored). The survival plots of the 5-7 fold coordination numbers N_n are illustrated in a log plot in Figure 5.4 A and B. In the log plot and low motivation, the survival plots of the different coordination numbers are close to a straight line, indicating an exponentially decreasing survival function, which hints at a constant risk of changing coordination numbers (similar to nuclear decay). The survival function for $N_n = 7$

---

[1] Censored data is a concept usually relevant in patient studies where a certain outcome is measured (e.g., death). When a participant enters a study after an unknown time of receiving a treatment that could influence the measured outcome, it is left censored. When the participant leaves before the outcome is measured, it is right censored.

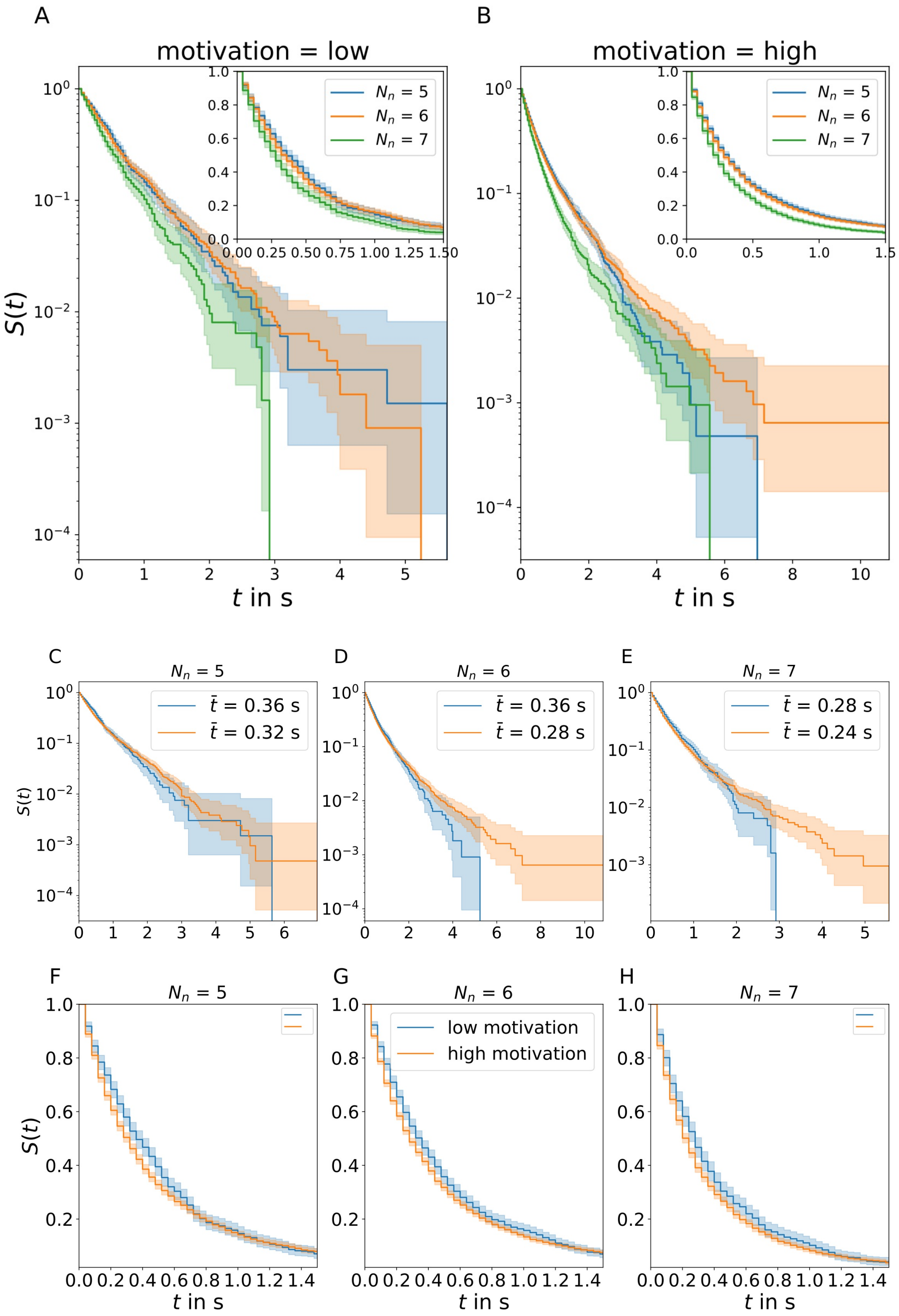

Figure 5.4: Survival function $S(t)$ of the coordination number for $N_n \in \{5, 6, 7\}$. (**A**)&(**B**) Compare the log-survival function of the coordination number for the respective motivation specified in the title. Panels (**C**)-(**E**) show the log-plot comparison between the motivation levels for the respective coordination number N_n specified in the title of the panels. The legend shows the median survival time $\bar{t}$. (**F**)-(**H**) show the same panels as C-E for $t < 1.5\,\text{s}$.

decays quicker than for $N_n = 5$ and $N_n = 6$, which are very close together. This is also evident in the median survival time $\bar{t}$ shown in the legend of Figure 5.4 C - E. The median survival time for $N_n = 5$ and $N_n = 6$ is equal with $\bar{t} = 0.36\,\mathrm{s}$ and $\bar{t} = 0.28\,\mathrm{s}$ for $N_n = 7$. The analogous survival function for high motivation in panel B of Figure 5.4 exhibits a heavy tail in the log plot, indicating a deceleration in the risk of death for a coordination number. This phenomenon can occur in systems where the risk of death is not homogenous, and there are configurations that are more stable compared to others in the cohort [228]. However, this is conjecture since there could be many reasons for this behavior. Similar to the case in low motivation, the 7-fold coordination number has the shortest median lifespan with $\bar{t} = 0.24$. For the 5- and 6-fold $\bar{t} = 0.28\,\mathrm{s}$ and $\bar{t} = 0.32\,\mathrm{s}$. The differences between the survival time of the different coordination numbers are measurable. Still, in all cases, the survival time is very short at about $(1/4 - 1/3)$ s, illustrating how the dynamical structural change. The results are not tested for statistical significance, but qualitatively a difference in the dynamics of the coordination number for high and low motivation is evident. This is further illustrated in panel C - H of Figure 5.4. In panels C - E, the heavy tail of high vs. low motivation is visible, while panels F-H show the faster early decay of the high motivation survival curve. For the difference in the tail between high and low motivation should be noted that for high motivation, there are twice as many experiments and generally more participants in the measurement area because of the high density, which could be the reason for the observed difference.

Next, the mean structure over time and space is analyzed, comparing the dynamics of the mean density $\langle \rho_n \rangle$, the mean hexagonal bond orientation measure $\langle \psi_6 \rangle$ and the mean coordination number $\langle N_n \rangle$ in the time interval of $0\,\mathrm{s} < t < 40\,\mathrm{s}$. The exact choice of the interval is arbitrary. However, during chosen one, there is still a large fraction of the participants in the system, and the most important features of the increase in density, the maximal density phase, and the subsequent decrease are visible. The mean value of the density $\langle \rho_n \rangle$ and the bond orientation parameter $\langle \psi_6 \rangle$ with the 95% interval of the data shown as error bars are illustrated in Figure 5.5 A and B. The mean is taken over all participants in the measurement area and all experiment runs (3 for low and 6 for high motivation). The density dynamics in the measurement area are strikingly similar for low and high motivation. For both motivations, the density increases in the experiment's first $5 - 7\,\mathrm{s}$. Between 5 and 15 s, the density for low motivation reaches a plateau and decreases from 20 s. For high motivation, the density reaches a maximum at around 10 - 12 s and decreases after about 20 s. Even though the dynamics around the maximal density differ slightly in regards to the maximal density, the low motivation density time series fits closely to the high motivation when scaled with a factor of 1.5. The bond orientation measure is static near $\langle\psi_6\rangle \approx 0$ for the whole duration of the experiment for both motivations, characterizing a fluid-like behavior. Panel C shows the time series of the mean coordination number $\langle N_n\rangle$, which is in both cases close to $N_n = 6$ during the whole run. The deviation for low motivation is larger, but the system's density is lower, and there are fewer runs. Because of the boundary conditions of the measurement area, the mean number can be influenced and deviate from $N_n = 6$. In Figure 5.5 D, the mean density $\langle\rho_n\rangle$ in respect to the distance from the bottleneck r between $10\,\mathrm{s} < t < 20\,\mathrm{s}$ illustrates an increase in density with distance to the bottleneck in the high motivation experiments, which saturates around $r \approx 1.25\,\mathrm{m}$. In contrast, for low motivation, the density profile is relatively flat. The scaling with the factor of 1.5 shows a good agreement between the low motivation density profile and the high motivation profile in the saturated part of the curve. Still, the dynamics differ closer to the bottleneck. In comparison, $\langle\psi_6\rangle$ in panel E is constantly close to zero for both motivations. To analyze the relation between the density and the order measure, the mean shape factor $\langle\zeta\rangle$ is plotted against the density ρ_n in the measurement area in panel F. For both motivations, the shape factor generally increases with the density. Interestingly at high densities, the shapes are far away from a regular hexagon ($\zeta \approx 1.103$) and closer to the shape factor of a square ($\zeta \approx 1.273$). For an illustration of the different shapes, see the Appendix Figure S7, where the shapes are sorted into three categories. The shape factor increase with density is steeper for low motivation than for high motivation. It should be considered that the mean density of the system for high motivation is higher than for low motivation. Therefore, the shapes are at different points of the density distribution of the respective system (see Figure 5.6 B). Rescaling the density by the mean density in the measurement area between $10\,\mathrm{s} < t < 20\,\mathrm{s}$ of the respective motivation collapses the curves close together, which is illustrated in panel G of Figure 5.5. Comparing the distributions of the measures in the measurement area and discussed time interval shows a remarkably close agreement between both motivations. The distribution of the shape factor with its minimum value translated to the origin $\zeta - 1$ is illustrated in Figure 5.6 A. For both motivations, the distributions are very close to each other with the mean for high motivation $\zeta \approx 1.231$ and for low motivation $\zeta \approx 1.237$ the difference in the

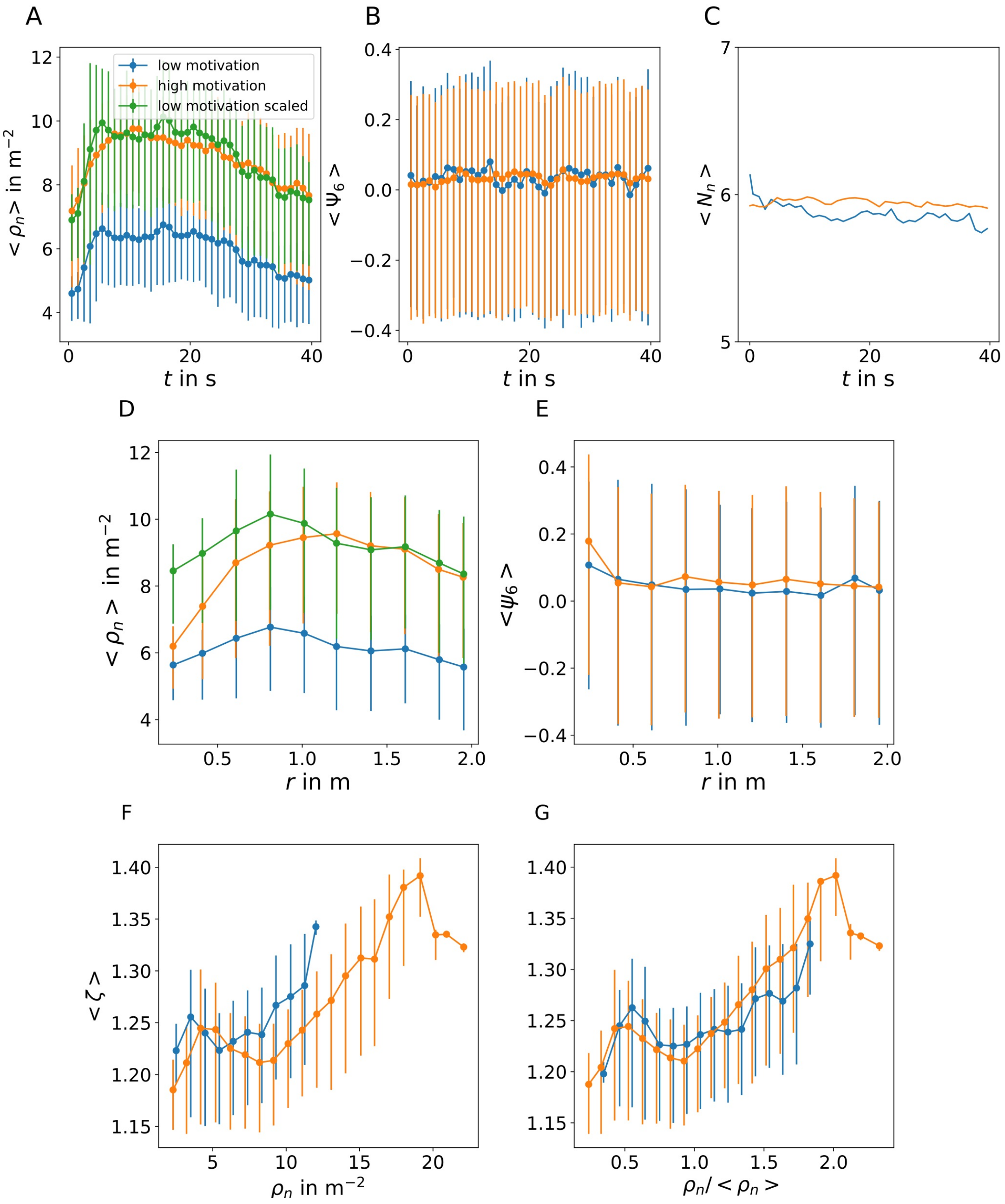

Figure 5.5: (**A**)-(**C**) Time series of the mean local density $\langle \rho_n \rangle$ (**A**), the mean hexagonal bond orientation factor $\langle \psi_6 \rangle$ (**B**) and the mean coordination number $\langle N_n \rangle$ (**C**). The values for low motivation and high motivation are shown in all three panels. Additionally, panel A displays a scaled version of the low motivation with $\alpha = 1.5$. (**D**)&(**E**) show the mean density $\langle \rho_n \rangle$ (**D**) and mean hexagonal bond orientation factor $\langle \psi_6 \rangle$ (**E**) in respect to the distance r from the bottleneck. The green line has the same scale factor as in (A). (**F**)&(**G**) depict the mean shape factor $\langle \zeta \rangle$ in respect to the density ρ_n (**F**) and to the rescaled density $\rho_n/\langle \rho_n \rangle$ (**G**). Error bars show the 95 % interval.

mean is statistical relevant ($p \ll 0.01$ using the t-test) but small. The distribution of $\zeta - 1$ is well fitted by the log-normal pdf

$$L(x, \mu, \sigma) = \frac{1}{x\sigma\sqrt{2\pi}} \exp\left(\frac{-(\ln(x) - \mu)^2}{2\sigma^2}\right), \tag{5.2}$$

With $\sigma \approx 0.3114$ and $\mu \approx -1.509$, pooling both high and low motivation together since the small difference in the distributions is not relevant considering the small effect on the shape. The relative error $\Delta P(\zeta) = |P(\zeta) - \hat{P}(\zeta)|/P(\zeta)$ of the fit, with the fitted value $\hat{P}(\zeta)$, is $\Delta P(\zeta) \approx 0.33$. The distributions of ζ for both motivations filtered for the coordination number $5 \leq N_n \leq 7$ exhibit the same shape regardless of N_n (Figure 5.6 D). The distributions are shifted with the smallest mean $N_n = 7$, $\langle\zeta(N_n = 7)\rangle \approx 1.208$. For $N_n = 6$ the mean shape factor is $\langle\zeta(N_n = 6)\rangle \approx 1.23$ and $\langle\zeta(N_n = 5)\rangle \approx 1.26$ with $p \ll 0.01$. As expected, the ζ is smallest for $N_n = 7$ and largest for $N_n = 5$ considering the value for the respective regular shapes (see Section 4.7). The local density distribution $P(\rho_n)$ in panel B of Figure 5.6 is in both cases for high and low motivation symmetrically distributed around their mean value close to a Gauss shape. A Gaussian distribution to the data shows a close fit (this illustrates the shape of the data, the densities are not Gauss distributed since negative values are not possible). The values of the fitted distribution for high and low motivation are $\mu \approx \{9.48, 6.46\}\,\mathrm{m}^{-2}$ and $\sigma \approx \{2.13, 1.57\}\,\mathrm{m}^{-2}$ respectively. Rescaling the density by the mean value of the distribution $\langle\rho_n\rangle$ for the respective motivation collapses them (see panel E in Figure 5.6). The distribution of N_n is also similar for both distributions with $\langle N_n\rangle \approx 5.96$ for high motivation and $\langle N_n\rangle \approx 5.84$ for low motivation. The difference is minor but statistically significant with $p \ll 0.01$. The Gaussian distribution fitted to the data of both motivations pooled together is a guide for the eye, showing the symmetry of the data. The values of the fit are $\mu \approx 5.93$ and $\sigma \approx 0.87$. The standard deviation σ is rather large, with the ratio between $N_n = 5$ and $N_n = 6$ being around 0.75 and 0.5 between $N_n = 7$ and $N_n = 6$. In conclusion, while the velocity dynamics of the participants differ dramatically between the experiments with low and high motivation, the same cannot be stated for the structure of the measured trajectories. The local structure of the system shifts dynamically on an individual scale. Measured over time, the different measures follow well-known distributions (log-normal for the shape factor and Gauss-like for the density and coordination number). For both motivations, the dynamic change in structure and the mean structure over multiple systems and time

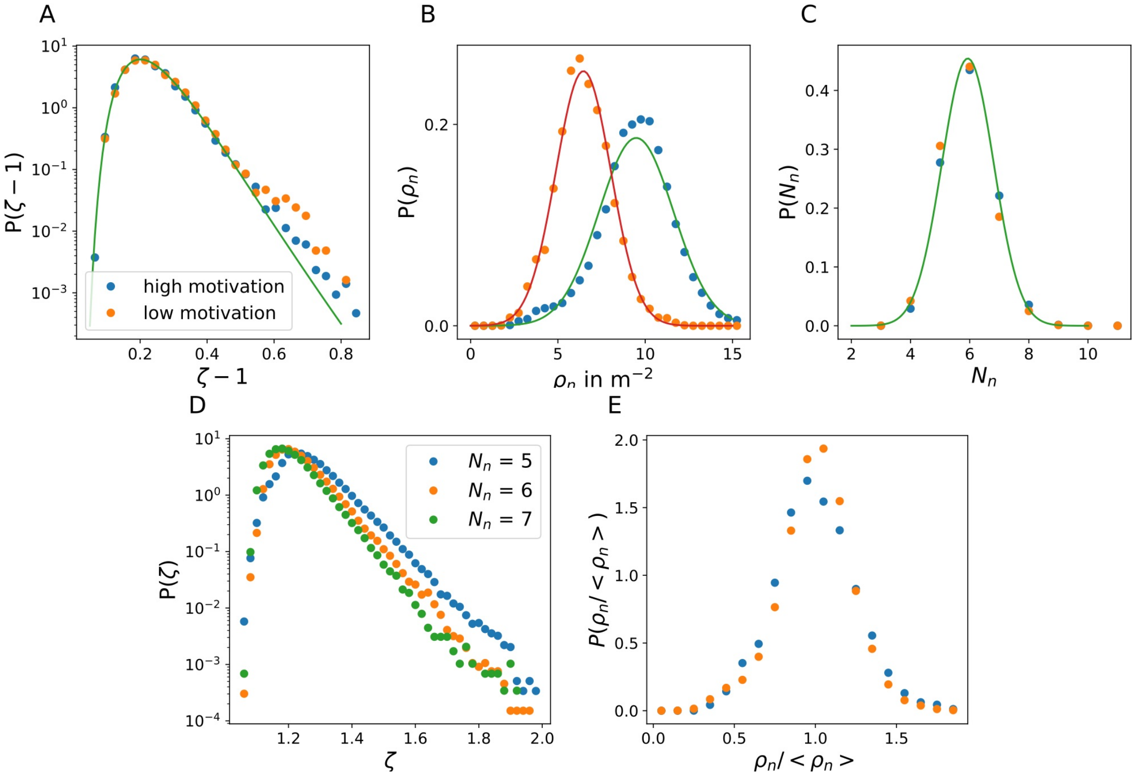

Figure 5.6: (**A**) Distribution of the translated shape factor ζ - 1, (**B**) the local density ρ_n and (**C**) the coordination number N_n. A log-normal distribution is fitted to the shape factor. The other fits show a normal distribution. (**D**) Shape factor for the coordination number N_n from 5 to 7 for both motivations. The mean for $\bar{\zeta}(N_n = 6) \approx 1.23$, $\bar{\zeta}(N_n = 5) \approx 1.27$, $\bar{\zeta}(N_n = 7) \approx 1.21$. (**E**) Distribution of the local density ρ_n scaled by the mean density $\rho_n/\langle\rho_n\rangle$.

is very similar, with only subtle differences compared to the dramatic change in the velocity dynamics.

5.1 Simulation of the experiment

This section compares simulations using the CSM to the experimentally observed structure. In contrast to simulations of granular matter [188, 195], the CSM is non-Newtonian and in non-equilibrium with a net flow. The simulations are conducted with $N = 190$ agents. In Table 5.1, the parameters of the CSM are summarized. The exit is set symmetrically around $x = 0$ m at $y = 0$ m with bottleneck width $w = 0.75\,\mathrm{m}$. The agent size is set to $l = 0.32\,\mathrm{m}$, which fits well to the mean neighbor distance $\langle d_n \rangle$ measured in the experiment (see Figure S9). The simulations are repeated $N_s = 50$ times with random initial positions and with an initial density close to the experiments of $\rho_0 = 4.5\,\mathrm{m}^{-2}$ as a boundary condition. The motivations are distinguished by the slope factor T (2.14) and the interaction distance d in the exponential repulsion factor (2.17), represented as the tuple $m = (T, d)$. For low motivation the parameters are set to $m = (1.0\,\mathrm{s}, 0.1\,\mathrm{m})$ and for high motivation the tuple is set to $m = (0.25\mathrm{s}, 0.05\mathrm{m})$. The idea behind the quantification of motivation in the CSM is discussed in Section 2.3. In the simulation at hand, the repulsion strength a_i in the exponential repulsion function $R(s)$ (2.17) is non-zero. A snapshot of the two conditions in the simulation and the local bond orientation parameter ψ_6 is illustrated in Figure 5.10 (top row). The increase in local density (3.6) of the system is visible, but a difference in the orientational order is not apparent.

For a quantitative analysis, the time series of $\langle \rho_n \rangle$ and $\langle \psi_6 \rangle$ and the 95% intervals of the measures are calculated in the measurement area as defined in Figure 5.2 in time steps of $\Delta t = 1$s analogous to Figure 5.5 in the time interval $0\mathrm{s} < t < 30\mathrm{s}$. The mean $\langle \circ \rangle$ is taken over all individual agents of all $N_s = 50$ ensembles of the system. The time interval is chosen because the mean local density is the most stable and contains the maximal density of the system. The time series are presented in Figure 5.7.

The mean local density $\langle \rho_n \rangle$ and mean hexagonal order $\langle \psi_6 \rangle$ increase substantially with the motivation. The system starts in a rather disordered state. The order increases from $0\mathrm{s} < t < 5\mathrm{s}$ and is substantially higher than in the experimental data, where the hexagonal order $\langle \psi_6 \rangle$ is close to constant over the whole measurement period ($10\mathrm{s} < t < 30\mathrm{s}$). An illustration of the difference in structure in the trajectory

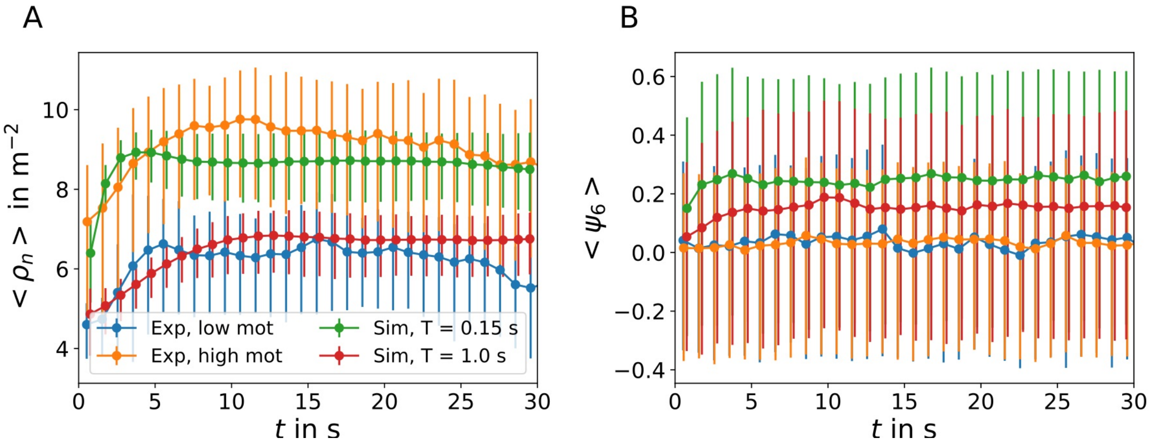

Figure 5.7: Time series of the simulation (Sim) and the experiment (Exp) for low and high motivation (mot) of the mean local density $\langle\rho_n\rangle$ (**A**) and the mean hexagonal order parameter $\langle\psi_6\rangle$ (**B**). The values are measured in the area specified in Figure 5.2. The bars show the 95% interval of the data for all agents i over all $N_s = 50$ ensembles.

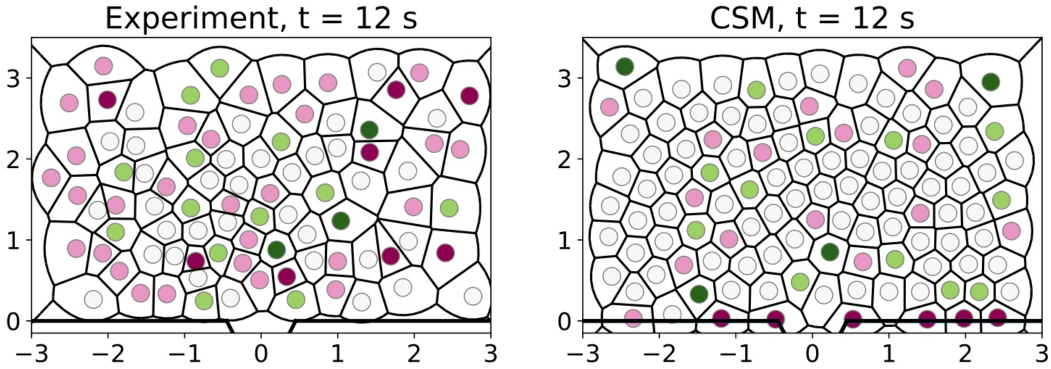

Figure 5.8: Voronoi-scatter plot of the experiment and the simulation **Left**: Snapshot of an experimental trajectory at $t = 12\,\text{s}$ and low motivation. **Right**: Snapshot of a CSM simulation at the same time as the experiment. The colors represent the coordination number N_n (white: $N_n = 6$, light green $N_n = 7$, light pink $N_n = 5$).

data of the experiment and the CSM is shown in the Voronoi-scatter plot in Figure 5.8. The plot shows the coordination number N_n, and the Voronoi cells are taken from the experimental data and a simulation at $t = 15\,\mathrm{s}$. The coordination number of the agents in the simulation is dominated by $N_n = 6$, displaying a clear preference for hexagonal order, with few 5-7 dislocations. It presents nearly regular hexagonal Voronoi cells in the system. In the experiment, the coordination number in the snapshot is noticeably more evenly distributed, and no preference in the shape of the Voronoi cells is visible. The variance in the distance to the neighboring agents j is lower in the simulations than in the experimental trajectory data. This can be further illustrated in the distributions of the local density and order parameters analogous to Figure 5.6. The distributions for the shape factor ζ, the local density ρ_n, and the coordination number N_n are calculated in the time interval $10\mathrm{s} < t < 20\mathrm{s}$. In Figure 5.9 the distributions for high and low motivation in the experiment (crosses) and the simulations (dots) of low motivation ($m = (1\,\mathrm{s}, 0.1\,\mathrm{m})$) and high motivation ($m = (0.15\mathrm{s}, 0.05\mathrm{m})$) are depicted. The vertical lines in the shape factor plot are the values for the shape factor of the regular hexagon ($\zeta \approx 1.103$) and regular pentagon ($\zeta \approx 1.156$). The distribution of the simulations for the shape factor ζ is used to analyze the microscopic order in the system. The ζ-distribution of the simulations differs from the experiments, as these exhibit much narrower peaks. The distribution of the simulation for low and high motivation also differs considerably. The low motivation simulation is unimodal with a peak near the value of the regular pentagon ($\zeta \approx 1.156$) and a saddle point between the value for a regular hexagon ($\zeta \approx 1.103$) and the regular pentagon. The distribution for the CSM of high motivation is, in contrast, bi-modal, with the same peak near the value for the regular pentagon and a second peak near the value for the regular hexagon. This is to be expected, considering the higher value of $\langle\psi_6\rangle$ in the time series analysis of Figure 5.7. The peak near the shape factor of a regular hexagon is also consistent with the higher density of the system, as this shape maximizes the packing fraction of discs. The distribution has an exponential tail (see log-plot in Figure S10) for both motivations and cannot be approximated by a log-normal distribution, as in the case of the experiments. The coordination number N_n of the experiment and the CSM are similar and symmetrically distributed around $N_n = 6$. The coordination number distribution of the simulations peaked narrower at $N_n = 6$. The peak of the high motivation simulations is narrower, indicating that the system has fewer defects than in the case of low motivation. The CSM for both motivations has fewer defects than observed in the experimental data. In conclusion, the CSM simulations can reproduce the measured densities fairly well in the experiments conducted in Navarra and Wuppertal [1, 32] but analyzing the microscopic structure of the system reveals

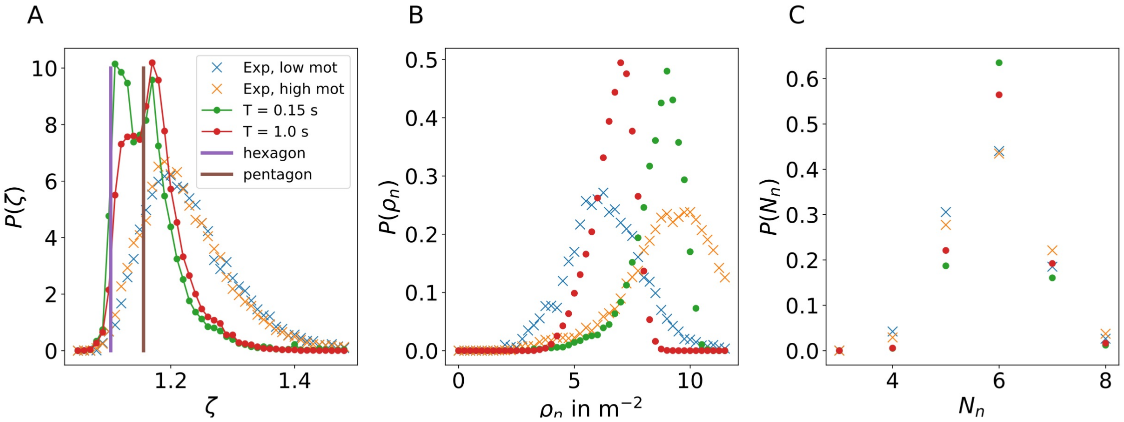

Figure 5.9: Distribution of the shape factor ζ (**A**), local density ρ_n (**B**), and coordination number N_n (**C**) for the CSM simulations (dots) and the experiments (crosses). The vertical lines in A show the shape factor of the regular hexagon and pentagon.

that the model differs significantly compared to the measured trajectories. The model has a higher hexagonal order, increasing with the motivation with fewer defects and clear peaks close to regular hexagons and pentagons in the shape factor distribution. Most notably, the shape factor distribution and coordination number distribution in the experiments do not differ significantly. The following sections investigate possible reasons for the difference in the model distributions and time series compared to the experiments. Apart from the differences between the model used in the simulations and the physical properties of the human shape, two effects are analyzed that could influence the structure of the measured system. One factor is the polydispersity in the participant's size. Even though the group in the experiment is quite homogenous (men in the military of similar age), a natural variation in body size could affect the microscopic structure. This influence of polydispersity is well studied in the granular matter, and colloids [195, 197, 203, 206]. Another factor could be errors in the measurement of the trajectories. While colloids and granular positions can be measured very well in experimental settings, the same is not true for the position of pedestrians, even in well-controlled experiments. Both factors are discussed in detail in the following sections.

Parameter	Variable	Value
Slope factor (motivation)	T	$\{0.15, 1\}$ s
Desired velocity	v_0	1.34 m/s
Initial density	ρ_i	4.3 m^{-2}
Agent size (hardcore exclusion)	l	0.32 m
Repulsion strength	a_i	2.5
Repulsion length	d	$\{0.05, 0.1\}$ m
Noise standard deviation	σ	0
Population	N	190
Floor field resolution	Δh	0.01 m
Wall avoidance distance	d_w	0.25 m
Bottleneck width	w	0.75 m
Corridor width	b	10 m

Table 5.1: Summary of model parameters and their values.

5.2 Influence of polydispersity on the structure in the CSM

Polydispersity in the size of granular materials and colloids is extensively studied in the context of the influence of the microscopic structure [195, 197, 203, 206]. Two effects of variance in particle size on the microscopic structure are the decrease in hexagonal order and the increase in defects in the granular medium. To analyze the effect of polydispersity, the radius r_a of agent i is chosen by a Gaussian distribution with mean $\mu = 0.16$m and standard deviation σ_r. Snapshots of the simulation with a different degree of polydispersity from $\sigma_r = 0$m to $\sigma_r = 0.06$m in $\Delta\sigma_r = 0.02$m steps are illustrated in Figure 5.10. This covers a wide range of polydisperse systems with the highest standard deviation in agent radius far beyond what is realistic in humans, as is obvious when looking at the simulations. For American human males at age 19, the standard deviation of the shoulder can be assumed to be about $\sigma \approx 0.02$ m [229]. It should also be noted that the probability of clogs in the simulations that arrest the flow increases with the standard deviation of the radius (see Figure 5.13). In a system with high diversity in agent size, it is more likely that large agents (compared to the bottleneck width) clog near the exit. Figure 5.11 shows the time series of the simulation for different standard deviations in the polydispersity in both low and high motivation simulations analogous to Figure 5.7. The mean neighborhood density ρ_n of the simulated system is not affected by the polydispersity of the agent

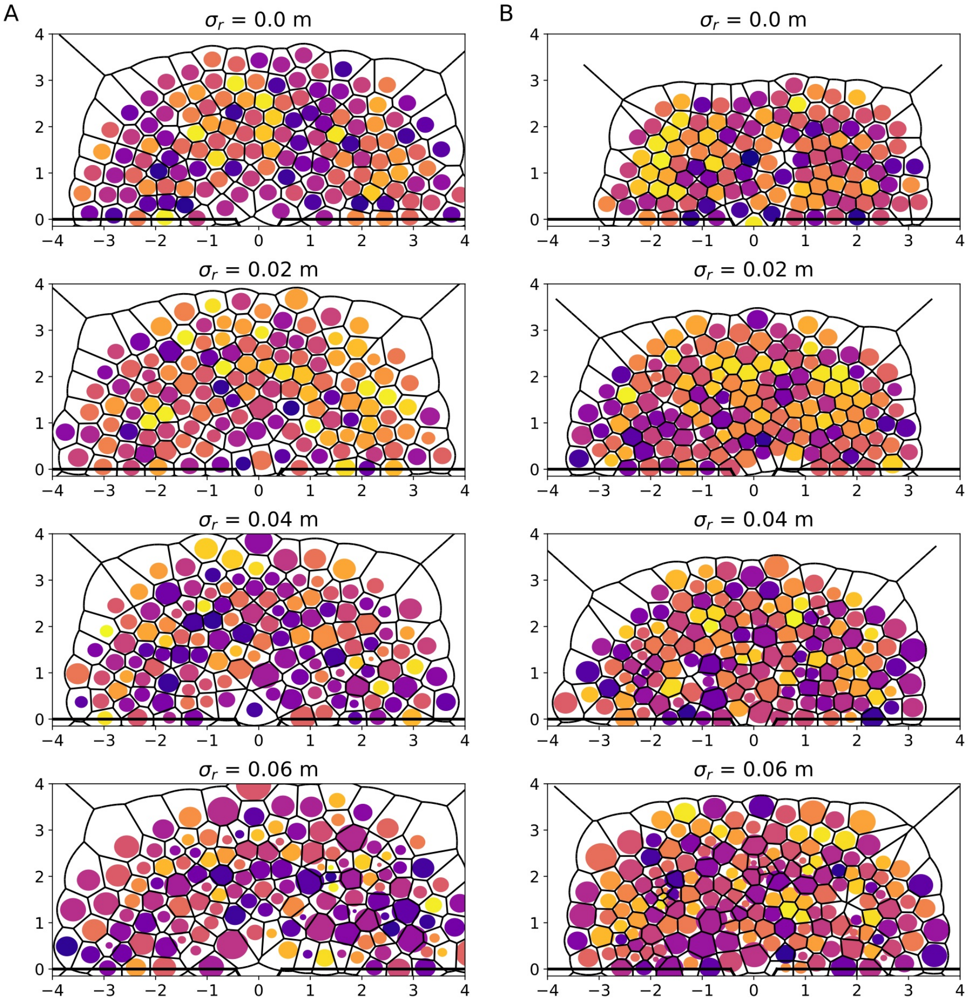

Figure 5.10: Snapshot of the CSM simulation with a polysipersity of $\sigma_r \in \{0, 0.02, 0.04, 0.06\}$ m specified in the title. The (**A**) column shows low motivation ($m = (1\text{s}, 0.1\,\text{m})$) and the (**B**) coloumn shows high motivation ($m = (0.15\text{s}, 0.05\,\text{m})$).

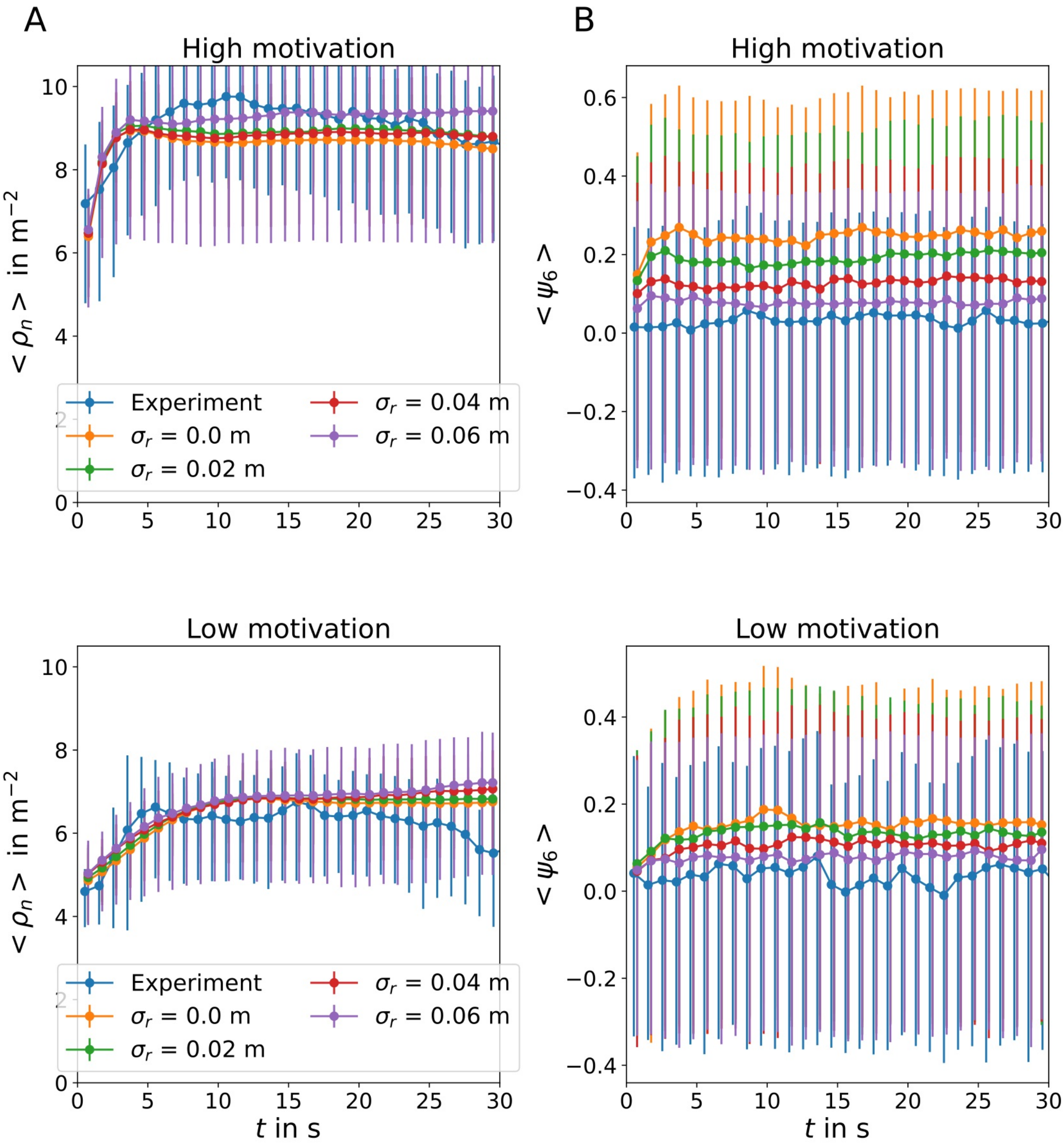

Figure 5.11: Time series of the mean local density $\langle\rho_n\rangle$ (column **A**) and mean hexagonal order $\langle\psi_6\rangle$ (column **B**) of the experiment and simulations with polydispersity σ_r. The motivation is specified in the panel titles.

radius r_a, but the orientation-order parameter ψ_6 decreases with increasing polydispersity for both high and low motivation, as expected when considering results from polydisperse granular systems. Surprisingly even a high standard deviation in the agent's radius of $\sigma = 0.06$ m of the simulated system has a higher orientational order than in the experiments for both motivations. This is illustrated more clearly in Figure 5.13 in the panel for the mean local density $\langle \rho_n \rangle$ and the mean orientational order $\langle \psi_6 \rangle$ in the time interval $10\,\mathrm{s} < t < 20\,\mathrm{s}$. The dotted lines show the values of the experiments. The mean value $\langle \psi_6 \rangle$ decreases substantially but is even for large values of σ larger than the experimentally measured values. The distributions in Figure 5.12 (analogous to Figure 5.9) show the effect of the polydispersity on the order and density measures. A reasonable polydispersity of $\sigma = 0.02$ m has a small effect on the shape-factor distribution. Both peaks are clearly visible in the simulations with high motivation and only slightly reduced. The same can be observed in the low motivation simulations, where the peak near the value of the regular pentagon is only slightly reduced. Even with $\sigma = 0.06$ m, the distribution for high motivation is bimodal, though the peaks are less pronounced and not as close to the regular hexagon and pentagon values. The distribution of the local density for high motivation simulation is not improved regarding fitting the experimental data by the polydispersity. For low motivation, the distribution fits well for $\sigma = 0.06$ m but is not sensitive to a polydispersity of $\sigma = 0.02$ m. The coordination number distribution is improved in both cases for a polydispersity between $\sigma = 0.04$ m to $\sigma = 0.06$ m.

A reasonable polydispersity shows only little improvement, however. To analyze this quantitatively, the mean square error $\mathrm{mse} = 1/n \sum_i (x_i - \hat{x}_i)^2$ is calculated for all distributions, where x_i is the simulation value for a certain measure and $\hat{x}_i$ is the corresponding empirical value. The results are summarized in Figure 5.13. The curve of the mse concerning the different measures has no coinciding minimum. Especially the $\mathrm{mse}(\zeta)$ is still large even for $\sigma = 0.06$ m and displays no minimum compared to the other measures that have a minimum in mse around $\sigma \approx 0.04$ m. To conclude, polydispersity in the size of the participants cannot explain why the microscopic measures of the simulations (ψ_6, ζ, N_n) differ from the empirical data. The simulations' structure depends on the system's polydispersity but is not very sensitive to small variances in agent size.

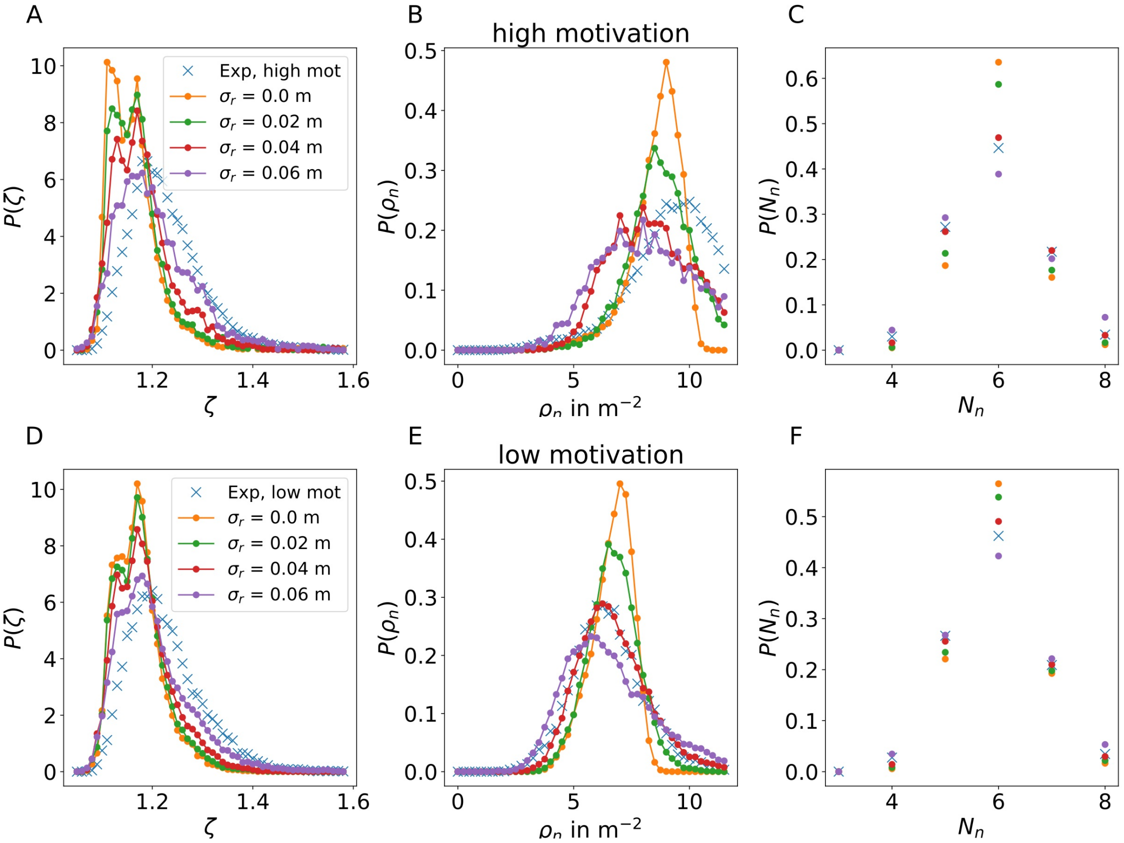

Figure 5.12: Analogous to Figure 5.9 a comparison of the distributions $P(\zeta)$ (**A**)&(**D**), $P(\rho_n)$ (**B**)&(**E**), and $P(N_n)$ (**C**)&(**F**) with polydispersity σ_r. High (A-C) and low motivation (D-F) are indicated in he title.

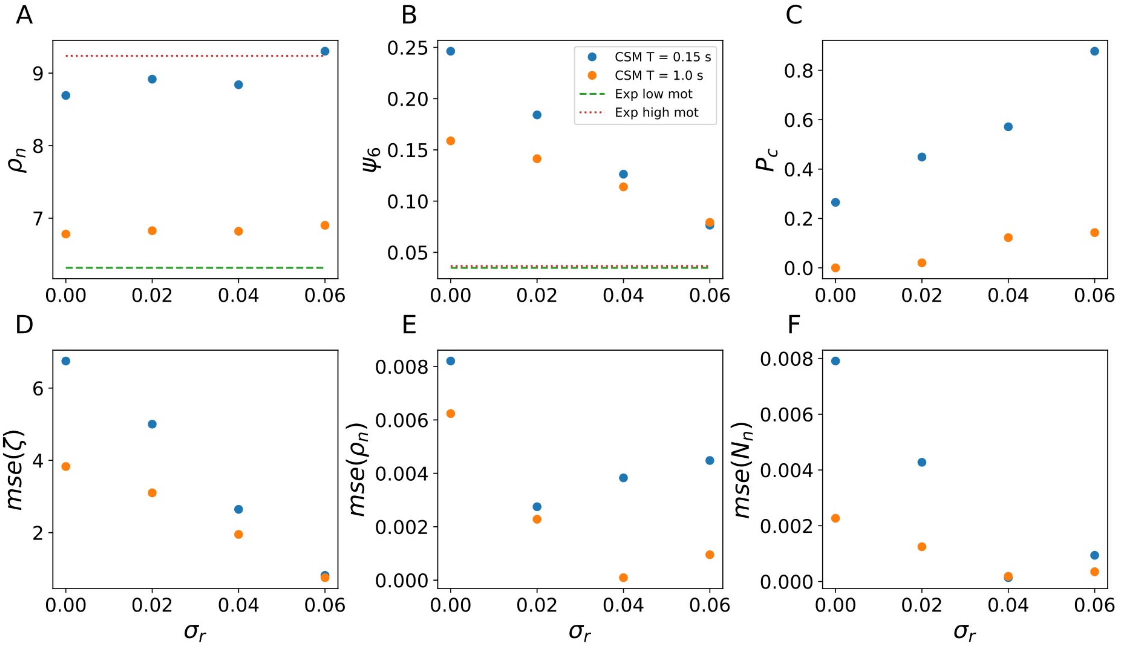

Figure 5.13: (**A**) Comparison of the density ρ_n in the CSM with respect to the polydispersity σ_r with the experimental data (dashed lines, see legend). (**B**) analogous to A the hexagonal bond orientation factor ψ_6 in respect to σ_r. (**C**) The fraction P_c of simulations that clog before evacuating the room in respect to σ_r. Panels (**D**)-(**F**) show the mse of the distributions in Figure 5.12 of the CSM and the experimental data for the shape factor ζ (panel D), the density ρ_n (panel E) and the coordination number N_n (panel F).

5.3 Influence of errors and noise in the trajectories

The trajectories in the experiments [1] are measured using the camera system's information by tracking the participants' heads. The participants wore red heads, which the image analysis software can track. The method to track the heads is quite precise [230], but the approach has several sources for errors in the exact position of the participant's center of gravity. The head of the participants moves about their body by swaying around or bending the upper body while walking (this is illustrated in Figure S8). Since there is no information on the exact height of the participants, an average height has to be assumed, which leads to an error in three-dimensional data that is mapped onto a two-dimensional plane. In the experiments [1] an error of $|\Delta \mathbf{x}| \approx 0.1$ m is estimated. The head and body sway effect in measuring the trajectories is illustrated in Figure 5.14 (center panel). The trajectories show periodic swaying perpendicular to the movement direction. The simulated trajectories illustrated in Figure 5.14 (left panel) are smooth in comparison. A simple way to introduce an error in the position of the simulated agents is to add an i.i.d. random variable with zero mean and variance σ^2. Specifically, a deviation of gaussian white noise $dx, dy = N(0, \sigma^2)$ is added onto the x and y component of the position $\mathbf{x}_i(t)$ of agent i. It should be stressed that this approach is quite different from the error in the trajectory analysis of video files. Adding random noise onto the position independently effectively disconnects the trajectories since the noise is added on the exact position of every time step saved (which is a subset of the time resolution of the simulation). The trajectories with added noise of a single run can thus be interpenetrated as multiple independent simulations at different points in time with the same initial conditions but some unspecified deviation in the measured trajectory from the exact trajectory that can be modeled by Gaussian white noise.

Even though the trajectories are disconnected, the effect of the noise on the simulation is shown in Figure 5.14 (right panel) to illustrate the trajectory deviation from the simulated positions. The deviation from the mean trajectory is reasonable compared to the sway observed in the experimental trajectories. A snapshot of the simulation showing the defects analogous to Figure 5.8 is shown in Figure 5.15 for low motivation. The simulation with noise and the experiment is not as clearly distinguishable as in Figure 5.8. Compared to the exact position, the noisy positions exhibit no preference for regular hexagonal shapes and have a larger number of defects. Displaying time series of $\langle \rho_n \rangle$ and $\langle \psi_6 \rangle$ in Figure 5.16 shows a remark-

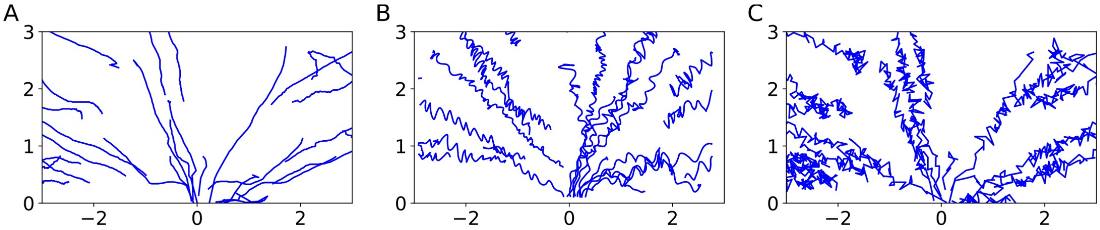

Figure 5.14: Comparison of the simulated trajectories and the experimental trajectories in the x-y plane. The plot shows a random sample of 30 trajectories from the CSM-simulations ((**A**)&(**C**)) and the experiment with low motivation ((**B**)) for $0\,\mathrm{s} < t < 30\,\mathrm{s}$. Panel A shows the simulation trajectory without added noise and panel C with added noise $\sigma = 0.07\,\mathrm{m}$.

able agreement of the simulations with added error and the empirical data of $\langle\psi_6\rangle$ for both low and high motivation. The increase in orientational order in the exact simulations trajectories is not detectable in the trajectories with added noise, and $\langle\psi_6\rangle$ is static in the time interval illustrated. The distributions of density and order measures (Figure 5.17) show that the trajectories with added noise fit very well with the experimental data. Especially for low motivation, all distributions of

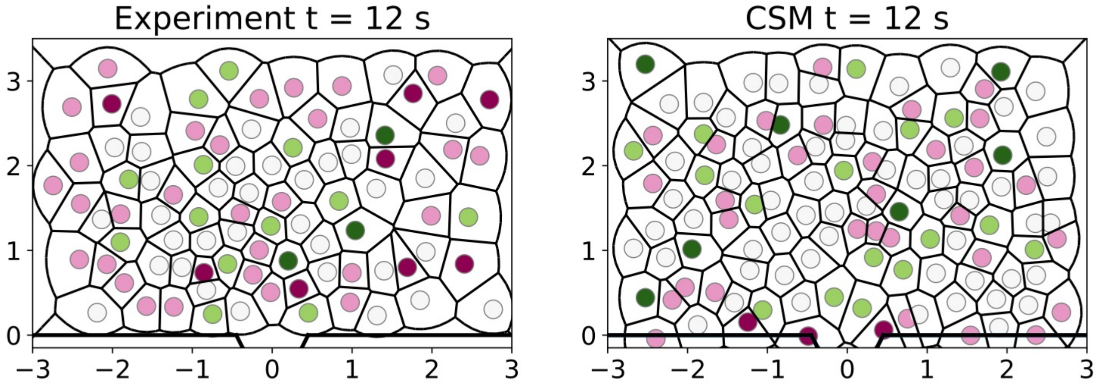

Figure 5.15: Analogous to Figure 5.8 the coordination number in the experiment [1] **left** and the CSM at 12s **right**. In this case, the positions of the simulated agents are deviated $\mathbf{x} = (x + dx, y + dy)$ by a random vector with entries $dx, dy = N(0, \sigma^2)$ and $\sigma = 0.07\,\mathrm{m}$.

the experiments and simulations with noise fall close together. Most importantly, the distributions of the shape factor ζ and the coordination number N_n fall close together when white noise is added on the x and y components with $\sigma = 0.07\,\mathrm{m}$. Figure 5.18 shows the effect of the noise on the order and density measures and the mse of the different simulated distributions with respect to the experiments. In contrast to the effect of polydispersity, noise in the trajectories is consistent with the fit to the experimental data, especially for low motivation. The values of the mse for low motivation have a minimum for all three measures (ζ, ρ_n and N_n) near $\sigma = 0.07\,\mathrm{m}$. The mean value of $\langle\psi_6\rangle$ in the time interval $10\,\mathrm{s} < t < 20\,\mathrm{s}$ is also close to the experimental values in this noise region. For high motivation, the structure measures behave similarly; only the local density mse(ρ_n) error does not exhibit a minimum near $\sigma = 0.07\,\mathrm{m}$. This is most likely connected to the issues the model is confronted with in high motivation and pushing situations discussed earlier. In Appendix A.4, the analysis is repeated for the social force model for low motivation. The values of the parameters are specified in table A.1. The social force model exhibits a much higher order in the simulations (see Figure S13 for $\sigma = 0\,\mathrm{m}$). The distribution for ζ has a sharp peak near the value of the regular hexagon.

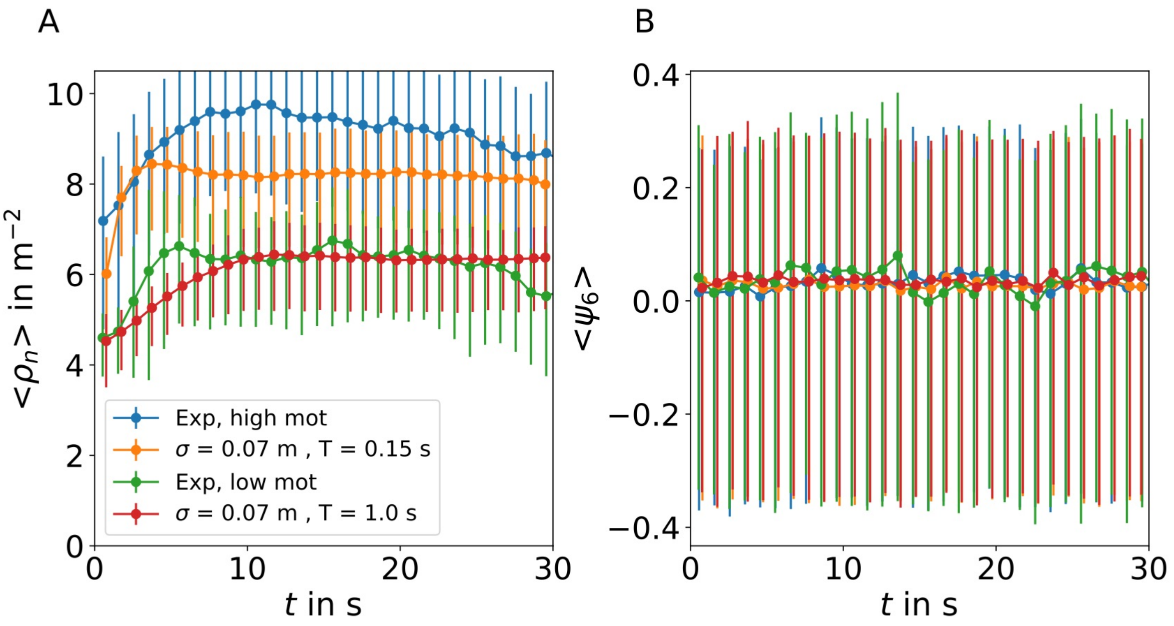

Figure 5.16: Time series of the simulations with added noise and the experiment for low and high motivation. (**A**) shows the mean local density $\langle\rho_n\rangle$, and (**B**) the mean orientational order-measure $\langle\psi_6\rangle$. The observables are measured in the area specified in Figure 5.2. The error bars show the 95% interval.

The density is sharply peaked with a small variance, and the coordination number is closely peaked around $N_n = 6$. Adding noise to the trajectory in this situation has a similar effect as the CSM on the structure. In this case, the mse of the shape factor ζ and the coordination number N_n minimizes around $\sigma \approx 0.09\,\mathrm{m}$, which is still inside the error range. Concerning the local density, the effect of the noise is not as consistent as in the CSM. There is no minimum of the mse(ρ_n) near $\sigma = 0.09$ m, and the mean density $\langle \rho_n \rangle$ of the system dips below the experimental value. In summary, the analysis of the CSM and SFM shows that rather small deviations of the measurement of the trajectory in the range of about $\langle |d\vec{x}| \rangle \approx 0.07$ m ($\langle |d\vec{x}| \rangle \approx 0.09$ for the SFM) from the motion of the center of gravity can transform distributions of the shape factor with distinct peaks onto the same distribution measured from the experimental data. This is also true for systems that exhibit very sharp peaks in the distributions of the order measures (ζ and N_n) as illustrated in the social force model. There exist noise strengths σ_m for both models (SFM and CSM), which merges their shape factor distribution to that of randomly distributed particles with radius r_i and volume exclusion (Appendix A.2 Figure S12), which also fits well to the experimental data. The results illustrate that the structure of the system is susceptible to errors in the measurement of the pedestrian position, which is inherently difficult to improve because of the flexible capabilities and movements of the human body. It is impossible to infer the precise position distribution from the measurements because the effect of the noise is an injective function. An improvement would be precisely tracking the center of gravity of the pedestrians in the experiments.

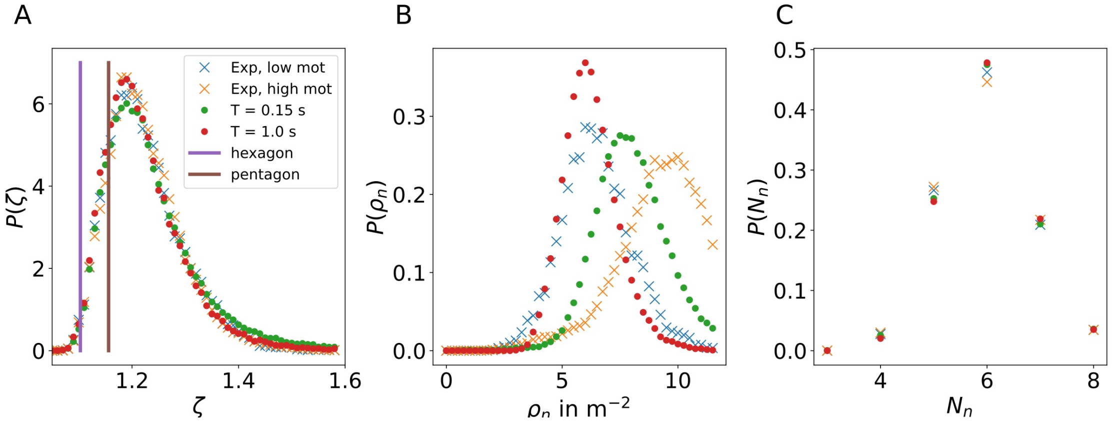

Figure 5.17: Distribution of the shape factor ζ (**A**) ,local density ρ_n (**B**), and coordination number N_n (**C**) for the CSM simulations with added noise $dx, dy = N(0, \sigma^2)$ and $\sigma = 0.07$ m. Dots are from the simulations and crosses from the experiments.

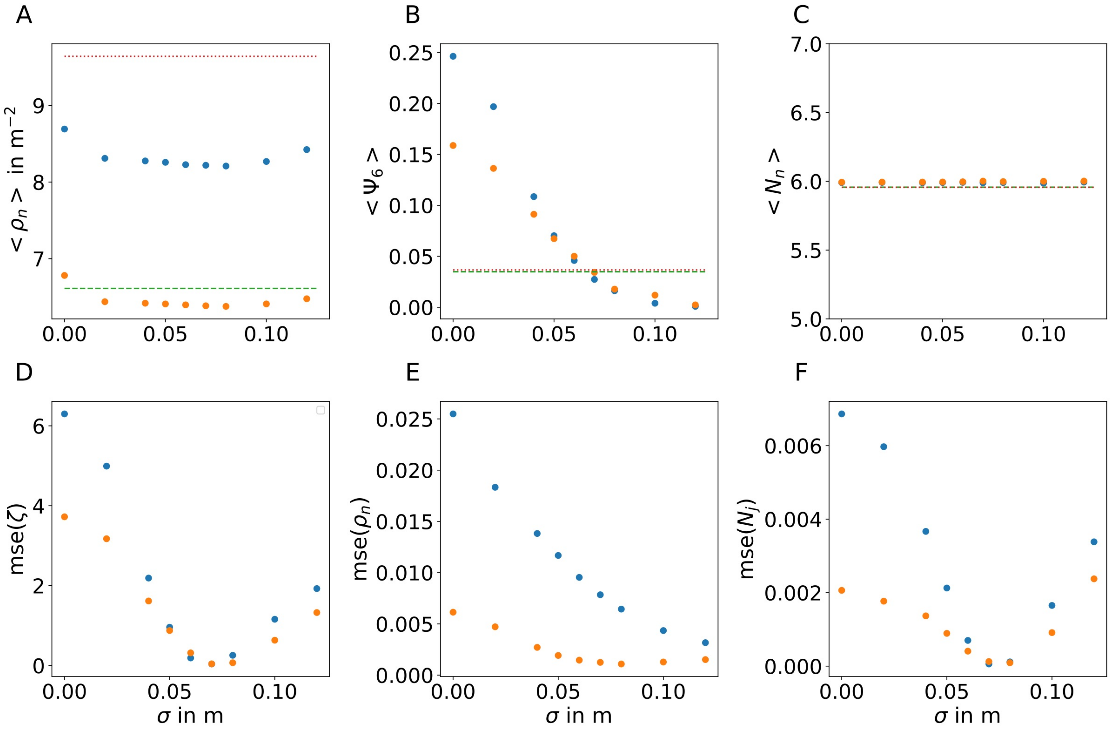

Figure 5.18: **(A)-(C)**: The mean value of the local density $\langle \rho_n \rangle$ (**A**), hexagonal-order-parameter $\langle \psi_6 \rangle$ (**B**) and the coordination number $\langle N_n \rangle$ (**C**) are represented in respect to the added noise on the position of the simulated agents. The dotted lines represent the experimental value for the different motivations, respectively. **(D)-(F)**: The mean square error (mse) of the distribution of the shape factor ζ **(A)**, local density ρ_n **(B)** and the coordination numberN_n **(C)** in respect to the experimental distributions (see Figure 5.17). The distributions are illustrated in Append A.2 Figure S11.

Chapter 6

Microscopic order in simulations of pedestrian bottleneck

This chapter continues the analysis of the spatial order in pedestrian models in bottleneck situations. The focus is on the collision-free speed model and its stochastic version (CSM, SCSM, Section 2.3), while also the social force model (SFM, Section 2.1) is used for comparison. At first, simulations with the same parameter set as in the low motivation simulations of the experiments in the previous section, with similar geometry and initial conditions, are conducted in a larger system. In the subsequent sections, a selection of parameters deemed especially interesting in the structure context is varied to explore their influence on the system. To reduce boundary effects, simulations with a large number of agents are conducted on the scale of $3000 \leq N \leq 8000$ using "periodic" boundary conditions and long simulation times. The boundary conditions are "periodic" in the sense that agents leaving the geometry through the exit appear again in the geometry far away from the exit in a specified area where they are placed randomly with zero speed initially. Specifically, the size of the geometry is determined by the set corridor width b and the corridor length l_c, which is determined by the initial density ρ_i of the system and the number of agents N, $l_c = N/(\rho_i b)$. The area for the redeployment of the agents that exited the geometry is between l_c and $l_c \times 1.5$ bounded by the corridor width to the sides. The simulation time depends on the specific system between $1500\,\mathrm{s} \leq t \leq 10000\,\mathrm{s}$. The exit's placement, geometry, and width are analogous to the previous section. As an introduction to the large-scale simulations and the order phenomena, a simulation of the system with a single set of parameters (see Table 6.1) run $N_s = 25$ times is presented in the following. The analysis of the measures is done in the area between

Parameter	Variable	Value
Slope factor (motivation)	T	1.0 s
Desired velocity	v_0	1.34 m/s
Agent size (hardcore exclusion)	l	0.34 m
Repulsion strength	a	2.5
Repulsion length	d	0.1 m
Noise standard deviation	σ	0
Population	N	8000
Floor field resolution	Δh	0.01 m
Wall avoidance distance	d_w	0.25 m
Corridor width	b	55.0 m
Initial density	ρ_i	2.5 m^{-2}
Bottleneck width	w	0.75 m

Table 6.1: Summary of model parameters and their values.

$|x| < 15\,\mathrm{m}$ to avoid boundary effects. The measurement distance to the bottleneck r is varied to analyze the different regions. As discussed in Section 2.3, the CSM is deterministic and can run into unfavorable or unrealistic configurations. In the case of the bottleneck, this can lead to clogs near the bottleneck that drive the whole system into a deadlock. Important factors for the likelihood of clogging in granular systems are mainly determined by the ratio between the exit width and the particle size. In granular matter, the flow through a hopper or bottleneck is described by the Beverloo law [231]. It states that in a granular system, the mass flow through a circular orifice scales with its diameter of the exit $D^{5/2}$ in three dimensions and $D^{3/2}$ in two dimensions [232]. In the simulations, the agent size is chosen, among other things, so clogs are unlikely. In the speed-based model, other parameters like the repulsion strength a_i, the slope factor T, or the repulsion length d also influence the clogging probability, which is discussed later. During the runtime of $t = 5000\,\mathrm{s}$, clogs can appear. In the case of the simulations with the parameters summarized in Table 6.1, around 44% of the systems clogged before the maximal runtime. The data of the simulations are only considered until the appearance of a clog. This is not a problem for the statistical analysis since only 4 out of the 25 simulations ran for less than 3000 s of simulation time before a clog appeared.

Exploring the structure measures: In Figure 6.1, a single run of the simulations is visualized with a Voronoi-scatter plot at different times and for different measures, namely the packing fraction ϕ (Row A), the bond orientation parameter Ψ_6 (Row B), the shape factor ζ (Row C) and the coordination number N_n (Row D) (See also video *a2_ 5d0_ 1OrderDensCoordCSM.mp4* in [226] showing Ψ_6, ρ and N_n). The local packing fraction of the system increases over time in the area further away from the bottleneck $r \gtrsim 2$ m. After the simulation starts, a packing fraction shock goes through the system. The beginning of that can be observed in the panel at $t = 10$ s near the bottleneck. The packing fraction ϕ after $t = 60$ s further away from the bottleneck ($r \gtrsim 6$ m) is higher than at $t = 4000$ s, which is during the stationary state of the system. The packing fraction increases with r and is not dependent on the angle. For a given distance r from the bottleneck, the packing fraction is rather homogeneous, with minor fluctuations compared to the other measures. This is especially evident in the bond orientation factor Ψ_6, which exhibits all possible values ($\Psi_6 \in [0, 1]$) at almost any distance from the bottleneck. The system starts in a low state of hexagonal order, but after 10 s small clusters of hexagonally structured agents appear near the bottleneck. At $t = 60$ s, a large number of these clusters ($\Psi_6 > 0.7$) appear in the whole system. At $t = 4000$ s in the stationary state, the frequency of these clusters reduces. A similar observation can be obtained from the shape factor ζ in Figure 6.1 row C. With the shape factor, different kind of structures appears more clearly in the system. Similar to the hexagonal order, the clusters with shape factor close to $\zeta \approx 1.1$ appear at $t = 60$ s and become rare at $t = 4000$ s (visible as the blue discs). There is also an abundance of agents with a shape factor of $1.15 \lesssim \zeta \lesssim 1.19$ (visible as purple/black discs), which are close in shape to pentagons. Agents with a larger shape factor $\zeta \gtrsim 1.19$ can also be observed, especially at $t = 10$ s but become rare at longer times when the system's structure is closer to a hexagonal pattern. The coordination number N_n is depicted in row D. The systems start with a large number of defects, and similar to the other measures, they decrease at first ($t = 60$ s) with a subsequent increase towards the stationary state. The defects observed in the panels are 5-7 fold dislocations (see Section 4.6). They are distributed unevenly in the space with large areas where the agent's coordination number is $N_n = 6$ and grain boundaries and smaller clusters of dislocations.

Hexagonal order classes: To analyze these relations further and simplify the continuous nature of Ψ_6, the agents are classified into two order classes. Agents with $\Psi_6 > 0.7$ are considered to be in the hexagonally ordered class, while agents

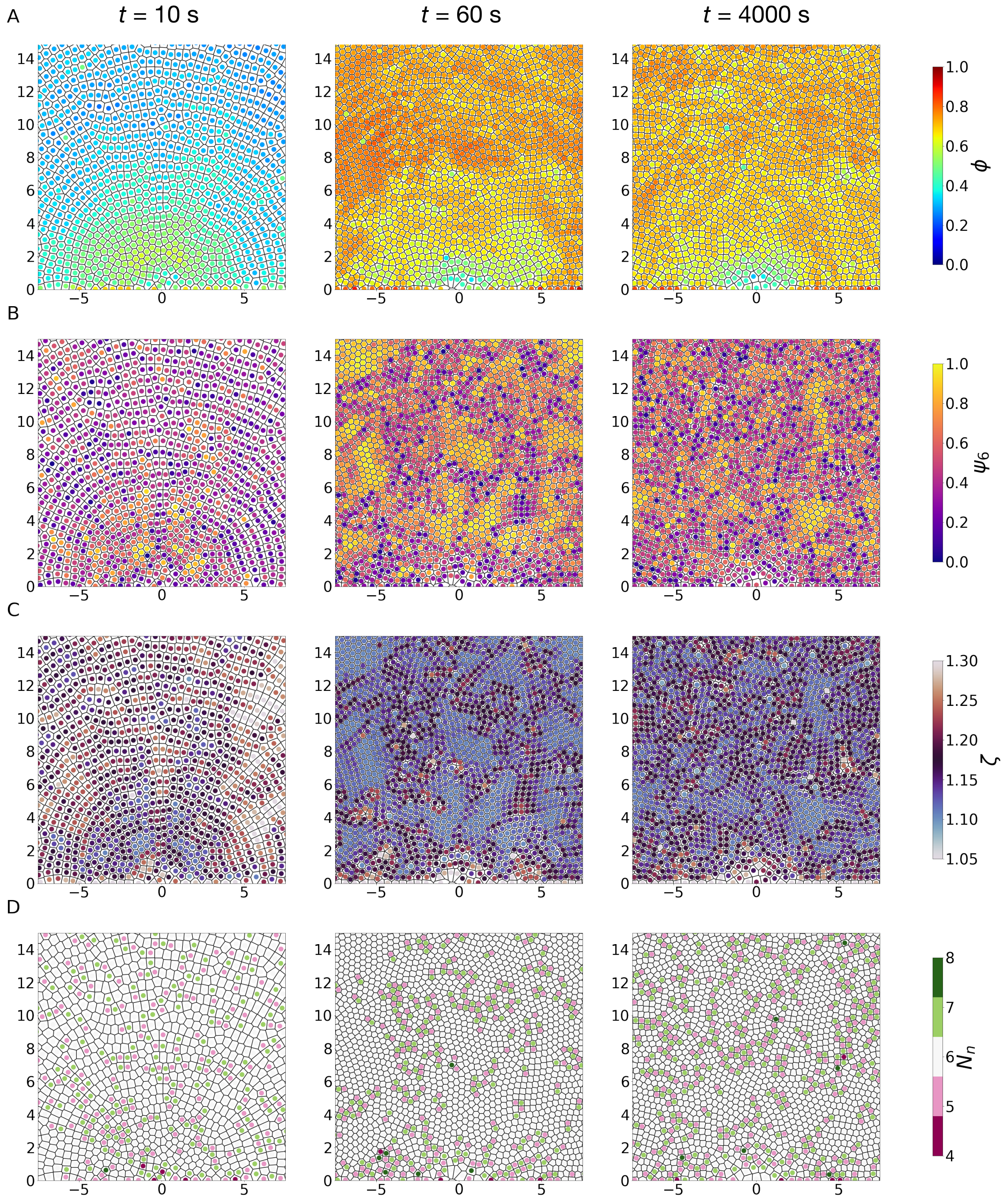

Figure 6.1: CSM bottleneck simulation at different times $t = \{10, 60, 4000\}$ s (see titles of top panels) with $N = 8000$, showing a variety of local measures. (**A**) The local packing fraction ϕ, (**B**) the bond orientation measure Ψ_6, (**C**) shape factor ζ and (**D**) the coordination number N_n.

with Ψ_6 below the threshold are considered disordered. The threshold is arbitrary but makes it possible to compare the structure with the work of [195], which uses the same threshold for their work on grain boundaries in polydisperse granular fluids. In the case of this thesis, the threshold should not be too strict about excluding a large amount of the structure but still represent the system close to hexagonal order. In Figure 6.4 A-C, the agents in the ordered class are shown in yellow at $t = 15$ s, $t = 60$ s, and $t = 4000$ s. The large clusters of highly ordered agents at $t = 60$ s are well visible, while the disordered grey area contains the dislocations and grain boundaries. At $t = 4000$ s, there are fewer small clusters in the system, while a small number of larger clusters are only observed near the bottleneck ($r < 10$ m). The time series of three different measures are depicted in Figure 6.2 A-C, namely the fraction of agents in the hexagonal class $P(\Psi_6 > 0.7)$, the fraction of agents with a hexagonal coordination number $P(N_n = 6)$ and the packing fraction ϕ close (0 m $< r <$ 10 m) and far away (12 m $< r <$ 25 m) from the bottleneck. All three measures show a sharp increase in the first 70 s with clearly visible peaks and then a decrease for longer times until they reach a stationary state at around $t > 1000$ s. At the peak, about 45% of the agents are in the ordered class far away from the bottleneck and about 35% close to the bottleneck. Interestingly, the values intersect for longer times, and in the stationary state, the fraction of highly hexagonally ordered agents is only 20% far from the bottleneck and 25% close to it. In the dense shaken granular system [195] the fraction of ordered particles is around 75% for mostly monodisperse particles and about 65% with increased polydispersity in particle size. The fraction $P(N_n = 6)$ behaves in a similar manner. It increases sharply and peaks around 85% far from the bottleneck and 75% close to it. The same intersection between the respective values is observed but later at around 500 s instead of 200 s. The hexagonal coordination number is high, with around 70% of agents having six neighbors. In contrast, the ordered fraction of agents is much lower. The decrease from the peak is much more substantial, being more than 50% from the peak for agents far away from the bottleneck and about 30% close to it, while only about 14% for the agent's hexagonal coordination number. The mean packing fraction $\langle\phi\rangle$ of the system shows an analogous behavior, increasing sharply in the first 70 s-100 s with a less pronounced peak and then decreasing to a value of $\langle\phi\rangle \approx 0.7$. In this case, at long times, the packing fraction is higher for agents far from the bottleneck.

The discussed measures with respect to the distance to the bottleneck r are depicted in Figure 6.2 D-F for the different times shown in Figure 6.1. The plots illustrate the system's evolution at different distances from the bottleneck. The fraction $P(\Psi_6 > 0.7)$ in panel D evolves in the early stages of the simulation from a system with a low hexagonal order far away from the bottleneck ($10\,\mathrm{s} < t < 20\,\mathrm{s}$, $r > 10\,\mathrm{m}$) quickly to an increasingly high hexagonal structure ($60\ \mathrm{s} < t < 70\ \mathrm{s}$). Close to the bottleneck $r < 4$, the fraction is static in the depicted time intervals. The fraction $P(\Psi_6 > 0.7)$ increases with distance from the bottleneck for longer times ($1000\ \mathrm{s} < t < 5000\ \mathrm{s}$) until $r \approx 4$ m where its maximum is and decreases from then on. The fraction of agents with a hexagonal coordination number $P(N_n = 6)$ in panel E increases at all times presented with distance to the bottleneck for $r < 7\,\mathrm{m}$. In contrast to the bond orientation in panel D, the fraction of agents with a hexagonal coordination number is similar at $10\ \mathrm{s} < t < 20\ \mathrm{s}$ as in the stationary state $1000\ \mathrm{s} < t < 5000\ \mathrm{s}$. In the time interval $60\,\mathrm{s} < t < 70\,\mathrm{s}$, the coordination number behaves similarly to the bond orientation factor, as it increases with distance to the bottleneck and is especially high far from the bottleneck, where between $80 - 90\%$ of agents have a coordination number $N_n = 6$ for $r > 16$m. In the stationary state, the fraction $P(N_n = 6)$ exhibits a maximum similar to the bond orientation, with a steep increase for $r < 5$ m and a shallow descent from there on out. The packing fraction in panel F is interesting compared to the behavior of the order measures. In the beginning, $10\ \mathrm{s} < t < 20\ \mathrm{s}$, the packing fraction and the bond orientation are very similar. As one expects, the bond orientation is higher where the packing fraction is high. At a later time, however, this is not true. In the time interval $60\ \mathrm{s} < t < 70\ \mathrm{s}$, the packing fraction increases with r until it has a maximum at $r \approx 12.5$ m from where it decreases, while the bond orientation increases monotonously with r. In the stationary state $t > 1000$ s, the packing fraction increases with r monotonously for $r < 16$ m, while the bond orientation decreases for $r > 4$ m. The maximum of the bond orientation is at a point where the packing fraction is comparatively low and sloped downwards towards the exit. This is counter-intuitive, as a larger packing fraction is usually associated with a higher hexagonal order [186, 188]. Two differences between the agent model and the granular system are, firstly: in this study, a net flow through a bottleneck exists, while in the granular study, the system is in a non-equilibrium stationary state through constant energy injection and dissipation. Secondly: the granular system interacts through contact forces, while in the speed-based model agents interacts with other agents through the repulsive function $R(s)$ (2.17) and the speed function (2.14) at a distance larger than the agent radius. The panels

G-I in Figure 6.2 show the heat map of the r-t plot, where the distance r to the bottleneck is on the y-axis and the time t of the simulation on the x-axis. The color of the heat map represents the value of the measure shown in the same order as in the previously discussed panels ($P(\Psi_6 > 0.7)$, ($N_n = 6$), and ϕ). In these panels, the wave of high order and packing fraction propagates through the system. In panel G, it can be observed that the fraction $P(\Psi_6 > 0.7)$ is rather constant for $r < 2.5\,\mathrm{m}$ for all times in the simulation. Between $2.5\,\mathrm{m} < r < 10\,\mathrm{m}$, the band of higher hexagonal order is visible, where around 30% of agents have a bond orientation of $\Psi_6 > 0.7$. This band forms already after $t > 100$ s. At $r > 10$ m, the wave of high order takes longer to decay. At its peak, around 54% of agents have a bond orientation of $\Psi_6 > 0.7$, but after around $t = 300$s, this value drops to around 12%. The plot of the fraction of the coordination number $P(N_n = 6)$ (panel H) reveals that the system already has a high fraction of agents with $N_n = 6$ at the beginning of the simulation, which increases quickly in the first 50 seconds, similar to the bond orientation a wave where a high fraction of agents with $N_n = 6$ goes through the system that decreases at longer times. The packing fraction behaves analogously (see panel I) With a wave going through the system in the first 80 seconds and a decrease afterwards. The ruggedness of the order measures is visible in the heat map, especially in the bond orientation factor, compared to the rather smooth density. Close to the bottleneck $r < 2.5$ m, the coordination number and packing fraction are also stationary from the beginning of the simulation.

Shape factor distribution: The shape factor ζ contains further information about the different local structures of the Voronoi cells. In Figure 6.3 A, the distributions of the shape factor at different distance intervals $r + dr$ from the bottleneck are illustrated, and the packing fraction ϕ. The mean is taken over all runs of the simulation from $1000\,\mathrm{s} < t < 5000\,\mathrm{s}$ in $\Delta T = 50$ s intervals. The distribution converts from monomodal with its maximum around $\zeta = 1.17$ close to the bottleneck ($0\,\mathrm{m} < r < 2\,\mathrm{m}$) to bimodal further away from the bottleneck. The bimodal peaks are close to the values of the regular hexagon ($\zeta \approx 1.10$) and pentagon ($\zeta \approx 1.15$). The distribution shifts closer to a hexagonal order at $4\,\mathrm{m} < r < 6\,\mathrm{m}$ and moves slightly away, with the peak closer to the value of the hexagon decreasing and moving to larger values while the value close to the regular pentagon increases. This shift is illustrated in Figure 6.3 B. The heat map intensity shows the distribution of the shape factor on the x-axis with respect to the distance to the bottleneck on the

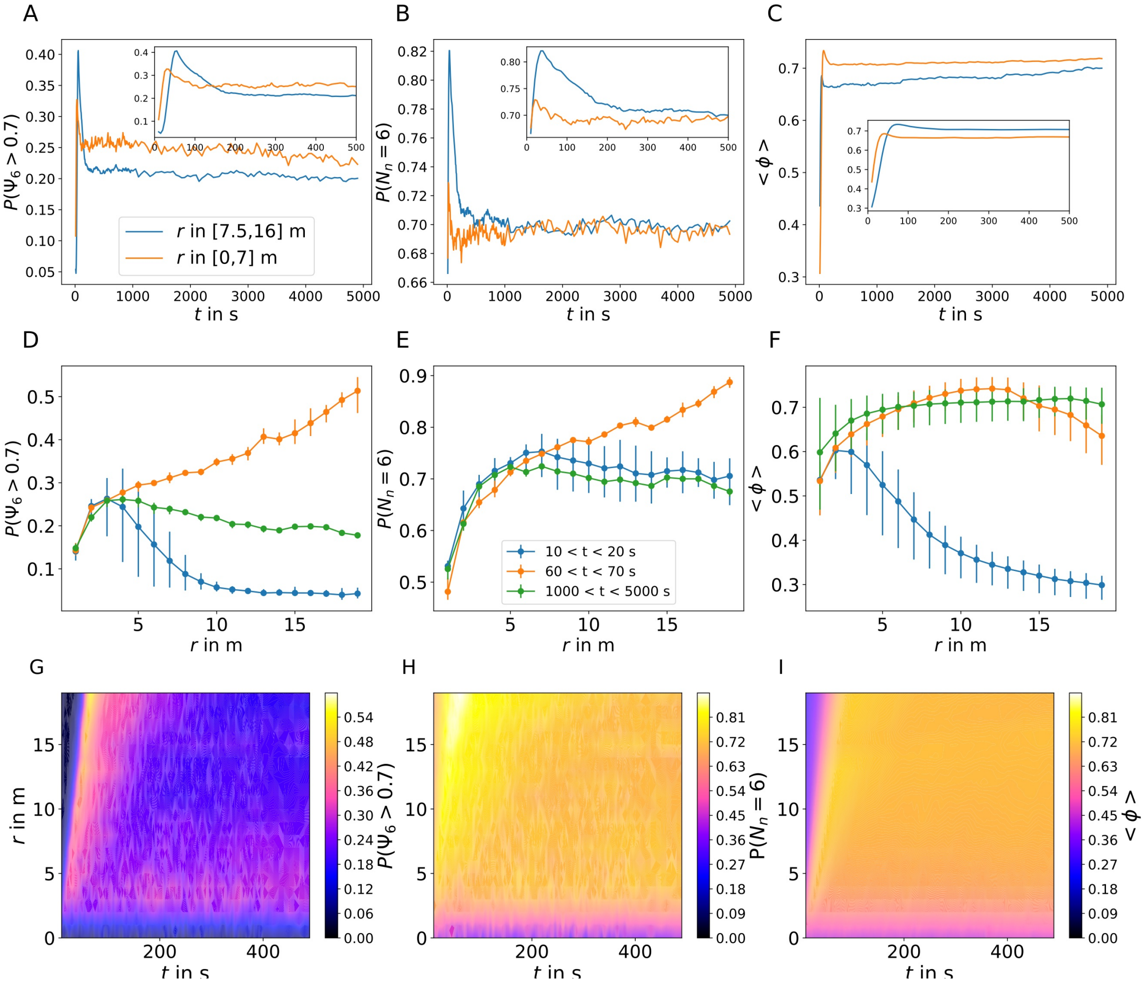

Figure 6.2: (**A**)-(**C**) Time series of the fraction of agents $P(\Psi_6 > 0.7)$, $P(N_n = 6)$ and the mean packing fraction $\langle\phi\rangle$ close to the bottleneck ($r < 7\,\mathrm{m}$) and far away ($7.5\,\mathrm{m} < r < 16\,\mathrm{m}$) for all 25 realisations of the system. The inset shows the time interval of $0\,\mathrm{s} < t < 500\,\mathrm{s}$.(**D**)-(**F**) Analogously the measures shown in A-C with respect to the distance r from the bottleneck at different times. The error bars show the 95% interval of the data. (**G**)-(**I**) Heat map of the r-t plot for the different measures in the same order as above for $t < 500\,\mathrm{s}$.

y-axis in $\Delta r = 1$ m intervals. The shift from monomodal to bimodal is continuous and occurs close to the bottleneck between $r = 0$ m and $r = 2.5$ m. The shift of the peak close to the hexagonal value towards the value of the pentagon starts at around $r \approx 3$ m and saturates near $r \approx 15$ m. The shape factor of the system shifts closer to hexagonal order with increasing distance from the bottleneck and then shifts away at larger distances. The packing fraction increases with distance to the bottleneck, as is evident from the values in the legend of Figure 6.3 A. This shows that the hexagonal order of the system is not a monotonous function of the mean packing fraction ϕ of the system. The packing fraction is chosen as a measure analogous to Reis et al. [188]. In their work, a granular fluid exited by vibration is in a non-equilibrium stationary state. They measure, among other quantities, the shape factor distribution of the system at different packing fractions. The granular system undergoes a similar transition from monomodal over bimodal, with the two peaks at a similar position (distributions of the granular fluid at different packing fractions are shown in Figure 6.3 C). The difference is that for denser configurations, the system transitions to a monomodal distribution, with the peak shifting closer to the shape factor of the regular hexagon as the packing fraction increases, even at a lower packing fraction than observed in the agent system ($\phi \approx 0.7$). To compare the granular fluid to the agent simulation, the agent system is divided into two sections close and far from the bottleneck as above. In this case close to the bottleneck is $(2.5\,\mathrm{m} < r < 7)$ m. The cut-off is at 2.5 m since this is approximately the distance where the distribution becomes bimodal. Far from the bottleneck is the system from $(7.5\,\mathrm{m} < r < 16)$ m. The distributions are depicted in Figure 6.3 C together with examples from the granular fluid at different packing fractions ϕ. The granular system with a packing fraction $\phi = 0.65$ shows a close resemblance to the agent system, both close and far away from the bottleneck.

Shape classes: Analogous to Reis et al. and Moucka and Nezbeda [186, 188] the shapes of the Voronoi cells in the system are categorized into three classes according to their shape factor ζ. In their work the first class contains all particles with a shape factor $\zeta_{min} < 1.159$, the second class contains all particles with shape factor $\zeta_{min} < \zeta < \zeta_u$ with $\zeta_u = 1.25$ and the third class contains all remaining particles with $\zeta_u < \zeta$. The classes are labeled A, B, and C, respectively. The classes are chosen so that at $\phi = 0.65$ in the granular system, where the two peaks of $P(\zeta)$ are closest in height, the classes A and B have equal proportions. This is also true for

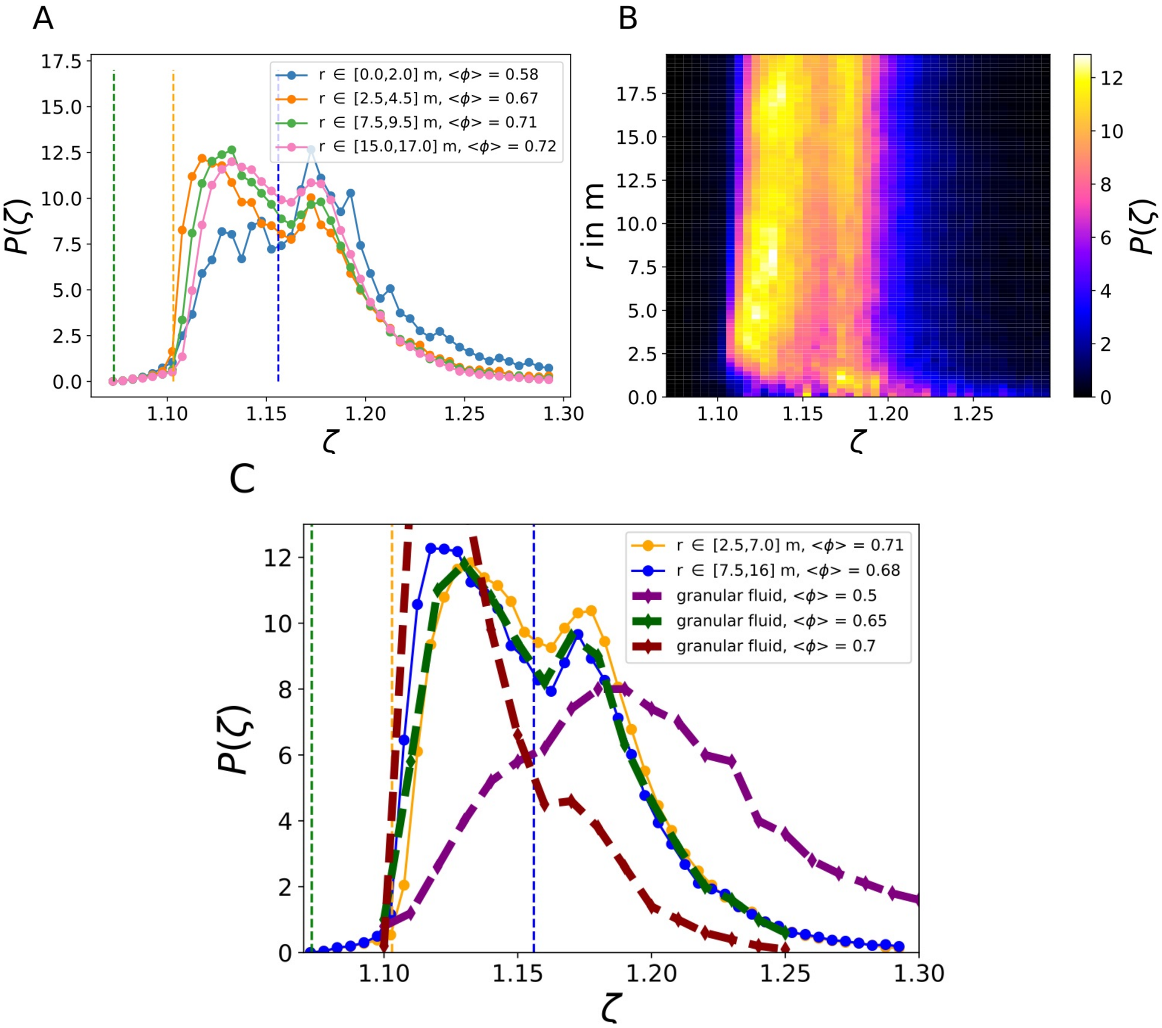

Figure 6.3: (**A**) Distribution of the shape factor ζ for $t > 1000$ s in $\Delta T = 50$ s time steps at different distance intervals from the bottleneck. The vertical dashed lines mark the values for the shape factor of the regular heptagon (green), hexagon (yellow), and pentagon (blue). (**B**) Heat map of the shape factor distribution at different distances r from the exit in $\Delta r = 1$ m intervals. **(C)** Comparison of the shape factor distribution of the agent simulation close ($2.5\text{ m} < r < 7\text{ m}$) and far ($7.5\text{ m} < r < 16\text{ m}$) from the bottleneck for $t > 1000$ s with the shape factor of a granular fluid at different mean packing fractions $\langle\phi\rangle$. The results for the granular fluid are taken from [188].

the agent system far from the bottleneck, where class A and B have a proportion of $P_A \approx 0.488$ and $P_B \approx 0.482$, while close to the bottleneck the proportions differ with $P_A \approx 0.532$ and $P_B \approx 0.403$. In the following, a different classification is introduced that highlights the hexagonal and pentagonal shapes of the system. For this, class A is set to be all shapes $\zeta_{min} < 1.125$, which is midway between the shape factor of the hexagon and the pentagon. as the upper boundary for class B $\zeta_u = 1.67$, so that class B and C have the roughly same proportion in the stationary state ($t > 1000$ s) far from the bottleneck ($r > 7.5$ m). The shape classes in the simulation at two different times are shown in Figure 6.4 D-F. The plot shows that class A colored in purple closely resembles the agents with $\Psi_6 > 0.7$ in panels A-C of Figure 6.4. Additional to highlight the agents with a high degree of hexagonal order, the other two classes give further information about the system. At the beginning of the simulation, most agents are in class C, marked in red in panels E-F. Quickly after 60 s, class A has large clusters analogous to the high hexagonal order shown in panel B, and class C portion lowered significantly. In the stationary state ($t = 4000$ s) class C appears to be more abundant compared to $t = 60$ s. Class B, colored in green, increases from 15 s on. It already makes out a high fraction after 60 s, which increases slightly in the stationary state. The mixing of the classes is quite heterogeneous. Especially class A builds distinguishable small clusters in the stationary state. The other two classes build a network of a large connected cluster throughout the system that is also distinguished from each other. The video *shape_class_det_2_5_0_1_1fpsCSM.mp4* [226] shows the evolution of the system depicted in Figure 6.4 D-F in more detail. For example the fraction of each class fluctuates substantially during the simulation and it illustrates how the hexagonal clusters near the bottleneck quickly form and break apart again. To illustrate the shape classes and which features they represent, examples of observed shapes with their color-coded class and the coordination number are shown in Figure 6.5. Panel A shows the agents in class A. The agent shapes and structure are close to that of a regular hexagon. In comparison, in panel B, the shape and form of the cluster is more comparable to an oblate hexagon, and the agents belong to class B. This class also contains more irregular-shaped regions, with mostly hexagonal coordination numbers, shown in panel C. Class C has irregular-shaped regions with a higher density of defects, shown in panel D. Another feature that can be observed are grain boundaries, depicted in panel E. In the center of the image, a line of class B and C agents are adjacent. The boundary shapes are close to that of a pentagon, even though their coordination number is mostly still $N_n = 6$, except for one defect in the boundary. The boundary separates two regions: a highly hexagonal cluster in the bottom left of class A and an oblate hexagonal cluster in the top right of class B. Another ordered feature that can be observed in the system is presented in panel F. Class C also contains clusters of agents whose spatial order is close to that of a square lattice. Surprisingly the coordination number in this cluster is still close to $N_n = 6$. One can see that the Voronoi cells contain small additional edges through small perturbations, increasing the coordination number. It is known that Voronoi cells are sensitive to perturbations in the case of the square lattice [233], but it is still surprising that there are no defects in this cluster. The reason is that these clusters evolve from hexagonal-shaped agent clusters. The shape classes and snapshots of Figure 6.5 illustrate the heterogenic nature of the system in regards to the spatial structure with a range of distinct features. To analyze the dynamics of the structure in regards to the shape classes the time series of the class fractions $p_s = N_s/(N_A + N_B + N_C)$ with $s \in \{\mathrm{A}, \mathrm{B}, \mathrm{C}\}$ is depicted in Figure 6.6 A&B. The described patterns discussed in the single realization in Figure 6.4 D-F become clear when looking at the time evolution of the classes.

Time evolution of the shape classes: Panel A of Figure 6.6 shows the time series of the shape classes close to the bottleneck ($r < 7\,\mathrm{m}$), while panel B depicts far from the bottleneck $7\,\mathrm{m} < r < 13\,\mathrm{m}$. The colored lines show the mean taken over all system realizations ($N_s = 25$) for the respective shape class according to the legend. The grey lines show the time series of each realization of the system. The insets depict the mean of all realizations from $0\,\mathrm{s} \leq t \leq 500\,\mathrm{s}$. For clarity, the time series of the individual realizations are omitted in the inlet. The evolution of the time series shows quantitatively what is qualitatively visible in the panels of Figure 6.4 D-F. The inlet of panel A (close to the bottleneck) shows the early evolution of the system ($t < 100\,\mathrm{s}$), where the systems starts out with most agents in shape class C ($p_C > 0.75$) and the subsequent decrease to a minimum around $t \approx 30\,\mathrm{s}$ where the fractions of agents with shape C is around $p_C \approx 0.35$. From there it increases until it is stationary at $p_C \approx 0.4$.

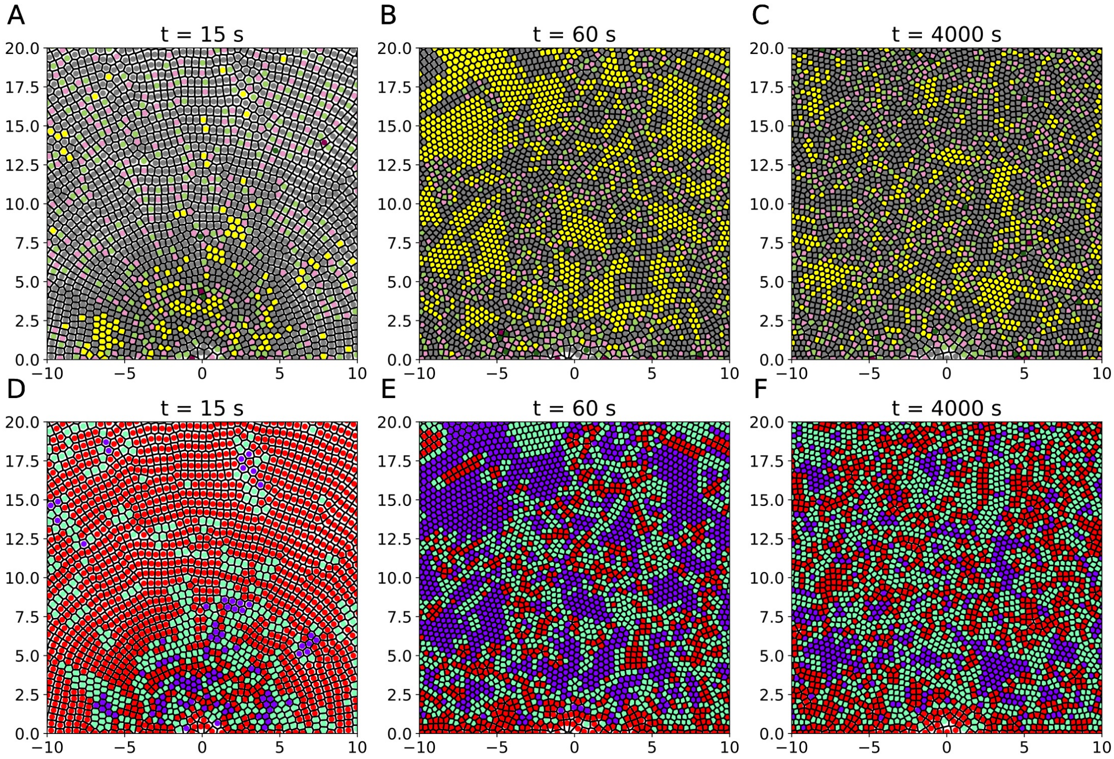

Figure 6.4: Snapshots of the simulation at $t = 15$ s, $t = 60$ s and $t = 4000$ s. Panels (**A**)-(**C**) depict agents with a bond orientation factor $\Psi_6 > 0.7$ in yellow and $\Psi_6 \leq 0.7$ in grey for the respective times. Defects are colored analogous to Figure 6.1. Panels (**D**)-(**F**) depict the shape classes A (purple, $\zeta \leq \zeta_{min} = 1.125$), B (green,$\zeta_{min} < \zeta < \zeta_u = 1.167$) and C (red, $\zeta_u \leq \zeta$).

The evolution of class A is almost a mirror image to shape C. In the beginning the fraction p_A increases sharply until it reaches a maximum at the same time ($t \approx 30$ s, $p_A \approx 0.33$) where p_C reaches the minimum. From there on it decreases until it reaches the stationary state at $t > 150$ s. Class B exhibits a more monotonous behavior. Its fraction p_B increases rapidly in the beginning and stabilizes quickly around $p_B \approx 0.4$ after $t \approx 35$ s. For longer times the fraction slightly decreases until around $p_B \approx 0.38$. Far from the bottleneck (7 m $< r <$ 13 m) shown in panel B of Figure 6.6 the evolution is similar but has some noticeable differences. Because the region is further away from the bottleneck, the maximum of class A and the minimum of class C appear later in time.

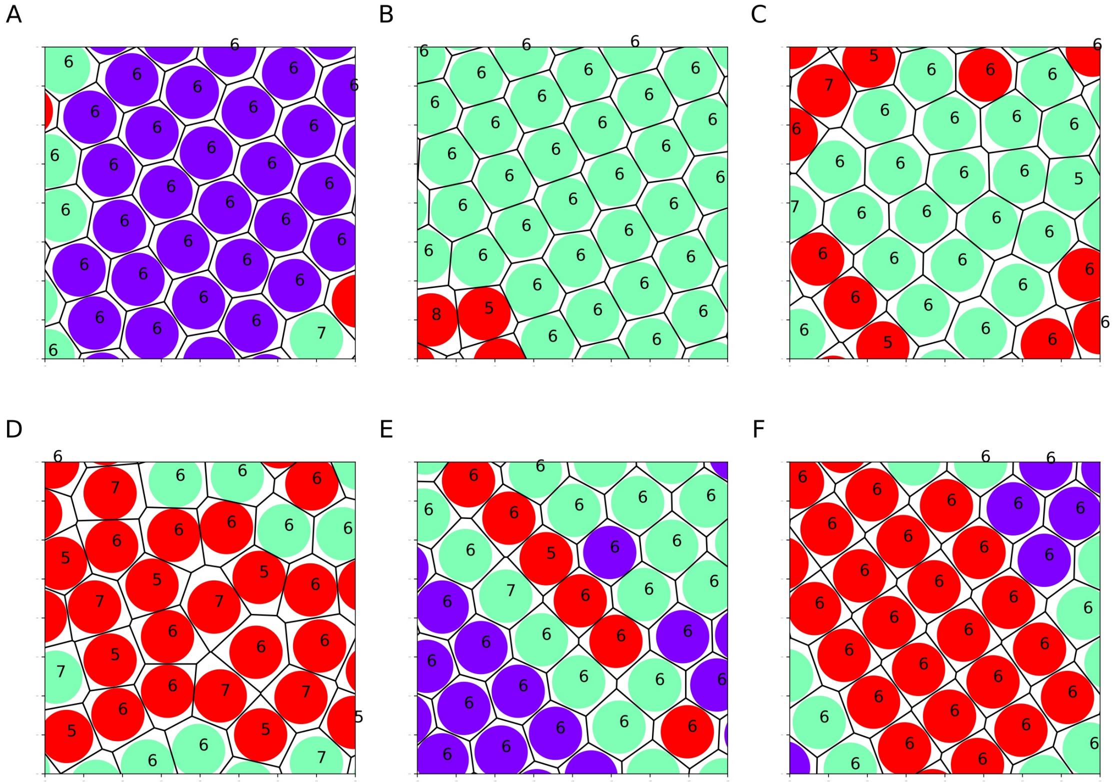

Figure 6.5: Examples of different shapes at different times and regions of the system. The color represents the shape class analogous to Figure 6.4 D-F. The numbers represent the coordination number N_n of the agents.

Both are more pronounced, with the minimum of class C being below 25 % and the maximum of shape A reaching over 30%. The decrease of class C to the minimum is non-monotonous and has a local maximum after around 10 s. At around the same time class A and B have a local minimum and increase from there on out. In the long term ($t > 1000$ s), near the bottleneck, Class C has a slightly higher proportion than class B, which is the other way around far from the bottleneck. The time series of the individual runs show that the proportions fluctuate substantially. This can also be observed in the video mentioned above, where large clusters of each class dynamically appear and break apart. Panels C-E in Figure 6.6 show the fraction of the shape classes in respect to the distance r to the bottleneck at different times analogous to Figure 6.2 D - F. The proportion of class A is similar to the fraction $P(\Psi_6 > 0.7)$ in Figure 6.2 D, with a wave-like increase in the beginning (panel C, between 10 s $< t <$ 20 s)), then the phase with a monotonous increase in proportion (panel D, between 60 s $< t <$ 70 s) and an increase to a maximum at around ≈ 3 m and $p_A \approx 0.24$ followed by a decrease to about $p_A \approx 0.12$ at further distances ($r \approx 17.5\, m$). Class B fraction, in the beginning, evolves similarly, increasing as a wave from the exit, with a scale factor of about 1.9 compared to class A (panel F, $10\,\text{s} < t < 20\,\text{s}$). At $60\,\text{s} < t < 70\,\text{s}$ in panel D, p_B increases with distance to the exit unit $r = 10$ m where it is maximal and decreases from there on. In the stationary state (panel E, $1000\,\text{s} < t < 5000\,\text{s}$) p_B increases monotonously with distance from, with a slight bump far way from the bottleneck $r > 15$ m. Class C interestingly

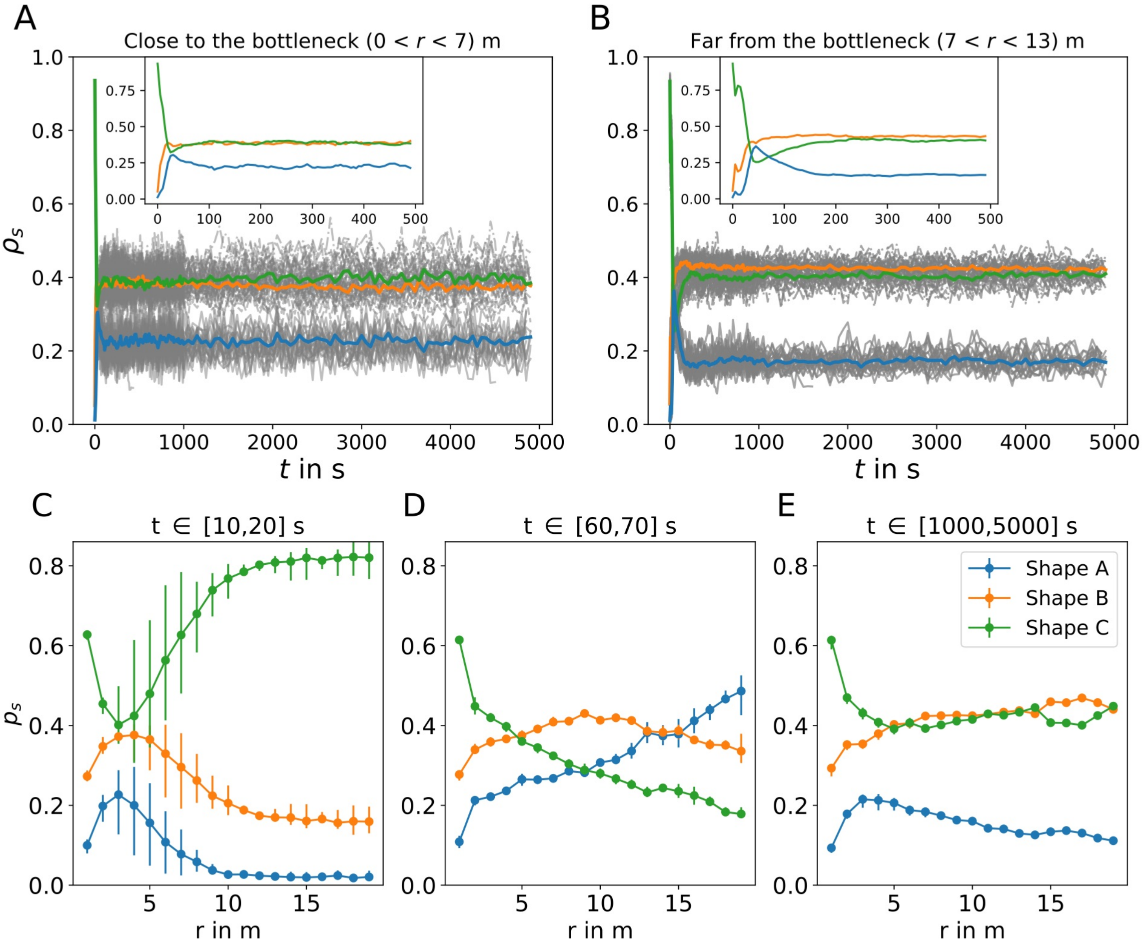

Figure 6.6: (**A**)&(**B**) Time series of the proportion p_s of the different shape classes close to the bottleneck (**A**, $0\,\text{m} < r < 7\,\text{m}$) and far from the bottleneck (**B**, $7\,\text{m} < r < 13\,\text{m}$, see Figure 6.4 D-E for details on the shape class definition). The colored lines show the mean over all 25 realizations of the system. The grey lines show the time series of the individual realizations of the system. (**C**)-(**E**) Proportion p_s of the shape classes with respect to the distance r from the bottleneck for different time intervals specified in the title of the panels. The error bars show the 95 % interval of the data.

evolves almost as the opposite of class A. It starts with a high fraction of $p_C \approx 0.8$ and decreases in a wave-like fashion from the exit out away from the bottleneck. At $60\,\text{s} < t < 70\,\text{s}$ the fraction of class A and C are a mirror image of each other with the mirror axis approximately at $y = 0.28$. In panel D. In the stationary state shape C has the highest fraction close to the bottleneck $r < 5$ m, with $p_C \approx 0.6$ directly in front of the bottleneck ($r < 2$ m). It decreases steeply with distance to the bottleneck and has a minimum at $r \approx 5\,\text{m}$ with $p_C \approx 0.39$, close to the maximum of p_A at $r \approx 3$ m. The fraction p_C increases from there on, similarly to the fraction p_B, with a bump in the opposite direction at $r > 15$ m compared to class B.

Comparison of the measures in the non stationary stage of the simulation: The dynamics and maxima in the hexagonal order at early times of the simulation ($t < 100\,\text{s}$) can be better understood when considering the speed and density profile of the system. In the video *shapeSpeedPackingFractionCSM.mp4* [226] and Figure 6.7 the dynamics are illustrated. In row A of Figure 6.7 the shape classes are illustrated analogous to Figure 6.4 for four different times shown in the title of the panels. The red half circles mark the distance from the bottleneck r in 2 m intervals beginning at $r = 1$ m. The panels help illustrate at what times and distances the large purple clusters of shape class A appear. Row B shows the velocity profile with four different colors. Blue agents are faster, while red agents are slower. Row C shows the mean packing fraction $\langle \phi \rangle$, the fraction p_A of class A, and the speed v_{nn} of the agents with respect to the distance from the bottleneck averaged over all 25 simulations. The plots in row C visualize the shock of high density and low speed traveling from the area close to the bottleneck. The area of high hexagonal order travels closely with the maximum density and the minimum speed in roughly the first 70 s. In the time between $70\,\text{s} < t < 350\,\text{s}$ (see video) the fraction of shape A p_A decreases further from the bottleneck $r > 5$ m, while it stays constant near the bottleneck. In the same time interval, the density and speed are rather stable concerning r. For $t > 350$ s, p_A reaches the final state, shown in the last right-most panel of Figure 6.7. Considering the model, density and speed are expected to influence the model's structure. The direction of the agent is determined by the floor field and the repulsion function $R(s)$ (2.17, see Section 2.3). Since the exponential repulsion is not dependent on the movement direction (i.e. field of view of the agent), it tends to order the particles hexagonally (equal distance to all neighbors). A certain density is needed for the interaction to be substantial in

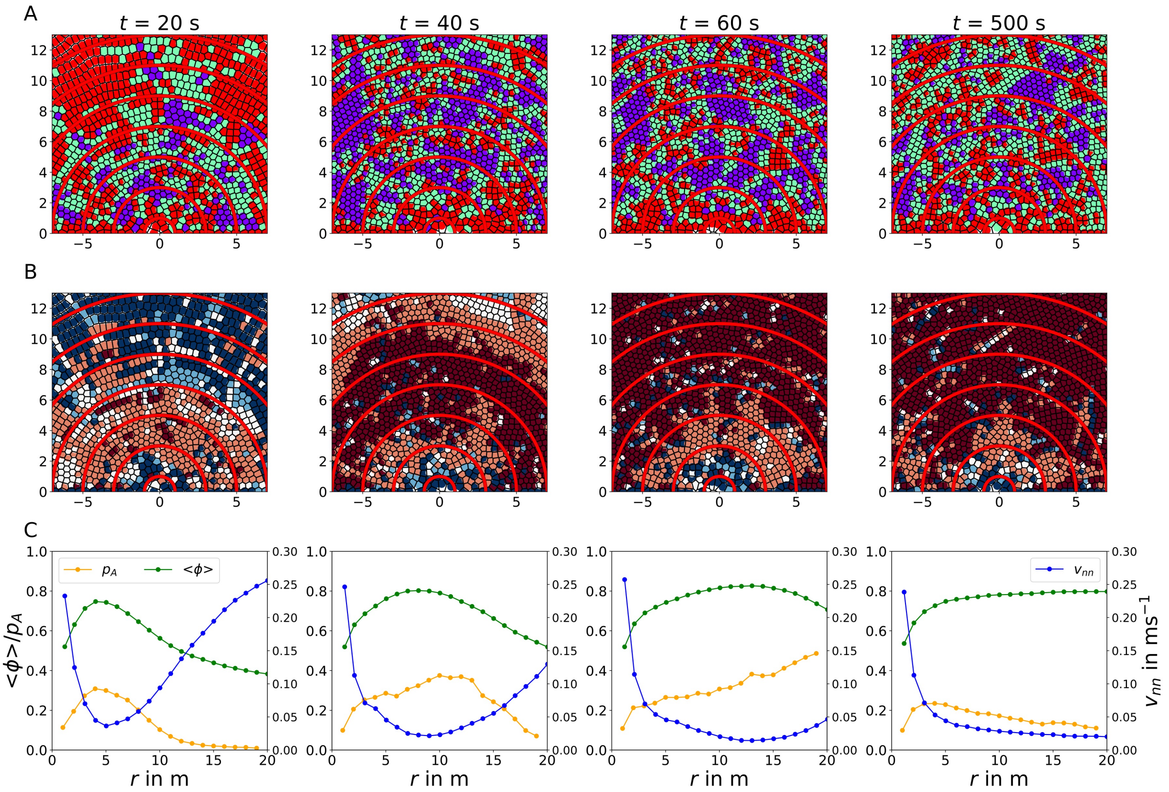

Figure 6.7: (**Row A**) Voronoi scatter plot illustration of the shape classes at different times analogous to Figure 6.4 D-F. (**Row B**) Voronoi scatter plot of the simulation. The colors represent the speed of the agents. Blue represents faster agents (darker color is faster), while red represents slower agents (darker color is slower). (**Row C**) On the double axis, the packing fraction ϕ and the fraction of agents in shape class A, p_A, in respect to the distance to bottleneck r is represented on the left axis. The speed of the agents v_{nn}, in respect to r is represented on the right axis.

the movement direction. The change in speed over the space is also an important factor for the structuring. For instance, the speed towards the bottleneck decreases substantially close to the bottleneck with distance. A large difference in the speed of neighboring agents destroys any order, as hexagonal clusters are pulled apart. Therefore a positive slope of the speed function $v(r)$ towards the bottleneck should have a decreasing effect on the order, which is observed as the speed and density waves traverse through the system. Even as the system's density increases, the fraction p_a decreases where the slope of $v(r)$ increases. Surprisingly the maximum of p_A at $r \approx 4\,\mathrm{m}$ in the stationary state is at a distance where the slope of $v(r)$ is already steeply increasing. The packing fraction at this stage is slightly decreasing and around $\phi \approx 0.65$. One reason for this could be that the system at higher density is quenched into a rather disordered state since the freedom of movement is too restricted for the agents to order themselves. As the packing fraction decreases, agents are more likely to order themselves hexagonally through the interactions. What is also noticeable in the dynamics is that the speed of the agent's increases in burst originating from the bottleneck throughout the system (see center panel *shapeSpeedPackingFraction.mp4*). This causes constant shifting of agent groups which influences the system's structure. In the following chapters, the focus lies on the influence of a subset of the model parameters. Since the parameter space is extremely large with 11 parameters that are considered in Table 6.1 a selection of parameters is considered. Especially the parameters that affect the direction vector $\mathbf{e}_i$ of the agents are of interest in influencing the structure. These are the repulsion strength a and repulsion length d in the exponential repulsion function $R(s)$ (2.17) and the noise added to the direction vector (2.19). The next chapters explore these parameters' influence on the system's structure, starting with the repulsion function $R(s)$.

6.1 Influence of exponential repulsion $R(s)$

The exponential repulsion function $R(s)$ directly influences the movement direction of the agents (2.17). Since the repulsion depends only on the distance s between the agents $s = r - l$, it is expected that a stronger repulsion function favors an equidistant ordering of the agents, leading to an increase in hexagonal order.

Directional interactions between agents can directly influence the density

Before the influence of the parameters a_j and d_j in the exponential repulsion $R(s)$ (2.17) on the structure in the CSM is analyzed, its effect on the density is discussed. At first glance, it seems counterintuitive that $R(s)$ influences the density directly since it only acts on the agent's direction but should not affect the distance the agent's arrest when encountering a stationary agent in their movement direction. A simple example is used to illustrate that the exponential repulsion can null the vector $\mathbf{e}_i$ and, therefore directly affect the system's density. To reiterate, the direction of

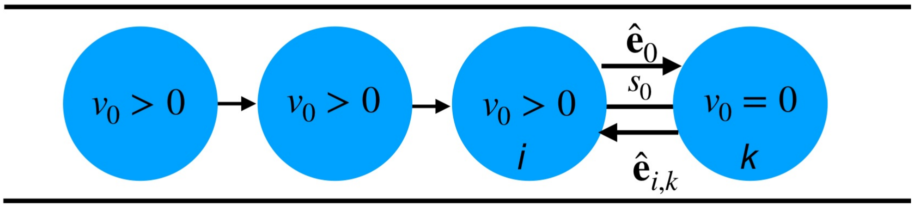

Figure 6.8: Illustration of the single file motion to the right in the CSM. The rightmost agent has the desired speed of $v_0 = 0$. All agents have the same parameter a and d.

the agent is determined by equation (2.17)

$$\hat{\mathbf{e}}_i(\mathbf{x}_i, \mathbf{x}_j, ...) = \frac{\hat{\mathbf{e}}_0 + \sum_{j \neq i} R(s_{i,j})\,\hat{\mathbf{e}}_{i,j}}{N},$$

with the function

$$R(s_{i,j}) = a_j e^{-(s_{i,j}-l)/d_j}. \tag{6.1}$$

Because of the collision avoidance in the CSM, the agents should stop before the distance $s_{i,j} < r_i + r_j$. In a simple scenario, it can be illustrated that the interaction $R(s_{i,j})\,\mathbf{e}_{i,j}$ affects the minimal distance under certain circumstances. The scenario is a system where agents move in single file motion through a corridor to the right, where the rightmost agent is stationary, with the desired velocity of $v_0 = 0$. All agents $j \in 1, ..., N$ exert the same exponential repulsion (6.1) with the parameter a and d, where the index j is dropped. Figure 6.8 illustrates this situation. The distance s_0 is the minimal distance of agent i left to the stationary agent k. Assuming only the speed function (2.14) acts on the agents' behavior, the minimal distance should be $\lim_{t\to\infty} s_0 = 0$ for $T > 0$ s. Considering the exponential interaction (2.17) and the speed function (2.13) in the one dimensional case, the velocity of the agents can also be $\mathbf{V}_i = 0$ if $\hat{\mathbf{e}}_i = \mathbf{0}$. In the case of only two agents i and k in the situation of Figure 6.8, this is true when

$$\hat{\mathbf{e}}_0 = -ae^{-s_0/d}\,\hat{\mathbf{e}}_{i,k}. \tag{6.2}$$

In the one dimensional case it is sufficient to only consider the x-component of the desired direction $\hat{\mathbf{e}}_0 = 1$ and the axis between i and k, $\hat{\mathbf{e}}_{i,k} = -1$. This reduces the equation (6.2) to

$$\max(\ln(a)d, 0) = s_0. \tag{6.3}$$

In this case $s_0 > 0$ if $a > 1$ and $d > 0$. For multiple agents in line, s_0 can be approximated by only considering the repulsion of nearest neighbors since the distance of the exponential repulsion is usually limited. In this case equation 6.3 is approximated by

$$\max(\ln(a/n)d, 0) \approx s_0, \tag{6.4}$$

with n the number of agents behind agent k. The approximation and simulation results are illustrated in Figure 6.9.

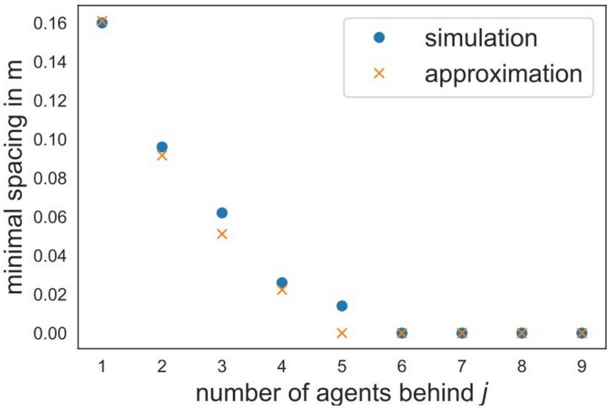

Figure 6.9: Comparison of the minimal spacing illustrated in Figure 6.8 for a simulation with $d = 0.1$ m and $a = 2.5$ (blue dots) and the approximation (6.4) (orange crosses).

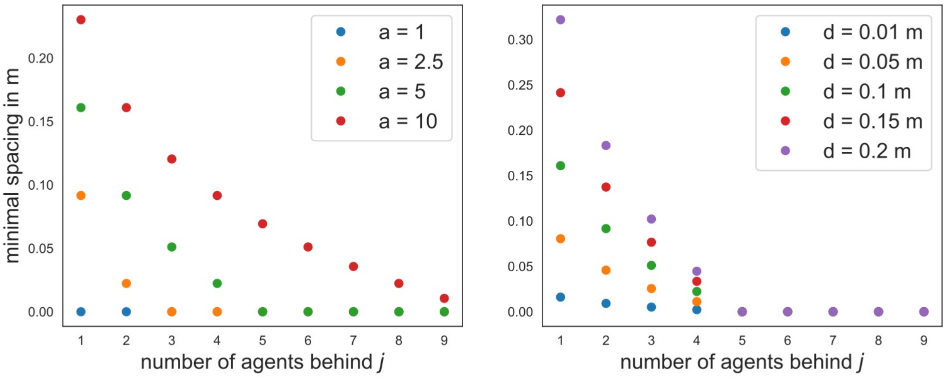

Figure 6.10: Illustration of the approximation (6.4) on the **left** with $d = 0.1\,\mathrm{m}$ for different values of a and on the **right** with $a = 5$ for different values of d.

6.1.1 Influence of the repulsion strength

With this effect in mind, the influence of the repulsion strength a and the repulsion length d on the large system with $N = 8000$ agents is analyzed. First, the influence of the repulsion strength a is presented by varying its value in one dimension. It scales the exponential repulsion as a proportional factor in equation (6.1). Figure 6.11 shows the simulation at $t = 1750\,\mathrm{s}$ for $a \in \{1.5, 2.5, 5, 7.5, 10, 15\}$. All other parameters are the same as in Table 6.1. The first thing to notice is that the parameter a significantly influences the shape of the agent cluster in front of the bottleneck. In the case of $a = 1.5$, the agents order themselves in a kind of urn shape, close to v-shaped. With a, the shape transforms into the semi-circle in front of the bottleneck. Both the v-shape and the semi-circle can be observed in empirical studies [1, 24], but it is questionable what shape would be observed on this kind of scale. The second thing to notice is the appearance of the crystalline ring near the boundary of the agent cluster for larger values of a, which extends further into the cluster as a increases. With this increase of order at the boundary, a decrease in the density is observed by looking at the size of the Voronoi cells. The boundary has a distinct interface between the area of high hexagonal order with few defects in between to the heterogeneous ordered area with smaller clusters of high hexagonal order and disordered areas in between. Since the slope factor T, which determines the rate of approach to another agent, is constant, this must be a result of the above-discussed effect of the agent-agent interaction on the movement direction vector $\hat{\mathbf{e}}_i$. Due to the stronger exponential interaction of the movement direction and the lower

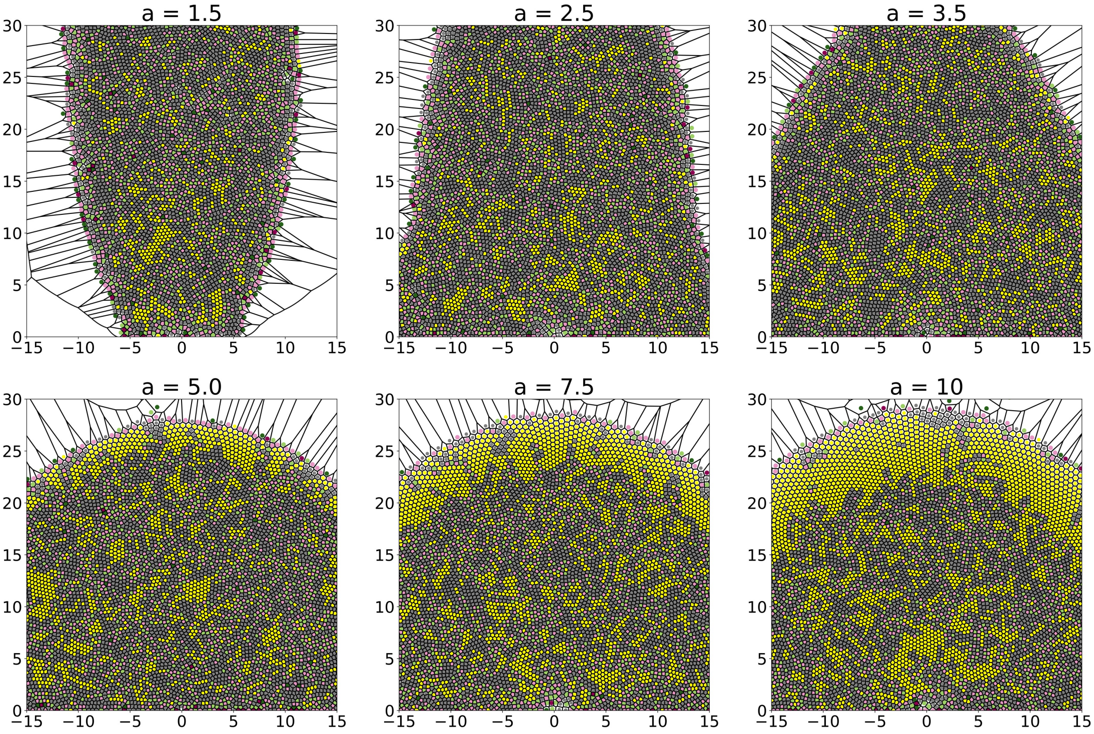

Figure 6.11: Voronoi-scatter plot of simulation runs with different repulsion strength a written on top of the panels at $t = 1750\,\mathrm{s}$. Yellow agents have bond orientation factor $\Psi_6 > 0.7$. Red and green agents have $N_n \neq 6$. See Figure 6.1 for the definition.

density, which allows the agent to move more freely in different directions, they can order themselves to build the "crystal ring", which nulls the direction vector. In the bulk of the system closer to the bottleneck ($4\,\mathrm{m} < r < 15\,\mathrm{m}$), an increase in the size of clusters with high order is observed, when increasing a.

Clogging: The system's probability of clogging depends strongly on the repulsion strength a. In Figure 6.12 A the fraction $P(T_c < 5000)$ of the $N_s = 20$ runs that clog at a time $T_c < 5000\,\mathrm{s}$ is presented in respect to a. For $a = 1$ all simulations clog before $t = 200\,\mathrm{s}$. As a increases the fraction $P(T_c < 5000)$ decreases with a minimum of $P(T_c < 5000) \approx 0.5$ for $a = 2.5$. Further increasing a increases the fraction $P(T_c < 5000)$ linearly until $a = 7.5$, where $P(T_c < 5000) \approx 0.9$. Still, there is enough data in the stationary state ($t > 1000\,\mathrm{s}$) for all tested a. The fraction $P(T_c > 1000)$ shown in panel B of Figure 6.12 shows, that this value is less sensitive for $a \geq 1.5$. The maximal time each simulation runs until the system clogs is shown in Appendix A.6 Figure S16.

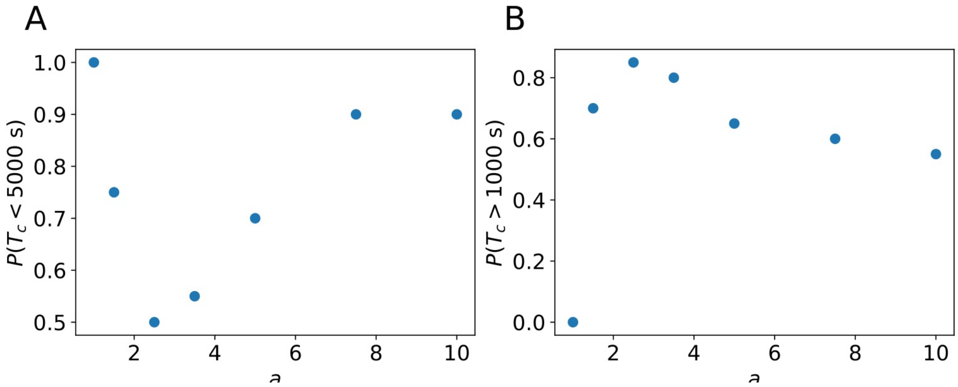

Figure 6.12: (**A**) Fraction of simulation runs $P(T_c < 5000\,\mathrm{s})$ that clogged before $t = 5000$ s of simulation time in respect to the repulsion strength a. (**B**) Shows analogously $P(T_c > 1000\,\mathrm{s})$.

Hexagonal order in respect to the distance from the bottleneck: The fraction of agents $P(\Psi_6 > 0.7)$ in respect to the distance to the bottleneck r is depicted in Figure 6.13 A. How the structure is affected by a differs depending on the distance to the bottleneck. Close to the bottleneck ($r < 4\,\mathrm{m}$) the effect is minor, with only a slight increase in the order for $a = 10$. The position of the maximum of $P(\Psi_6 > 0.7)$ is independent of a at $r \approx 4\,\mathrm{m}$. With increasing a, the downward slope of $P(\Psi_6 > 0.7)$ decreases with further distance r from the maximum. For $a \geq 3.5$, the ring of higher order forms near the boundary. The transition zone to the ring is in a small area. The maximum of $P(\Psi_6 > 0.7)$ and the width inside the ring increases with a. Panel B of Figure 6.13 shows the packing fraction ϕ in respect to r. The density increases with a for $r < 20\,\mathrm{m}$. The increase is steeper close to the bottleneck at $r < 5\,\mathrm{m}$. For $a \geq 3.5$, there is a point far from the bottleneck, near the boundary of the agent cluster, where the packing fraction starts to decrease. This decrease is significant for $a \geq 7.5$, where the high order ring also starts to manifest. This is illustrated in Figure 6.13 C-E, where ϕ and $P(\Psi_6 > 0.7)$ are in the same panel for $a \in \{5, 7.5, 10\}$. The sharp increase of hexagonal order near the boundary coincides with the decrease in density caused by the agent-agent interaction acting on the movement direction $\hat{\mathbf{e}}_i$ discussed above. Since any deviation from the equilibrium

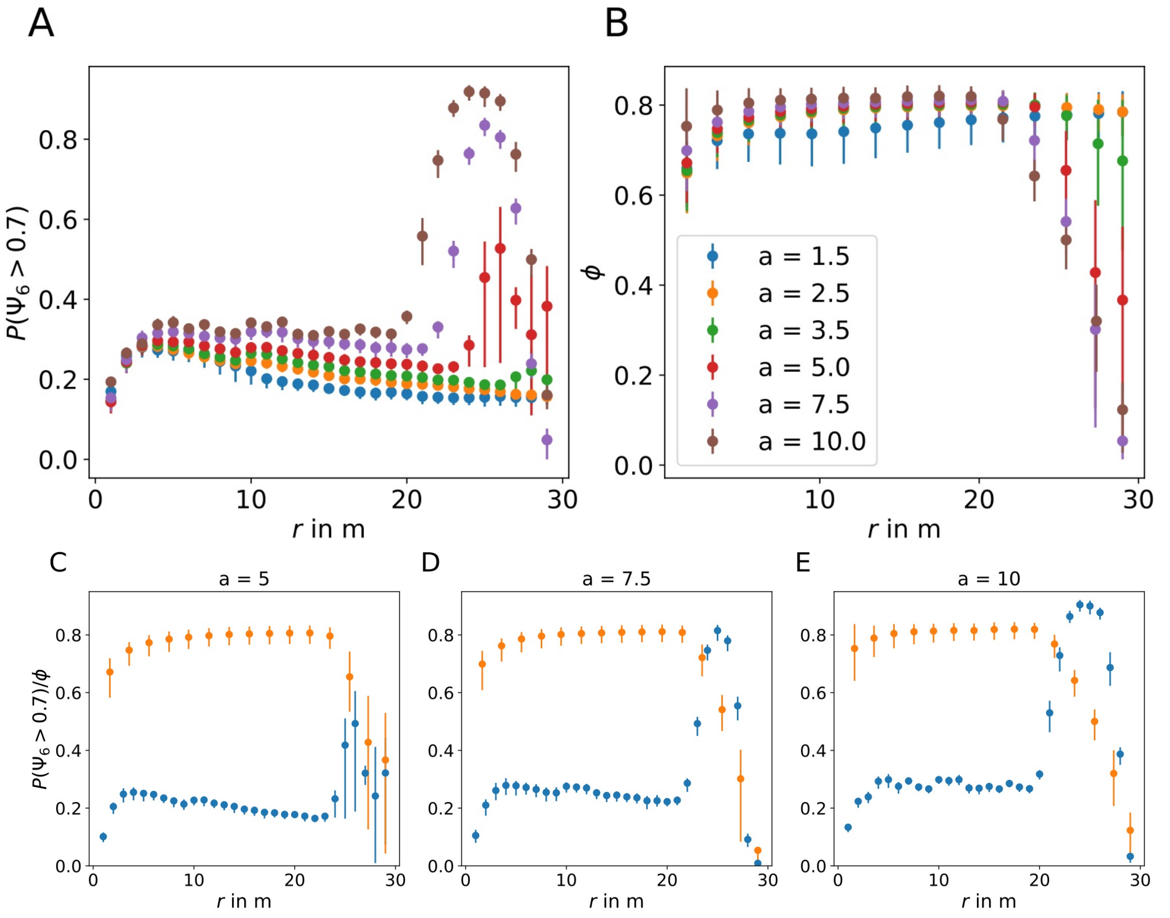

Figure 6.13: (**A**) Hexagonal order $P(\Psi_6 > 0.7)$ in respect to the distance from the bottleneck r for different values of the repulsion strength a. (**B**) Analogous to A for the packing fraction ϕ. (**C**)-(**E**) Direct comparison of the packing fraction ϕ and $P(\Psi_6 > 0.7)$ for $a \in \{5.0, 7.5, 10.0\}$.

position where $\hat{\mathbf{e}}_i = \mathbf{0}$ gives the agent more freedom in its movement, they can order themselves into the hexagonal structure before being quenched into a disordered state observed closer to the bottleneck. To analyze the increase in order with a, the packing fraction ϕ and hexagonal order $P(\Psi_6 > 0.7)$ are measured in squares of $4\,\mathrm{m}^2$ at different distances from the bottleneck, where the distance is the position of the lower side of the square. The results are shown in Figure 6.15 A. The squares are at $d_b \in \{0, 5, 7, 14, 21\}$ m from the bottleneck. Close to the bottleneck for the area with $d_b = 0$ m barely any increase in order with a is observed. Surprisingly $P(\Psi_6 > 0.7)$ decreases from $a = 1.5$ to $a = 2.5$ for $d_b = 5$ m and $d_b = 7$ m. For $d_b = 5$ m, $d_b = 7$ m and $d_b = 14$ m $P(\Psi_6 > 0.7)$ increases with a, with a decreasing slope towards larger a. The order at $d_b = 5$m is consistently higher than at $d_b = 7$m

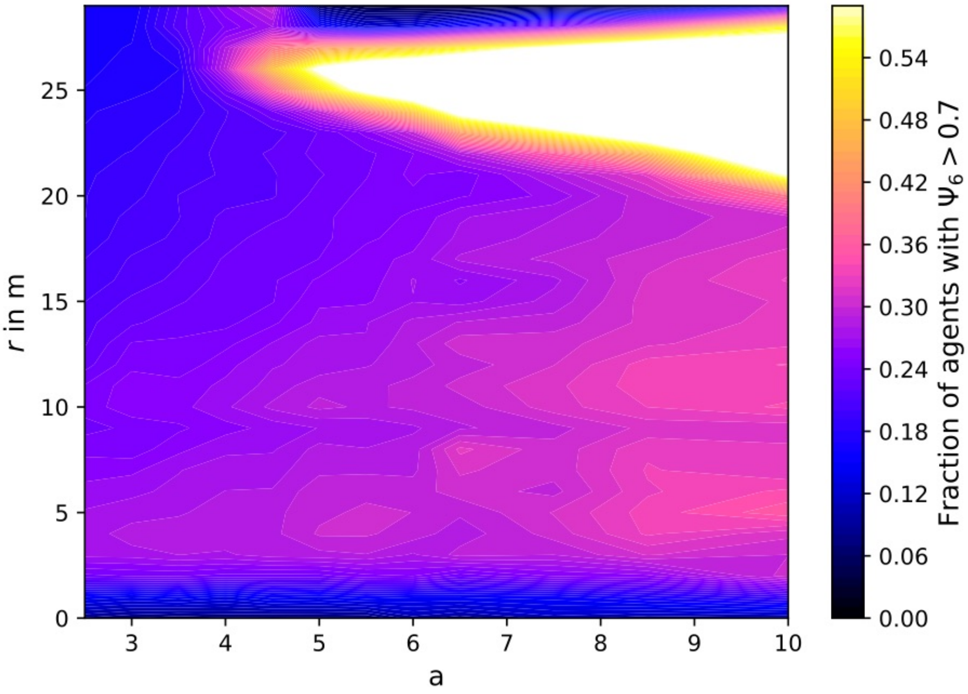

Figure 6.14: Smoothed heat map showing $P(\Psi_6 > 0.7)$ on the r-a plane.

and the order at $d_b = 5\,\mathrm{m}$ and $d_b = 7\,\mathrm{m}$ is higher than at $d_b = 14\,\mathrm{m}$. At $d_b = 21\,\mathrm{m}$ the increase in order is steeper compared to the other distances and for $a \geq 7.5$ the transition into the crystalline ring is observed. In Panel B of Figure 6.15 the packing fraction in the same measurement area in respect to a is depicted. For $a \leq 3.5$ and $d_b \leq 7\,\mathrm{m}$ the packing fraction decreases to a minimum and subsequently increases. Comparing the packing fraction ϕ to the order $P(\Psi_6 > 0.7)$ shows, that the highest packing fraction does not coincide with the highest order, which one might assume since the hexagonal packing has the largest packing fraction. Close to the bottleneck the packing fraction increases significantly for $a \geq 3.5$ but the order changes only slightly. Between $d_b = 5\mathrm{m}$ and $d_b = 14\mathrm{m}$ the packing fraction increases with distance for all a, while it is the other way around for the order. So while the packing fraction and order increases with a for $d_b < 21\,\mathrm{m}$ and $a > 2.5\,\mathrm{m}$, there is no clear relation, that a higher density coincides with high order in the system. It should be also noted that while the packing fraction is dependent on the repulsion strength the change is rather small compared to the change in the order $P(\Psi_6 > 0.7)$. When taking $a = 2.5$ as a baseline, the packing fraction increase to $a = 10$ is between 3 - 5 % between $d_b = 5\,\mathrm{m}$ to $d_b = 14\,\mathrm{m}$. The increase in hexagonal order in the same interval is about 33 - 56 %. Only close to the bottleneck the increase in density form $a = 2.5$ to $a = 10$ is larger with 14 % compared to a 10% change in hexagonally ordered agents. To illustrate the gradual change in hexagonal order of the system and the transition to the crystalline ring, Figure 6.14 shows a heat map of $P(\Psi_6 > 0.7)$ on the r-a plane. The y-axis shows the distance r of the bottleneck in respect to the repulsion strength a shown on the x-axis. For this plots simulations with $a \in \{2.5, 3.0, 3.5, 4.0, 4.5, 5.0, 5.5, 6.0, 6.5, 7.5, 8.5, 10\}$ are conducted with 20 runs per simulations and $t_{max} = 4000$ s, over all non-clogged states the fraction $P(\Psi_6 > 0.7)$ is measured every 90 s for $t > 1000$ s. Figure 6.14 illustrates the change of the hexagonal order over r. The crystalline ring starts to appear around $a \approx 4.5$, with a sharp interface between the hexagonally low ordered region for $a < 4.5$ and $a > 4.5$. With increasing a the region increases in size both closer and further away from the bottleneck, presenting as a cone-shape in the r-a plane. In the region of $2.5\,\mathrm{m} < r < 19\,\mathrm{m}$ in the presented part, the hexagonal order increases with a. As a increases the fraction $P(\Psi_6 > 0.7)$ increases at further distances r from the bottleneck. Very close to the bottleneck $r < 2.5\,\mathrm{m}$ the hexagonal order is not influenced by the strength of the repulsion, illustrating that in this region the dynamics are not determined by the interaction of the desired direction $\hat{\mathbf{e}}_i$ of the

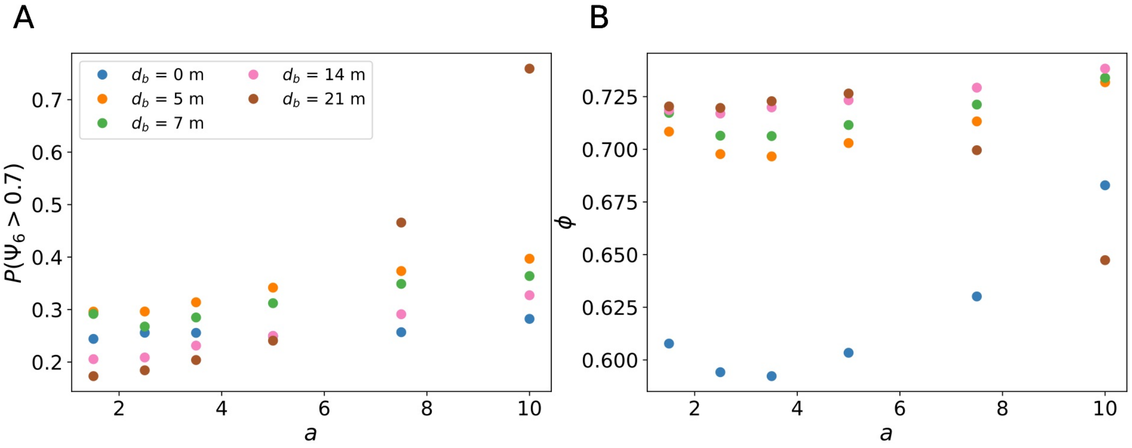

Figure 6.15: (**A**) Fraction of hexagonally ordered agents $P(\Psi_6 > 0.7)$ and (**B**) packing fraction ϕ in the measurement area ($-2\,\mathrm{m} < x < 2\,\mathrm{m}$ and $d_b < y < d_b + 4\,\mathrm{m}$) in respect to the repulsion strength a.

agents.

Shape Factor: Continuing to the shape factor ζ, the distribution $P(\zeta)$ is depicted in Figure 6.16 close to the bottleneck $0\,\mathrm{m} < r < 7\,\mathrm{m}$ (A) and far from the bottleneck $7\,\mathrm{m} < r < 14\,\mathrm{m}$ (B) with $|x| < 10\,\mathrm{m}$. The general shape of the distribution is not dependent on a close and far from the bottleneck. The distribution is bi-modal, with a higher peak close to the hexagonal shape and a smaller peak close to the pentagonal shape with an exponential tail. The increase of a increases the height of the first peak close to the hexagonal value, close and far from the bottleneck. The increase is lager far from the bottleneck, where it increases from $a = 2.5$ to $a = 10$ by about 23 %, compared to 11% close to the bottleneck. The height of the second peak is rather unaffected by a change in a and is roughly static both close and far from the bottleneck. The exponential tail of the distribution decreases more steeply with increasing a, especially far from the bottleneck. In Figure 6.17 the effect of a on the shape classes further illustrates how the repulsion strength affects the shapes of the system (see Figure 6.4 for the definition of the classes). The shape classes close to the bottleneck (panel A) and far away (panel B) show similar behavior. With increasing a, the proportion p_A of shape class A in the system increases. The proportion p_B of class B increases slightly close to the bottleneck and is roughly constant far away from the bottleneck for $a \geq 2.5$. The proportion p_C of class C decreases in both distant regimes. The increase of class A and decrease of class C is more pronounced far from the bottleneck, where class A increases by 54% from

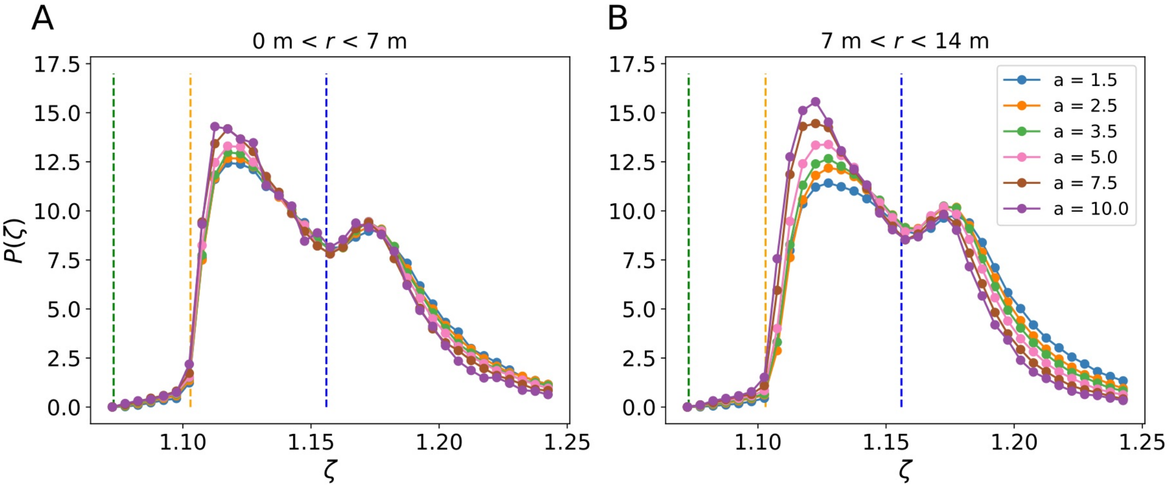

Figure 6.16: Shape factor distribution $P(\zeta)$ for different repulsion strengths a close to the bottleneck (**A**) and far from the bottleneck (**B**).

$a = 2.5$ to $a = 10$ and class C decreases by about 27 %. Compared to $r < 7$ m, where p_A increases by about 18 % and p_C decreases by about 14%. The proportion of class B increases just by 4 % close to the bottleneck and stays constant far away. Panels C&D in Figure 6.17 shows the shape classes in a simulation with $a = 2.5$ in C and $a = 10$ in D at $t = 1950$ s. The plot further illustrates the change in the shape classes. The clusters consisting of agents in shape class A are larger for $a = 10$ compared to $a = 2.5$ and the number of clusters in class C decreases. The shape factor distribution for $a = 10$ over the distance r is also discussed briefly in the Appendix A.6.

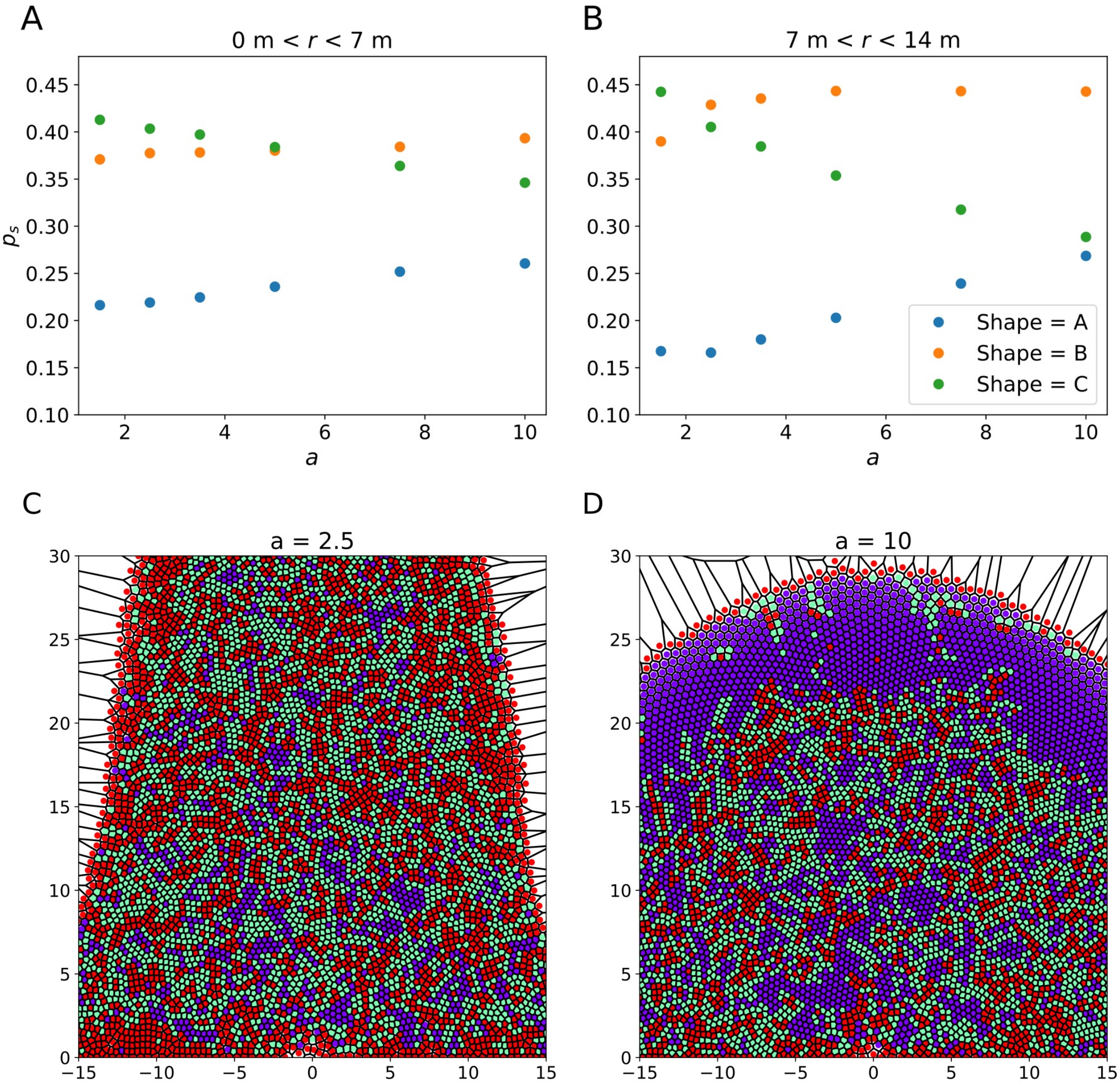

Figure 6.17: (**A**)&(**B**) Fraction p_s of the shape classes $s \in \{\mathrm{A}, \mathrm{B}, \mathrm{C}\}$ in respect to the repulsion strength a close to the bottleneck (**A**) and far from the bottleneck (**B**). (**C**&**D**) Example of the shape classes in a Voronoi-scatter plot at $t = 1950\,\mathrm{s}$ for $a = 2.5$ (**C**) and $a = 10$ (**D**), with violet (class A), green (class B) and red (class C).

6.1.2 Influence of the repulsion length

Continuing with the effect of the repulsion length d on the dynamics and spatial structure of the system, the value of d is varied orthogonally to the analysis of the previous section. The starting point is again the parameter set summarized in Table

6.1 and d is varied ($d \in \{0.05, 0.1, 0.15, 0.2, 0.25, 0.3, 0.5\}$ m). The repulsion length

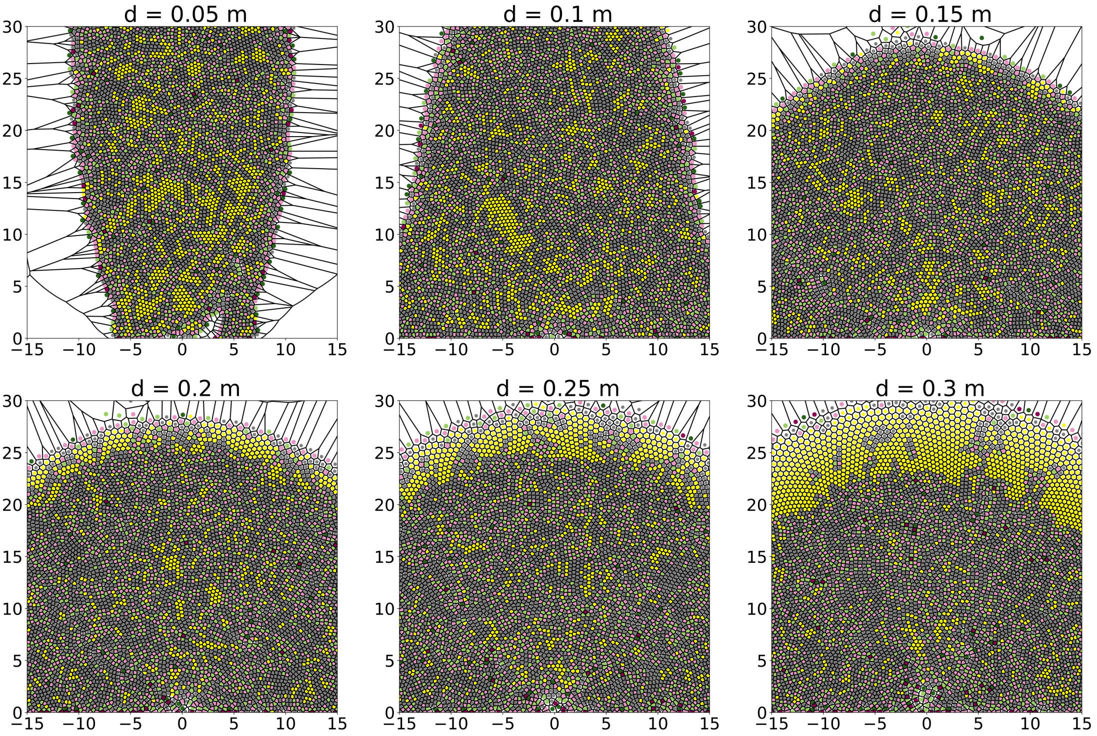

Figure 6.18: Scatter-Voronoi plot of simulation runs with different repulsion lengths d written in the panel title at $t = 3000$ s. Yellow agents have a bond orientation factor $\Psi_6 > 0.7$. Green and red agents represent coordination numbers $N_n \neq 6$ (see Figure 6.1).

rescales the effective distance of the exponential interaction, where $R(s) = 1/e$. Knowing the influence of the repulsion strength on the structure and hexagonal order of the system presented in the previous section, one might expect that the repulsion length has a similar influence of increased order in the bulk of the system with increasing d. Figure 6.18 contains snapshots of the system at $t = 3000$ s for different values of d specified in the panels' title. The change in structure and shape of the bulk of agents with increasing d is visible. Analogous to the increase in a, the shape of the bulk transforms from a parabola at $d = 0.05$ m to a half circle at $d > 0.1$ m. At $d > 0.15$ m, the crystal ring forms analogous to the repulsion strength $a > 4$. The hexagonal order in the bulk closer to the bottleneck $r < 16$ m shows surprising results. Compared to the increase in a, an increase in the repulsion length d seems to decrease the fraction of agents with a hexagonal order $P(\Psi_6 > 0.7)$ in the system. Additionally, the order of the system is more dependent on the distance r and angle Θ from the bottleneck. For $d \geq 0.15$ m, the system becomes partially jammed. There is a hopper-like accumulation of agents at each side from the bottleneck, where the agents are arrested in a stable configuration. In between the jammed agents, other agents can move to the exit. This is illustrated and the Appendix A.6 Figure S18. Inside the jammed region, the packing fraction is increased (see Appendix A.6 Figure S19). The different structures become clearer when looking at a slice of the system in an r interval and calculating the measures with respect to the angle Θ from the exit. Figure 6.19 A-C shows the fraction of agents $P(\Psi_6 > 0.7)$ in panel A, the packing fraction ϕ in B and the speed measured over 50 s intervals in C. The fraction $P(\Psi_6 > 0.7)$ and packing fraction ϕ are measured over all realizations of the system, while the speed is measured for one specific run at six different times $t > 1000$ s. In panel A the structure profile over the angle shows that for $d = 0.05$ m and $d = 0.2$ m, the fraction $P(\Psi_6 > 0.7)$ are larger closer to the center of the system, with the maximal fraction for $d = 0.05$ s. In the system with $d = 0.05$ m, the high fraction of hexagonally structured agents coincides with the high-density region presented in panel B. As shown in Figure 6.18 the bulk of agents is more compact on the x-axis in the elongated shape. In comparison, the system with $d = 0.2$ m has the highest fraction $P(\Psi_6 > 0.7)$, where the ϕ is lowest. The packing fraction, in this case, is constant in the center with respect to the angle Θ until $\theta \approx 0.5$ on the right side of the system and $\theta \approx -0.9$ on the left side. From there, the packing fraction increases, while the fraction of hexagonally ordered particles decreases to $P(\Psi_6 > 0.7) \approx 0.1$. For $d = 0.1$ m, the packing fraction is rather flat over the angle Θ. Compared to the other values, the fraction $P(\Psi_6 > 0.7)$ is also rather flat concerning the angle and only decreases close to the boundary, where the agents are close to the wall. Looking at the mean speed $\langle v \rangle_{50}$ measured in 50 s interval of a single simulation run at different times in panel C the jammed region is clearly visible. While the speed for $d = 0.1$ m is rather constant over the angle Θ, only decreasing near the boundary wall, the speed for $d = 0.2$ m is $\langle v \rangle_{50} = 0$ m/s for $|\Theta| > 1$. The speed for $d = 0.05$ m is constant in the high-density region of the system and increases in the boundary region. The fraction of clogged systems also increases with d.

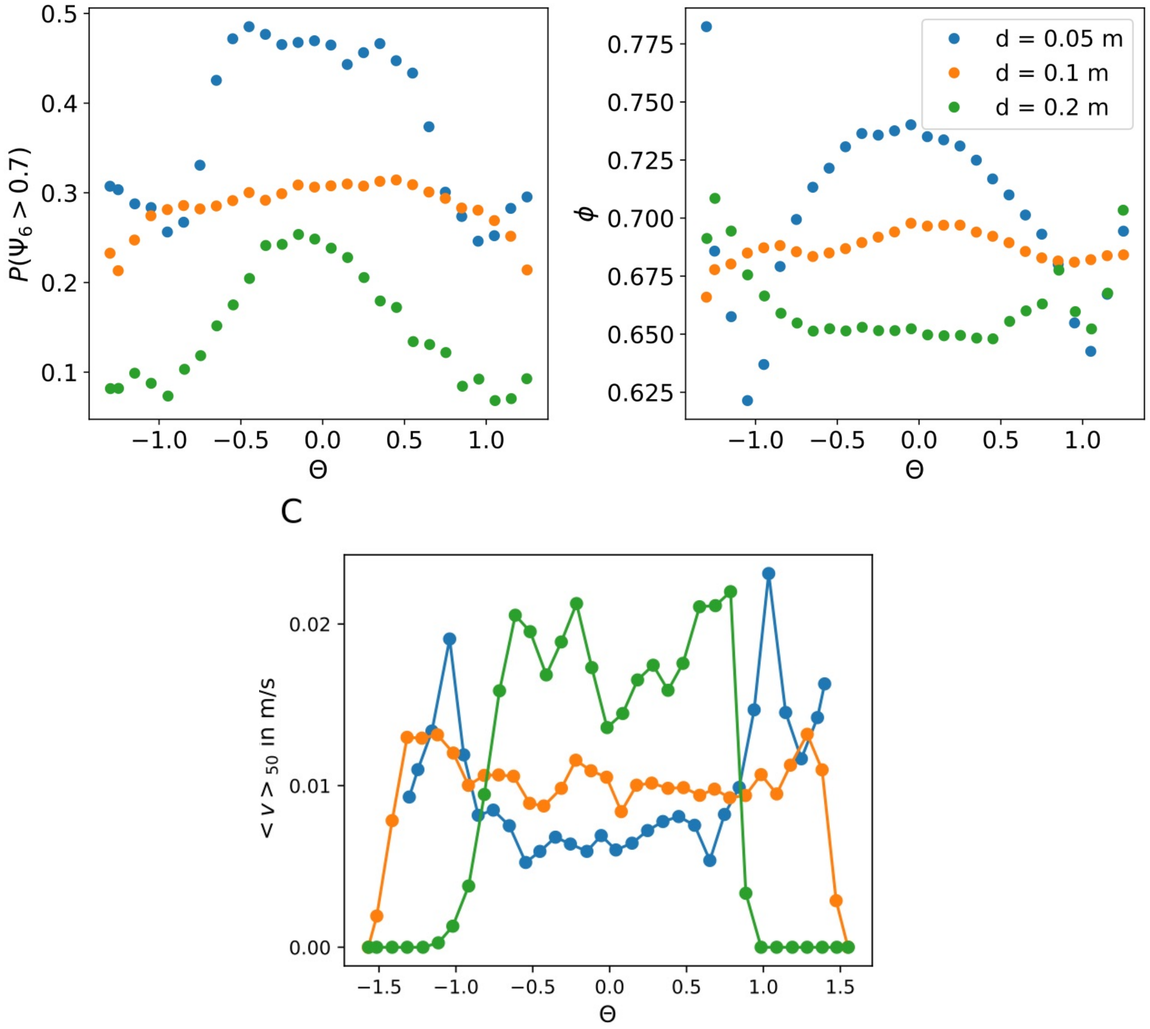

Figure 6.19: (**A**) Fraction of agents $P(\Psi_6 > 0.7)$ in respect to the angle Θ from the exit in the region $6\,\mathrm{m} < r < 8\,\mathrm{m}$. (**B**) Mean packing fraction ϕ in respect to the angel Θ from the exit. (**C**) Mean velocity $\langle v \rangle_{50}$ in respect to the angle Θ for a single run.

Clogging: In Figure 6.20 the fraction $P(T_c < 5000\,\text{s})$ of systems where the clog time $T_c < 5000\,\text{s}$ is depicted in panel A and $P(T_c > 1000\,\text{s})$ in panel B. In the 20 conducted runs, all systems with $d \leq 0.1$ m do not clog before $t = 1000$ s while only about $30\% - 40\%$ of systems with $0.2 \leq d \leq 0.3$ run longer than 1000 s before clogging. For $d = 0.5\,\text{m}$, all of the runs clog before 1000 s. For $d > 0.1\,m$, about $70 - 100\%$ of the simulations clog before reaching the maximal time of 5000 s, while about 60% with $d = 0.1\,\text{m}$ reach the maximal time and almost 90% for $d = 0.05\,\text{m}$. Similar to the repulsion strength a, an increase in the repulsion length increases the clogging probability for the set of parameters at hand on the orthogonal section analyzed. A reason for this behavior could be that because of the increased interaction length, the agents can not utilize gaps between neighboring agents efficiently, causing a higher likelihood of gridlocks in the system.

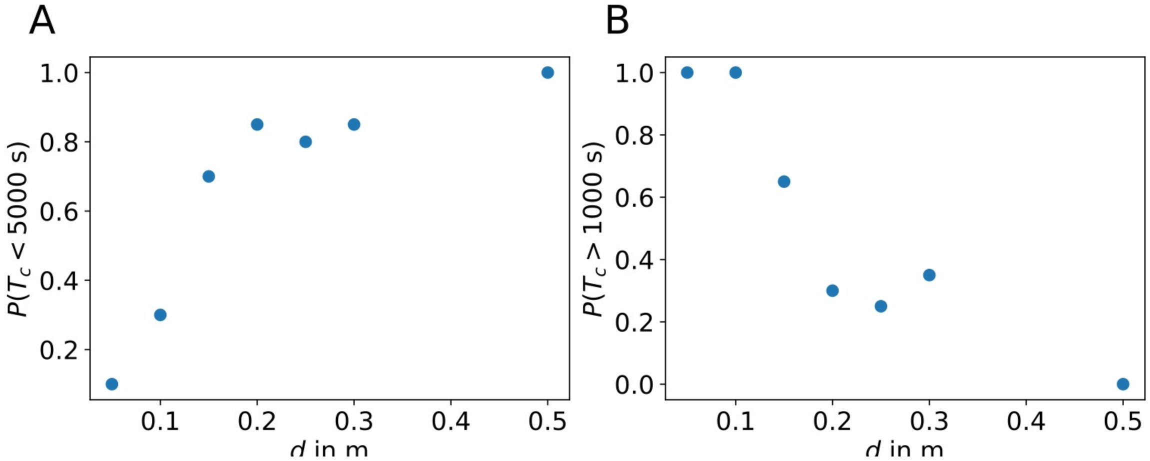

Figure 6.20: (**A**) Fraction of simulation runs that clogged before $t = 5000$ in respect to the repulsion length d. (**B**) Shows analogously $P(T_c > 1000\,\text{s})$.

Hexagonal order in respect to the distance from the bottleneck: Comparing the fraction $P(\Psi_6 > 0.7)$ with respect to the distance from the bottleneck r shown in Figure 6.21 A. Analogous to the repulsion strength a, the crystalline ring forms with an increase of d already visible for $d = 0.15$ m. The ring coincides with the decrease in packing fraction at further distances, showing again that the effect of agent-agent interaction acting on the direction $\hat{\mathbf{e}}_i$ is important for this occurrence. Apart from the crystalline region surprisingly consistent with an increase in d, the fraction $P(\Psi_6 > 0.7)$ decreases at all distances r from the bottleneck. The shape of the curves for $d \leq 0.15$ m and $r \leq 24$ m is similar in that they increase with r

close to the bottleneck as they reach a maximum and decrease from there on. For the runs with $d > 0.15$ m, the curves are very close together, with only a slight increase in hexagonal order from the bottleneck and a rather flat curve for further distances, excluding the crystalline ring. The packing fraction profile in panel B visualizes the decrease in packing fraction with increasing d at all distances and the above-mentioned sharp decrease in packing fraction with increasing $d \geq 0.15$ m far from the bottleneck. Consistent with the above analysis, the density profile increases with r and saturates at further distances, excluding the decreasing region ($r > 20$ m) for large $d \geq 0.15$ m. Panel C shows analogous to Figure 6.14 the heat map of the fraction $P(\Psi_6 > 0.7)$ in the r-d plane. The map illustrates the sharp decrease of hexagonal order with increasing d starting far away from the bottleneck and moving towards it. In contrast to the variation in the repulsion strength a, where the hexagonal order close to the bottleneck was only slightly affected by a variation of the parameter, in the case of d, a clear decrease in order near the bottleneck is observed. The appearance of the crystalline ring is qualitatively similar to its appearance in the r-a plane, starting around $r = 0.15$ m and increasing in width in a cone shape with increasing d. Analogous to Figure 6.15, Figure 6.22 shows the hexagonal order $P(\Psi_6 > 0.7)$ (panel A) and packing fraction ϕ (panel B) in a square measurement area at different distances d_b from the bottleneck in respect to d (see Figure caption for details). In this case, the values are shown in a log-log plot. The measurement areas are symmetrically around the $x = 0$ m. The plot illustrates the rather consistent decrease in hexagonal order and packing fraction with an increase in d at all measurement distances. Interestingly the order of $P(\Psi_6 > 0.7)$ with respect to the distance d_b is in reverse compared to the ϕ for $d_b > 0$ m. The distance d_b where the packing fraction is largest ($d_b = 14$ m) has a consistently smaller fraction $P(\Psi_6 > 0.7)$ than at distances with a lower packing fraction ($d_b = 5$ m and $d_b = 7$ m). The more drastic change in the order and density measure close to the bottleneck ($d_b = 0$) is also visible in the plot. Compared to the variation in the repulsion strength a close to the bottleneck, the measure is static, and the change in order and density is comparable to the further distances. This likely stems from the low-order jammed funnel in the system, which decreases the hexagonal order significantly and is visible at all distances. The packing fraction decrease has a similar origin as discussed in Section 3, where due to the jammed agents at the sides of the bottleneck, the corridor effectively is narrowed. The hexagonal order and density decrease are close to linear in the log-log plot. This is not

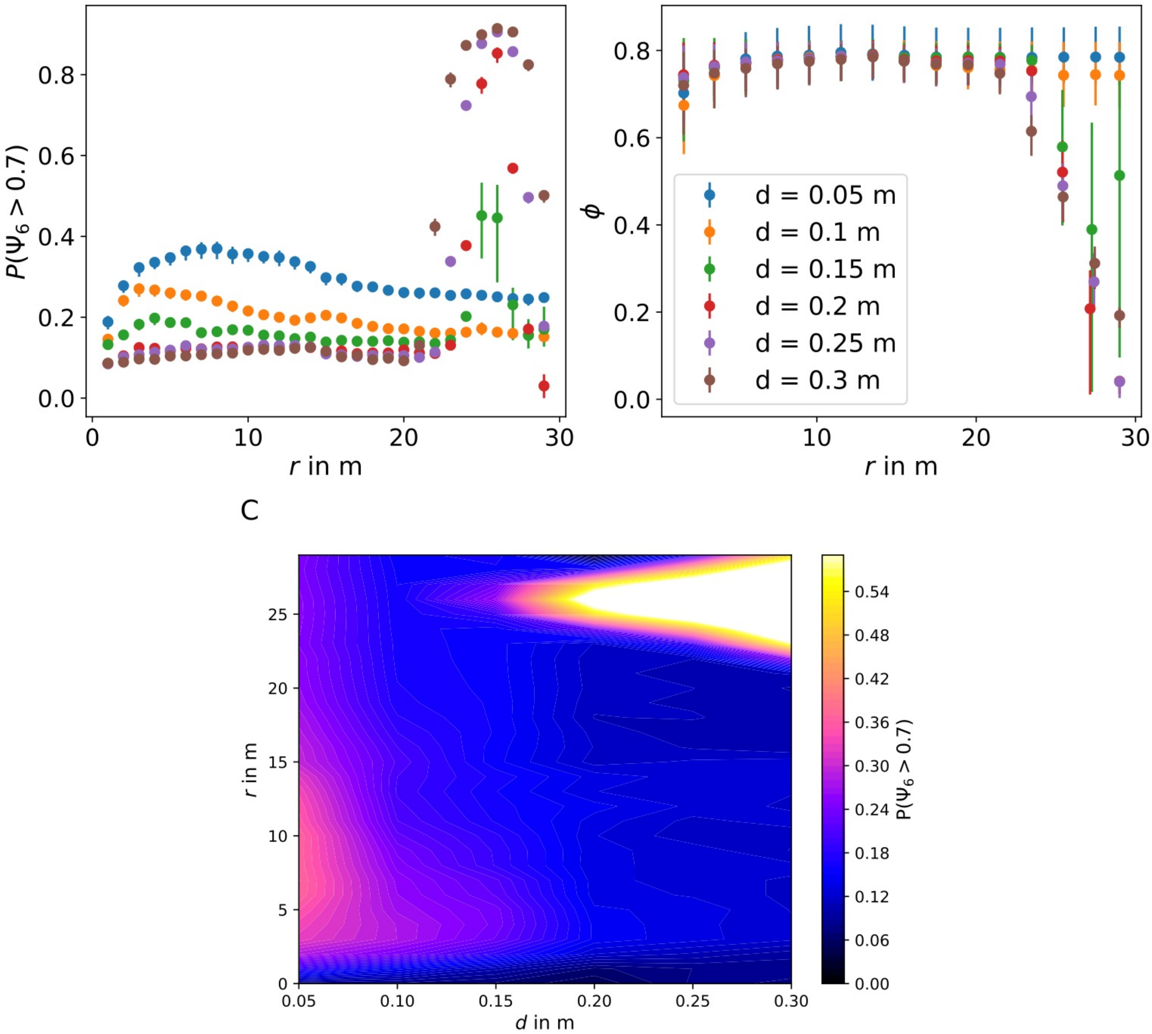

Figure 6.21: (**A**) Fraction $P(\Psi_6 > 0.7)$ in respect to the distance from the bottleneck r for different values of the repulsion length d. (**B**) Analogous to A for the packing fraction ϕ. (**C**) Smoothed heat map showing $P(\Psi_6 > 0.7)$ on the r-d plane.

to say that there is a power law governing the dynamics, as the data is insufficient to investigate this properly, but it is in contrast to a, where the increase is close to linear for both the hexagonal order and the packing fraction. In the case of d, the measures decay faster than linear but not exponentially.

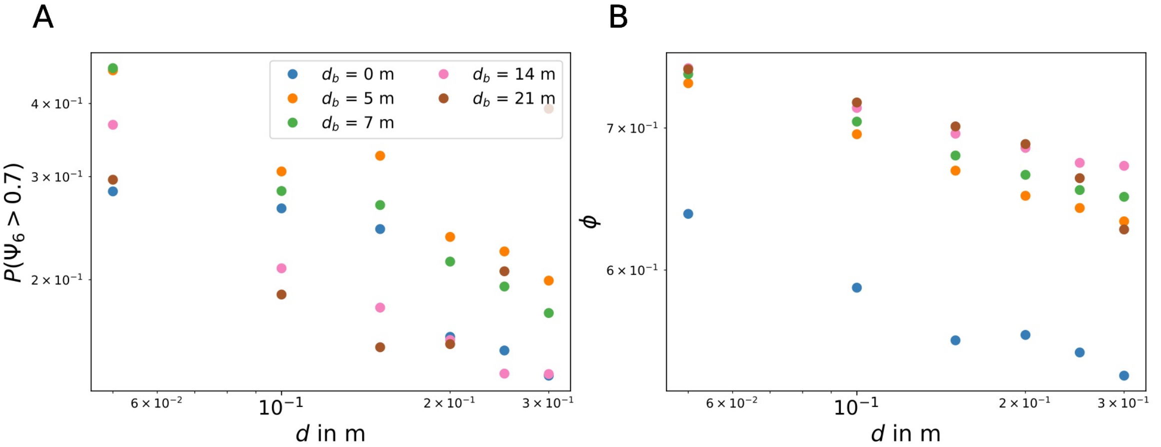

Figure 6.22: Log-log plot of (**A**) the fraction of agents $P(\Psi_6 > 0.7)$ and (**B**) the packing fraction ϕ in the measurement area ($-2 < x < 2\,\mathrm{m}$ and $d_b < y < d_b + 4\,\mathrm{m}$) in respect to the repulsion length d.

Shape Factor: The shape factor distribution $P(\zeta)$ in Figure 6.23 analogous to Figure 6.16 and 6.3 shows the effect of d on the occurrence of the various shapes. Again the system displays a bimodal distribution for $d < 0.15\mathrm{m}$. For $d = 0.05\mathrm{m}$, the first peak is pronounced compared to the second peak with it being a factor of two larger. For both close and far away from the bottleneck (panel A and B), increasing d decreases the first peak and the distribution turns mono-modal between $d = 0.15\mathrm{m}$ to $d = 0.2\,\mathrm{m}$, with the single peak being between $1.185 < \zeta < 1.2$. As a comparison the distribution of the granular fluid from [188] for $\phi = 0.5$ is shown in panel A. For increasing d, the distribution becomes similar to the example of the granular fluid, though the granular fluid is shifted further to larger values of ζ. Comparing the distribution close to the bottleneck and far away, the shapes of the distributions are rather similar, in regards to the position of their peaks and the modality. There are slight differences in how pronounced the peaks are. For $d = 0.05$ m the peak near $\zeta = 1.1$ is more pronounced far from the bottleneck, while the opposite is true for $d = 0.1\mathrm{m}$. For $d > 0.15\mathrm{m}$, the left flank of the distribution is shifted towards smaller values of ζ far away from the bottleneck. The more pronounced differences between the distributions for increasing d show the transition of the system from the state where a laminar flow towards the bottleneck is more likely (meaning the likelihood of regions with jammed agents is low) to the regime where the system is partially jammed (meaning a high likelihood of jammed regions). This becomes more obvious when considering the shape classes (see Figure 6.4 for the classification). In Figure 6.24, the frequency-log-plot of the shape factor classes is plotted in respect to d close and far from the bottleneck. At $d = 0.05\,\mathrm{m}$, the frequency of the three classes is close to each other. Increasing d reduces the frequency of class A dramatically and especially increases the frequency of class C. In comparison, while about 30% of agents close and far from the bottleneck are in shape class A for $d = 0.05\,\mathrm{m}$, less than 5% are in that class for $d = 0.3\,\mathrm{m}$. The increase of shape class C is roughly 35% close and far from the bottleneck of about $60 - 70\%$. The decrease in class A is especially steep between $d = 0.15\,\mathrm{m}$ and $d = 0.2\,\mathrm{m}$ close to the bottleneck. Class B increases at first between $d = 0.05\,\mathrm{m}$ and $d = 0.1\,\mathrm{m}$ and decreases from there on. The difference is much smaller to class A and B, from around 36% to 25% close to the bottleneck and staying almost constant far from the bottleneck. The increase and decrease of shape C and A is roughly exponential from $d = 0.05\,\mathrm{m}$ to $d = 0.2\,\mathrm{m}$ and saturates for $d > 0.2\,\mathrm{m}$. Panels C and D of Figure 6.24 shows a snapshot of the system for $d = 0.05\,\mathrm{m}$ in panel C and $d = 0.3\,\mathrm{m}$ in panel D at $t = 3000\,\mathrm{s}$. The system with $d = 0.05\,\mathrm{m}$ exhibits large clusters of hexagonally ordered class A agents in the bulk of the system. In contrast, the abundance of class C agents in the bulk of the system with $d = 0.3\,\mathrm{m}$ is visible, with only a few agents being in class A close

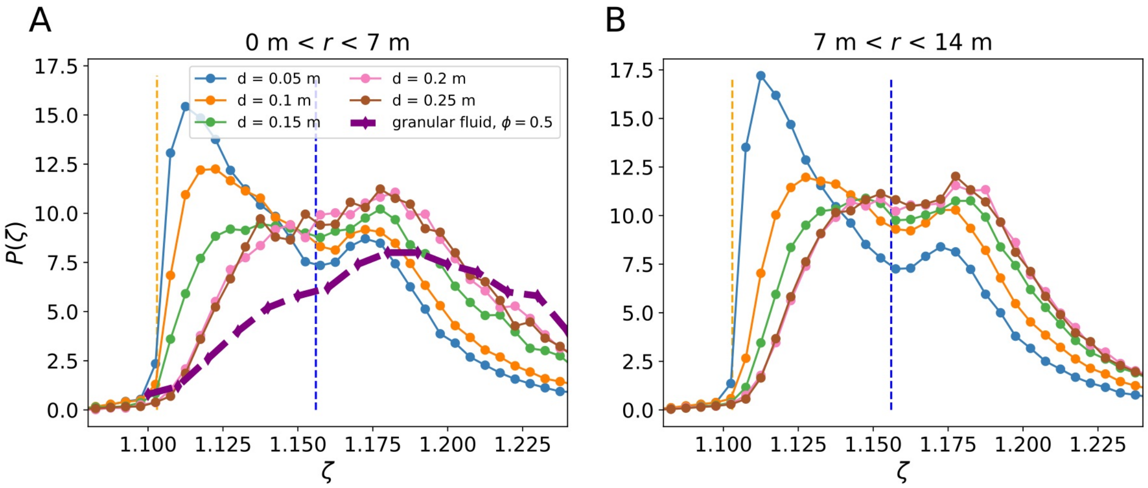

Figure 6.23: Distribution of the shape factor for different repulsion lengths d close to the bottleneck (**A**) and far from the bottleneck (**B**).

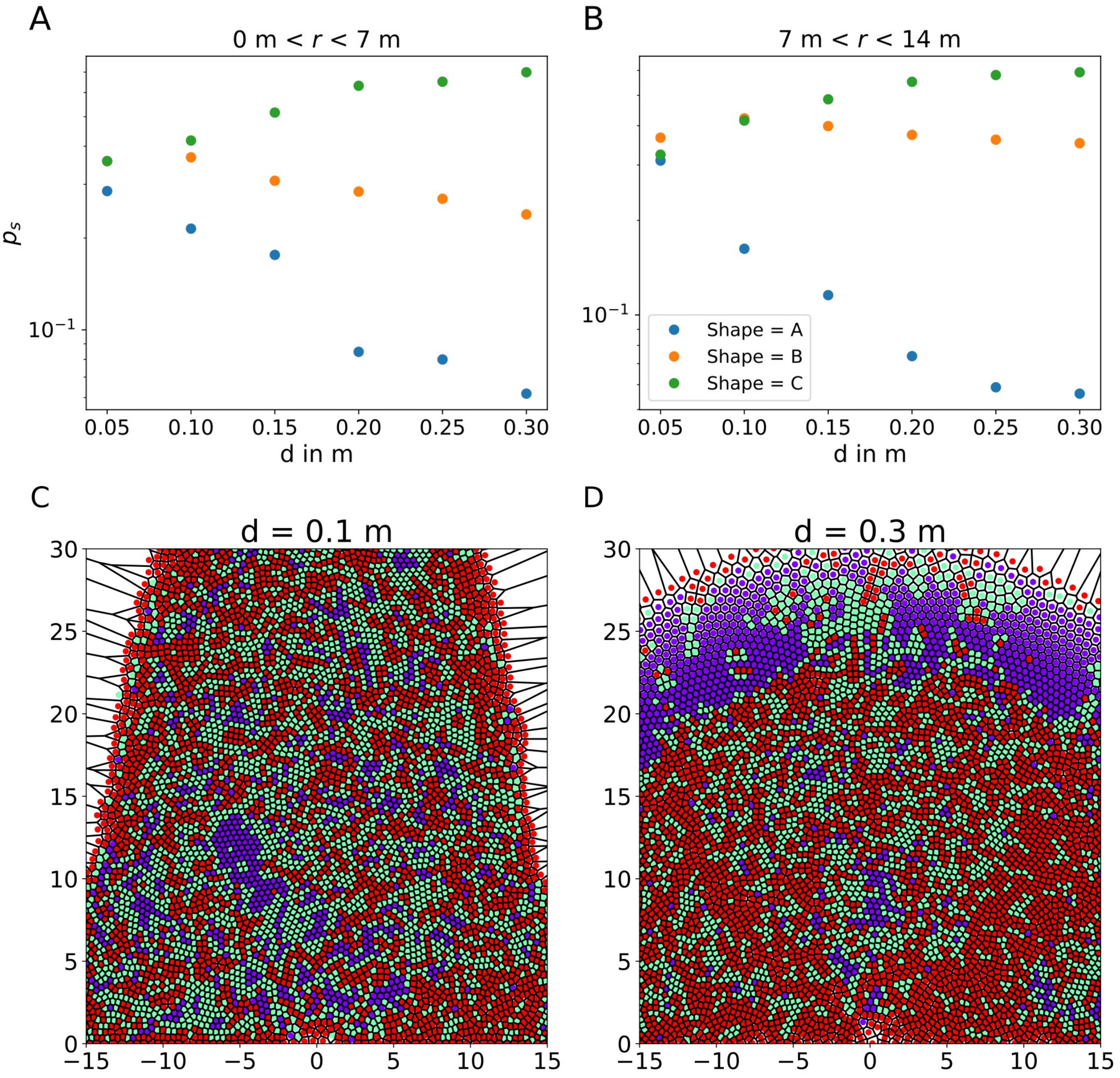

Figure 6.24: (**A**)&(**B**) Log-plot of the fraction p_s of the shape classes in respect to the repulsion strength d close to the bottleneck (**A**) and far from the bottleneck (**B**). (**C**)&(**D**) Example of the simulation at $t = 3000$ s for $d = 0.05$ m (**C**) and $d = 0.3$ m (**D**).

to the bottleneck in the system's center. The jammed agent funnel is visible, where the frequency of class C on the sides is highest, compared to the fluid funnel, where class B agents are abundant. The interface between the crystalline ring and the bulk of the system is sharp, where the frequency of class A agents dominates in the ring. Transitioning into the bulk, the class almost completely disappears. Close to the bottleneck in the narrow funnel ($r < 2.5\,\mathrm{m}$) where the agents flow, almost only class C agents are observed. In summary, the repulsion length d has a significant influence on the dynamics of the system. A variation in d changes the system's bulk shape, changing the spatial structure of the system from a relatively even mix of the shape classes with the appearance of large hexagonal clusters to a system with almost no hexagonal order in the bulk and partially jammed flow. A possible reason for this behavior is that due to the long interaction range on the agent's direction vector $\hat{\mathbf{e}}_i$, the agents cannot efficiently use gaps between their surrounding neighbors, leading to a more significant likelihood for jams and reducing the potential to equalize their distance to their neighbors.

6.1.3 Exploring the a-d plane

The parameter space investigation is extended to analyze further the effect of a and d on the system. In the previous two sections, the a-d plane is analyzed in an orthogonal direction from the parameter value fitted to the experiments in Section 5.1 in the a and d direction. The extension is now to investigate several combinations of a and d in the two-dimensional plane. Six values on the plane are chosen in each direction giving 36 combinations. Each simulation is run 20 times, and the observables are calculated for $t > 1000\,\mathrm{s}$ in $\Delta t = 100\,\mathrm{s}$ steps until 5000 s. The remaining parameters are identical as in the previous sections of this chapter and summarized in Table 6.1. Figure 6.25 illustrates a snapshot of all conducted simulations sorted on the a-d plane. The agents with $\Psi_6 > 0.7$ are marked in yellow. The values tested are $a \in \{1.0, 1.5, 2.5, 5.0, 7.5, 10.0\}$, and $d \in \{0.01, 0.05, 0.1, 0.2, 0.3, 0.5\}$ m. The plot shows all combinations of the two parameters with the magnitude indicated on the axis and specified in the title of the panels. The plot illustrates the structural heterogeneity and the system's dynamics on the a-d plane. From the snapshot, one can observe certain regions on the plane. For example, values of $d \leq 0.05$ m and $a \geq 2.5$ have a large fraction $P(\Psi_6 > 0.7)$, with agents in the hexagonal order class dominating the system. Large values of $d \geq 0.2$ m combined with values for the

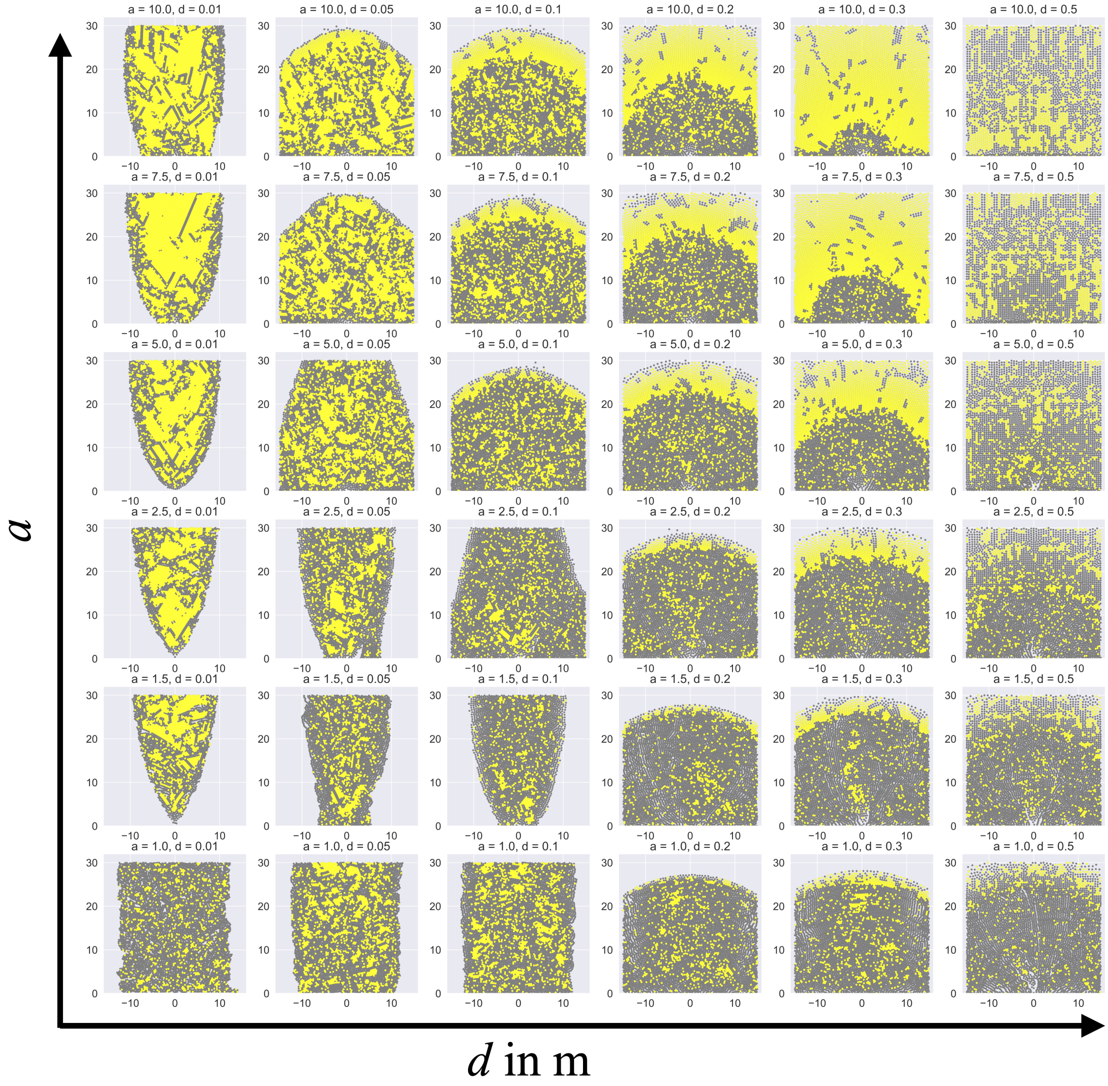

Figure 6.25: Scatter plot of snapshots of the simulations at $t = 4000\,\mathrm{s}$ on the a-d plane. Yellow coloured agents have a hexagonal order of $\Psi_6 > 0.7$.

repulsion strength not exceeding $a = 5$ tend to have a lower fraction of hexagonally ordered agents in the bulk near the bottleneck ($r < 14$m). An interesting dynamic is observed in systems with a value of $a \geq 5.0$. With increasing d, the hexagonal order near the bulk declines from $d = 0.05$ m to $d = 0.1$ m. From there on out, the crystalline ring expands further towards the bottleneck with increasing d, dominating the majority of the system for $d = 0.3$ m and $a \geq 7.5$. At $d = 0.5$ m, the dynamics change with the disappearance of the crystalline ring but still a high fraction of hexagonally ordered agents, especially for $a = 10$. An abundance of agents are also ordered in square clusters in this region. This is further illustrated in the Appendix A.6 in Figure S22. A possible reason for the behavior could be interactions with the system's boundary, which has a rectangular geometry, but this is conjecture. There also exists a boundary going through the system depending on a and d where the agents' bulk shape changes from a parabola to a half circle. The system's partial jamming and clogging probability also depends on a and d. This is better illustrated in the scatter plot of the speed function and local packing fraction in Appendix A.6 Figure S20 and Figure S21. It isn't easy in the spatially heterogeneous and dynamical system to clearly characterize the systems attributes of structure and order. Certain areas are highlighted and analyzed to classify the landscape and possible transitions. The classification focuses on the following attributes: hexagonal order, packing fraction, clogging fraction, bulk shape, and partial jamming. The hexagonal order is measured for $t > 1000$ s in the region $|x| < 5$ m, 4 m $< y < 15$ m. This area is chosen to characterize the inner bulk of the system and reduce the influence of the boundary, especially in the parabola-shaped system. The measure should also exclude the crystalline ring unless it is dominating the system (see $a = 10$ and $d = 0.3$ m in Figure 6.25). The packing fraction is calculated in the same area. The clogging fraction is defined as the fraction of runs $P(T_c < 1000\,\mathrm{s})$ where the clogging event happens at a time $T_c < 1000$ s. The bulk shape can be seen from the scatter plots, and a partially jammed state is deducted from videos and snapshots of the agents' speed (see "*aDSpeedCSM.mp4*" and "*aDOrderCSM.mp4*",[226]). A system is considered partially jammed when the large stable and jammed regions occur in all runs. The clogging fraction, hexagonal order, and packing fraction measures are continuous, while the bulk shape and the partially jammed state are categorical. The continuous measures are depicted in a heat map on the a-d plane in Figure 6.26. Panel A shows the fraction of clogged systems $P(T_c < 1000\,\mathrm{s})$, panel B the hexagonal order $P(\Psi_6 > 0.7)$ and panel C the packing fraction ϕ. Comparing the

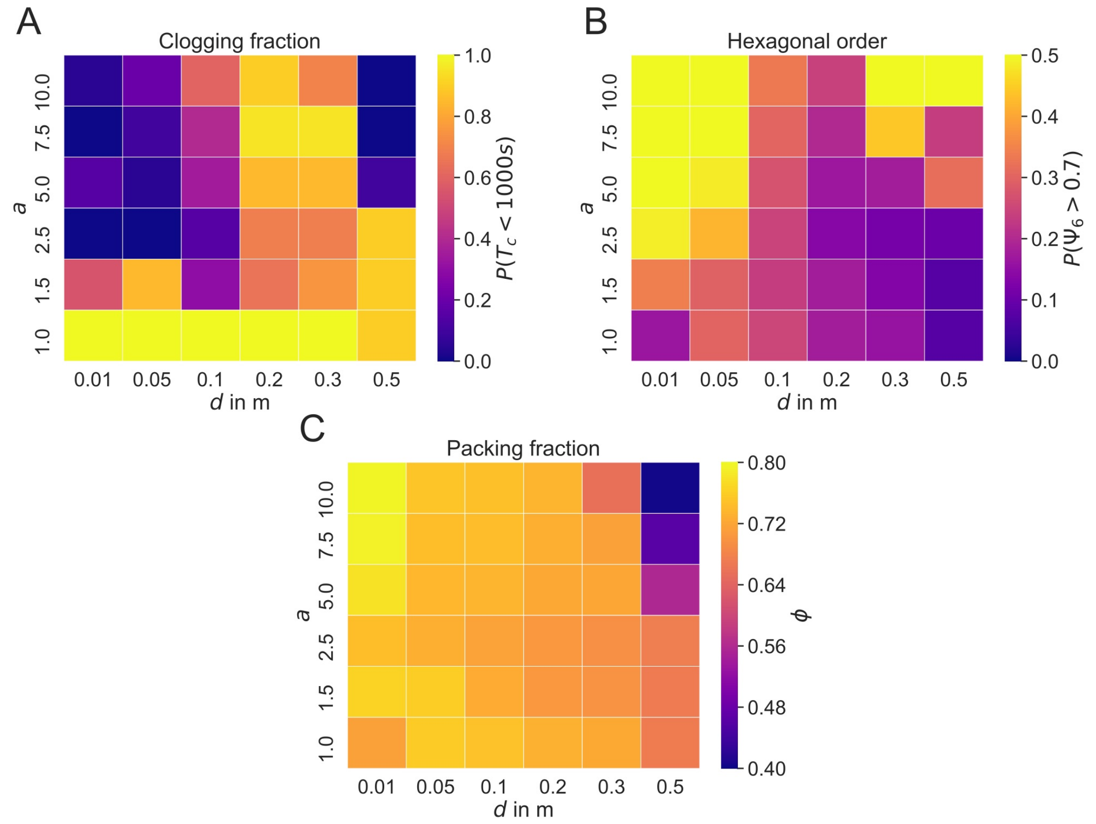

Figure 6.26: Heat maps of the a-d plane for the simulated parameter pairs: (**A**) the fraction $P(Tc < 1000\,\mathrm{s})$ of systems that clog at a time $Tc < 1000\,\mathrm{s}$, (**B**) the fraction of agents $P(\Psi_6 > 0.7)$ in the measurement area and (**C**) the packing fraction of the system in the measurement area $|x| < 5\,\mathrm{m}$, and $4\,\mathrm{m} < y < 15\,\mathrm{m}$.

three measures, one sees that the clogging fraction and hexagonal order have a more rugged structure with multiple minima and maxima in the landscape. The packing fraction ϕ in contrast has a smoother surface with high packing fraction region ($d \leq 0.3$ m and $a \geq 5.0$) and a low packing fraction region ($d > 0.3$ and $a \geq 5$). The clogging fraction has two distinct regions with a low fraction of clogged systems for $d \leq 0.5$ m and $a \geq 2.5$ and for $d = 0.5$ m and $a \geq 5.0$. The regions with a low clogging fraction coincide with high hexagonal order. The regions with a higher clogging fraction are in the interval $a = 1.0$ or $d \geq 0.2$ m, coinciding with a low hexagonal order. The order increases with a reduction in the repulsion length d and an increase in the repulsion strength a. The exception of this rule manifests in the second maximum at $d = 0.5$ m and $a = 10.0$. This region stems from the effect of agent-agent interaction on the direction vector $\hat{\mathbf{e}}_i$ discussed above. In this case, the repulsion function $R(s)$ is significant enough so that the crystalline ring extends

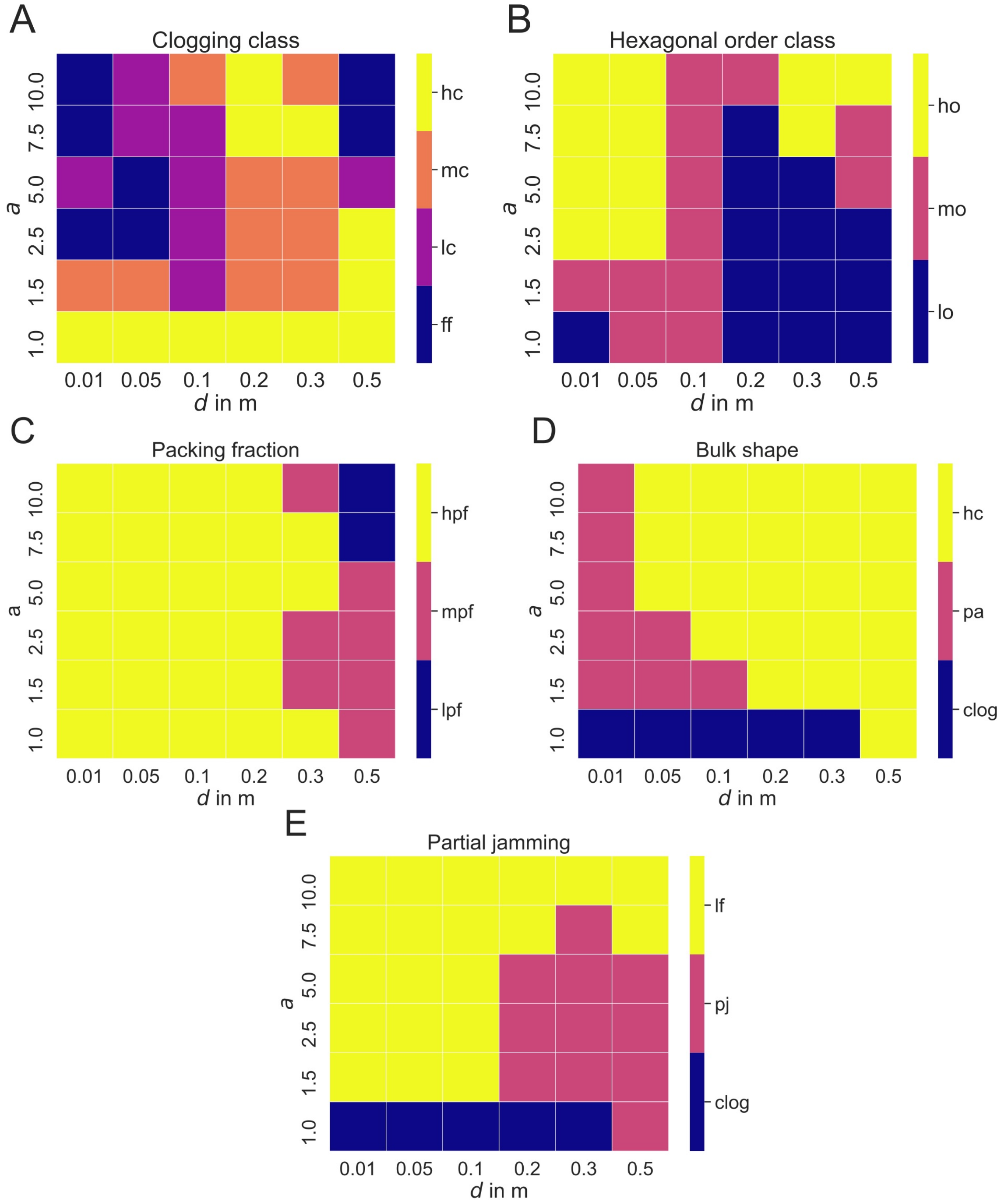

Figure 6.27: The categorized map of the measures and attributes of the system in the a-d plane. (**A**) depicts the clogging classes, (**B**) depicts the hexagonal order classes, (**C**) the packing fraction class (**D**) the bulk shape, and (**E**) the partial jamming.

close to the bottleneck (see Figure 6.25). At this point, the packing fraction of the whole system is reduced significantly, and this effect dominates the interactions between the agents. To simplify the different maps and discuss them with the system's categorical attributions, the continuous measures are classified. The clogging fraction is categorized into four classes according to the above defined metric for the clogging in the system in the following way.

$$\text{clog class} = \begin{cases} \text{free-flow (ff)} & P(T_c < 1000\,\mathrm{s}) < 0.1, \\ \text{low clogging (lc)} & 0.1 \leq P(T_c < 1000\,\mathrm{s}) < 0.5, \\ \text{medium clogging (mc)} & 0.5 \leq P(T_c < 1000\,\mathrm{s}) < 0.9, \\ \text{high clogging (hc)} & 0.9 \leq P(T_c < 1000\,\mathrm{s}). \end{cases} \tag{6.5}$$

Analogous the hexagonal order is categorized into three classes:

$$\text{hex order class} = \begin{cases} \text{low hex order (lo)} & P(\Psi_6 > 0.7) < 0.2, \\ \text{medium hex order (mo)} & 0.2 \leq P(\Psi_6 > 0.7)\,\mathrm{s}) < 0.4, \\ \text{high hex order (ho)} & 0.4 \leq P(\Psi_6 > 0.7), \end{cases} \tag{6.6}$$

and for the packing fraction

$$\text{packing class} = \begin{cases} \text{low packing fraction (lp)} & \phi < 0.5, \\ \text{medium packing fraction (mp)} & 0.5 \leq \phi < 0.6, \\ \text{high packing fraction (hp)} & 0.7 \leq \phi. \end{cases} \tag{6.7}$$

Since no clear phase transitions are observed in the system, the choice of the classes is not obvious. The boundaries are chosen to illustrate and highlight the different sections of the measures on the *a*-*d* plane. The categorical measures are the bulk shape which can either be closer to a parabola (pa) or a half circle (hc) and the occurrence of partial jamming, which is categorized as (pj) if it occurs or as laminar flow (lf) if it does not. All five categorizations maps are depicted in Figure 6.27. The categorization helps to visualize the heterogeneity of the system and the relationship between the different measures. The categorization of the clogging fraction in panel A illustrates the different areas of clogging probabilities. The probability for high clogging (hc) is at the boundaries of the measured map, for either small values of

$a = 1.$ or large values of $d = 0.5$ excluding the zone where to agent-agent interaction acting on the direction $\hat{\mathbf{e}}_i$ dominates the dynamics ($a \geq 7.5$ and $d \geq 0.3$ m). Interestingly in the area of large a, the clogging frequency is low for either small values of $d \leq 0.05$ m or large values of $d = 0.5$ m. In between is an island of high clogging frequencies. Compared with the hexagonal order, it shows that a lower clogging probability usually coincides with high hexagonal order. Though this is not exclusively true, as seen in the example $a = 7.5$ and $d = 0.3$ m. The area of low hexagonal order shown in panel B coincides with the partially jammed area in panel E, which also coincide with higher clogging frequencies (mc-hc). The bulk shape in panel D divides the space into two sections, where there is a non-linear decreasing relationship between a and d that determines the shape of the bulk. The attributes shown in Figure 6.27 can be collected and visualized in a comprehensive map of

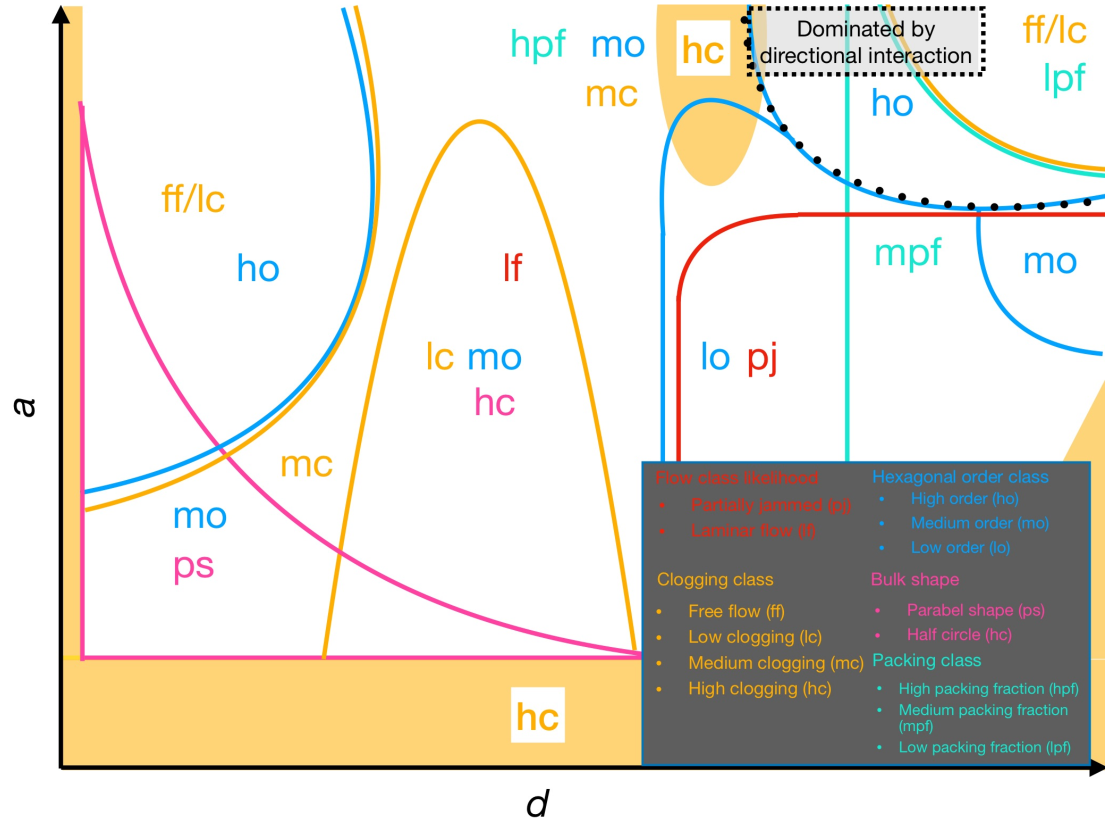

Figure 6.28: Illustration of the different hypothetical areas of attributes on the a-d plane. The attributes and their abbreviations are explained in the legend. The black dotted line illustrates the boundary where the dynamics are dominated by the agent-agent interaction acting on the movement direction.

the *a*-*d* plane hypothesizing the different areas and their boundaries in Figure 6.28. Since only a small area of the *a*-*d* plane is probed with the simulations, the exact boundaries are not known and are inferred as a rough estimate. The idea is to visualize the attributes mentioned above to illustrate their complex relationships.

6.2 Influence of noise in the movement direction

The previous section analyzed the CSM with a focus on the exponential interaction acting on the movement direction of the agents (see Section 2.3). Depending on the exponential repulsion function $R(s)$ (equation (2.17)), the system can exhibit unrealistic dynamics in the context of empirical pedestrian systems. Especially the problem of stable clogs that arrest the flow indefinitely and partial jams where part of the system is in a stable arrested state are unrealistic in real-world scenarios. Depending on the initial conditions and the parameters, the system can get stuck in these undesired states indefinitely. Because the system is deterministic apart from the random initial conditions, it cannot escape these states. One way to improve this is to add an external noise onto the desired direction of the agent $\hat{\mathbf{e}}_i$, which allows the system to explore a wider state space as discussed in Chapter 2. The introduction of extrinsic noise usually has a minor influence on quantities like the system's density. However, the noise could influence the system's spatial structure in the movement direction. In atomic equilibrium systems, an increase in thermal noise is usually associated with decreased order. In non-equilibrium systems, surprising behavior can emerge through the noise. For example, the effect of freezing by heating in a cellular automata model with counter flow [155, 234]. In empirical studies of granular materials, ordered structures are observed in dense shaken granular fluids [188, 207].

6.2.1 SCSM with repulsion

In this section, the noise in the system is introduced as described in Section 2.3. The noise on the direction $\hat{\mathbf{e}}_0$ of the agent is added as a two-dimensional vector ζ with normal-distributed entries $\mathrm{N}(0, \sigma^2)$ with zero mean and standard deviation σ and subsequently normalized (see equation (2.19)). The effects of the noise for different $\sigma \in \{0.3, 0.7, 1.0\}$ is illustrated in Figure 6.29 for 10000 vectors. An important effect, especially for higher values of σ, is the possibility of backward movement, which can

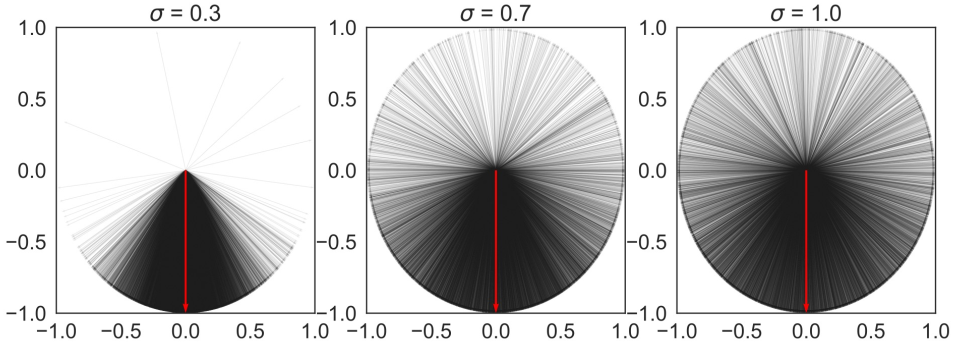

Figure 6.29: Illustration of the effect the noise has on the movement direction of the agent for different $\sigma \in \{0.3, 0.7, 1.0\}$. The red vector shows the original direction, and the black vectors are 10000 outcomes with added noise.

help dissolve clogs in the system [140]. The noise levels represented in Figure 6.29 are introduced in the system for three different values of $d \in \{0.05, 0.2, 0.3\}$ m and $a \in \{2.5, 5.0, 10.0\}$. The other values are equal to Table 6.1. The simulation is run for $t = 5000$ s with $N_s = 10$ realisations per parameter set. The focus is set on the stationary state of the system at $t \geq 1000$ s and $\Delta t = 100$ s. Snapshots of the system in the d-σ plane are depicted in Figure 6.30 in the left array of panels and a-σ plane in the right array. The increasing noise in the system affects the hexagonal order significantly in all simulated systems. In the system with $d = 0.05$ m, the noise also changes the shape of the bulk. While the system without noise has a parabolic shape (see Figure 6.25), the increasing noise transforms it into a half-circle shape with increased order. For $d = 0.3$ m, the hexagonal order near the bulk increases with large yellow clusters visible in the panel. Interestingly the crystalline ring at the system's edge diminishes with increased noise. Analogous to the previous section the continuous measures of hexagonal order $P(\Psi_6 > 0.7)$, the clogging fraction P_{T_c} and the mean packing fraction ϕ are measured and the values are illustrated in Figure 6.31. In this case, the clogging time T_c is defined as the time when the system is in a clogged state. This is necessary since clogs are not indefinitely stable in a system with extrinsic stochastic noise compared to the CSM. There is a non-zero chance that a clog dissolves due to the noise in the movement direction (e.g., through the backwards movement of agents), which can destabilize the arch. The fraction $P_{T_c} = T_c/T_{tot}$ is then defined as the fraction of the total time T_{tot} the system is in a clogged state. It is measured by comparing the time series of the agents in the area Ω bounded by $4\,\text{m} < y < 6\,\text{m}$ and $|x| < 2$ m. When the mean of the absolute difference in the y-position $\langle |y_i(t_0) - y_i(t_1)| \rangle < \epsilon$ of all agents $i \in \Omega$ is smaller than the threshold value ϵ between t_0 and $t_1 = t_0 + \Delta t$, the system is considered to be clogged. In this case the value for the threshold $\epsilon = 0.02$ m. The value is chosen arbitrarily, but it should be large enough to consider slight fluctuations in the clogged state. Because of the large time steps ΔT, the method only detects prolonged clogs in the system. However, it is still sufficient to characterize the different parameters regarding the clogging fraction. Figure 6.31 A and D show P_{T_c} for the d-σ and a-σ plane respectively. The clogging fraction decreases with the increase of noise σ. The ten individual runs observe no clogs in some of the systems. The runs with $d = 0.3$ m and $a = 10$ have a high chance of clogging in the deterministic case (see previous section) and still do with a smaller amount of noise of $\sigma = 0.3$. With increasing noise, the clogging fraction decreases from over 60% to roughly under 20% in the sample with $\sigma = 1$. The hexagonal order measure $P(\Psi_6 > 0.7)$ and the mean packing fraction ϕ are calculated in the area $|x| \leq 5$m and $4\text{m} \leq y \leq 15$m illustrated by the red square in the center panel of the right array in Figure 6.30. Comparing $P(\Psi_6 > 0.7)$ in panels B and E to ϕ in panels C and F illustrates that while ϕ is only slightly affected by the noise, the hexagonal order increases consistently with an

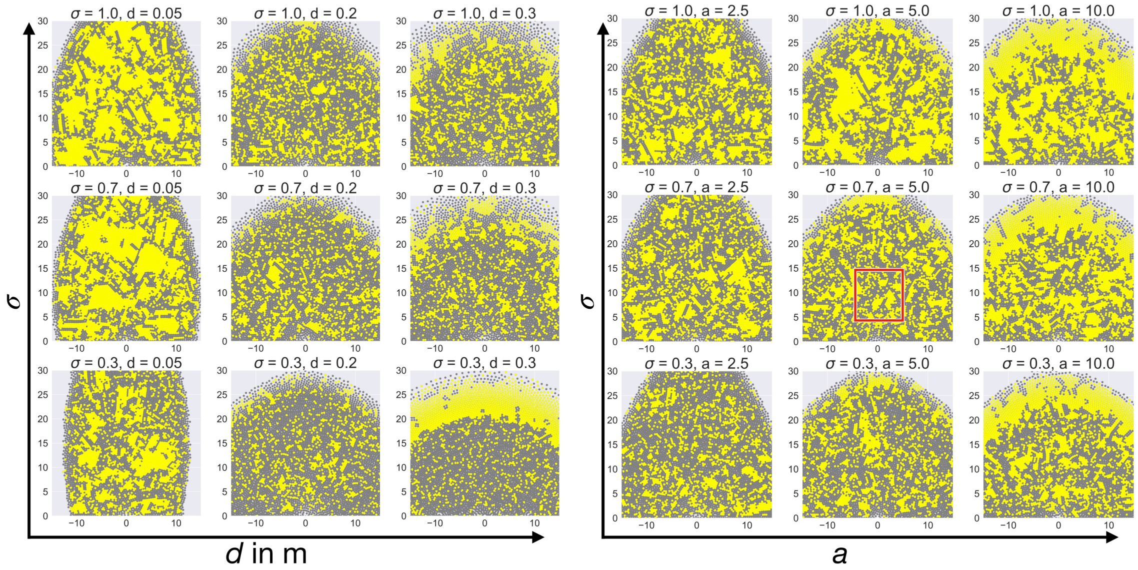

Figure 6.30: (**Left array**): Snapshot of the simulation on the d-σ plane for $d \in \{0.05, 0.2, 0.3\}$ m and $\sigma \in \{0.3, 0.7, 1.0\}$ at $t = 3000$s. (**Right array**): Analogous on the a-σ plane for $a \in \{2.5, 5.0, 10.0\}$. Yellow agents have a hexagonal order $\Psi_6 > 0.7$. The red rectangle in the center panel of the right array marks the measurement area used for Figure 6.31.

increase in noise, independent of the parameters for d and a. The hexagonal order

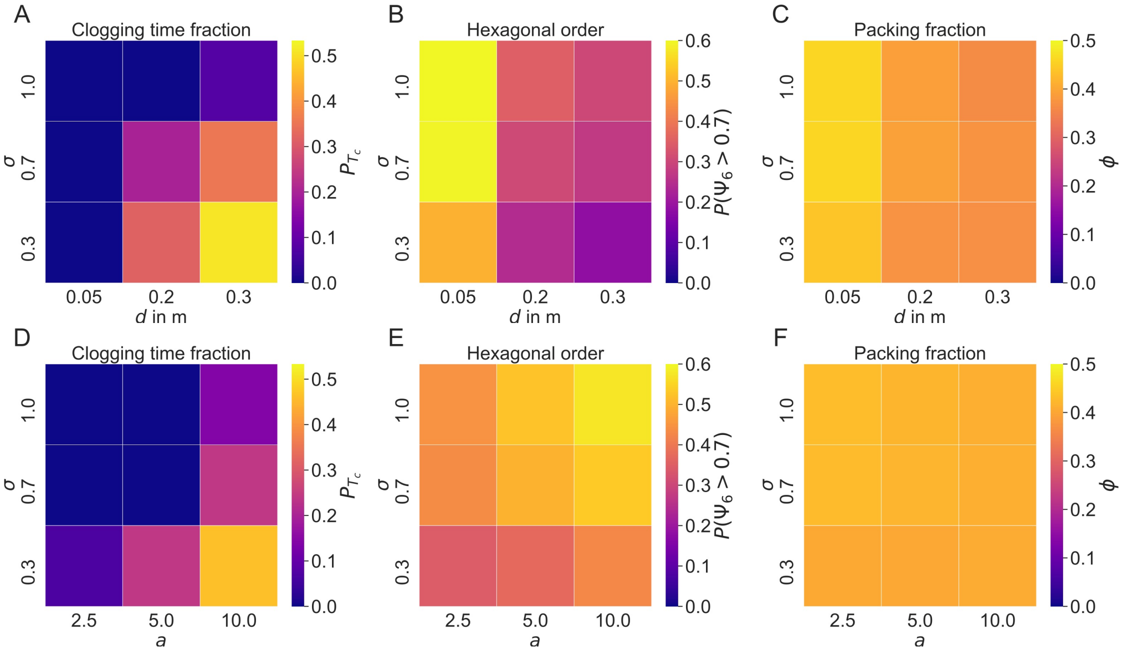

Figure 6.31: Heat maps of the Clogging time fraction P_{T_c} (**A**)&(**D**), Hexagonal order $P(\Psi_6 > 0.7)$ (**B**)&(**E**) and mean packing fraction ϕ (**C**)&(**F**). Panel (**A**)-(**C**) show the simulations on the d-σ plane and(**D**)-(**F**) on the a-σ plane. The measurement area for ϕ and $P(\Psi_6 > 0.7)$ is illustrated in Figure 6.30.

$P(\Psi_6 > 0.7)$ and packing fraction ϕ with respect to the distance of the bottleneck r for the simulated values of a, d and σ are plotted in Figure 6.32. Panels A-C show the values of the d-σ plane and D-F of the a-σ plane. All systems have in common that the packing fraction and hexagonal order increases with distance to the bottleneck until $r \approx 5$ m. The noise increases the maximum, where the fraction $P(\Psi_6 > 0.7)$ saturates, but close to the bottleneck ($r < 3$ m), it does not affect the order for $d < 0.3\,\text{m}$ and $\sigma > 0.3$. The packing fraction ϕ near the bottleneck ($r < 5\,\text{m}$) is only slightly affected for $a = 10$ and $d > 0.05\,\text{m}$, where ϕ decreases with increasing σ. In the cases where a crystalline ring forms ($d \in \{0.2, 0.3\}$ and $a \in \{5, 10\}$), increasing noise decreases the order in the ring, and for $d = 0.2\,\text{m}$ it disappears when $\sigma > 0.3$. The observed decline in packing fraction at $r > 20$ m is also affected by increasing noise. The slope of the packing fraction decline decreases in this case but is still substantial in all systems. This means that an increased noise decreases hexagonal order in a low-density environment. The shape factor distribution of the systems is shown in Figure 6.33 for the d-σ plane in panels A and B, and the a-σ plane in C and D. The distribution are calculated close to the bottleneck ($0\,\text{m} < r < 7$) m and far away 7 m $< r <$ 14 m. They exhibit the bimodal feature (except for $d = 0.3$ m and $\sigma = 0.3$ near the bottleneck) with a high peak close to the hexagonal value of ζ and a smaller peak close to the pentagonal value. The noise generally increases the peak near the hexagonal value of the system and decreases the second peak close to the pentagonal value. In the systems with varying d the increase especially close to the bottleneck is substantial for the values $d = 0.2$ m and $d = 0.3$ m. These systems partially jam without noise, but a sufficient amount of noise can break the jammed state. This is especially visible for $d = 0.3$ m, where the system is partially jammed with $\sigma = 0.3$. The shape factor distribution transforms from the mono-modal peak observed in this state (see also Figure 6.23) to the bi-modal shape observed in the laminar systems. Compared to the distribution with no noise (see Figure 6.16 and 6.23) the hexagonal peak is much higher already for $\sigma = 0.3$. The dark red plot shows the distribution of the granular fluid at $\phi = 0.7$ from [188]. For certain parameters ($d = 0.05$ m and $a \in \{5, 10\}$), the distributions of the agent system becomes comparable with a granular fluid. To illustrate the effect of the noise on

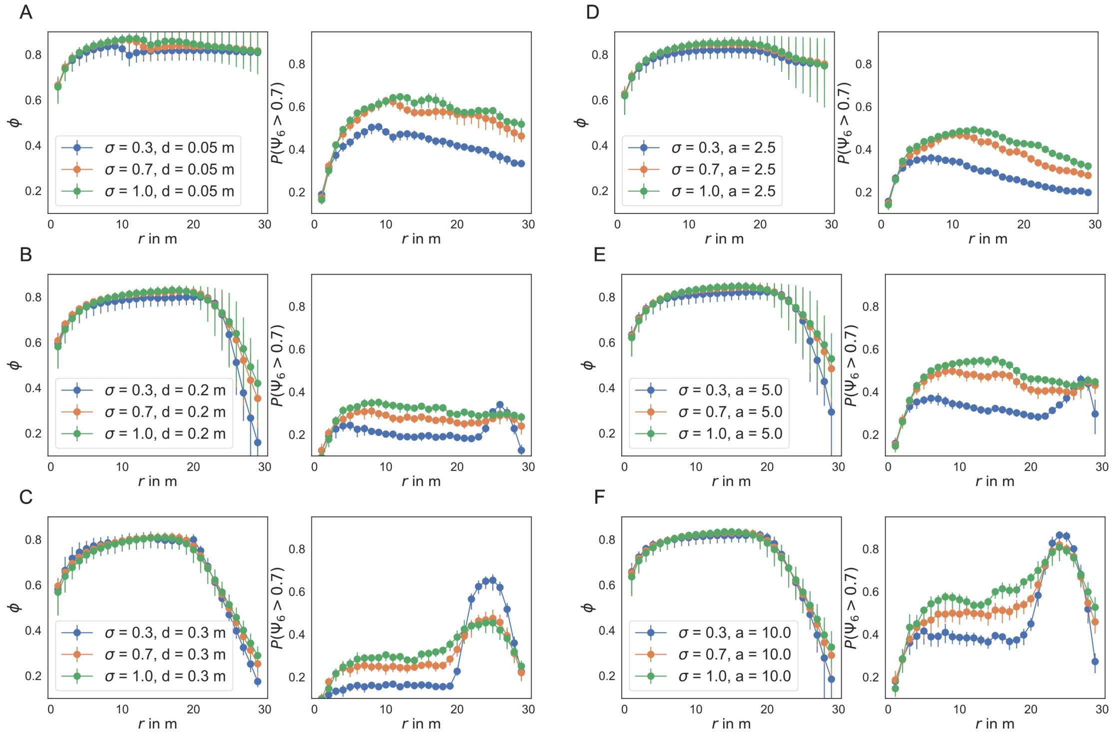

Figure 6.32: The packing fraction ϕ and hexagonal order $P(\Psi_6 > 0.7)$ with respect to the distance to the bottleneck r. The d-σ plane is depicted in panels (**A**)-(**C**) and the a-σ plane in panels (**D**)-(**F**).

the shape factor, the shape factor classes are shown in the scatter plot in Figure

6.34 for $d = 0.3$ m (A-C) and $a = 10$ (E-G). In panels A-C, the different dynamics are visible in the snapshot of the system. For $\sigma = 0.3$ the jammed hopper can be observed analogous to Figure 6.24, where the density of class C agents is high. The increased noise de solves this state, and an increase of clusters with shape class A is visible over the whole system. In panels E-G, the system already has a high number of clusters of class A for $\sigma = 0.3$, but this increases substantially, and the agents in class A dominate the system for $\sigma = 1.0$ where the clusters are connected to large areas of high hexagonal order.

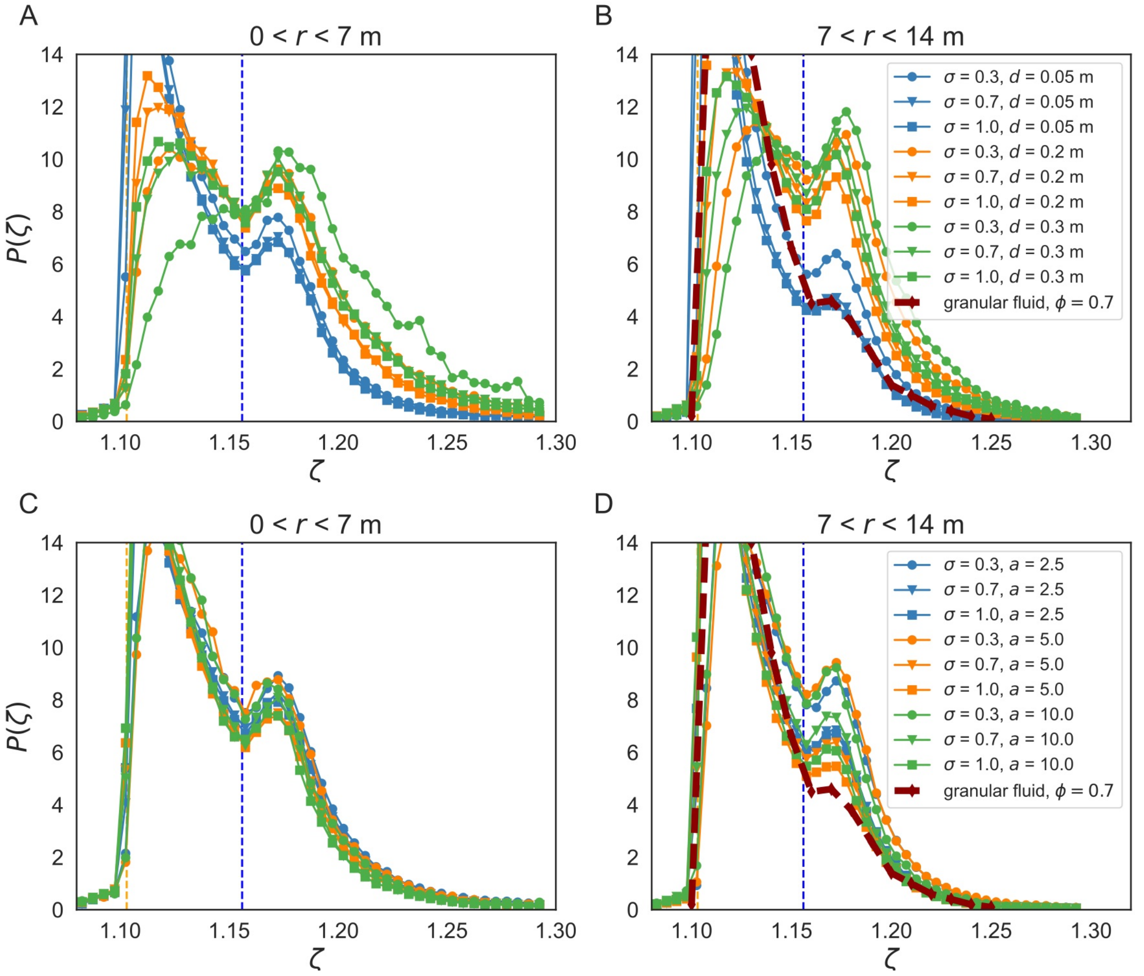

Figure 6.33: Shape factor distribution $P(\zeta)$ of the different values in the d-σ plane (**A**)&(**B**) and the a-σ plane (**C**)&(**D**). The values of the granular fluid are depicted as the red dashed line for $\phi = 0.7$.

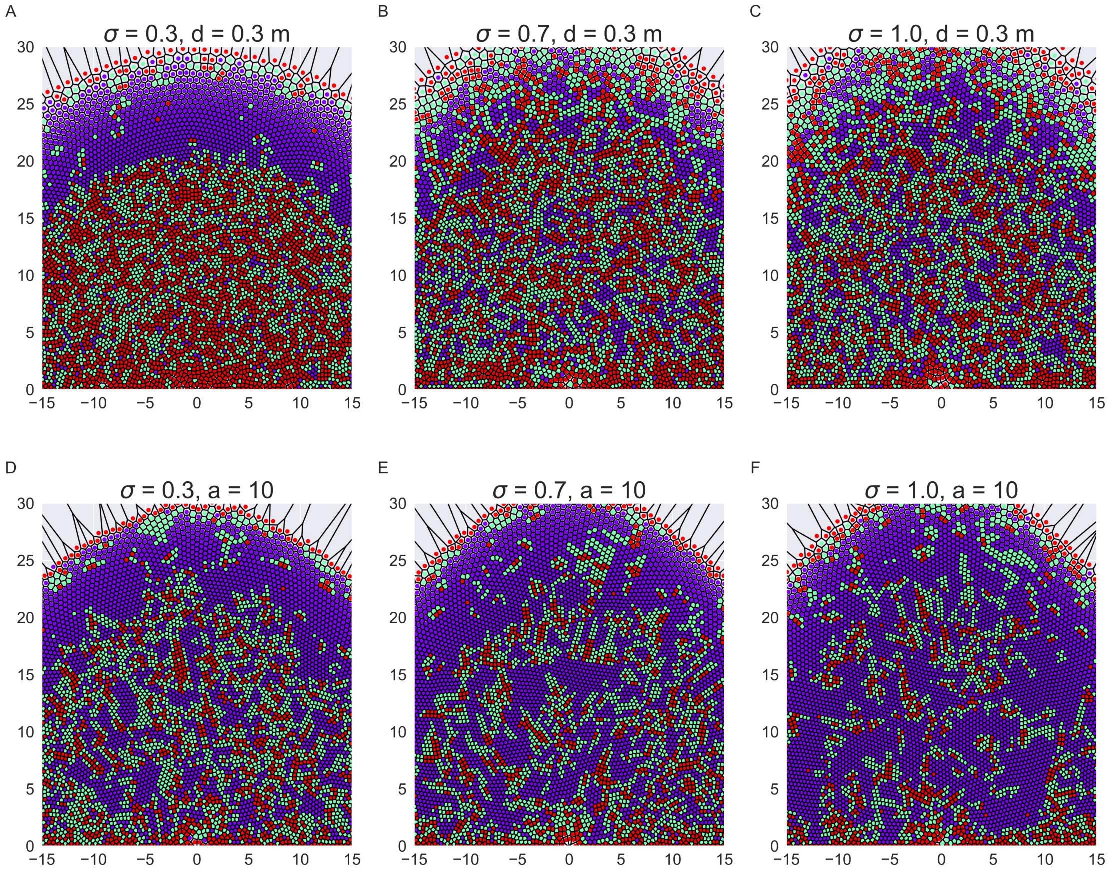

Figure 6.34: Snapshot of the simulation showing the shape classes in a system with $d = 0.3$ m and $\sigma \in \{0.3, 0.7, 1.0\}$ in panels (**A**)-(**C**) in the stationary state. Panels (**E**)-(**G**) show analogous the system with $a = 10$. The remaining variables are the same as in Table 6.1.

6.2.2 SCSM with no repulsion

To investigate the stochastic CSM (SCSM), simulations are conducted in a system, where the exponential repulsion of the agents is constant $R(s) = 0$. in this case the desired direction of the agent is determined by the floor field $\mathbf{e}_0$ (2.18) with the added noise vector ζ (2.19) (see Section 2.3 for details) analogous to the model used in Section 3. The values of σ are varied with $\sigma \in \{0.0, 0.05, 0.1, 0.2, 0.3, 0.4, 0.5, 0.7, 1.0, 2.0, 3.0, 7.0, 10.0\}$. The system's dynamics with noise slow down compared to the CSM with its exponential interaction (see Appendix A.7 Figure S24). The simulations are therefore run for $T = 10000$ s. The stationary state is taken for $t > 4000$ s. An example snapshot of the system for different σ is presented in Figure 6.35. The evolution of the dynamics is illustrated in video *noiseVarianceSCSM.mp4* [226]. For $\sigma = 0$, the system is non-stochastic apart from the random initial conditions. Because there is no exponential repulsion, the agents follow the floor field until they interact with another agent such that both their speed functions are $V(s_{i,j}) = 0$. These agents are then condensation cells where other agents get stuck, leading to the observed pattern. Increasing the noise distributes the agents more homogeneously, with no large empty zones inside the bulk of the agents. Similar to the CSM with exponential repulsion, the bulk shape changes. Between $\sigma = 0.2$ and $\sigma = 0.4$ the bulk of the agents transforms the shape, from almost rectangular to a parabola. further increasing the noise transforms the bulk shape from a parabola to a half circle for a larger noise ($\sigma = 3.0$). The increasing noise also increases the hexagonal order of the system. The hexagonal clusters grow in size, and for $\sigma = 10.0$, it is almost a single large connected cluster of high hexagonal order. Noticeably especially in the systems with large values of σ, the fraction of agents with a high hexagonal order decreases near the bottleneck substantially. In the video *noiseVarianceSCSM.mp4* [226], it is visible that the system clogs when the noise is not sufficiently large.

Clogging: Figure 6.36 A shows the clogging time fraction P_{T_c} in respect to σ for $t > 4000\ s$. There is a sharp transition in the system, wherein the measured systems for small $\sigma < 0.2$, $P_{T_c} = 1$ and for $\sigma \leq 0.2$ the clogging time fraction $P_{T_c} < 1$ and tends to zero as σ increases. This could be a phase transition, but more simulations are needed to answer this question definitively. The change in shape from the rectangular bulk to the parabola stems from the transition of the clogged system to the free-flowing system. The noise in the systems leads to the agents being able to explore a larger space around their path determined by the floor field.

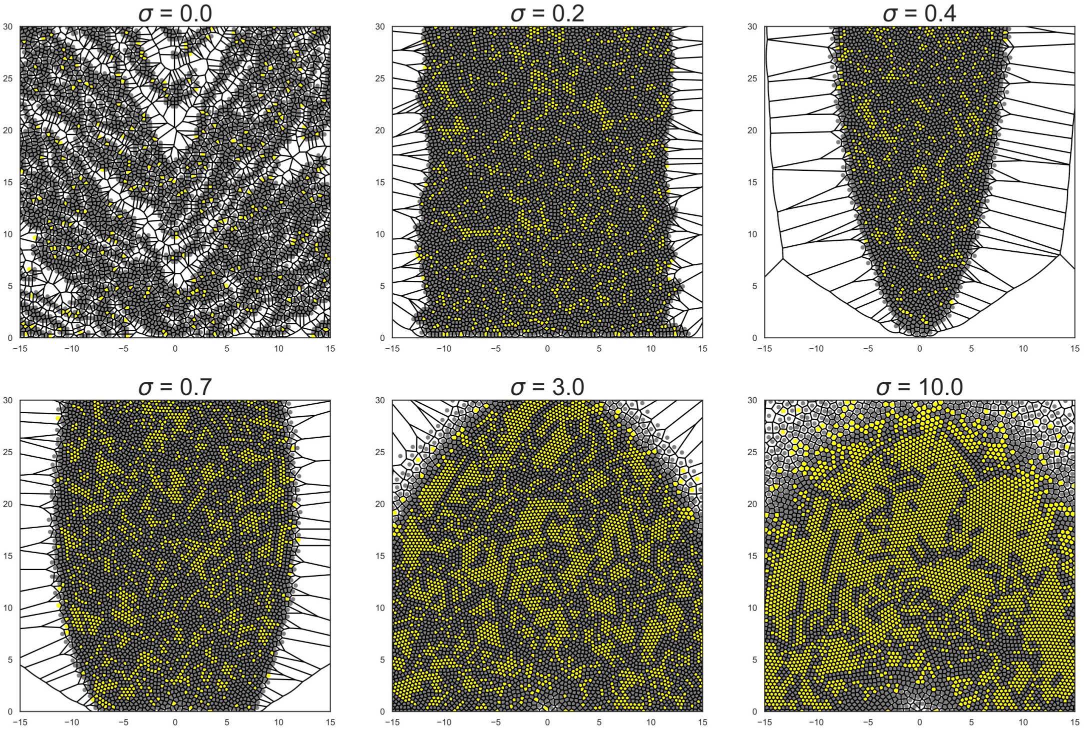

Figure 6.35: A snapshot of the simulations at $t = 9000\,\mathrm{s}$ with different σ specified in the title of the panels. Yellow agents have a hexagonal order parameter $\Psi_6 > 0.7$.

When the agents stick close to the floor field when $\sigma < 0.7$, they order themselves in the parabolic shape, while if they can explore a larger region, they can minimize their distance to the exit by ordering themselves in a half circle. To compare the structure between different σ over the space of the system,

Hexagonal order in respect to the distance from the bottleneck: Figure 6.36 B-C shows the packing fraction ϕ and the hexagonal order $P(\Psi_6 > 0.7)$ in respect to r and for different values of σ. Both in the ϕ plot (panel B) and the $P(\Psi_6 > 0.7)$ plot (panel C) the difference between the clogged states ($\sigma = 0.0$ and $\sigma = 0.05$) and the free-flowing states are visible. In the free-flowing state, the packing fraction and hexagonal order decrease towards the exit, while both values increase in the clogged state. The reason is that in the clogged state, no dynamics near the exit exist that could decrease the density and the hexagonal order. In the free-flowing state, the speed of the agents increases near the bottleneck with decreasing r, which lowers the density and pulls apart the hexagonally ordered clusters. In the free-flowing state ($\sigma \geq 0.3$ in the Figure 6.36) both the packing fraction ϕ and hexagonal order $P(\Psi_6 > 0.7)$ increase with distance to the bottleneck r. Interestingly, while the packing fraction differs with respect to σ near the bottleneck, the fraction of hexagonally ordered agents varies very little with σ and $r < 4\,\mathrm{m}$. For large $\sigma \geq 3$, the packing fraction of the system decreases at larger distances further from the bottleneck, similar to large values of a and d in the previous Section 6.1. In this case, the decreasing packing fraction also decreases the hexagonal order in the system. The reason for this effect is, in this case, not a result of the agent-agent interaction acting on the direction vector. For systems with larger noise, it is increasingly more likely that the agents will perform backward steps. In the bulk of the system, they can still pack close together since they are inhibited from moving back by other agents because it is still more likely for them to move forward. Near the boundary, this preference is weakened because fewer agents surround each other, and agents can move at a higher speed backward at the boundary. In this case, the noise decreases the hexagonal order in the system. The packing fraction in the free-flowing states increases monotonically for $\sigma < 3.0$, while the hexagonal order saturates or even decreases with increasing distance. For $\sigma = 3.0$ the maximum of $P(\Psi_6 > 0.7)$ and ϕ do not coincide, while they do for $\sigma = 10$. The relationship between ϕ, $P(\Psi_6 > 0.7)$ and σ is illustrated for different distance slices r and $r + \Delta r$ of the system in panels D and E of Figure 6.36. Panel D shows the packing fraction ϕ with respect to σ at a close, intermediate and far distance from the bottleneck. The transition from the clogged to the free-flowing state is visible as a sudden decrease in packing fraction followed by an increase with σ. The packing fraction reaches at all distant slices a maximum shifting further to higher values of σ with increasing distance to the bottleneck. The hexagonal order, in contrast, increases monotonically with σ in all distance slices after the transition. Showing that a higher density does not necessarily increase the hexagonal order. At close distances $(0.5\,\mathrm{m} < r < 3.5\,)\mathrm{m}$ the hexagonal order saturates at around $P(\Psi_6 > 0.7) \approx 0.2$ for $\sigma \geq 0.7$. At the intermediate distance the hexagonal order increases steadily and starts to saturate between $\sigma = 7$ and $\sigma = 10$ around $P(\Psi_6 > 0.7) \approx 0.42$. At the far distance, the hexagonal order is monotonically increasing in the free-flowing state and does not saturate in the simulated regime presented, reaching up to $P(\Psi_6 > 0.7) \approx 0.69$. The dynamics show that a certain density is necessary for the system to exhibit

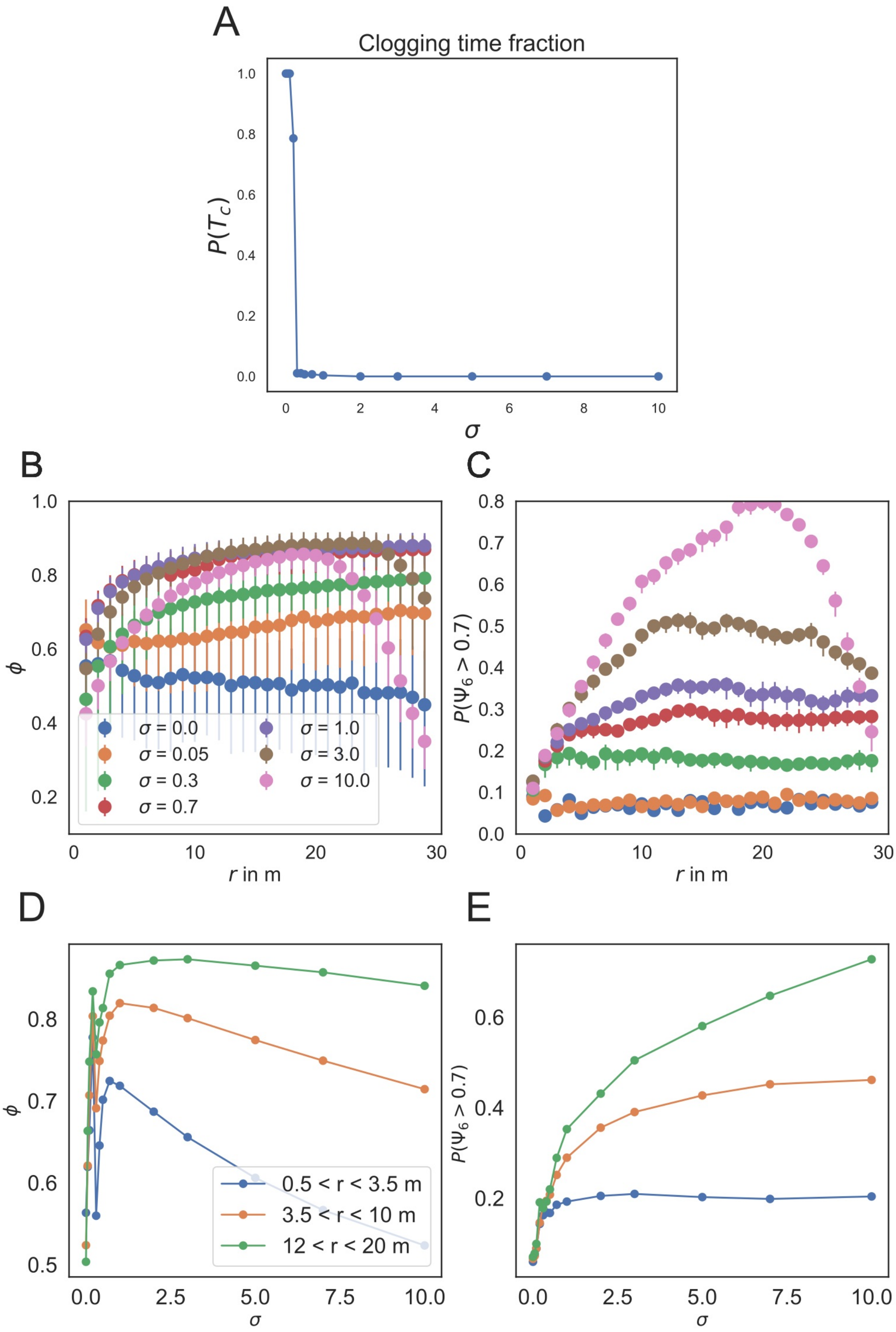

Figure 6.36: (**A**) Clogging time fraction P_{T_c} of the system in respect to σ. (**B**) Packing fraction ϕ in respect to the distance to the bottleneck r. (**C**) Hexagonal order $P(\Psi_6 > 0.7)$ in respect to r. (**D**) Packing fraction ϕ in different radial intervals in respect to σ with $|x| < 15\,\mathrm{m}$. (**E**) Analogous to D the hexagonal order $P(\Psi_6 > 0.7)$.

hexagonal order but that a higher density does not universally coincide with high hexagonal order. The packing fraction and hexagonal order at different distances r from the bottleneck and for varying values of σ are presented as a heat map in Figure 6.37. This plot comprehensibly illustrates the effects shown in panel D-E of Figure 6.36. In the plot, the landscape shows that there are single peaks for the measures in both landscapes in the observed plane beyond the transition point to free-flow. The maximum of the packing fraction is far away from the bottleneck between $(20\,\mathrm{m} < r < 25\,)$m for $2 < \sigma < 4$, while the maximum in hexagonal order is observed at $(15\,\mathrm{m} < r < 20\,)$m and $\sigma > 10$. The plot also illustrates how the noise affects the packing fraction and hexagonal order near the bottleneck ($r < 4\,\mathrm{m}$). The continuous expansion of the low packing fraction zone near the bottleneck is visible, while the slope of the hexagonal order is largely unaffected by the noise.

Shape Factor: The shape factor distribution for a subset of σ-values are depicted in Figure 6.38 A&B. The distributions are similar to the deterministic case in the sense that in the free-flowing regime for $\sigma > 0.3$, they are bi-model with a peak close to the hexagonal shape factor $\zeta \approx 1.103$ and one close to the pentagonal shape factor $\zeta \approx 1.156$. In the SCSM the peak near the hexagonal shape is sharper already for $\sigma = 0.7$ compared to the wider peaks that are observed in the CSM (e.g. see Figure 6.16, 6.23). The transition of the shape factor distribution with increasing σ is similar to the two-dimensional granular fluid in [188] depicted in panel B of Figure 6.38. At low packing fractions $\phi = 0.55$ the granular system has a similar wide distribution towards larger values of ζ as the system with $\sigma = 0.1$. At higher noise values, the agent system has the bimodal distribution with sharper peaks compared to the granular system at $\phi = 0.65$. For higher packing fractions, the second peak disappears in the granular system near $\zeta = 1.156$, while the agent's system has a sharper peak near the hexagonal order and a smaller peak near the pentagonal value. The evolution of the shape factor with σ in the stationary state is shown in the heat map in panels C and D. The transition from the clogged state to the free-flowing state is especially visible close to the bottleneck, where the distribution shifts from a wide peak around $\zeta = 1.225$ to a narrower peak around $\zeta = 1.175$. The continuous shift towards the hexagonal shape factor can be observed for increasing σ in the free-flowing state and the continuous decrease of the second peak. The fraction of the shape classes p_s, $s \in \{A, B, C\}$ in panels E and F of Figure 6.38 further illustrate the effect of the noise on the shape factor. Near the bottleneck

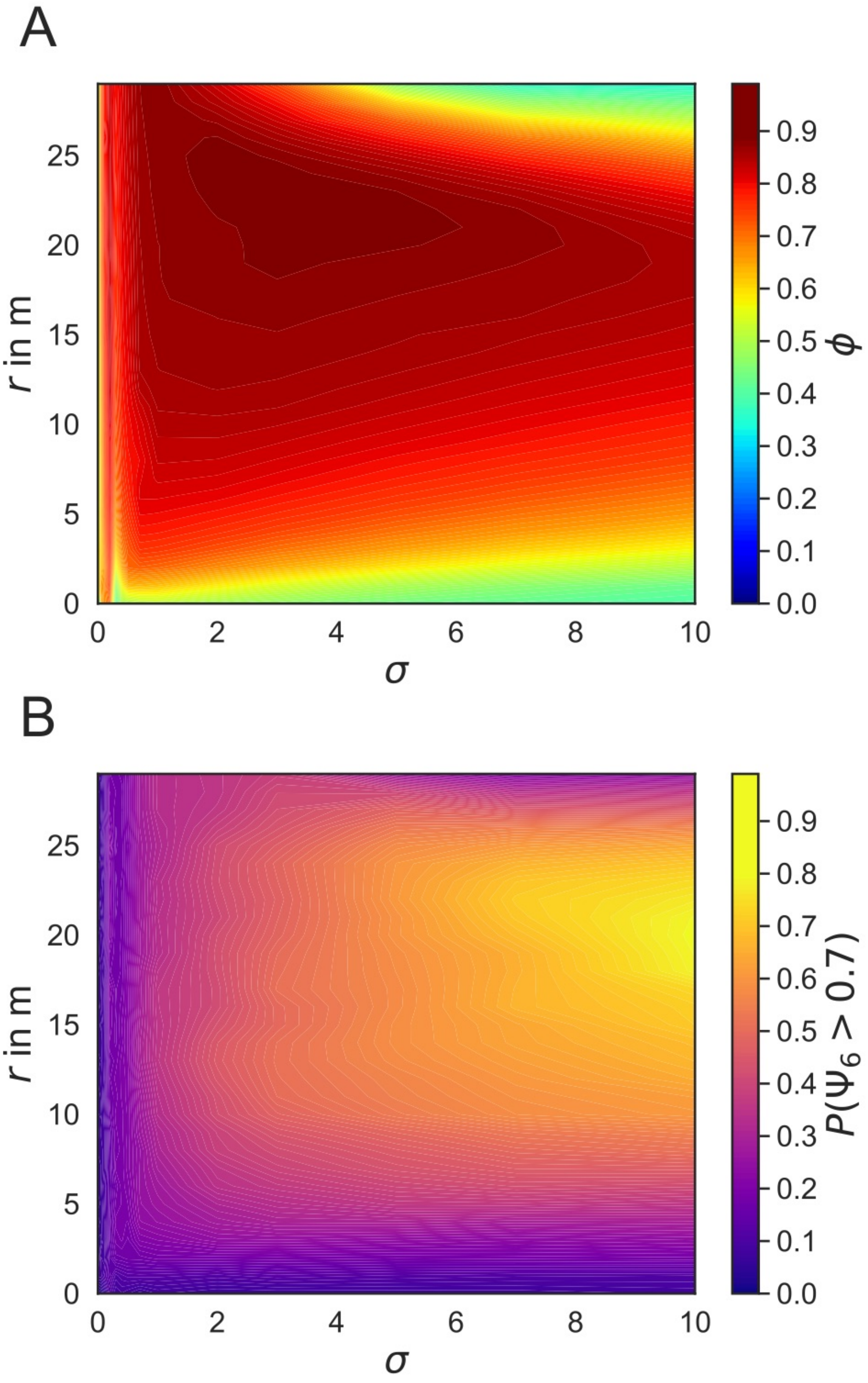

Figure 6.37: (**A**) Heat map of the packing fraction ϕ at distance r from the bottleneck for $t > 4000\,\mathrm{s}$ in respect to the noise σ. (**B**) Analogous to A, the fraction of hexagonally ordered agents $P(\Psi_6 > 0.7)$.

(panel C) the noise increases both p_A and p_B with increasing σ, while p_C decreases. Far from the bottleneck, only the fraction p_A of the hexagonal order increases, while p_B and p_C decrease. There the hexagonal class dominates the system when $\sigma \leq 2$ Near $\sigma = 0$ the system starts with a majority of the system in shape class C with $p_C > 0.9$, and decreases steeply with increasing σ. A snapshot of the shape classes in the Voronoi-scatter plot is depicted in Appendix A.7 Figure S23.

The reason noise increases order: The system favors a hexagonal order with large noise values due to the interactions between the agents in the system. This can be illustrated in an one-dimensional example in Figure 6.39. When the agent density is sufficiently large, the speed to the left and right is limited by the speed function (2.14), which linearly decreases with the neighbor distance. In the one-dimensional system, the agent can only choose to get to the left or right. If this choice is done at random with equal probability $p_{\text{right}} = p_{\text{left}} = 0.5$, the agents tends to not deviate far from the position of equal distance to its neighbors. The reason is that in a system with sufficient density (meaning that the speed dependence is in the linear regime of equation (2.14), the speed of the agents is larger in the direction of the neighbor that is further away. Therefore the agent will tend to move closer to the center of its two neighbors. The same is true in two dimensions; for disc-shaped agents, which tend to a hexagonal configuration. In the case of the bottleneck scenario, the agents are biased towards the bottleneck exit; therefore, the direction probability is not symmetric in the space. In the one-dimensional case, if a bias two one direction is present, the equilibrium position would not be the center between the neighbors but offset into the direction of the bias since the bias would negate the slower speed into the more preferred direction to a certain extent. A directional bias also increases the density of the system. In a system with equal probability to the left and right, a cluster of agents would diffuse apart from each other if there are no boundaries inhibiting their movement. In the case of a directional bias paired with a bottleneck that slows down the agent movement in the preferred direction, the system's density will increase. Still, the order (equal distance to the neighbors) will decrease. This explains why the packing fraction maxima in Figure 6.37 do not correspond to the hexagonal order maxima.

The equilibrium position of the agent in the one-dimensional system is determined by the product $p_l V(d_l)\Delta t$ of the probability p_l to move left and the distance $V(d_l)\Delta t$ traversed in the time interval Δt with the one-dimensional speed-function $V(d_l) =$

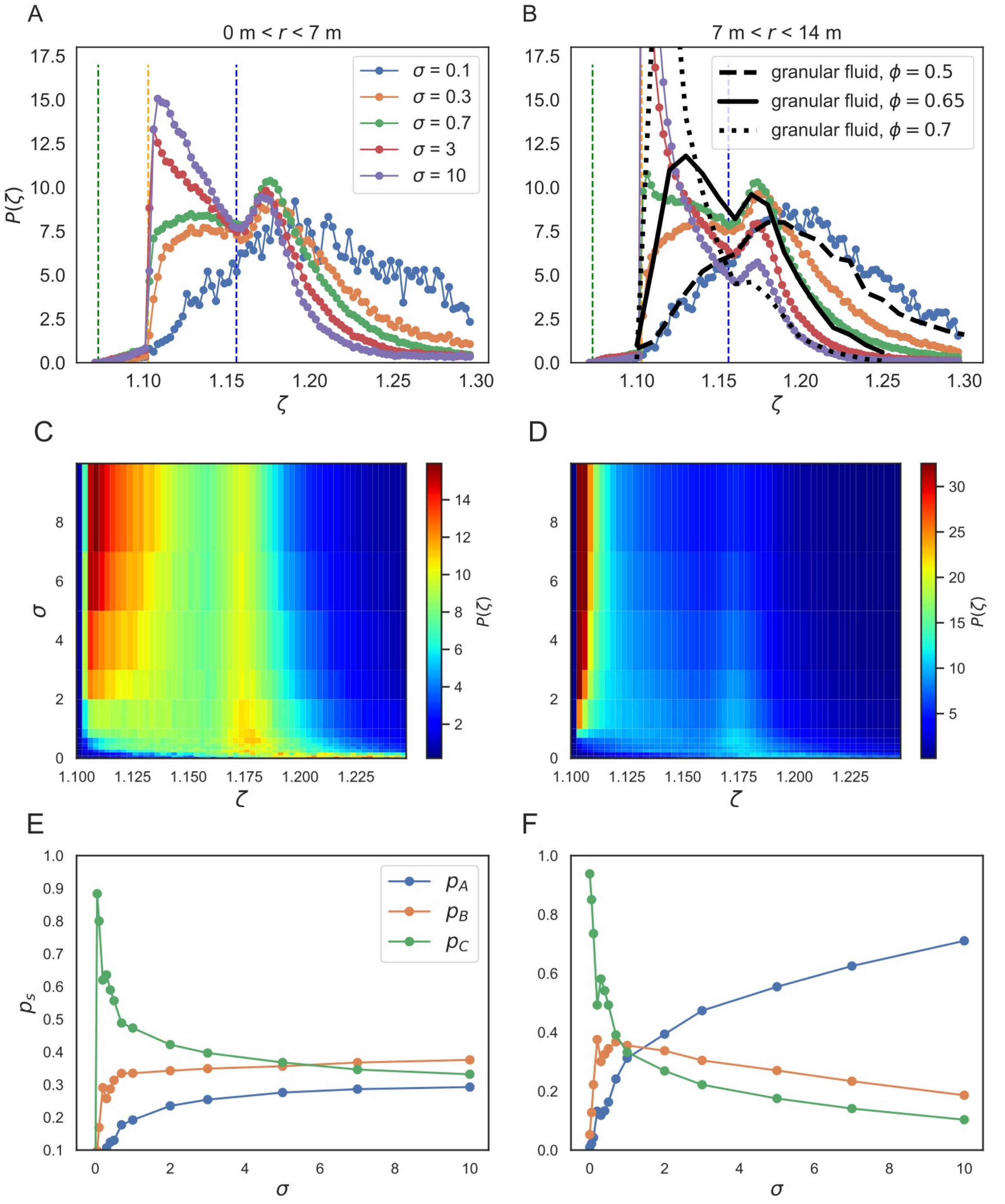

Figure 6.38: (**A**) Distribution of the shape factor close to the bottleneck ($0\,\mathrm{m} < r < 7\,\mathrm{m}$) for different values of σ. (**B**) Analogous to A far from the bottleneck ($12\,\mathrm{m} < r < 20\,\mathrm{m}$). The black lines show the distribution of the granular fluid in [188]. The vertical lines show ζ of the regular heptagon (green), hexagon (yellow), and pentagon (blue). (**C**)&(**D**) Heat map of the shape factor distribution $P(\zeta)$ on the σ-ζ plane. (**E**)&(**F**) The fraction p_s of the three shape classes $s \in \{A, B, C\}$ in the system. The distance from the bottleneck is equal to A and B, respectively.

d_l/T and d_l the distance to the left neighbor. When this is equal to the analogous product $p_r\, V(d_r)\, \Delta t$ of the probability p_r to go right and the distance d_r to the right neighbor, the equilibrium position is reached.
The variable T is the slope factor introduced in (2.14). Rewriting the probability $p_l = p$ and $p_r = 1 - p = \alpha p$, with $\alpha = (1-p)/p$ the equilibrium position is

$$d_l = \alpha\, d_r. \tag{6.8}$$

Knowing the total distance $d = d_l + d_r$ between the left neighbor and the right one, the distance to the right neighbor can be rewritten as

$$d_r = \frac{d}{1+\alpha}. \tag{6.9}$$

The variance of the position is not straightforward to calculate, because the final position of the agent after t_{max} time steps depends on the path taken by the agent. In the standard case of a random walk with Bernoulli trials, where the variance $\mathrm{var}(x(t_{max})) = 2\, t_{max}$, with $X(t_{max})$ the position after t_{max} time steps increases linearly and quadratically with the step length s. Because of the self-correcting feature in the one-dimensional SCSM, the variance saturates after some time. In

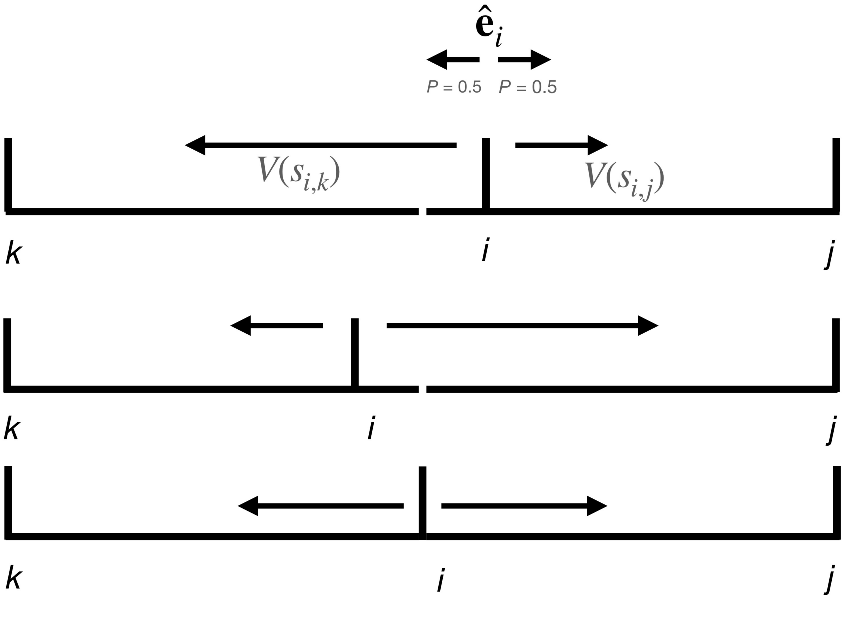

Figure 6.39: Illustration of a one dimensional random walk, where agent i interacts with its static neighbors through the speed function (2.14).

Figure 6.40 A the variance $\mathrm{var}(X(t_{max}))$ of the postion X of the agent after t_{max} time steps of a simulation are shown for different values of T. The system is simulated with $d = 1$, starting position $d_l = d_r = 0.5$, $p_l = p_r = 0.5$ and $\Delta t = 0.01$ s and is repeated 2000 times. The plot shows that the variance of the position $X(t_{max})$ saturates at around $t_{max} = 5000$ s. In panel B the dependence of the variance on the slope factor T is presented. For this the simulations are run for $t_{max} = 20000$ s. The variance of the agents position $\mathrm{var}(X(t_{max}))$ in respect to T follows a power law and decreases with increasing T. The reason is that for smaller values of T the agent's speed increases more steeply with distance to the neighbors, which increases the step size near the equilibrium position.

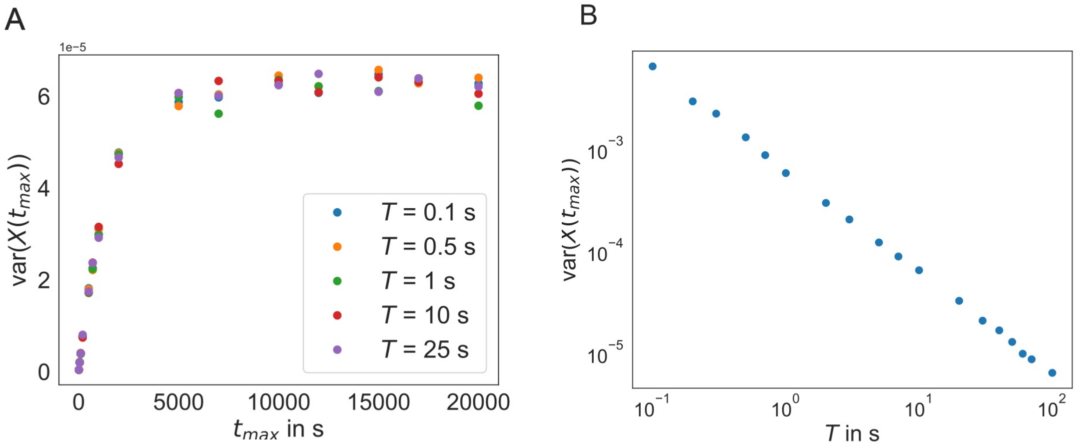

Figure 6.40: (**A**) Variance in the position of the one-dimensional SCSM with static neighbors (see Figure 6.39) after a runtime of $t = t_{max}$, starting in an equidistant position. (**B**) Variance after $t_{max} = 20000$ s on the y-axis with respect to the slope factor T on the x-axis.

Discussing two specific noise strengths: The following discusses the time evolution of two systems with $\sigma \in \{0.7, 3.0\}$. The snapshot at different times is depicted in Figure 6.41. Yellow agents have an hexagonal order parameter $\Psi_6 > 0.7$ and the green and red color show the coordination number $N_n > 6$ and $N_n < 6$ respectively analogous to Figure 6.1. At $t = 40$ s the density of hexagonal order in the system with $\sigma = 3$ is still low, compared to the case with $\sigma = 0.7$ where the packing fraction is visibly higher (indicated by the smaller Voronoi cells). In both cases, the density of 5-7 fold defects is still high. At $t = 400$ s the system with $\sigma = 0.7$ has already a high packing fraction and is close to the final urn shape. In contrast, in the system with $\sigma = 3$, the packing fraction gradient is still visible, with a considerably lower packing fraction far from the bottleneck. Still, the system has a high fraction of hexagonal order with large clusters of ordered agents. Closer to the bottleneck ($5\,\mathrm{m} < r < 10\,\mathrm{m}$) grain boundaries separate the smaller hexagonal clusters. The system evolves into this structure over time, illustrated in the panel at $t = 4000\,\mathrm{s}$. The system with $\sigma = 0.7$ exhibits a higher order at $t = 40\,\mathrm{s}$ compared to the stationary state at $t = 4000\,\mathrm{s}$. The dynamics can be observed in more detail in the video *noiseVariance307SCSM.mp4* [226].

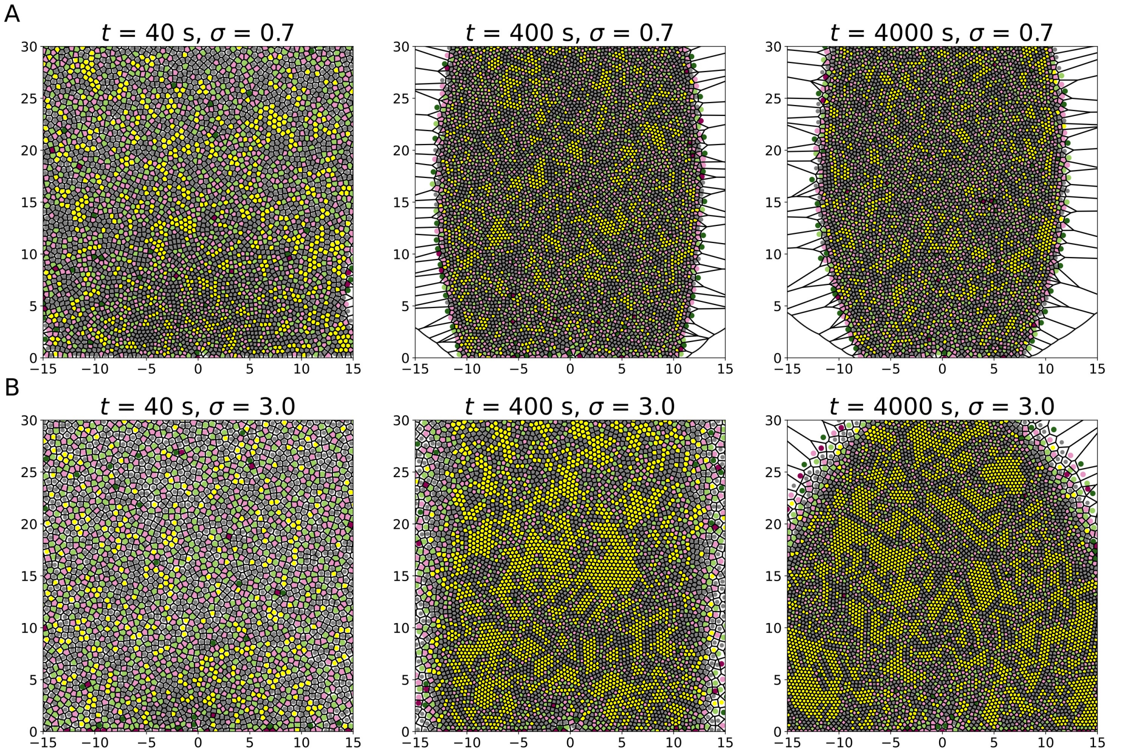

Figure 6.41: Snapshots of the system with $\sigma = 0.7$ (**Row A**) and $\sigma = 3$ (**Row B**). The yellow agents have a value for the bond orientation factor $\Psi_6 > 0.7$. The red and green agents have a coordination number $N_n \neq 6$, see Figure 5.2. The systems are presented at different times t specified in the title of the panels.

The time series of the different measures is shown in Figure 6.42, of the system with $\sigma = 0.7$ in panels A-D and $\sigma = 3$ in panels E-H. The plots show the measures of the hexagonal order $P(\Psi_6 > 0.7)$ (A and E), the fraction of agents with coordination number $P(N_n = 6)$ (B and F), the packing fraction ϕ (C and G) and the no-noise speed V_{nn}. The plots show the measure close to the bottleneck ($0\,\mathrm{m} \leq r < 3.5\,\mathrm{m}$), at a medium distance $(3.5 \leq r \leq 10)$ m and far away $12\,\mathrm{m} \leq r \leq 20\,\mathrm{m}$ (D and H). Comparing panels A-D with $\sigma = 0.7$ to E-H with $\sigma = 3.0$ illustrates that the time evolution of the different measures is qualitatively rather similar. For instance, the measure of the hexagonal order (A and E) shows a peak early on in the system at the medium distance that decreases into the stationary state. At the far distance both system show a wider maximum before $t = 2000$ s that decreases slightly between $(2000\,\mathrm{s} < t < 5500)$ s and increases again. At close distances both systems quickly relax into the stationary state with $P(\Psi_6 > 0,7) \approx 0.2$. Analogous is the evolution of the coordination number fraction $P(N_n = 6)$. A subtle difference between the systems is a small peak in the $\sigma = 0.7$ system (in $P(\Psi_6 > 0.7)$ and $P(N_n = 6)$) around $t \approx 80$ s, overlaying with the peak at medium distance.

The packing fraction ϕ and the no-noise speed V_{nn} are shown in panel C, G and D, H. Qualitatively V_{nn} is inversely proportional to the packing fraction $V_{nn} \propto \phi^{-1}$, since the speed function (2.14) is linearly dependent on the distance to the closest agent in the headway (2.5). The aforementioned high-order peaks in both systems coincide with a high packing fraction and a low speed. The speed and density plot also show how the dynamics shift from the beginning of the system's evolution to later stages. This is especially visible in the $\sigma = 3$ case. In the beginning, the system's density is lower, further away from the system in the density-increasing phase. After some time ($t \approx 100\ s$), the relationship flips, and the system reaches the maximal packing fraction far away from the bottleneck. The decrease in packing fraction and increase in speed are caused by the stationary outflow of pedestrians at the bottleneck. Because of continuity, the speed increases towards the bottleneck. Figure 6.43 shows this dynamic over the whole system as an r-t heat map. The map illustrates the different measures $P(\Psi_6 > 0.7)$ (A and D), $P(N_n = 6)$ (B and E) and ϕ (C and F), where the colour represents the value of the measure. The speed is omitted because of the inverse relationship between the speed and the packing fraction. The comparison between the noise levels shows that the system's dynamics exhibit the same features. For $t < 4000$ s, a wave of increasing order and packing fraction travels through both systems, followed by a valley of decreasing hexagonal order and packing fraction. The difference is (apart from the absolute values of the measures) that the wave speed is higher in the system with $\sigma = 0.7$ compared to $\sigma = 3.0$. After that, the system stabilizes into the stationary state. The plots also show that while the order measures go through a valley after the initial increase, the packing fraction does not exhibit the same behavior. This is especially visible in the evolution of the packing fraction for $\sigma = 0.7$, where the system stabilizes to a stationary state after the initial wave of high packing fraction. The lines in panels D and F illustrate the speed of the high hexagonal order wave and the packing fraction wave. They are fitted heuristically to illustrate that both waves propagate with different velocities through the system. The slope of the hexagonal order line is $m = 1/120\,\mathrm{m/s}$ while for the packing fraction the wave moves approximately with $m = 1/100\,\mathrm{m/s}$.

6.2.3 Packing Fraction and hexagonal order in the SCSM

To get a better understanding of the relationship between the packing fraction of the system and the hexagonal order, $P(\Psi_6 > 0.7)$ is plotted against ϕ at certain distances from the bottleneck $r < r < r + \Delta r$ with $\Delta r = 1$ m, at different time intervals $t_0 < t < t_1$. The results are shown in Figure 6.44 for the system with $\sigma = 3$, but are analogous for $\sigma = 0.7$ (See Appendix A.7 Figure S25) on a different time scale. At the beginning of the simulation, one can observe two sequences in the $P(\Psi_6 > 0.7)$-ϕ space, traversing from a low packing fraction and low hexagonal order region of the space to high hexagonal order and high packing fraction region. The two sequences can be separated into areas close to the bottleneck (blue dots) and far away from the bottleneck (green-red dots). This is especially visible at $250\text{s} \leq t \leq 270\text{s}$. Depending on where in the system one measures the packing fraction and order, one can be in two different locations on the order-packing fraction space for the same value of ϕ. Over time the branch far from the bottleneck contracts to a small region. The branch close to the bottleneck stabilizes into a linear relationship. An important difference between the two branches is how the packing fraction changes over the space. Close to the bottleneck, the packing fraction increases with increasing distance to the bottleneck. At the earlier time stages ($t \leq 530$ s), there is a maximum at a certain distance from the bottleneck, where the packing fraction decreases with distance r from the bottleneck. Since the speed is connected to the packing fraction, the agents far from the bottleneck decrease their speed as they move closer to the bottleneck, which allows them to form hexagonal structures, increasing $P(\Psi_6 > 0.7)$ and ϕ over time. In contrast, any structure is pulled apart with the increasing speed of the agents near the bottleneck. At $8000\text{ s} \leq t \leq 9000\text{ s}$, there is a linear relationship between the packing fraction and the hexagonal order of the system, as the region

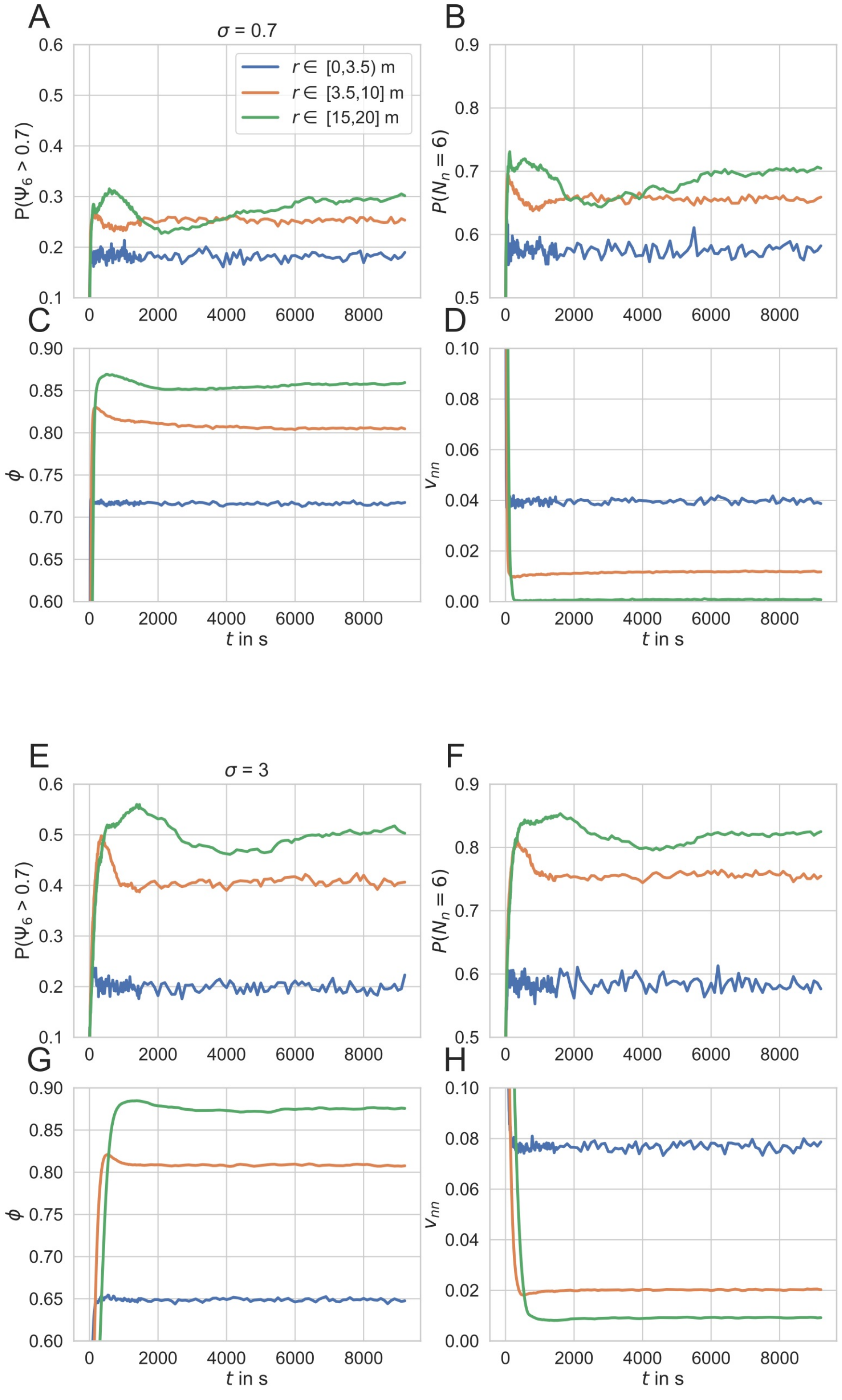

Figure 6.42: Time series of the hexagonal order $P(\Psi_6 > 0.7)$ (**A**)&(**E**), fraction of the coordination number $P(N_n = 6)$ (**B**)&(**F**), packing fraction ϕ (**C**)&(**G**), and no-noise speed V_{nn} (**D**)&(**H**), for the system with noise strength $\sigma = 0.7$, (A-D) and $\sigma = 3$, (E-H). The measures are taken at three distant intervals $r + dr$ from the bottleneck specified in the legend with $|x| < 15\,\mathrm{m}$.

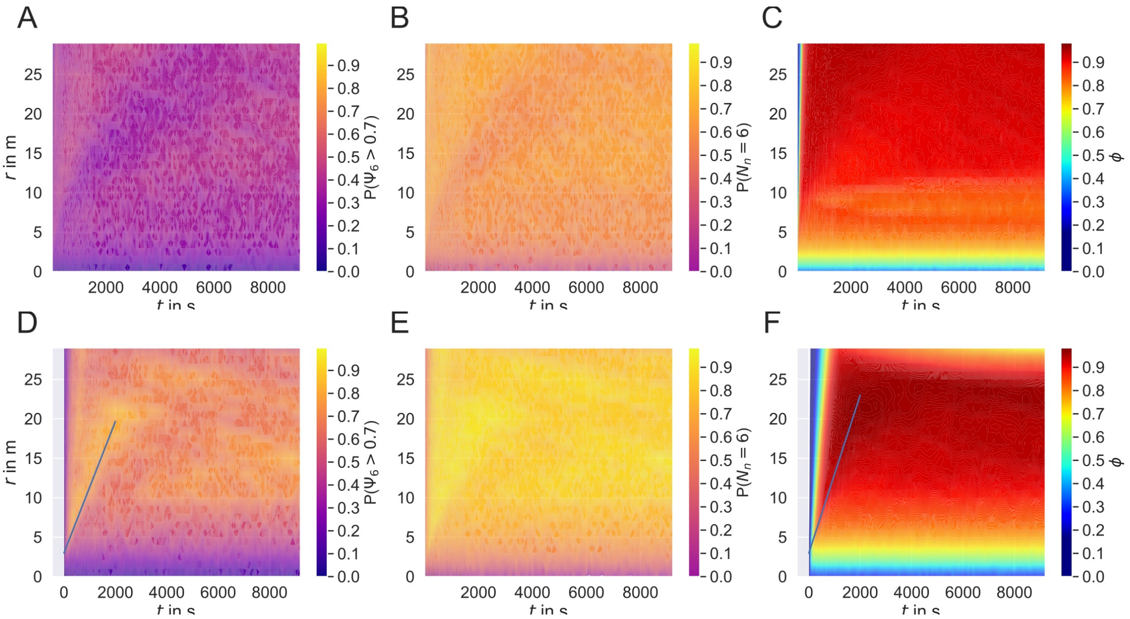

Figure 6.43: Heat map of the measures $P(\Psi_6 < 0.7)$ (**A**)&(**D**), $P(N_n = 6)$ (**B**)&(**E**) and ϕ (**C**)&(**F**) on the r-t plane. (A)-(C) show the system with $\sigma = 0.7$ and (D)-(E) for $\sigma = 3$.

far from the bottleneck contracted and has a mostly static packing fraction. The evolution of the plot illustrates that the density is only part of the influence on the hexagonal order.

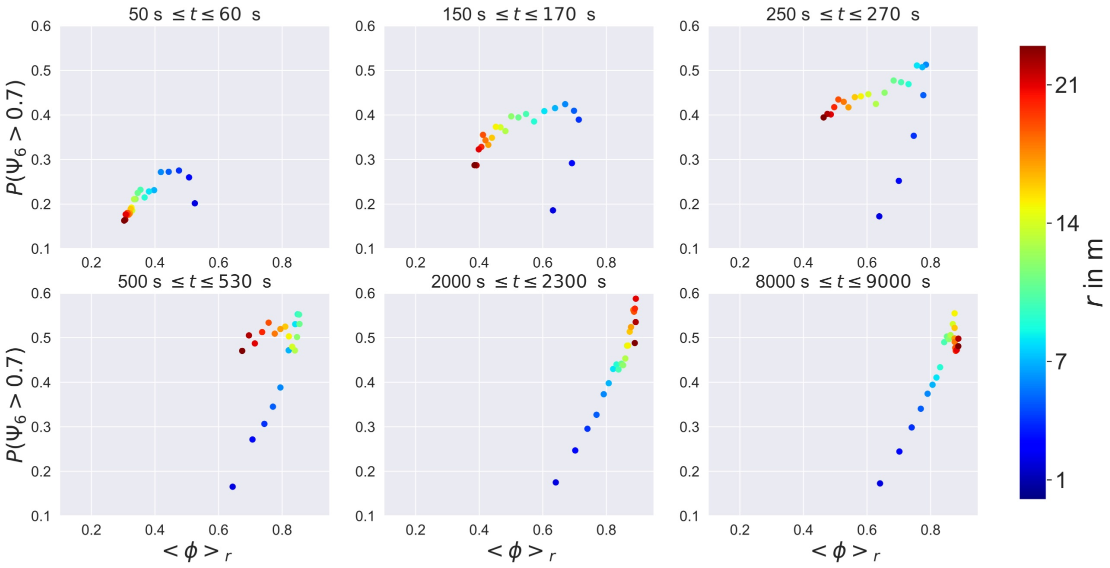

Figure 6.44: Plot of the hexagonal order $P(\Psi_6 > 0.7)$ in the system with $\sigma = 3.0$ in respect to the packing fraction ϕ at different times of the simulation and different distance intervals $r + \Delta r$ from the bottleneck indicated by the color. The value of $\Delta r = 1$ m and the time intervals are indicated in panel titles.

This can be further analyzed when investigating the trajectory of the points in Figure 6.44 over time on the hexagonal order-packing fraction plane for $\sigma = 3$. For a subset of distance intervals this is shown in Figure 6.45 A&B. The colors of the points represent the distance interval to the bottleneck, where the observables are measured. The system starts in a low packing fraction and hexagonal order state. The plot shows that in the beginning of the simulation, at all distances, the hexagonal order increases monotonically with the packing fraction until $\phi \approx 0.67$. Starting from that point, the trajectory of the hexagonal order at $r = 15$m decreases with increasing packing fraction. The same can be observed for further distances around $\phi \approx 0.72$. The trajectories exhibit interesting behavior at a large packing fraction, $\phi > 0.7$. After the phase of decreasing order for $r > 15$ m, a steep increase occurs at the highest observed packing fractions of the system, followed by an equally steep decrease. The systems oscillates in a band of ϕ between $0.43 < P(\Psi_6 > 0.7) < 0.56$ depending on the distance from the bottleneck. Close to the bottleneck ($r = 10$ m and $r = 5$ m), the system does not exhibit the initial decrease before oscillating at the high packing fraction zone. For $r = 5$ m, the increase is linear with ϕ. This illustrates that the packing fraction and hexagonal order are not stationary after the same time passed in the system. The ϕ-wave moves quicker than the hexagonal order wave. A visual representation of the order wave in the order field $\Psi_6(\mathbf{r})$, density field $\rho(\mathbf{r})$ and the speed field $V_{nn}(\mathbf{r})$ is shown in the video *noiseFieldTimeSeriesSCSM.mp4* [226]. Snapshots of this video and the description of the panels are presented in Appendix A.7 Figure S27. In the video the hexagonal order is highlighted between $0.6 < \Psi_6 < 0.7$, meaning that $\Psi_6 > 0.7$ is represented as bright yellow spots and $\Psi_6 < 0.6$ as dark purple spots. The video shows the formation of a ring with high hexagonal order at around $t = 500$ s. From there on, for $t > 500$ s, the wave-like decrease of the Ψ_6 can be observed, while the density and speed reach their stationary state, illustrating the delayed response of the hexagonal order on the changes in the speed and density fields of the system. The relationship between the packing fraction ϕ and the hexagonal order in the system can be further analyzed using the definition of the mean packing fraction $\langle\phi\rangle$. The system is sliced into distance intervals $r + \Delta r$ from the bottleneck with $\Delta r = 1$ m. The mean packing fraction $\langle\phi\rangle$ in the slices is calculated over the time evolution in the system and rounded to the second digit to define mean packing fraction classes ϕ_c. Figure 6.46 shows the distribution of the ϕ of agents in the same mean packing fraction class $P(\phi|\langle\phi\rangle = \phi_c)$ at different distance intervals specified in the title. The

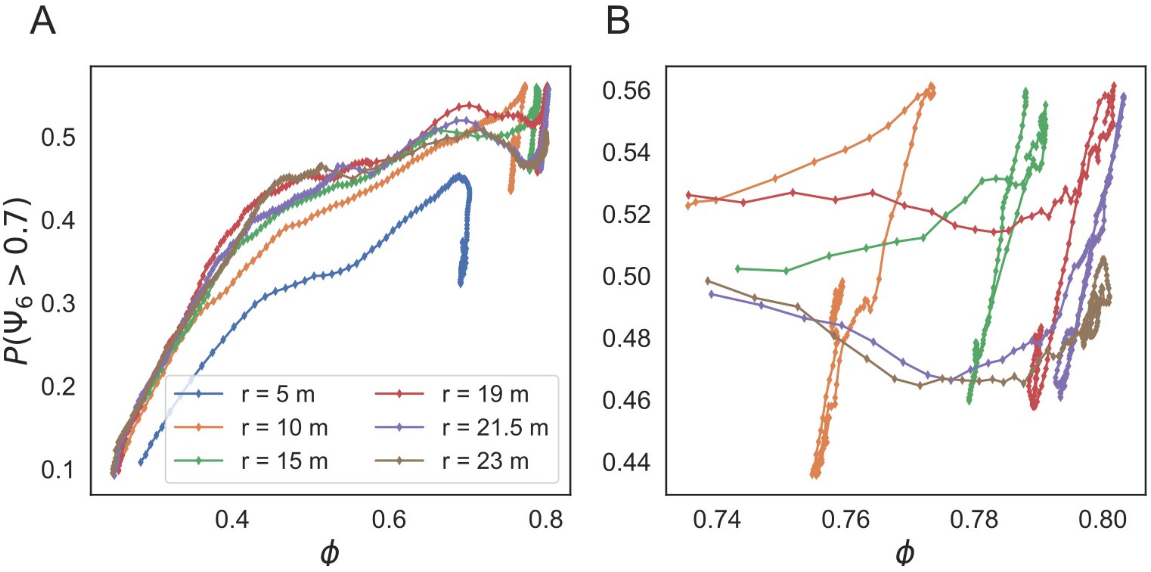

Figure 6.45: The hexagonal order $P(\Psi_6 > 0.7)$ in respect to the packing fraction ϕ at different distances r from the bottleneck with $\sigma = 3$. The dots show the time evolution of the system, where each dot is one point in time on the space. (**A**) shows the entire trajectory and (**B**) shows the interval $\phi > 0.74$.

distribution at all distances has Gaussian shapes when they are not too close to the maximal packing fraction of $\phi_{max} \approx 0.9$. Near ϕ_{max}, the distribution is skewed to the right. Close to ϕ_{max}, the distribution depends on the order in the system since only the hexagonal order clusters can achieve the maximal ϕ_{max}, skewing the distribution. Figure 6.47 shows analogously the mean hexagonal order $\langle \Psi_6 \rangle$ with respect to ϕ of the agents in the aforementioned mean packing fraction classes at the same distance intervals. Outliers in the plots are filtered by the density distribution, only considering agents in the 95% interval of the distribution $P(\phi | \langle \phi \rangle = \phi_c)$. The plot shows the relationship between the hexagonal order and the packing fraction close ($0\,\text{m} < r < 10\,\text{m}$) and far ($12\,\text{m} < r < 17\,\text{m}$) from the bottleneck. Far from the bottleneck is a clear, mostly monotonic and nonlinear relation between ϕ and the Ψ_6. The maximal hexagonal order of the system correlates with the ϕ. Close to the bottleneck, the correlation is not as clear, especially for lower packing fractions. Surprisingly, the mean hexagonal order at higher packing fractions decreases at the edge of the distribution. For a large enough packing fraction, $\langle \phi \rangle > 0.6$ the relationship between the $\langle \Psi_6 \rangle$ and ϕ are very similar in their respective packing fraction class, though the shape of the function $\langle \Psi_6 \rangle(\phi)$ shifted by the value of the mean $\langle \phi \rangle$ differs. Using the transformation of the central limit theorem (CLT) for every individual agent

$$\phi_i^* = \frac{\sqrt{n}(\phi_i - \langle \phi \rangle)}{\text{std}(\phi)}, \tag{6.10}$$

a rescaled version of the packing fraction distribution can be analyzed. With $n = 1$, the new distribution $P(\phi^*)$ is shown in Figure 6.48 C for selected packing fraction classes shown in panel A between $0.55 < \langle \phi_c \rangle < 0.8$. The distribution of the transformed packing fractions $P(\phi^*)$ fall close together and are already approximating a standard normal distribution even though $n = 1$. Comparing the mean hexagonal bond orientation $\langle \Psi_6 \rangle$ in panel B for the packing fraction ϕ and panel D for ϕ^*, the different curves do not fall onto each other, especially for $\phi^* > 0$. What is noticeable is that the data points follow the shape of a sigmoid function, starting with their min value at $\langle \Psi_6 \rangle \approx 0.5$ and saturating at $\langle \Psi_6 \rangle = 1.0$. Fitting a logistic function of the form

$$g(x) = \frac{0.5}{1 + \exp(-k_0(x - x_0))} + 0.5 \tag{6.11}$$

approximates well to the measured data points of $\langle \Psi_6 \rangle(\phi^*)$ (see black lines in panel D of Figure 6.48). The fit parameter k_0 and x_0 in respect to the $\langle \phi \rangle$ are shown in Figure 6.49 A and B. The fit parameter k_0 in respect to $\langle \phi \rangle$ can be well described by a power law $k_0(\langle\phi\rangle) = ax^b$ with $a \approx 4.52 \pm 0.11$ and $b \approx 3.72 \pm 0.09$. For $\langle\phi\rangle < 0.7$ the value of the fitting parameter x_0 is also well described by a power law with $a \approx 0.25 \pm 0.011$ and $b \approx -3.46 \pm 0.11$. For $\langle\phi\rangle > 0.7$, x_0 is nearly static around $x_0 \approx 0.52$, meaning there is a shift in the sigmoidal character of the function that approaches a constant value near the maximal packing fraction.

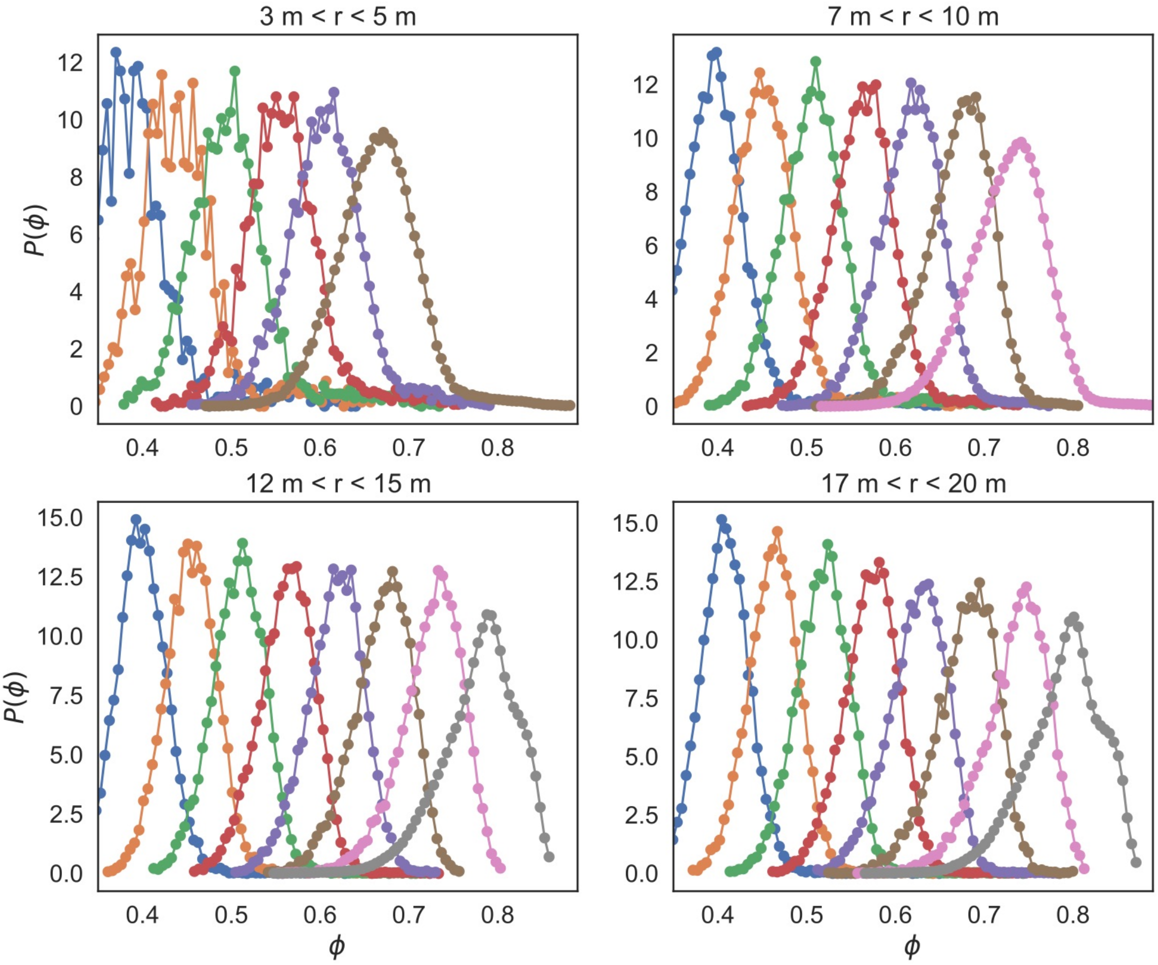

Figure 6.46: Distribution $P(\phi)$ of the packing fraction of agents that are in the same mean packing fraction class in the distance interval specified in the title of the panels.

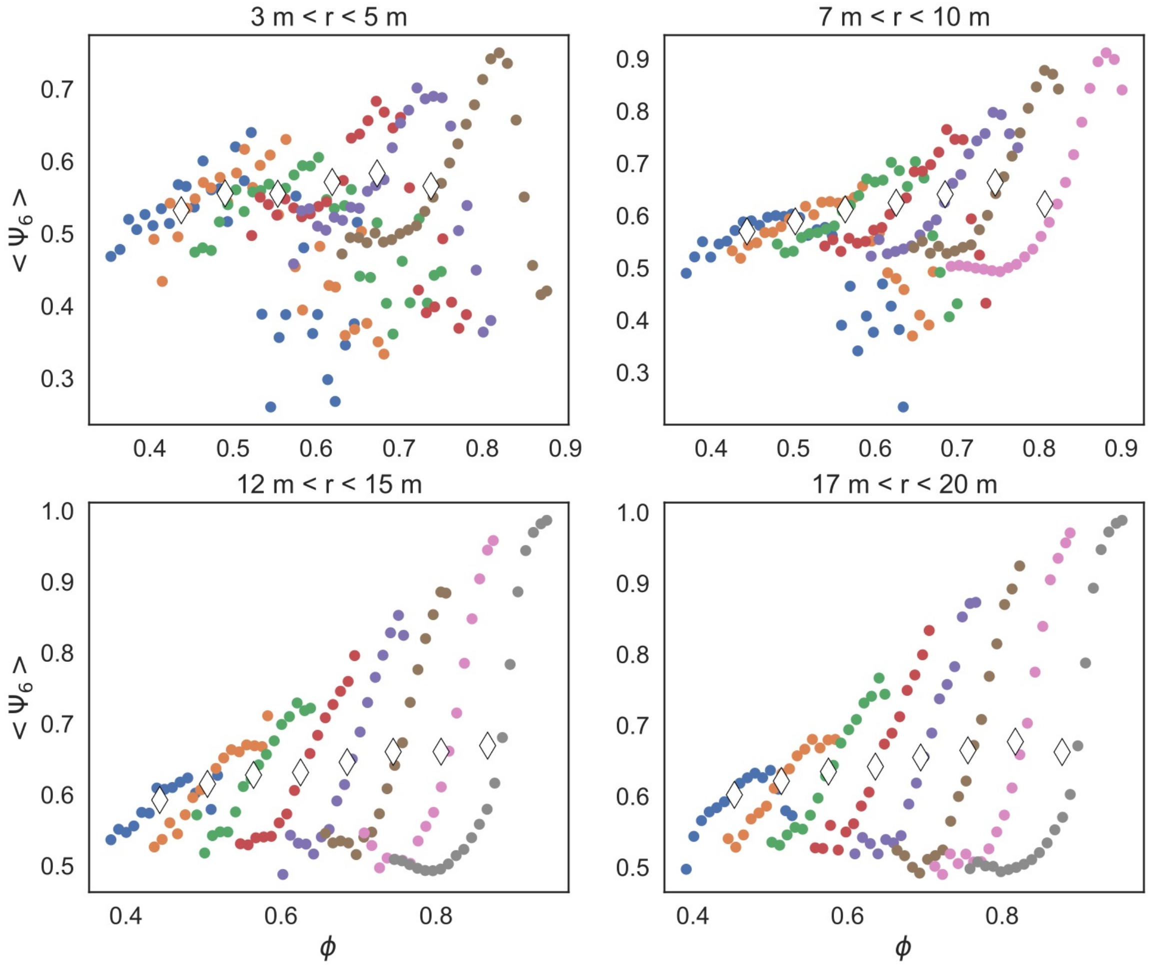

Figure 6.47: Analogous to Figure 6.46 the relationship between the mean hexagonal order $\langle \Psi_6 \rangle$ and the packing fraction ϕ.

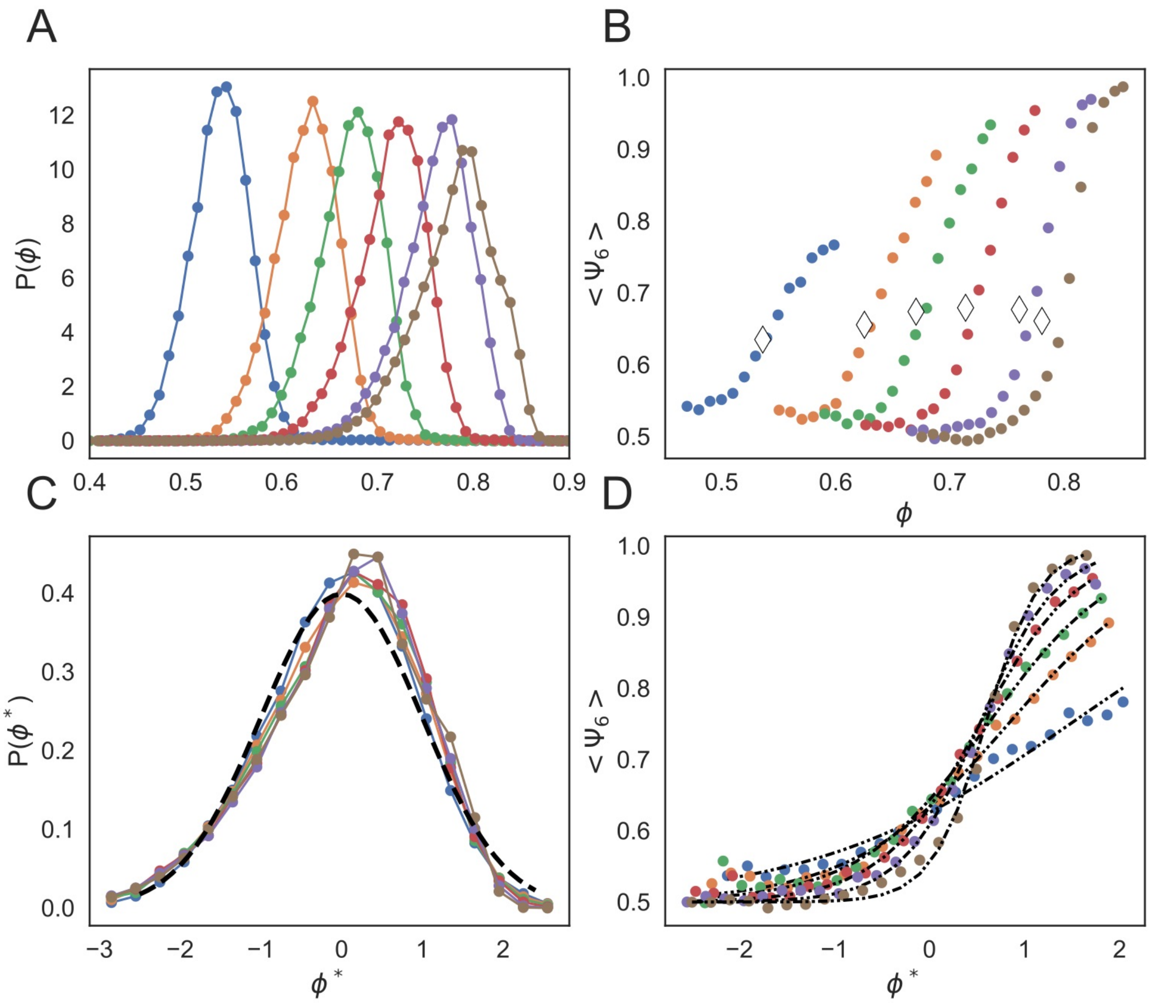

Figure 6.48: (**A**) Distribution $P(\phi)$ of selected packing fraction classes ϕ_c. (**B**) Analogous to A the mean hexagonal bond orientation factor $\langle\Psi_6\rangle$ in respect to ϕ. The diamonds indicate the mean value of $\langle\Psi_6\rangle$. (**C**) The transformed distribution $P(\phi^*)$, using equation (6.10), of the packing fraction classes shown in panel A. (**D**) Analogous to B, $\langle\Psi_6\rangle$ in respect to ϕ^*.

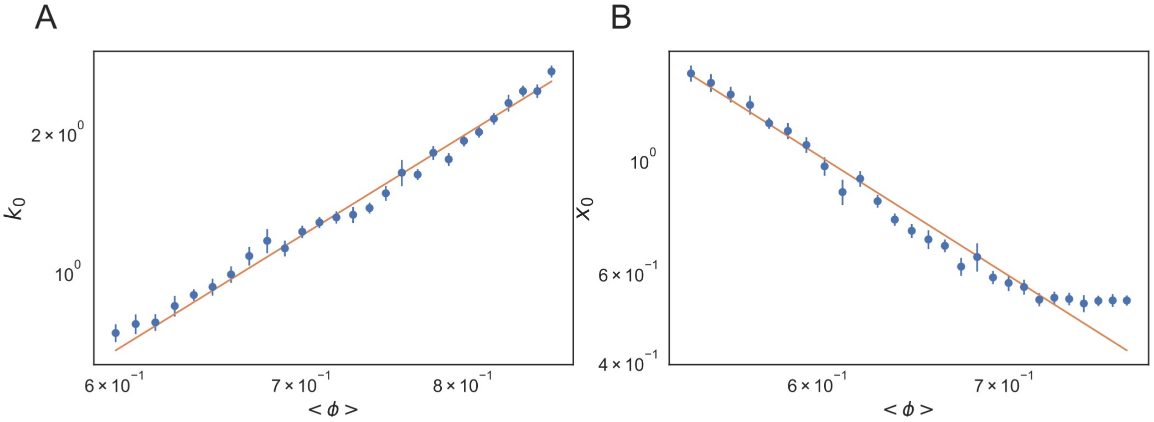

Figure 6.49: Plot of the fitting parameter k_0 (**A**) and x_0 (**B**) of the logistic function (6.11) in respect to the mean packing fraction class $\langle\phi\rangle$.

6.3 Influence of the slope factor T

At last, there is one parameter left in the (S)CSM that determines the interaction between agents. The slope factor T in equation (2.14) determines the slope of the linear distance-speed relation between agents. Here the influence is discussed in the SCSM analogous to Section 3 with $a = 0$ and $\sigma = 0.7$. The reason is that lower values of T increase the density substantially and cause partial or total clogging of the system, which is reduced in the stochastic version. Analogous to the previous simulations the model is run for $t = 10000$ s with $T \in \{0.1, 0.3, 0.5, 0.8, 1.0, 1.2\}$ s and all other parameters set equal to Table 6.1. What would be expected following the discussion in the previous Section 6.2 around Figure 6.39 and 6.40 is that a smaller value of T might decrease the order in the system since the interaction of the agents becomes relevant at a higher packing fraction increasing the variance in position. Figure 6.50 shows the simulation at $T = 9200$ s for the six different values of T (see also video "*slopeFactorNoiseSCSM.mp4*" [226]). Looking at the snapshots, the effect of T seems minor on the system's structure. Only for $T = 0.1$ s the hexagonal order seems to be increased, but this cannot be definitively stated from this snapshot. The time series of the mean measures analogous to Figure 6.42 for $P(\Psi_6 > 0.7)$, $P(N_n = 6)$, ϕ and v_{nn} are shown in Figure 6.51 for $T = 0.1$ s (A-D) and $T = 1.2$ s (E-H). The time series for $T = 1.2$ s behaves identical to $T = 1.0$ s and $\sigma = 0.7$ discussed in the previous section in Figure 6.42. For $T = 0.1$s, the time series of the measures exhibit a different behavior. In the case of $T = 1.0$ s and $T = 1.2$ s there is a maximum early in the simulation $T \approx 700$ s for $P(\Psi_6 > 0.7)$, $P(N_n = 6)$,

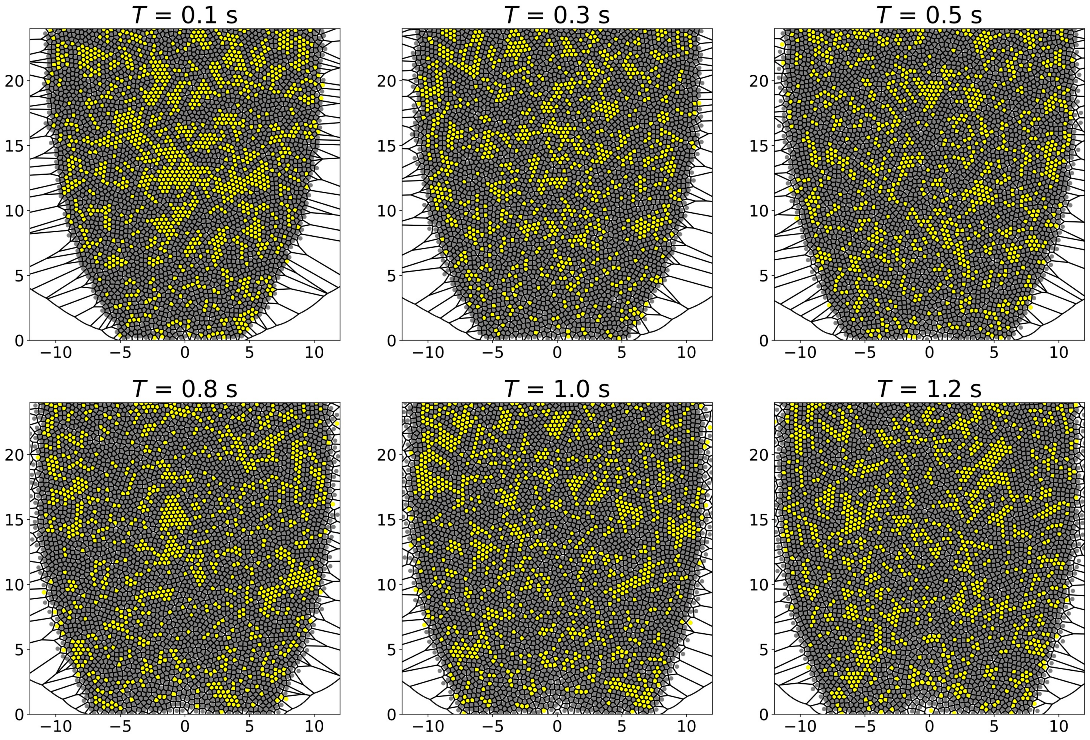

Figure 6.50: Voronoi-scatter plot of the stochastic optimal velocity model with different values for the slope factor T specified in the title of the panels at $t = 9200\,\mathrm{s}$ of simulation time with $T \in \{0.1, 0.3, 0.5, 0.8, 1.0, 1.2\}$ s. The yellow agents have a hexagonal bond orientation factor of $\Psi_6 > 0.7$.

ϕ and a minimum for v_{nn}. The system with $T = 0.1$ s behaves monotonously in comparison, where except for fluctuations in the measurement, the measures of order and packing fraction increase from $t = 0\,\mathrm{s}$ steadily until they saturate. Far from the bottleneck the hexagonal order for $T = 0.1\,\mathrm{s}$ saturates at a larger value of $P(\Psi_6 > 0.7) \approx 0.34$ compared to $P(\Psi_6 > 0.7) \approx 0.3$ for $T = 1.2\,\mathrm{s}$. Next the system is analyzed in the stationary state ($t > 4000\,\mathrm{s}$) with a focus on the packing fraction and the hexagonal order presented in Figure 6.53 A-E, analogous to Figure 6.36. Panel A shows the clogging time fraction P_{T_c} with respect to the slope factor T. The influence of T on P_{T_c} is minor between $T = 1.2\,\mathrm{s}$ and $T = 0.5\,\mathrm{s}$. For smaller values of T, P_{T_c} increases rapidly from close to $P_{T_c} \approx 0$ to $P_{T_c} \approx 0.35$ at $T = 0.1\,\mathrm{s}$. For the analysis of the packing fraction, ϕ and the hexagonal order $P(\Psi_6 > 0.7)$, the clogged states are removed, and only the flowing state is analyzed. Panel B and C show ϕ and $P(\Psi_6 > 0.7)$ in respect to r for the tested values of T. The differences between the system far from the bottleneck are subtle. Especially for the measured values of $T > 0.1\,\mathrm{s}$ the hexagonal order and the packing fraction are close together. Close to the bottleneck $r < 7\,\mathrm{m}$ the packing fraction ϕ increases with decreasing slope factor T, which is already discussed in Section 3. For $T = 0.1\,\mathrm{s}$ the system's hexagonal order significantly increases far from the bottleneck. Panels D-E show the influence of T at different distances r analogous to Figure 6.36. The two graphs show that an increase in T monotonically decreases the packing fraction ϕ at all three distance intervals measured in the system. Interestingly the hexagonal order has a non monotonous relationship, where at the intermediate and far distance the hexagonal order $P(\Psi_6 > 0.7)$ decreases from $T = 0.1\,\mathrm{s}$ to $T = 0.3\,\mathrm{s}$ and increases from there on out with increasing T. Close to the bottleneck is a slight increase in hexagonal order with increasing slope factor $T > 0.1\,\mathrm{s}$ is observed. As discussed above, the decrease of the hexagonal order with T is not unexpected, but the increase for very small values of T is surprising. The shape factor distribution of the system is shown close to the bottleneck (Figure 6.52 A) and far away (Figure 6.52 B). The distribution has at both distances for all values of T a distinct peak at around $\zeta = 1.18$. Close to the bottleneck, there is no peak near the hexagonal value of $\zeta \approx 1.103$, and the difference in the distribution with varying T is small. Far from the bottleneck, the peak near the hexagonal region decreases slightly with increasing T for $T > 0.3\mathrm{s}$. For $T = 0.1\mathrm{s}$, the peak increases significantly compared to the other values. The tail of the distribution for increasing values $\zeta > 1.18$ is exponential. The fraction of the shape classes in respect to T shown in panel C and D of Figure 6.52 vary slightly for $T > 0.1\,\mathrm{s}$. At $T = 0.1\,\mathrm{s}$ the fraction of p_A increases far from the bottleneck while p_C decreases. The same is true close to the bottleneck to a lesser extent. In summary, the slope factor T influences the density and hexagonal order of the system. As expected from the results from Section 6.2 the density consistently increases with a decreasing value of T. The hexagonal order decreases with an decreasing value of T and increases again between $T = 0.3\,\mathrm{s}$ and $T = 0.1\,\mathrm{s}$. The reason for this behavior is not clear.

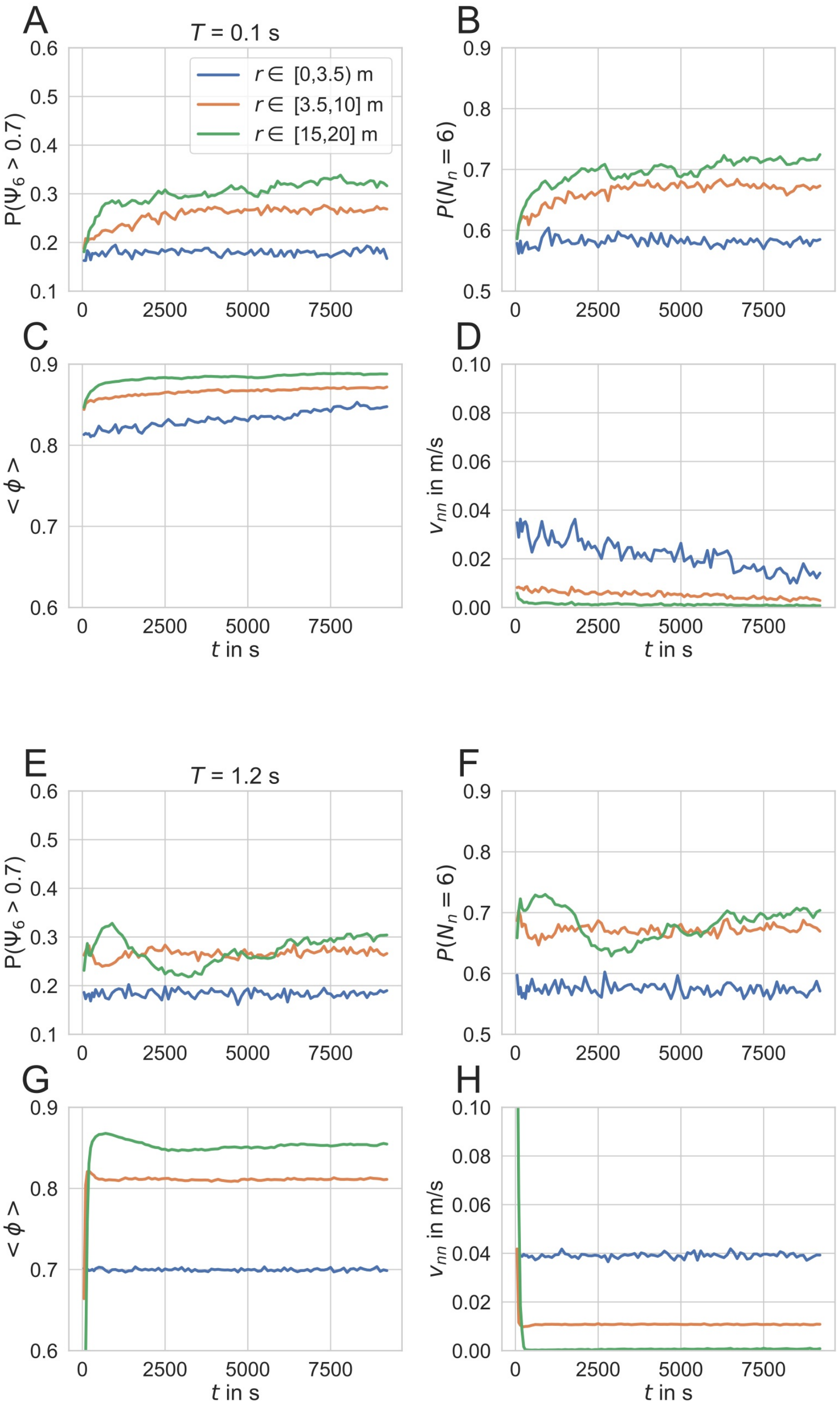

Figure 6.51: Time series of the hexagonal order $P(\Psi_6 > 0.7)$ (**A**)&(**E**), fraction of the coordination number $P(N_n = 6)$ (**B**)&(**F**), mean packing fraction $\langle \phi \rangle$ (**C**)&(**G**) and no-noise speed V_{nn} (**D**)&(**H**), for the system with slope factors $T = 0.1\,\mathrm{s}$, (A-D) and $T = 1.2\,\mathrm{s}$, (E-H). The measures are taken at three distant intervals $r + dr$ from the bottleneck specified in the legend.

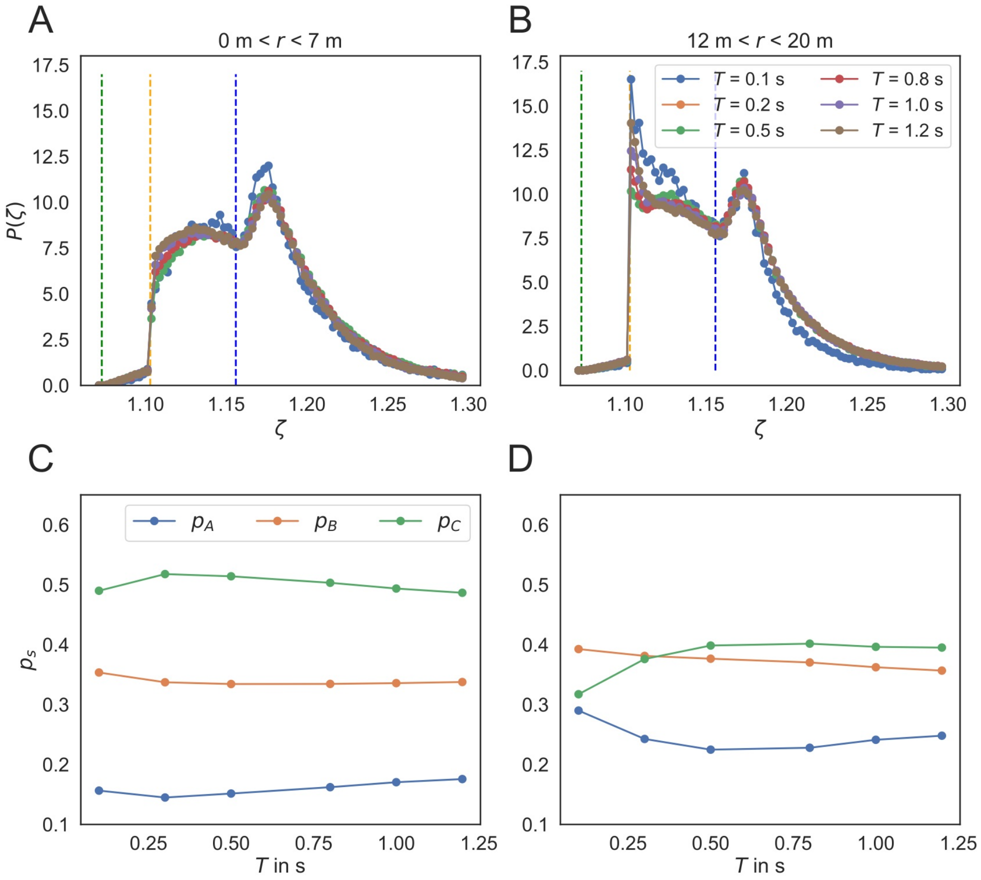

Figure 6.52: (**A**) Distribution of the shape factor close to the bottleneck for different T ($0\text{ m} < r < 7\text{ m}$). (**B**) Analogous to A far from the bottleneck ($12\text{ m} < r < 20\text{ m}$). (**C&D**) The fraction p_s with $s \in \{A, B, C\}$ of the three shape classes in the system. The distance from the bottleneck is equal to A and B, respectively.

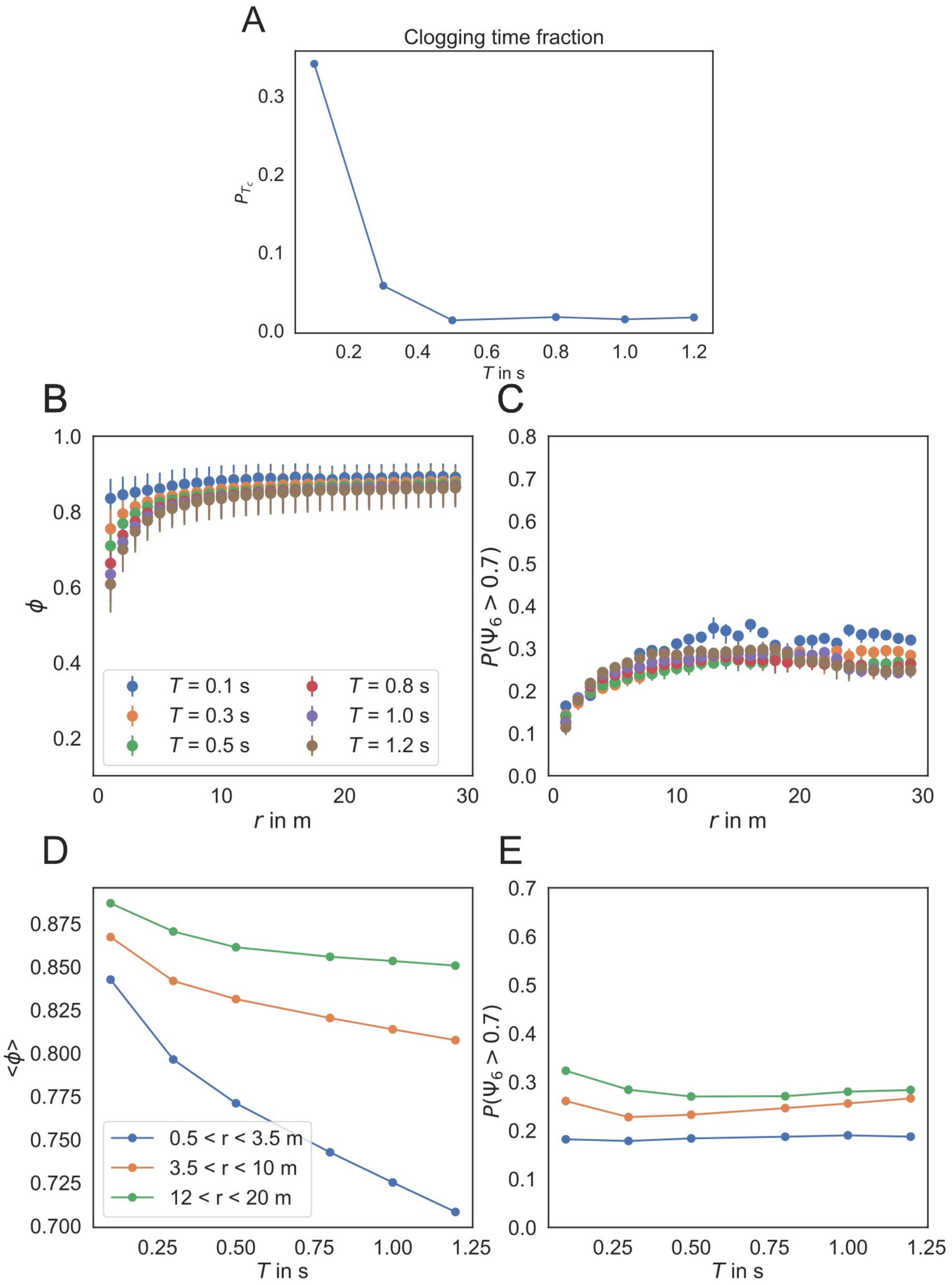

Figure 6.53: (**A**) Clogging time fraction P_{T_c} of the system in respect to T (**B**) Packing fraction ϕ in respect to the distance to the bottleneck r. (**C**) Hexagonal order $P(\Psi_6 > 0.7)$ in respect to r. (**D**) Mean packing fraction $\langle\phi\rangle$ in different radial intervals in respect to T. (**E**) Analogous to D the hexagonal order $P(\Psi_6 > 0.7)$.

6.4 Distribution of high order clusters

In this section, the method described in Section 4.8 is utilized to analyze the clusters of agents with a high hexagonal order in the system. The clusters are classified as follows: in the first step, the packing-fraction-field $\phi(\mathbf{r})$ and the hexagonal order field $\Psi_6(\mathbf{r})$ are calculated using equation (4.21). An example of the field for the SCSM using the simulation data from Section 6.2 with $a = 0$, $\sigma = 3$, and all other parameters equal to the summary in Table 6.1 is shown in Figure 6.54 A. The field is of a snapshot at $t = 4200\ s$ in the system. The bright yellow spots show regions with a high hexagonal order, where Ψ_6 is close to one. The field is calculated using a Gaussian kernel to approximate the delta function $\delta(x) = 1/(\sqrt{\pi}a)\ \exp(-x^2/a^2)$ analogous to Section 3. The value used for $a = 0.12$ m, which corresponds to a full width at half maximum fwhm $= 0.2$ m. The field in panel A exhibits large patches of constant hexagonal order at the boundaries, caused by the low density and lack of neighboring agents. To eliminate the boundary area, the field $\Psi_6(\mathbf{r})$ is filtered using the packing fraction field $\phi(\mathbf{r})$. When the value of $\phi(\mathbf{r}) < 0.4$ the value of $\Psi_6(\mathbf{r})$ is set to zero. The filter process results are shown in panel B, where a clear boundary is visible. The next step is to filter out the areas of high order in the field, using equation (4.22), with $\epsilon = 0.7$ in panel C. The areas of high order are shown as the bright yellow spots that take the value of 1 and the blue areas 0. The Hoshen-Koppelmann algorithm can be utilized on this grid to distinguish the different clusters. The result of the clustering is shown in panel D. The labeled data is a $n \times m$ array with the clusters-labels going from 1 to n_l, where each pixel in the graphic belongs to one of the labels or not. Pixels not belonging to a cluster are marked with a 0. To calculate the distribution of cluster sizes, the pixelated areas have to be converted to the number of agents in this area. This cannot be done exactly, but to estimate it, the hexagonal structure of the ordered clusters can be utilized. The area of the cluster consisting of pixels with side length Δx can be converted to the agent number by the equation

$$N_c \approx \lceil N_p \frac{(\Delta x)^2}{\pi(l/2)^2}\, \eta \rfloor, \tag{6.12}$$

where $\lceil x \rfloor$ denotes the rounding to the nearest integer number, N_c the approximate number of agents in the cluster, N_p the number of pixels in the cluster with side length Δx, l the diameter of the disc shape agents, and $\eta \approx 0.9069$ the packing

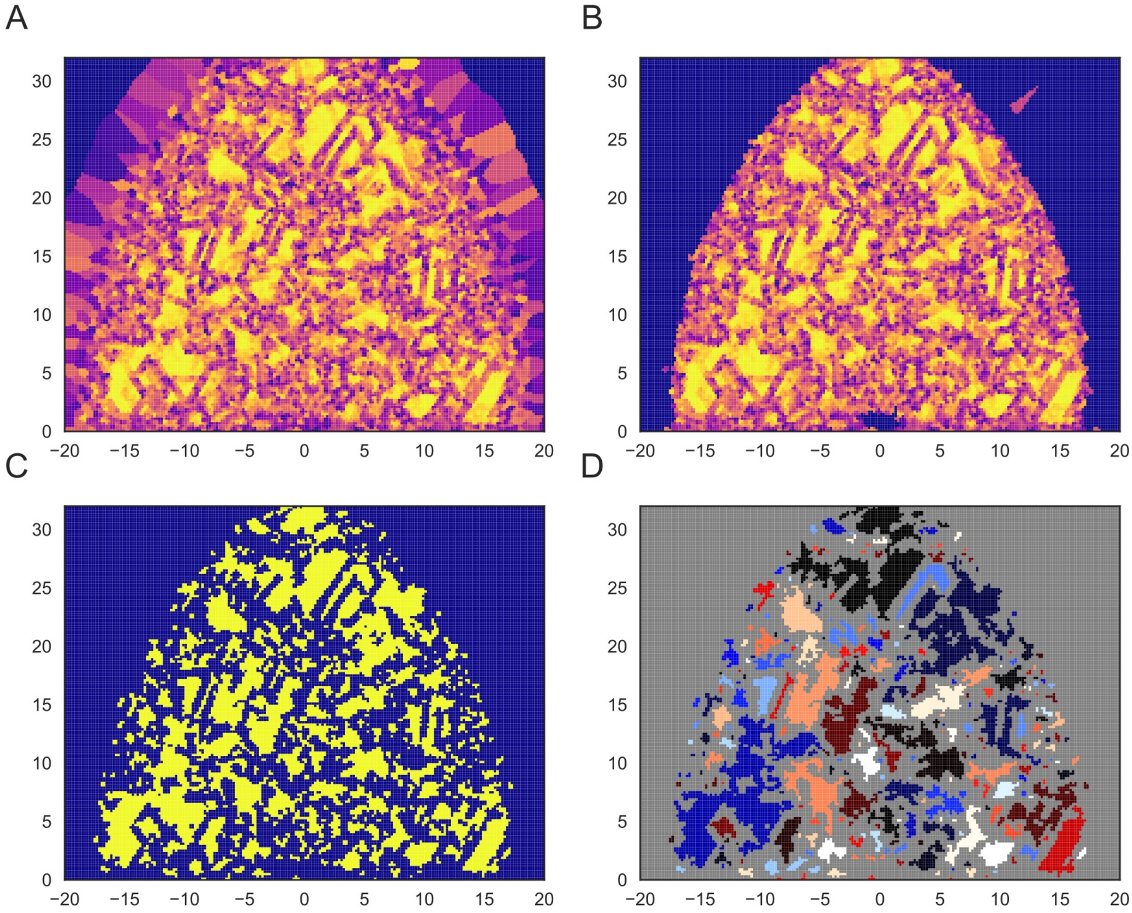

Figure 6.54: Illustration of the clustering process described in Section 4.8. (**A**) Example of the hexagonal order field $\Psi_6(\mathbf{r})$. Yellow areas mark a high hexagonal order. (**B**) The hexagonal order field is filtered for areas with a packing fraction $\phi(\mathbf{r}) > 0.4$. (**C**) The field $\Psi_6(\mathbf{r})$ is filtered for areas of high order with $\epsilon \geq 0.7$. Yellow areas have the value 1 and blue areas 0. (**D**) Colouring of the clusters using the Hoshen-Koppelmann algorithm (Section 4.8).

density of densest circular packing. The resolution of Figure 6.54 is $\Delta x = 0.2\,\mathrm{m}$, which is used throughout this section. Figure 6.55 A-D shows the distribution of cluster sizes for different models (panel A&B the SCSM with $a = 0$ and C&D the CSM with $\sigma = 0$) and different thresholds ϵ for the clusters (see equation (4.22)). The other parameters are equal and defined in Table 6.1. The values of σ in the stochastic model are chosen to be the same as in the simulations of Section 3 with

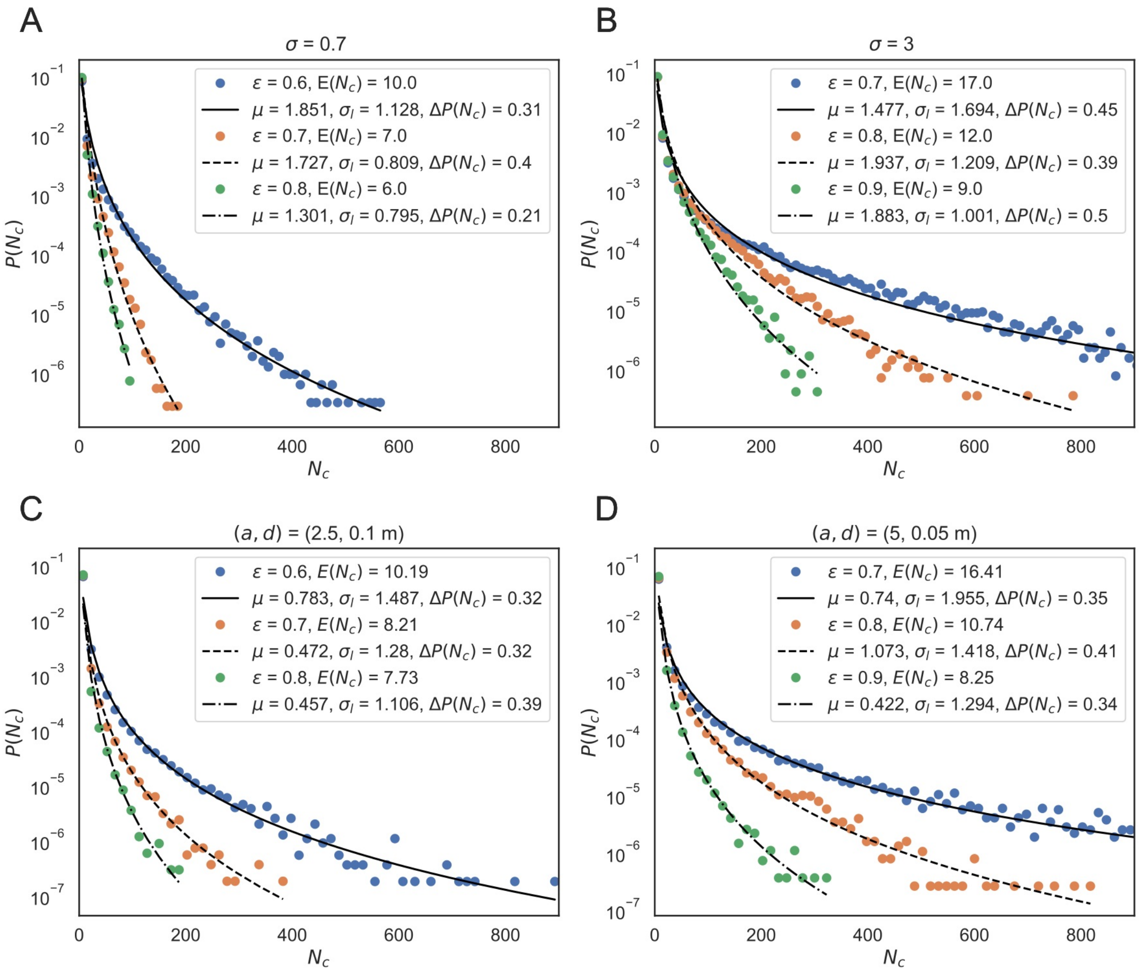

Figure 6.55: Log-plot of the cluster size distribution defined by the hexagonal order of the system $\Psi_6 > \epsilon$ specified in the legend. The black lines show the fit of a log-normal distribution to the log of the data with the fit parameter for μ and σ_l shown in the legend. The relative deviation $\Delta P(N_c)$ is shown in the legend. Panels (**A**) and(**B**) are the SCSM with nor repulsion, and $\sigma = 0.7$ in A and $\sigma = 3$ in panel B. Panels (**C**) and(**D**) show the CSM with $a = 2.5$ and $d = 0.1$ m in panel C and $a = 5$ and $d = 0.05$ m in panel D.

$\sigma = 0.7$ and a case with higher hexagonal order ($\sigma = 3$). For the deterministic case similarly the parameters used are the ones to simulate the experiments in Section 5.1 with $a = 2.5$ and $d = 0.1$ m. The second case is chosen to have a higher hexagonal order and a low clogging probability with $a = 5$ and $d = 0.05$ m (see Section 6.1). The threshold ϵ in each case of Figure 6.55 A-D influences the distribution's tail. In the log-plot, the distributions exponential tail is visible, with the base depending on the threshold ϵ for the cluster. This is especially visible for the smallest value of ϵ tested respectively. Though the fraction of smaller clusters is less affected by the threshold (see also Appendix A.8 Figure S28). The black lines show a fit to the data of a log-normal distribution

$$p(x) = \frac{1}{x\sigma_l\sqrt{2\pi}} \exp\left(-\frac{(\ln(x)-\mu)^2}{2\sigma_l^2}\right), \tag{6.13}$$

with μ the expectation value of the variable $\ln(x)$ and σ_l its standard deviation. The log-normal distribution describes natural growth processes. These processes are often driven by, e.g., particles that accumulate and cause small percentage changes in the growth, which are additive on a log scale. The lines are fitted by minimizing the mean square error mse $= 1/N \sum_i (y_i - \hat{y_i})$, where y_i is the measures data point and $\hat{y_i}$ is the fitted value. In this case, the log value $y = \log(P(N_c))$ is used to fit the data since most of the data points are in the tail of the distribution. The relative error of the fits is given in the legend of the panels $\Delta P(N_c) = 1/N \sum_i |P_i(N_c) - \hat{P}_i(N_c)|/P_i(N_c)$, where $\hat{P}_i(N_c)$ is the fitted value. The relative error in both models is in the range of 21 %-50%. Considering the inhomogeneity of the system, its finite size, and the number of systems tested, the log-normal distribution fits the data well. The legends also show the mean value of the measured cluster sizes $E(N_c)$. The value of $E(N_c)$ is rather small in all system between $6 < E(N_c) < 17$ depending on the model parameters and ϵ. Looking at the example in Figure 6.54 D, it seems like in the case of $\sigma = 3$ and $\epsilon = 0.7$ larger clusters are much more abundant. It has to be considered that the system is of finite size, and smaller clusters have many more opportunities to form in the flowing system than large clusters that take up large portions of the space. Comparing the shapes of the distributions between the different parameters of the model, it is noticeable that they are similar depending on ϵ. It could be that the distributions of the models with different parameters are equivalent for a certain pair of values for ϵ. To test this for both models, the data from the simulation with $\sigma = 0.7$ and $(a, d) = (2.5, 0.1\,\text{m})$ is clustered with an $\epsilon = 0.7$ and the data from the simulations with $\sigma = 3$ and $(a, d) = (5, 0.05\,\text{m})$ are fitted by varying the value of ϵ and minimizing the distance $1/N \times \sum_i (\log(P_{i0}(N_c)) - \log(P_{i1}(N_c)))^2$, where the numbers 0 and 1 refer to the parameter sets of the simulation. The result is shown in Figure 6.56 A for the stochastic model and B for the deterministic model. For the stochastic model, the difference in the tail is quite large, but for smaller clusters $N_c < 100$, they fit close together. It should be considered that there is few data in the tail, and the

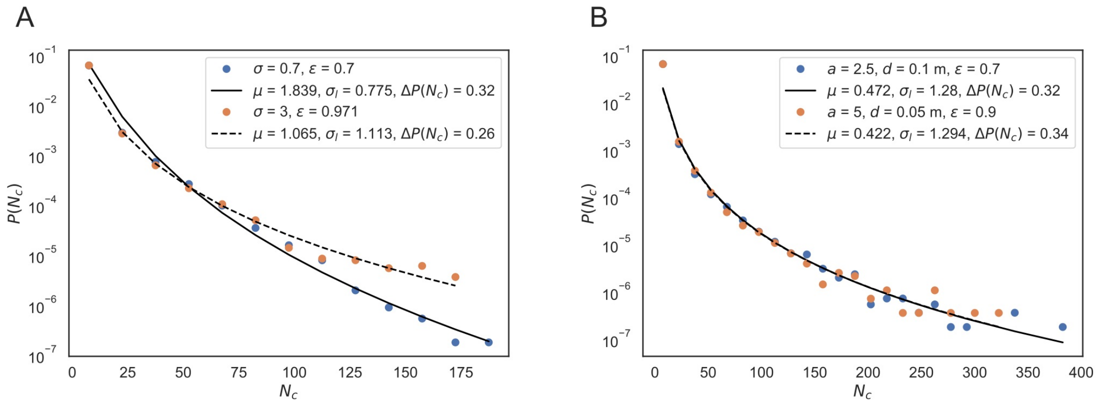

Figure 6.56: Comparison of the cluster size distribution $P(N_c)$ of the two models with different parameters (see legend), where the threshold ϵ is varied to minimize the distance between the distribution. Black lines show the individual fit of the log-normal distribution. Panel (**A**) shows the SCSM, and panel (**B**) the deterministic model.

difference could be because of the small count. The relative difference between the two simulated distributions is $\Delta P(N_c) = 0.37$. Because of the difference in the tail, the parameters μ and σ_j for the fit are not close. In panel B, the two distributions are very close throughout the whole scale of N_c, with the fitting parameters being closer to each other. The relative distance $\Delta P(N_c) = 0.29$ is smaller than the stochastic model. In general, this shows that the hexagonal structure of the systems with different parameters are similar depending on the threshold ϵ for the order criteria. Analogously it can be analyzed if between the two models the structure is similar when varying ϵ. Figure 6.57 shows analogous to Figure 6.56 a comparison between the stochastic model and the deterministic model with random initial conditions. Panel A compares the stochastic model with $\sigma = 0.7$ to the deterministic model with $a = 2.5$ and $d = 0.1$ m, while panel B compares the stochastic model with $\sigma = 3$ to the deterministic model with $a = 5$ and $d = 0.05$ m. The pairs are chosen because they are closer together in their hexagonal order. The mse of the logarithmic value of $P(N_c)$ between the models is again minimized, and the log-normal distribution is fitted to the data. In both cases, the distribution's shape difference is visible. In the deterministic model, the slope of the distribution is steeper in the beginning and exhibits a longer tail to larger clusters than the stochastic model. Side by side, the shape of the respective models with different variables is again comparable. The relative difference between the simulation data in panel A is $\Delta P(N_c) = 0.78$ and in panel B $\Delta P(N_c) = 0.52$. In both instances, the relative difference is larger than

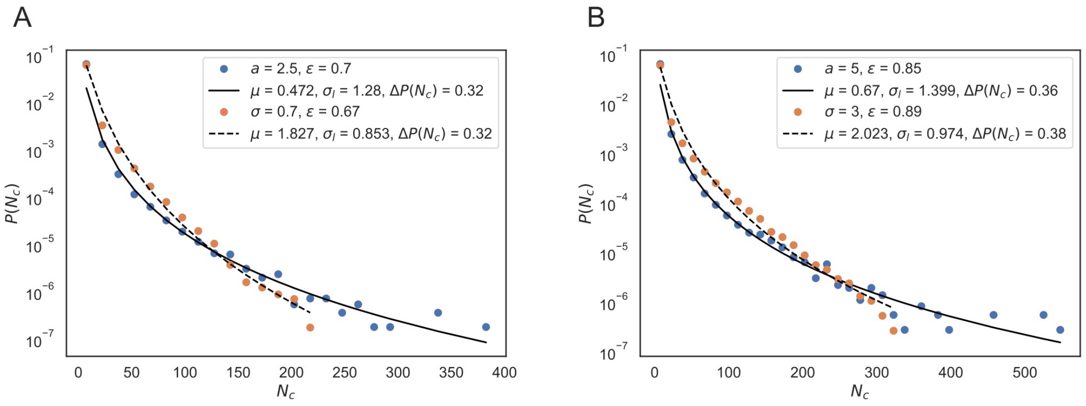

Figure 6.57: Comparing the deterministic CSM to the stochastic SCSM analogous to Figure 6.56. Panel (**A**) shows the comparison of the CSM with $a = 2.5$ and $d = 0.1$ m with the SCSM with $\sigma = 0.7$. Panel (**B**) shows the comparison between the SCSM with $\sigma = 3$ and the CSM with $a = 5$ and $d = 0.05$ m. The values of ϵ are shown in the legend.

in comparing the model parameters in Figure 6.56. In conclusion, the presented method is useful for analyzing the clustering of continuous and discrete variables in trajectory data. In this case, the clustering of hexagonal order is analyzed in the system but could also be utilized for other measures in the system, e.g., density or speed. The threshold ϵ and the distributions of the cluster sizes make it possible to compare the global order in the system and the finer structure of the ordered clusters in the system.

6.5 Order in the social force model

In this section, the social force model (SFM) (see Section 2.1) is analyzed analogously to the CSM in the preceding sections of this chapter. Previous work discusses the effect ordering in the SFM has on the evacuation dynamics [39]. Due to the symmetric nature of the body and social forces in the model, it is expected that there is a high hexagonal order in the system when using mono-dispersed circular agents. The system is analyzed for a single parameter set with the specific values for the parameters of the SFM being equal to the parameters used in Helbing et al. [23], which were also used in Cheng et al., [39]. The values are summarized in Table 6.2. The simulations run for $t_{max} = 3200\ s$. The system run is shorter than for the CSM because of the higher computational demand, but the SFM relaxes rather quickly. This is evident in Figure 6.58, which depicts the Voronoi-scatter plot of the system with the hexagonal order parameter analogous to Figure 6.41 but in this case, the Coordination number N_n and the hexagonal order $\Psi_6 > 0.7$ is depicted in separate panels.

Parameter	Variable	Value
Agent mass	m	89 kg
Desired velocity	v_0	1.34 m/s
Agent size (spring like repulsion)	l	0.34 m
social force strength	A_i	2×10^3 N
social force length	B_i	0.08 m
Acceleration time	τ	0.5 $\mathrm{m/s^2}$
Simulation time steps	Δt	0.001 s
Agent stiffness (Hooks law)	K	1.2×10^5 $\mathrm{kg/s^2}$
Agent friction	κ	2.4×10^5 kg/(m s)
Population	N	8000
Floor field resolution	Δh	0.01 m
Wall avoidance distance	d_w	0.25 m
Corridor width	b	55.0 m
Exit width	w	0.75 m
Initial density	ρ_i	2.5 $\mathrm{m^{-2}}$

Table 6.2: Summary of model parameters and their values.

The plot shows how the system quickly transforms from the initially disordered state into an almost entirely crystallized state in the bulk ($r < 15$ m). The system initially consists of a polycrystal structure separated by grain boundaries, which can be seen as a line of defects ($t = 20$ s). At later times ($t = 100$ s), there are only a few 5-7 fold defects in the system, and it is highly ordered into hexagons even very close to the bottleneck (see also video "*SFM.mp4*" [226]). For about $r < 0.5$ m, the hexagonal order decreases near the bottleneck. The time series of the packing fraction ϕ and the hexagonal order $P(\Psi_6 > 0.7)$ depicted in Figure 6.59 A and B, respectively, show that the system quickly relaxes into the stationary state in under 200 s. The social force in the case of a large number of agents is not sufficient to prevent the agents from overlapping. The agents in the bulk ($r < 16$ m) are compressed, which in turn increases their packing fraction over the limit of $\phi_{max} \approx 0.9$. Further from the bottleneck near the boundaries of the system $r > 16$ m, the packing fraction and, in turn, the hexagonal order of the system decreases. Close to the bottleneck $0\,\mathrm{m} \leq r < 3.5$ m, the agents are as packed, as at the intermediate distance $3.5\,\mathrm{m} \leq r \leq 10\,\mathrm{m}$ but the hexagonal order is significantly higher, close to $P(\Psi_6 > 0.7) \approx 1$. The relation of the packing fraction and the hexagonal order with respect to the distance from the bottleneck r are depicted in Figure 6.60. Similar to the CSM, the hexagonal order and packing fraction increase with distance from the bottleneck to a maximum at around $r \approx 2.5$ m for ϕ and $r \approx 7$ m for $P(\Psi_6 > 0.7)$. Near the system's boundary at $r > 14$ m, the downward slope of the packing fraction increases together with hexagonal order. This is where the social force is sufficient to separate the agents from overlapping, and the packing fraction moves below ϕ_{max}. This decreases the hexagonal order, as agents in a lower density have more freedom to move. The shape factor distribution in Figure 6.61 close to the bottleneck ($0\,\mathrm{m} < r < 7)\,m$) and far away ($7\,\mathrm{m} < r < 14)\,\mathrm{m}$) also shows

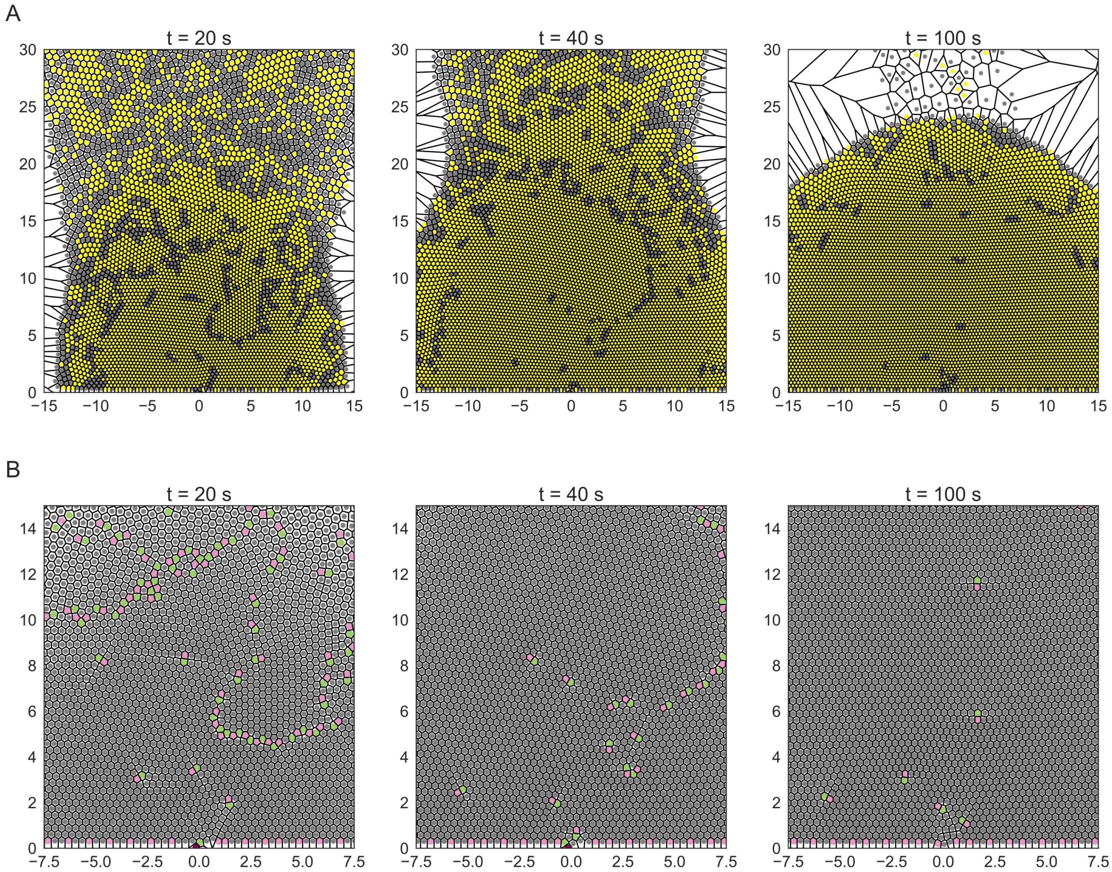

Figure 6.58: Snapshots of a simulation run at $t \in \{20, 40, 100\}$ s. (**Row A**) shows the hexagonal order, agents with $\Psi_6 > 0.7$ are marked in yellow. (**Row B**) Represents the coordination number N_n. Agents with $N_n = 6$ are grey, while agents with $N_n = 5$ are red and $N_n = 7$ are green.

that the system has a very narrow and high peak near the hexagonal shape factor $\zeta \approx 1.101$ with a majority of the agents being included, especially further away from the bottleneck. A small peak near $\zeta = 1.19$ is also observed, which contains the system's 7-5 fold defects.

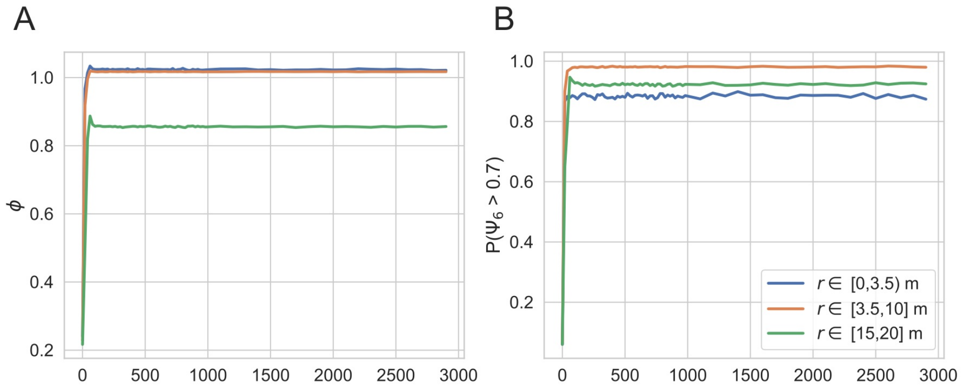

Figure 6.59: Time series of the packing fraction ϕ (**A**) and the hexagonal order $P(\Psi_6 > 0.7)$ at different distance intervals from the bottleneck r.

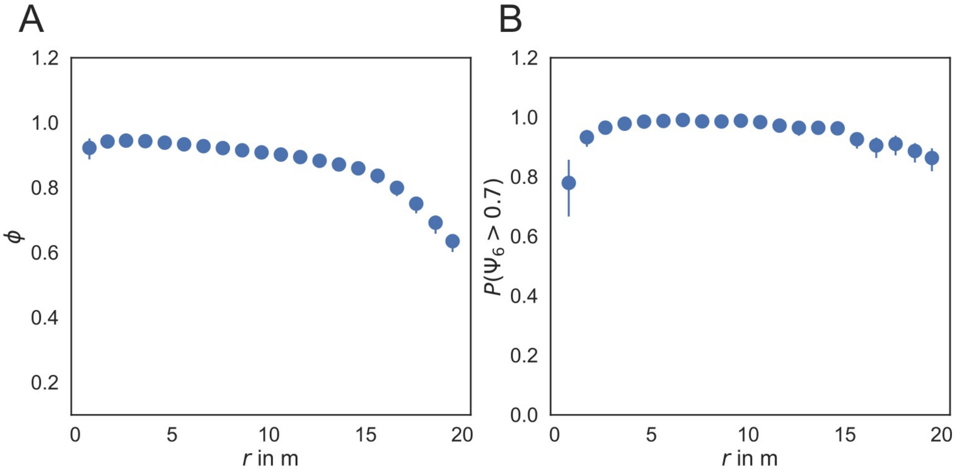

Figure 6.60: The packing fraction ϕ (**A**) and the hexagonal order $P(\Psi_6 > 0.7)$ (**B**) in respect to the distance r from the bottleneck.

In summary, the SFM exhibits an almost crystalline order in the bottleneck scenario in the whole system, except very close to the bottleneck ($r < 0.5\,\mathrm{m}$). The hexagonal order $P(\Psi_6 > 0.7) \approx 1$ and the shape factor has a narrow and high peak near the hexagonal value, including the majority of agents. Only a few defects are observed in the system after a short time. The ordering stems from the hook body force and

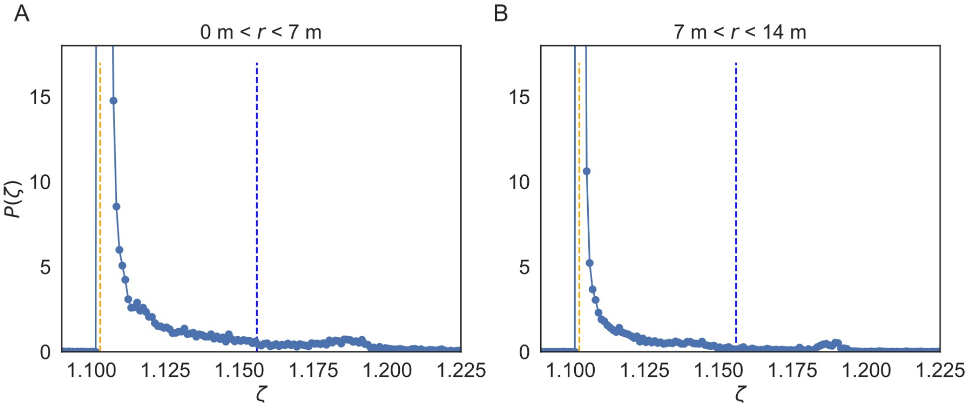

Figure 6.61: Shape factor distribution of the SFM for $t > 500$ s close to the bottleneck (**A**) and far from the bottleneck (**B**).

the social force, which are isotropic in space. In the following section, an anisotropic social force is introduced to the model to analyze its effect on the structure.

6.5.1 Anisotropic interactions influence on the structure

In its most basic form, the social force acting on an agent is isotropic in space, meaning that the strength of the social force only depends on the distance between two agents. In some variations, the social force can also depend on the position in space in relation to the movement direction. In this section, the system at the bottleneck is analyzed with an anisotropic social force, where the strength of the force exerted by agent j at position $\mathbf{x}_j$ acting on agent i at position $\mathbf{x}_i$ is dependent on the angle between the vector $\hat{\mathbf{e}}_{i,j} = (\mathbf{x}_i - \mathbf{x}_j)/|\mathbf{x}_i - \mathbf{x}_j|$ and the movement direction $\hat{\mathbf{e}}_i = \mathbf{v}_i/|\mathbf{v}_i|$. The relation is implemented using the factor ω in equation (2.6) with $\mathbf{f}_i^{soc} = \omega\,\mathbf{f}_{i,0}^{soc}$ as follows:

$$\omega = \begin{cases} 1 & \text{if} \quad \hat{\mathbf{e}}_{i,j} \cdot \hat{\mathbf{e}}_i > k \\ 0 & \text{if} \quad \text{otherwise}, \end{cases} \tag{6.14}$$

Population	N	3000
Bottleneck width	w	1.27 m

Table 6.3: Model parameters that differ from the larger SFM simulation summarized in Table 6.2.

The factor $k \in [-1, 1]$ limits the angle between the movement direction and the position of neighboring agents for the social force to be felt. For $k = -1$, the social force is symmetric, depending only on the distance between agents. For $k = 1$, no social force is felt from any direction, and the agents only interact via the body force. The previous section shows that the symmetrical case with $k = -1$ leads to almost crystalline order in the bulk. Since the body force is also symmetric, it is expected that for $k = 1$, the system should be ordered hexagonally and packed densely. To investigate the effect of k on the system, simulations are run with $N = 3000$ agents and $N = 5$ runs per value of k, which is varied between $-1 < k < 1$. The simulation time is set to $t_{max} = 1500$s. The bottleneck is widened to $w = 1.27$m so that clogging is avoided in the case of $k > 0$. Figure 6.62 shows a snapshot of the simulations at $t = 1200$ s for different values of k specified in the title of the panels. The smaller system with the widened exit has a high degree of hexagonal order but exhibits more defects compared to the previous case, with grain boundaries appearing in the bulk of the system. The effect of k is surprising. For $k = -1$, the social force is symmetric. Increasing k cancels the social force from neighboring agents behind agent i regarding its moving direction. From the panels, it is evident that this effect is minor. Even at $k = -0.2$, the system does not change significantly in its structure.

This changes near $k = 0$, where the systems' behavior differs drastically. Near the exit, a tightly packed crystalline core is surrounded by a somewhat disordered and less dense ring for $r > 7.5$ m and $k = 0.05$. At $k = 0$ (where the space is separated equally), the situation is similar where the crystalline core is around $r < 5$m, and the density in the outer region and the hexagonal order decrease further. For $k = -0.05$, the system starts to compress, and a crystalline core forms for $r < 7.5$ m with a high density and a sharp transition to a disordered region. For $k = 0.15$, the social force is already insufficient to keep the agents apart close to the bottleneck, and the system compresses into a high-density crystalline bulk near the exit. The dynamics around $k = 0$ are illustrated in the video "anisotropicSFM.mp4" [226]. The video shows the formation of the crystalline cores in the first 500 s of the simulation. After that, the two phases in the systems are relatively stable. Inside the cores, defects move from the bottleneck outwards. Increasing $k > 15$ does not alter the dynamics further in a significant way. The mean of the packing fraction and hexagonal order in respect to k for all systems for $t > 500$ s is shown in Figure 6.63 in the region $|x| < 3$ m and 1 m $< r < 10$ m. The transition around $k = 0$ is evident in the increase in packing fraction. Interestingly, the packing fraction decreases slightly after the transition, even though the social force acting on an agent is stronger for smaller k.

The hexagonal order increases with increasing asymmetry in the system from $k = -1$ to $k = -0.2$. At the transition, the hexagonal order decreases substantially but increases continuously after passing the critical $k = 0$ point.

In the snapshots of Figure 6.62, one can see that the order and packing fraction depend on the distance from the bottleneck. Figure 6.64 shows the packing fraction ϕ (panel A) and the hexagonal order $P(\Psi_6 > 0.7)$ (panel B) with respect to the distance to the bottleneck r.

Because of the superposition of the forces and the increase in pressure with the number of agents behind an agent, the hexagonal order and packing fraction decrease with further distances r to the bottleneck (apart from the region close to the bottleneck $r < 3$ m). The curves differ in shape and slope depending on the value of k. For $k < 0$, the slope of the packing fraction $\frac{d\phi(r)}{dr}$ decreases monotonically for $r > 3$ m and becomes roughly constant for $r > 6$ m. At the transition point $k = 0$, the shape of the curve changes, where the slope does not decrease monotonically. The steepest slope between $5\,\text{m} < r < 7\,\text{m}$ and flattens for larger distances where the packing fraction decreases with a shallow linear slope. For $k = 0.05$, the packing fraction behaves similarly to $k = 0$ but generally has a higher packing fraction. At $k = 1$, the agents become packed, and there is a slight shallow linear decrease until the system's edge.

The hexagonal order shows interesting behavior. For $k = -1$, the symmetrical case where the social force is independent of the special relationship between the agents has two maxima. It increases with distance to the bottleneck close to the exit $r < 3$ m and has a valley at around $r \approx 5.5$ m, which is not observed in the previous simulation with $N = 8000$ agents and the bottleneck width of 0.75 m. From this simulation, it cannot be pointed out which of the two changes is responsible for this behavior. The smaller agent number decreases the pressure in the bulk of the system, but it would be expected to have a monotonous effect on the hexagonal order. An increase in the door width should affect the system structure and could lead to non-monotonous behavior due to speed bursts going through the system. In the extreme case when the bottleneck is very wide, there is no high-density shock that travels through the system, and the hexagonal order would be lowered. For $k < 0$, the valley in the hexagonal order increases with increasing k, while overall, the hexagonal order close to the bottleneck increases. At $k = 0$, the valley disappears, and there is a peak in the hexagonal order at $r \approx 4$ m and decreases from there

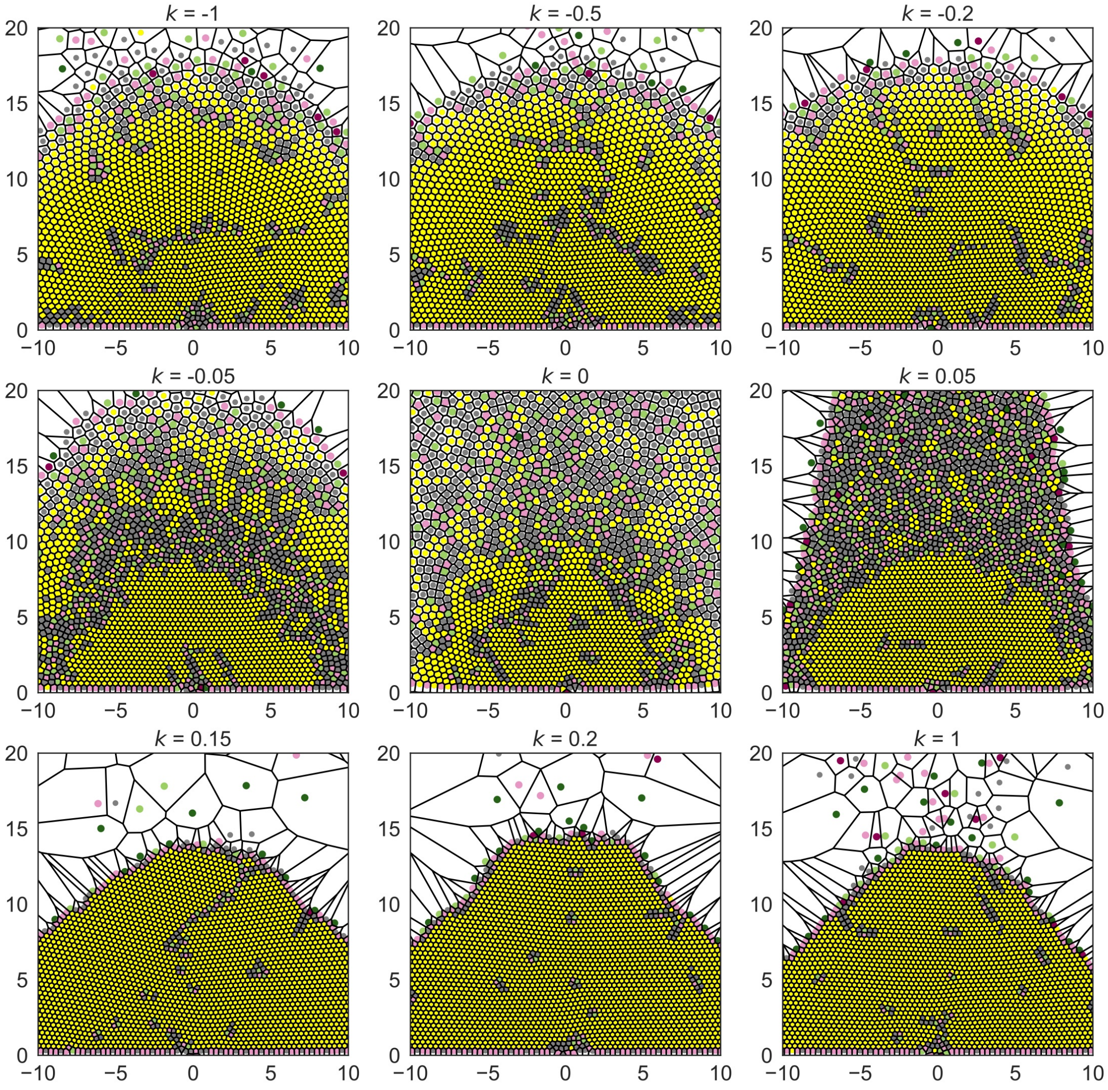

Figure 6.62: Snapshot of the simulation at $t = 1000\,\mathrm{s}$ with different values for the cut-off-angle k specified in the title. Yellow agents have a hexagonal order $\Psi_6 > 0.7$. Red and green colours show the coordination number $N_n \neq 6$ analogous to Figure 6.1.

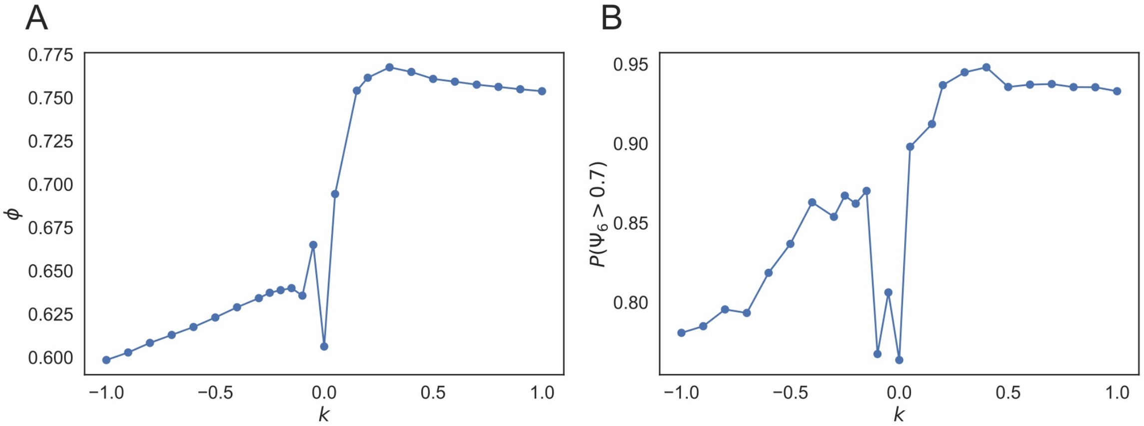

Figure 6.63: The mean value of the packing fraction ϕ (**A**) and the hexagonal order $P(\Psi_6 > 0.7)$ (**B**) in respect to k. The values are measure in the area $|x| < 3\,\text{m}$ and $(0.5\,\text{m} < r < 10)$ m.

on to a minimal value of around $P(\Psi_6 > 0.7) \approx 0.4$. For $k > 0$, the system has a plateau with a high hexagonal order close to $P(\Psi_6 > 0.7) = 1$ and a point where the hexagonal order sharply decreases. At $k = 0.05$, the point is around $r \approx 8$ m, where the system decreases but still has a rather high packing fraction. At $k = 1$, the hexagonal order decreases with the packing fraction at the edge of the bulk.

The shape factor distribution $P(\zeta)$ in Figure 6.65 A and B is presented for selected values of k close to the bottleneck $0\,\text{m} < r < 6\,\text{m}$ and far away from the bottleneck $8.5\ \text{m} < r < 16\ \text{m}$ for $|x| < 3$ m. Close to the bottleneck, the system has a single peak near the hexagonal shape value for all k. In contrast, far from the bottleneck, depending on the value of k, there is either a single peak distribution or a bimodal distribution similar to the CSM for $k \in \{-0.05, 0., 0.05\}$. The panels C-E show the shape factor distribution at different distances r from the bottleneck with $|x| < 3\text{m}$ as a heat map. At $k = -0.05$, the valley is visible, where the peak near the hexagonal order disappears between $9\ \text{m} < r < 12\ \text{m}$. For $r > 8$ m, the distribution turns bimodal continuously. At $k = 0$, The distribution also shifts continuously away from the crystalline phase with a single peak to the wider bimodal distribution at $r \approx 6$ m. At $k = 0.05$, The shift from the single narrow peak to the wide bimodal distribution is sharp at $r = 10$ m in a continuous transition.

One aspect of the SFM that needs to be considered is the situation where the distance to the neighbors $\langle d \rangle = \sum_{\langle i,j \rangle} |\mathbf{x}_i - \mathbf{x}_j|/N_n - l < 0$, where $\langle i, j \rangle$ denotes agents j that are neighbors of agent i meaning that there is an overlap with at least one of the neighboring agents. In this case, the body force (2.3) becomes

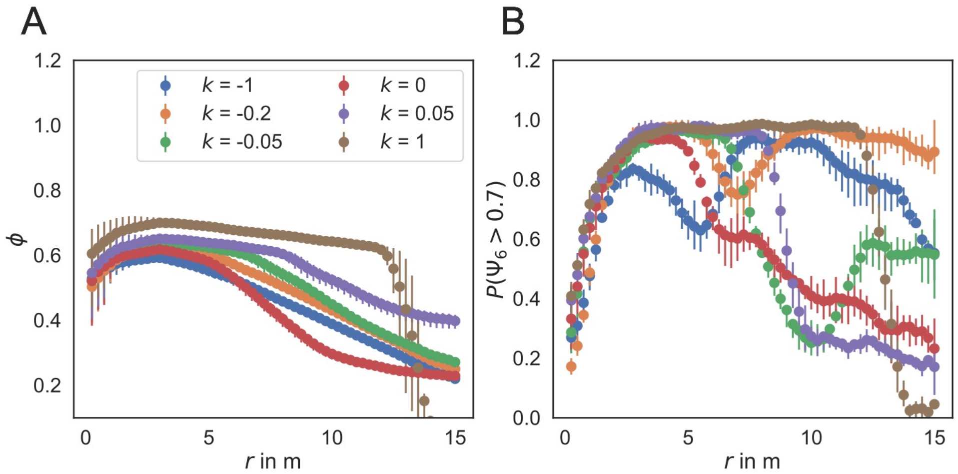

Figure 6.64: (**A**) packing fraction ϕ in respect to the radius r from the bottleneck for different cut off angles k. (**B**) Analogous to A the hexagonal order $P(\Psi_6 > 0.7)$ in respect to the radius.

relevant. When the body force is the dominant force in the system, it will form a tightly packed crystalline bulk (Figure 6.62). Hypothetically the interface near the transition point between the amorphous state and the crystalline state could be caused by the increased relevance of the body force closer to the bottleneck due to increased pressure in the system. To analyze this, the fraction of neighbors $P(\langle d \rangle < 0)$ are measured, which have a negative mean distance to their neighbors, highlighting the situation where the social force is insufficient to ensure the exclusion principle. The results are shown in Figure 6.66, where the overlapping fraction $P(\langle d \rangle < 0)$ is compared to the hexagonal order $P(\Psi_6 > 0.7)$. The comparison shows that the correlation between the hexagonal order and the overlapping fraction is limited in all cases. This is not surprising when $k = -1$ since, in this case, the social force is also symmetrical in space but interestingly also in the cases where k is close to 0 or $k = 1$ the fraction $P(\langle d \rangle < 0)$ decreases before the hexagonal order does in respect to the distance to the bottleneck. Looking at the fraction $P(\langle d \rangle < 0.015\,\mathrm{m})$, there is a correlation with hexagonal order in all cases. When $k < 0$, The first peak of the hexagonal order correlates with the fraction of agents with a mean neighbor distance $\langle d \rangle < 0.015$, and for $k \geq 0$, the decrease in order correlates with this measure. So even if the overlap does not dominate the system, a small enough distance between agents with their neighbors can be associated with high hexagonal order. In this state, the system could be partially overlapping or non-overlapping. Due to the close distance, any larger deviations from the hexagonal

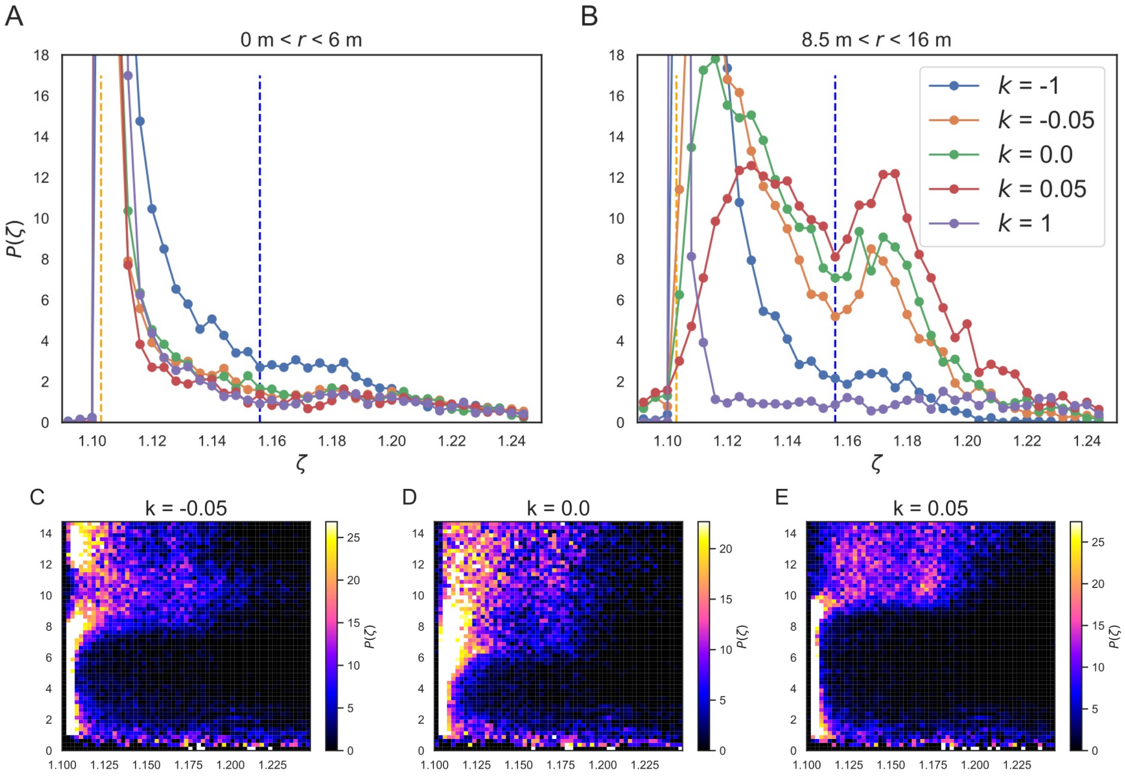

Figure 6.65: Shape factor distribution $P(\zeta)$ for selected values of k. Panel (**A**) and (**B**) show the distribution close to the bottleneck (**A**) and far away (**B**). Panels (**C**)-(**E**) show the heat map of the shape factor distribution $P(\zeta)$ with the distance of the bottleneck r on the $y-$axis and the value of ζ on the $x-$axis close to the phase transition at $k = 0$ (k values are specified in the title of the panel).

order would lead to overlap, forcing the agent closer to the equidistant position due to the body force. This points to the idea that at the interface close to the transition, the system changes from the amorphous to the crystalline state when body forces become relevant.

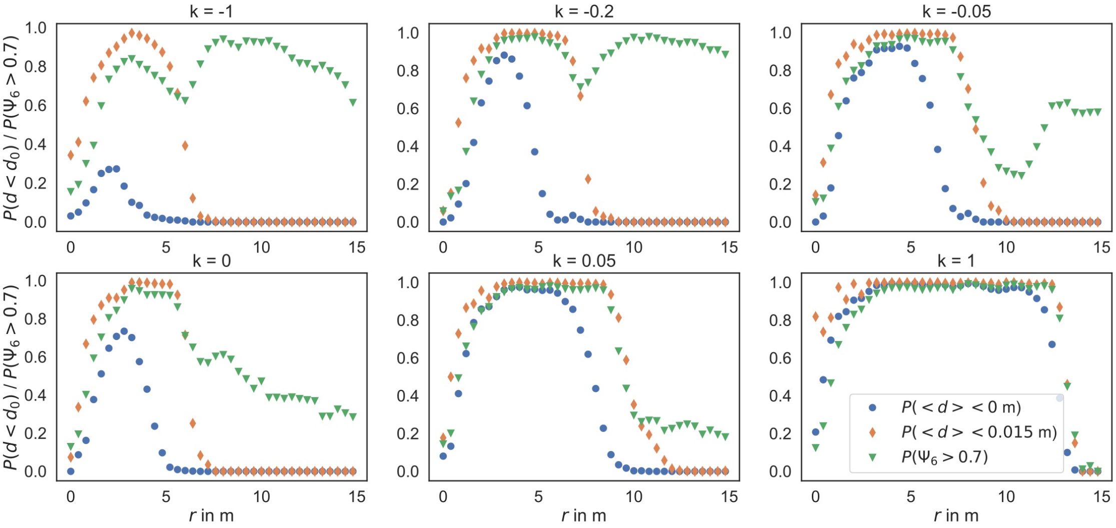

Figure 6.66: The fraction of agents $P(\langle d \rangle < d_0)$ that have a mean neighbor distance $\langle d \rangle$ that is smaller than $d_0 \in \{0, 0.015\}$ m and the hexagonal order $P(\Psi_6 < 0.7)$ in respect to the distance from the bottleneck r. The panels show systems with different cut-off angles k.

Chapter 7

Summary, conclusion and outlook

The study of pedestrian dynamics is an important field when cities seek to pedestrianize car-centric infrastructure and increase the focus on mass transportation. Moreover, large-scale events like concerts, festivals, and protests are frequent and need special consideration, especially in emergency evacuations and overcrowding. A better understanding of the dynamics and interfaces between the interdisciplinary approaches and the microscopic interactions could become an important factor in improving safety and efficiency.

Bottlenecks are a critical feature since they are unavoidable in infrastructure planning. They have a relatively simple geometry but exhibit rich dynamics with self-organizing phenomena like clogging through arch formation in high-density situations. Emergent phenomena and the spatial structure of pedestrians in experiments and simulations are the central topics investigated in this work, introducing solid-state physics and granular materials methods to explore a novel microscopic view of crowds moving through a bottleneck.

The recently discovered phenomenon of decreasing density and lane formation [13, 32] in bottleneck scenarios with narrow corridors leading to the exit is the first focal point in this work that is also published [33, 156]. The simple SCSM model can reproduce these phenomena, first suspected to be an effect of social interactions, surprisingly well. The model uses simple collision avoidance and volume exclusion as the only interaction between agents and a single parameter to model different motivation states. The individual runs of the simulations are conducted with static and homogeneous parameters. The only variables are the corridor width b and the slope factor T, which models motivation's effects. The model reproduces the density increase in front of the bottleneck, the occurrence of lane formation in narrow corridors, and the time to target T_w with respect to the distance r. The model's simplicity demonstrates that the observed effect of lane formation and density increase does not need to consider social effects as an explanation. However, other observations in the data can not be explained with the simple model, like the occurrence of high density for low motivation (see Figure 3.6 A, $b = 5.6\,\mathrm{m}$ and $\rho \approx 7.8\,\mathrm{m}^{-2}$). In general, this approach highlights the challenge of distinguishing effects stemming from social psychology in pedestrian experiments from behavior emerging through self-organization caused by the microscopic interactions of the participants, even in simple scenarios like the bottleneck. This work is a first attempt at distinguishing social and physical effects that lead to emergent behavior. For the future, a more general framework is needed to solve this problem effectively, though there is no simple solution for this at the moment. The best available approach is to use a model with simple interactions and simulate scenarios where social psychological effects are suspected, using homogenous interaction and minimal variables.

The second focal point of this work is tightly related to the general issue of distinguishing the origin of emergent effects in pedestrian dynamics and obtaining a better understanding of microscopic interactions between pedestrians and the influence of the spatial structure in bottleneck scenarios. The main idea is to introduce methods from the related topic of granular materials and glasses discussed in Chapter 4 to analyze the structure in pedestrian crowds and provide a novel perspective into the dynamics of pedestrian experiments and agent-based simulations. This approach introduces measures of the microscopic structure to the field of pedestrian dynamics, making it possible to compare results from granular matter experiments with pedestrian systems.

The measures detect patterns in the system's spatial structure that lead to a larger overall order. Most notably, the hexagonal bond orientation factor Ψ_6 (4.17), the coordination number N_n and the shape factor ζ (4.20) show surprising results when analyzed in the experiments with high and low motivation [1] (Chapter 5).

Even though the density and overall dynamics in the experiments differ significantly between low and high motivation conditions, with the observation of a collective swaying motion in the high motivation case versus a "laminar flow" in the low motivation case, the structure measures indicate almost no difference in the hexagonal order Ψ_6 of the system, the distribution of the shape factor $P(\zeta)$ or the distribution of the coordination number $P(N_n)$. The measures are consistent with a random distribution of particles with volume exclusion or a Leonard-Jones liquid. Simulations of the experiment using the CSM reveal a different structure in the system compared to the empirical data. The hexagonal order factor has a higher value closer to one than compared to the experiment, and the shape factor distribution has distinct peaks near the hexagonal value of the shape factor and the pentagonal value. Between high and low motivation, modeled by the slope factor T and the interactions distance d, the hexagonal structure increases with increasing motivation, detected by an increase in Ψ_6 and an increasing peak near the hexagonal value of $P(\zeta)$. The difference between the CSM and the experiment can not be explained by the polydispersity of the system's agent sizes, even in a system with a wide range of agent radii; the system is closer to a hexagonal structure. One consideration is that the trajectories of the empirical system are measured with an error in the exact position due to the software's limitation and the three-dimensional body's movement. Approximating this error as Gaußian white noise added to the trajectories of the CSM reveals that realistically small amount ($\Delta|\mathbf{x}| \approx 0.07\,\mathrm{m}$) of deviation added to the simulated trajectories reproduces the same lack of hexagonal order and distribution of the shape factor $P(\zeta)$ as in the experiments. Similarly, adding noise to trajectories simulated by the SFM ($\Delta|\mathbf{x}| \approx 0.09\,\mathrm{m}$) shows a similar result. This hints at the possibility that any set of trajectories simulated with an adequate model for pedestrian dynamics can be mapped to the experimental distribution with a sufficient addition of noise. The discovery illustrates the challenge in analyzing the structure of empirical systems because of the difficulty in gaining precise trajectories of the center of gravity moving through space. The injective nature of these errors in the trajectory makes it impossible to estimate a more accurate trajectory from the given data. Though improvements in the trajectory measurement (using, for example, 3d tracking of the body) could help estimate a more precise measure of the structure since when the error is small enough in the measurement, the distribution of the shape factor and the hexagonal order in the system should be closer to the actual distribution, which in turn can be compared to existing models.

The results from the simulations of the SCSM [33, 156], CSM [18], and SFM [16] in small systems with the number of agents being between $N = 55$ and $N = 190$ show interesting behavior in their structure and density. To further investigate this, the aim of Chapter 6 is to analyze the influence of the microscopic interactions on the overall structure, density, and dynamics of the models. To accomplish this, simulations of large systems with the number of agents being in-between $N = 1500$ to $N = 8000$ are needed, which run for a long time between $t = 1500\,\mathrm{s}$ to $t = 10000\,\mathrm{s}$.

To accomplish this, efficient implementations of the models using JuPedSim [141] are run and analyzed on the JURECA cluster provided by the Jülich Super Computing Center (JSC) using several custom-developed scripts to efficiently calculate the structure measures with the help of the data science stack (NumPy, scipy, pandas, etc.) in python. The important features of the CSM are collision avoidance, which ensures volume exclusion in the continuous model, and the interactions between agents with other agents influencing the direction, which reduces the probability of gridlocking the system. The structure analysis in the bottleneck scenario has multiple challenges compared to the granular fluid. The apparent difference is that shaken granular materials are governed by Newtonian physics with symmetrical interactions (especially when the granular consists of symmetric discs or spherical pellets). The pedestrian models consist of active agents that Newtonian dynamics can govern (SFM, but depending on the implementation, the third law can be violated) but do not in velocity-based models, like the CSM and SCSM. Most important is the net flow in the bottleneck system, which is usually not present in the structure analysis of granular fluids. The system has to be separated in space into different sections where the dynamics, density, and structure measures differ.

Close to the bottleneck, the dynamics and structure are less determined by the interaction in the model and more by the physics of continuity in the flow, where the speed of the agents increases steeply with decreasing distance to the bottleneck, producing a more significant difference in speed between neighboring agents. In comparison, regions far from the bottleneck have an isotropic density in close vicinity to one agent. One could assume that in this region, the structure is mainly dictated by the density of the system and the directional interactions.

Surprisingly in the CSM, the hexagonal order measure decreases with further distance to the bottleneck in the isotropic density regime. Further exploration of the parameters governing the directional interaction in the CSM (namely the interaction strength a and the interaction distance d in (6.1)) reveal their influence on the general structure. Taking the experimentally fitted value from Chapter 5 as a pivot and varying the parameters a and d orthogonally shows interesting effects on the structure in the system. Most notably, there is a boundary for the value of a and d at which the system develops a crystalline ring with a high hexagonal order at the boundary that expands in size with increasing a and d. The reason for this is that under certain circumstances, the interactions on the direction vector $\hat{\mathbf{e}}_i$ can nullify the velocity vector $\mathbf{V}_i = \mathbf{0}$, which reduces the density of the system and produces a strong coupling between neighboring agents. In the bulk, the order increases with a and decreases with d.

The result illustrates that short-ranged strong interactions structure the system closer into a hexagonal order, while a long-range interaction causes the system to be discorded with prevalent partial jamming in the bulk. The discovery of the strong influence on the dynamics is further studied when looking at the a-d plane, varying the parameters in a rectangle on the plane for 36 different pairs. Probing the plane is computationally challenging, needing a high amount of computational resources since large-scale simulations of the continuous model are needed for each point on the plane, leading to the output of large data sets. The results illustrate the dynamics and structural heterogeneity on the plane. For example, the shape of the bulk can differ from a narrowing cone towards the bottleneck to a half-circle shape with the bottleneck being its center, depending on both the value of a and d. The measure of hexagonal order $P(\Psi_6 > 0.7)$ and clogging fraction $P(T_c < 1000\,\mathrm{s})$ exhibit a complex topography with multiple valleys and peaks in different regions. The measures are categorized into classes to illustrate the different phases the system can be in from which a hypothetical phase diagram is built. However, it is unclear from the probed space and the number of realizations of each system if and where possible phase transitions can occur. For example, in some regions, the system clogs for all realizations, which could point to a possible clogged phase, where the flow arrests for any initial agent distribution. The diagram illustrates the complexity of the space realized by the directional interactions in the system. Some of the issues discussed in the CSM that lead to unrealistic behavior, like clogging and partial jamming, can be solved by introducing noise in the trajectory, which leads to the introduction of the SCSM. Usually, noise in the trajectory does not majorly influence macroscopic quantities like the density of the system. It helps to avoid undesirable states the system cannot escape otherwise because of its deterministic evolution. The SCSM simulations with a non-zero value for the exponential repulsion ($a > 0$ and $d > 0\,\mathrm{m}$) illustrate how the noise significantly influences the system's structure. The likelihood of clogs in the system is reduced, and the packing fraction is only slightly influenced. However, the system's structure changes significantly far from the bottleneck. In regions with higher density, the system increases its hexagonal order, while in low-density regions (the crystalline ring), the hexagonal order reduces. The noise combined with the speed function self-corrects the system to an equidistant position from its neighbors, favoring hexagonal order. Especially when the density slowly increases (i.e., in the bottleneck with a large value of the noise term σ causing the system to propagate to the exit slowly), the system will reach a high hexagonal order far from the bottleneck. This is evident in the SCSM with $a = 0$ and $\sigma > 0$, where only the noise deviates the direction of the agents from their desired path defined by the floor field. Increasing noise reduces the fraction of clogged systems from 1 to 0 in a sharp transition, separating the system into a clogged phase and a free-flowing phase where the hexagonal order far from the bottleneck increases with increasing noise. Close to the bottleneck, though, the dynamics differ. The noise does not influence the order of the system, illustrating the change in dynamics of the bottleneck system with distance to the exit. This relation is visible in the order density plot, where two sequences appear, with different hexagonal order for the same packing fraction depending on the distance from the bottleneck (and with this, the difference in the flow dynamics). In contrast to the CSM, the SCSM does not show the same behavior for the hexagonal order with distance to the bottleneck. While the CSM has a maximum in the fraction $P(\Psi_6 > 0.7)$ near the bottleneck, in the SCSM, the hexagonal fraction increases from the bottleneck and saturates, only decreasing near the edge. This shows the influence of the directional interactions in a model on the general structure of the system, which should be considered when developing a model. It becomes apparent when comparing the CSM and SCSM to the SFM.

The SFM in its original form [16] with mono-disperse agents represented by discs exhibits very high hexagonal order in the bottleneck scenario, being crystalline in the bulk of the system with only a few defects. Similar to the CSM, exponential interactions determine the dynamics of the system. However, in this case, they represent isotropic forces, which move the particles into equidistant positions to equalize the forces acting on them. Breaking the isotropy in the SFM by only letting the social force of agents in a particular "viewing angle" reveal an interesting effect.

The system undergoes a sharp transition when the viewing angle reaches 180°. Near this transition, the hexagonal order in the system decreases far from the bottleneck while the packing fraction increases with a narrower viewing angle. Further decreasing the viewing angle turns the system into a closely packed crystalline bulk. In this regime, the social force is insufficient to separate the agents leading to the isotropic body force ensuring the volume exclusion.

Near the transition point, the system separates into a crystalline core close to the bottleneck and a disordered region far from the bottleneck with a high number of defects and low hexagonal order. The important factor is at which point the social force is sufficient to separate the agents and at which packing fraction do contact forces become the leading interaction. Near the bottleneck, where the pressure from a large number of surrounding agents increases, the body force is the relevant force, which crystallizes the system. A narrow interface separates the transition to the disordered region.

The isotropy in the original SFM is crucial for the crystalline order in the system. Far from the bottleneck near the transition point, the distribution of the shape factor in the disordered region becomes more comparable with the CSM and SCSM. This observation could be a starting point for further work to compare different model types and kinds of interaction and categorize these into different structure classes.

In shaken granular fluids, the packing fraction is the main indicator for the hexagonal order in the system. Its order increases monotonically with increasing packing fraction, and the shape factor distribution shifts closer to the hexagonal value turning from a bimodal to a monomodal distribution with an exponential tail [186, 188]. In the pedestrian system, it is challenging to probe the system for the influence of the packing fraction since it can not be influenced as an independent variable without influencing other variables in the system. Because of the narrow bottleneck, it is set up to evolve into a certain packing fraction in the stationary state, which other parameters can only influence in the system. In a force-based system like the SFM with isotropic interactions, the packing fraction is tightly related to the hexagonal order since the forces are related to the neighbor distance, and a stronger force reduces the ability of an agent to move away from its equidistant position. In the CSM, a high packing fraction does not structure the agents in that way. Here, a high packing fraction hinders movement since the speed function $V(s)$ is anti-proportional dependent on the distance to the interacting neighbor. If the interaction terms are insufficient to structure the agents, they get quenched into a disordered state. Especially a short reaching (small d) but strong (large a) interaction causes the system to exhibit high hexagonal order. In this case, a lower packing fraction can increase order since the agents have more freedom to move and build a crystalline structure through the interactions. This is observed in the crystalline ring for sufficiently high values of a and d in the exponential repulsion. Besides that special case, a low packing fraction in the CSM is connected to an increasing flow towards the bottleneck, significantly influencing the structure. In the SCSM, the problem of quenching disorder is similar. With small noise in the desired direction, the agents can not sufficiently probe the space before quenched into disorder. With strong noise in the direction, the system slowly contracts into a dense configuration, letting the agents probe their space sufficiently. This leads to order because of the interaction with the speed function combined with a lower packing fraction since the bias towards the exit becomes small compared to the noise. The different models illustrate how the kind of interaction influences the structure with density.

For future research, it would be for one interesting to compare shaken granular matter with the system further. Preferable data from experiments in bottlenecks could be used to compare its structure with the models. For pedestrian modeling, the measures could be probed in other scenarios to analyze the difference in structure under varying conditions. Different bottleneck sizes and geometries would be a next step to compare the model behavior and search for universal behavior.

Bibliography

[1] A. Garcimartín, D. Maza, J. M. Pastor, D. R. Parisi, C. Martín-Gómez, and I. Zuriguel. Redefining the role of obstacles in pedestrian evacuation. *New Journal of Physics*, 20:123025, 2018.

[2] I. Zuriguel, I. Echeverría, D. Maza, R. C. Hidalgo, C. Martín-Gómez, and A. Garcimartín. Contact forces and dynamics of pedestrians evacuating a room: The column effect. *Safety Science*, 121:394–402, 2020.

[3] C. Rogsch, M. Schreckenberg, E. Tribble, W. Klingsch, and T. Kretz. Was It Panic? An Overview About Mass-Emergencies and Their Origins All Over the World for Recent Years. *Pedestrian and Evacuation Dynamics 2008*, pages 743 –755, 2010.

[4] W. A. Buchmueller S. Parameters of pedestrians, pedestrian traffic and walking facilities. *Schriftreihe des IVT, ETH Zürich*, 2007.

[5] U. Weidmann. Transporttechnik der Fußgänger: transporttechnische Eigenschaften des Fußgängerverkehrs, Literaturauswertung. *IVT Schriftenreihe*, 90, 1993.

[6] M. Chraibi, A. Tordeux, A. Schadschneider, and A. Seyfried. Modelling of Pedestrian and Evacuation Dynamics. *Encyclopedia of Complexity and Systems Science*, pages 1–22, 2018.

[7] A. Schadschneider, D. Chowdhury, and K. Nishinari. *Stochastic transport in complex systems: From molecules to vehicles*. Elsevier, 2011.

[8] A. Schadschneider, M. Chraibi, A. Seyfried, A. Tordeux, and J. Zhang. Pedestrian Dynamics: From empirical results to modeling. *Crowd Dynamics, Volume 1*, page 63–102, 2018.

[9] I. von Sivers, A. Templeton, G. Köster, J. Drury, and A. Philippides. Humans do not always act selfishly: Social Identity and helping in emergency evacuation simulation. *Transportation Research Procedia*, 2:585–593, 2014.

[10] I. von Sivers, A. Templeton, F. Künzner, G. Köster, J. Drury, A. Philippides, T. Neckel, and H.-J. Bungartz. Modelling social identification and helping in evacuation simulation. *Safety Science*, 89:288–300, 2016.

[11] A. Templeton, J. Drury, and A. Philippides. From mindless masses to small groups: Conceptualizing collective behavior in crowd modeling. *Review of General Psychology*, 19:215–229, 2015.

[12] E. D. Kuligowski and S. M. Gwynne. The need for behavioral theory in evacuation modeling. *Pedestrian and Evacuation Dynamics 2008*, page 721–732, 2009.

[13] A. Sieben, J. Schumann, and A. Seyfried. Collective phenomena in crowds—Where pedestrian dynamics need social psychology. *PLOS ONE*, 12:1–19, 06 2017.

[14] S. Hoogendoorn and W. Daamen. Self-organization in pedestrian flow. *Traffic and Granular Flow '03*, page 373–382, 2005.

[15] M. Haghani. Empirical methods in pedestrian, crowd and evacuation dynamics: Part II. Field methods and controversial topics. *Safety Science*, 129:104760, 2020.

[16] D. Helbing and P. Molnar. Social force model for pedestrian dynamics. *Physical Review E*, 51:4282, 1995.

[17] D. Helbing, P. Molnár, I. J. Farkas, and K. Bolay. Self-organizing pedestrian movement. *Environment and Planning B: Planning and Design*, 28:361–383, 2001.

[18] A. Tordeux, M. Chraibi, and A. Seyfried. Collision-free speed model for pedestrian dynamics. In *Traffic and Granular Flow'15*, pages 225–232. Springer, 2016.

[19] A. Schadschneider. Cellular Automaton Approach to Pedestrian Dynamics - Theory. *Pedestrian and Evacuation Dynamics*, pages 75–86, 2001.

[20] C. von Krüchten. *Development of a cognitive and decision-based model for pedestrian dynamics.* PhD thesis, Universität zu Köln, 2019.

[21] Q. Xu, M. Chraibi, A. Tordeux, and J. Zhang. Generalized collision-free velocity model for pedestrian dynamics. *Physica A: Statistical Mechanics and its Applications*, 535:122521, 2019.

[22] Q. Xu, M. Chraibi, and A. Seyfried. Anticipation in a velocity-based model for pedestrian dynamics. *Transportation Research Part C: Emerging Technologies*, 133:103464, 2021.

[23] D. Helbing, I. Farkas, and T. Vicsek. Simulating dynamical features of escape panic. *Nature*, 407:487–490, 2000.

[24] A. Garcimartín, I. Zuriguel, J. Pastor, C. Martín-Gómez, and D. Parisi. Experimental evidence of the “Faster Is Slower” effect. *Transportation Research Procedia*, 2:760–767, 2014.

[25] A. Garcimartín, J. Pastor, L. Ferrer, J. Ramos, C. Martín-Gómez, and I. Zuriguel. Flow and clogging of a sheep herd passing through a bottleneck. *Physical Review E*, 91(2):022808, 2015.

[26] P. A. Gago, D. R. Parisi, and L. A. Pugnaloni. “faster is slower” effect in granular flows. *Traffic and Granular Flow ’11*, page 317–324, 2013.

[27] R. L. Stoop and P. Tierno. Clogging and jamming of colloidal monolayers driven across disordered landscapes. *Communications Physics*, 1(1):68, 2018.

[28] C. Feliciani and K. Nishinari. Empirical analysis of the lane formation process in bidirectional pedestrian flow. *Physical Review E*, 94(3):032304, 2016.

[29] T. Vissers, A. Wysocki, M. Rex, H. Löwen, C. P. Royall, A. Imhof, and A. van Blaaderen. Lane formation in driven mixtures of oppositely charged colloids. *Soft Matter*, 7:2352, 2011.

[30] J. Dzubiella, G. Hoffmann, and H. Löwen. Lane formation in colloidal mixtures driven by an external field. *Physical Review E*, 65:021402, 2002.

[31] T. Vicsek, A. Czirok, E. Ben-Jacob, I. Cohen, and O. Shochet. Novel type of phase transition in a system of self-driven particles. *Physical Review Letters*, 75:1226–1229, 1995.

[32] J. Adrian, A. Seyfried, and A. Sieben. Crowds in front of bottlenecks at entrances from the perspective of physics and social psychology. *Journal of the Royal Society Interface*, 17:20190871, 2020.

[33] J. Rzezonka, M. Chraibi, A. Seyfried, B. Hein, and A. Schadschneider. An attempt to distinguish physical and socio-psychological influences on pedestrian bottleneck. *Royal Society Open Science*, 9:211822, 2022.

[34] M. Boltes, J. Zhang, A. Tordeux, A. Schadschneider, and A. Seyfried. Empirical results of pedestrian and evacuation dynamics. *Encyclopedia of Complexity and Systems Science*, 16:1–29, 2018.

[35] J. Zhang, W. Klingsch, A. Schadschneider, and A. Seyfried. Ordering in bidirectional pedestrian flows and its influence on the fundamental diagram. *Journal of Statistical Mechanics: Theory and Experiment*, 2012:P02002, 2012.

[36] J. Porzycki, J. Wąs, L. Hedayatifar, F. Hassanibesheli, and K. Kułakowski. Velocity correlations and spatial dependencies between neighbors in a unidirectional flow of pedestrians. *Physical Review E*, 96:022307, 2017.

[37] J. Porzycki, M. Mycek, R. Lubaś, and J. Wąs. Pedestrian spatial self-organization according to its nearest neighbor position. *Transportation Research Procedia*, 2:201–206, 2014.

[38] C. Feliciani and K. Nishinari. Measurement of congestion and intrinsic risk in pedestrian crowds. *Transportation Research Part C: Emerging Technologies*, 91:124–155, 2018.

[39] C. Cheng, J. Li, and Z. Yao. Ordering leads to multiple fast tracks in simulated collective escape of human crowds. *Soft Matter*, 17:5524–5531, 2021.

[40] J. Adrian, N. Bode, M. Amos, M. Baratchi, M. Beermann, M. Boltes, A. Corbetta, G. Dezecache, J. Drury, Z. Fu, et al. A glossary for research on human crowd dynamics. *Collective Dynamics*, 4:1–13, 2019.

[41] D. Dieckmann. Die Feuersicherheit in Theatern. *Jung München*, 1911.

[42] M. Boltes, J. Adrian, and A.-K. Raytarowski. A hybrid tracking system of full-body motion inside crowds. *Sensors*, 21:2108, 2021.

[43] J. J. Fruin. Pedestrian Planning and Design. Technical Report 538, 1971.

[44] H. E. Nelson. Emergency movement. *The SFPE Handbook of Fire Protection Engineering*, 2002.

[45] V. Predtechenskii and A. Milinskii. Planning for foot traffic flow in buildings, 1978. *Amerind, New Delhi*, 1978.

[46] A. Kirchner, H. Klüpfel, K. Nishinari, A. Schadschneider, and M. Schreckenberg. Discretization effects and the influence of walking speed in cellular automata models for pedestrian dynamics. *Journal of Statistical Mechanics: Theory and Experiment*, 2004:P10011, 2004.

[47] A. Seyfried, B. Steffen, and T. Lippert. Basics of modelling the pedestrian flow. *Physica A: Statistical Mechanics and its Applications*, 368:232–238, 2006.

[48] U. Chattaraj, A. Seyfried, and P. Chakroborty. Comparison of pedestrian fundamental diagram across cultures. *Advances in Complex Systems*, 12:393–405, 2009.

[49] D. Helbing, A. Johansson, and H. Z. Al-Abideen. Dynamics of crowd disasters: An empirical study. *Physical Review E*, 75:046109, 2007.

[50] J. F. Morrall, L. L. Ratnayake, and S. P. N. Comparison of Central Business District Pedestrian Characteristics in Canada and Sri Lanka. *Transportation Research Record*, 1294:57–61, 1991.

[51] J. Wang, M. Boltes, A. Seyfried, A. Tordeux, J. Zhang, V. Ziemer, and W. Weng. Influence of gender on the fundamental diagram and gait characteristics. *Traffic and Granular Flow '17*, page 225–234, 2019.

[52] W. H. Lam, J. Y. Lee, K. Chan, and P. Goh. A generalised function for modeling bi-directional flow effects on indoor walkways in Hong Kong. *Transportation Research Part A: Policy and Practice*, 37:789–810, 2003.

[53] B. Pushkarev and J. Zupan. Capacity of walkways. *Transportation Research Record*, pages 1–15, 1975.

[54] W. Daamen and S. P. Hoogendoorn. Flow-density relations for pedestrian traffic. *Traffic and Granular Flow'05*, page 315–322, 2005.

[55] A. Seyfried, T. Rupprecht, A. Winkens, O. Passon, B. Steffen, W. Klingsch, and M. Boltes. Capacity estimation for emergency exits and bottlenecks. *Interflam 2007*, pages 247–258, 2007.

[56] J. L. Pauls, J. J. Fruin, and J. M. Zupan. Minimum stair width for evacuation, overtaking movement and counterflow—technical bases and suggestions for the past, present and future. In *Pedestrian and evacuation dynamics 2005*, pages 57–69. Springer, 2007.

[57] W. Daamen and S. Hoogendoorn. Experimental research of pedestrian walking behavior. *Transportation Research Record: Journal of the Transportation Research Board*, pages 20–30, 2003.

[58] T. Kretz, A. Grünebohm, and M. Schreckenberg. Experimental study of pedestrian flow through a bottleneck. *Journal of Statistical Mechanics: Theory and Experiment*, 2006:P10014, 2006.

[59] H. C. Muir, D. M. Bottomley, and C. Marrison. Effects of motivation and cabin configuration on emergency aircraft evacuation behavior and rates of Egress. *The International Journal of Aviation Psychology*, 6:57–77, 1996.

[60] W. Tian, W. Song, J. Ma, Z. Fang, A. Seyfried, and J. Liddle. Experimental study of pedestrian behaviors in a corridor based on digital image processing. *Fire Safety Journal*, 47:8–15, 2012.

[61] J. Liddle, A. Seyfried, W. Klingsch, T. Rupprecht, A. Schadschneider, and A. Winkens. An experimental study of pedestrian congestions: influence of bottleneck width and length. *arXiv preprint arXiv:0911.4350*, 2009.

[62] A. Schadschneider and A. Seyfried. Validation of CA models of pedestrian dynamics with fundamental diagrams. *Cybernetics and Systems*, 40:367–389, 2009.

[63] A. Seyfried, T. Rupprecht, A. Winkens, O. Passon, B. Steffen, W. Klingsch, and M. Boltes. Capacity estimation for emergency exits and bottlenecks. *Interflam 2007*, pages 247–258, 2007.

[64] R. Nagai, M. Fukamachi, and T. Nagatani. Evacuation of crawlers and walkers from corridor through an exit. *Physica A: Statistical Mechanics and its Applications*, 367:449–460, 2006.

[65] M. Moussaid, E. G. Guillot, M. Moreau, J. Fehrenbach, O. Chabiron, S. Lemercier, J. Pettré, C. Appert-Rolland, P. Degond, and G. Theraulaz. Traffic instabilities in self-organized pedestrian crowds. *PLoS Computational Biology*, 8:e1002442, 2012.

[66] Pedestrian Data Archive. `http://ped.fz-juelich.de/da/2009bidirFree`. Accessed: 2022-09-10.

[67] K. Yamori. Going with the flow: Micro–macro dynamics in the macrobehavioral patterns of pedestrian crowds. *Psychological Review*, 105:530–557, 1998.

[68] C. Burstedd, A. Kirchner, K. Klauck, A. Schadschneider, and J. Zittartz. Cellular Automaton Approach to Pedestrian Dynamics - Applications. In *Pedestrian and Evacuation Dynamics*, page 87–98. Springer, 2001.

[69] J. Chakrabarti, J. Dzubiella, and H. Löwen. Reentrance effect in the lane formation of driven colloids. *Physical Review E*, 70:012401, 2004.

[70] M. Rex and H. Löwen. Lane formation in oppositely charged colloids driven by an electric field: Chaining and two-dimensional crystallization. *Physical Review E*, 75:051402, 2007.

[71] M. Muramatsu, T. Irie, and T. Nagatani. Jamming transition in pedestrian counter flow. *Physica A: Statistical Mechanics and its Applications*, 267:487–498, 1999.

[72] J. Zhang, W. Klingsch, A. Schadschneider, and A. Seyfried. Ordering in bidirectional pedestrian flows and its influence on the fundamental diagram. *Journal of Statistical Mechanics: Theory and Experiment*, 2012:P02002, 2012.

[73] A. Seyfried, M. Boltes, J. Kähler, W. Klingsch, A. Portz, T. Rupprecht, A. Schadschneider, B. Steffen, and A. Winkens. Enhanced empirical data for the fundamental diagram and the flow through bottlenecks. *Pedestrian and Evacuation Dynamics 2008*, pages 145–156, 2010.

[74] A. Seyfried, A. Portz, and A. Schadschneider. Phase coexistence in congested states of pedestrian dynamics. *Lecture Notes in Computer Science*, 6350:496–505, 2010.

[75] R. Barlovic, L. Santen, A. Schadschneider, and M. Schreckenberg. Metastable states in cellular automata for traffic flow. *The European Physical Journal B-Condensed Matter and Complex Systems*, 5:793–800, 1998.

[76] A. Garcimartín, I. Zuriguel, L. A. Pugnaloni, and A. Janda. Shape of jamming arches in two-dimensional deposits of granular materials. *Physical Review E*, 82:031306, 2010.

[77] R. Arevalo and I. Zuriguel. Clogging of granular materials in silos: Effect of gravity and outlet size. *Soft Matter*, 12:123–130, 2016.

[78] S. G. Leyva, R. L. Stoop, P. Tierno, and I. Pagonabarraga. Dynamics and clogging of colloidal monolayers magnetically driven through a heterogeneous landscape. *Soft Matter*, 16:6985–6992, 2020.

[79] A. Garcimartin, J. M. Pastor, C. Martin-Gomez, D. Parisi, and I. Zuriguel. Pedestrian Data Archive. `http://ped.fz-juelich.de/extda/garcimartin2013`. Accessed: 2022-09-10.

[80] A. Garcimartín, J. M. Pastor, C. Martín-Gómez, D. Parisi, and I. Zuriguel. Pedestrian collective motion in competitive room evacuation. *Scientific reports*, 7:10792, 2017.

[81] A. Garcimartin, D. R. Parisi, J. M. Pastor, C. Martín-Gomez, and I. Zuriguel. Flow of pedestrians through narrow doors with different competitiveness. *Journal of Statistical Mechanics: Theory and Experiment*, 2016:043402, 2016.

[82] J. M. Pastor, A. Garcimartín, P. A. Gago, J. P. Peralta, C. Martín-Gómez, L. M. Ferrer, D. Maza, D. R. Parisi, L. A. Pugnaloni, and I. Zuriguel. Experimental proof of faster-is-slower in systems of frictional particles flowing through constrictions. *Physical Review E*, 92:062817, 2015.

[83] R. Caitano, B. Guerrero, R. González, I. Zuriguel, and A. Garcimartín. Characterization of the clogging transition in vibrated granular media. *Physical Review Letters*, 127:148002, 2021.

[84] M. Haghani, M. Sarvi, and Z. Shahhoseini. When 'push' does not come to 'shove': Revisiting 'faster is slower' in collective egress of human crowds. *Transportation Research Part A: Policy and Practice*, 122:51, 2019.

[85] M. Haghani and M. Sarvi. Simulating pedestrian flow through narrow exits. *Physics Letters A*, 383:110–120, 2019.

[86] S. P. Hoogendoorn and W. Daamen. Pedestrian behavior at bottlenecks. *Transportation Science*, 39:147–159, 2005.

[87] A. Seyfried, O. Passon, B. Steffen, M. Boltes, T. Rupprecht, and W. Klingsch. New insights into pedestrian flow through bottlenecks. *Transportation Science*, 43:395–406, 2009.

[88] A. Schadschneider, W. Klingsch, H. Klüpfel, T. Kretz, C. Rogsch, and A. Seyfried. *Evacuation Dynamics: Empirical Results, Modeling and Applications*, pages 3142–3176. Springer, New York, 2009.

[89] M. Haghani, E. Cristiani, N. W. F. Bode, M. Boltes, and A. Corbetta. Panic, Irrationality, and Herding: Three Ambiguous Terms in Crowd Dynamics Research. *Journal of Advanced Transportation*, 2019:1–58, 2019.

[90] E. Üsten, H. Lügering, and A. Sieben. Pushing and Non-pushing Forward Motion in Crowds: A Systematic Psychological Observation Method for Rating Individual Behavior in Pedestrian Dynamics. *Collective Dynamics*, 7:1–16, 2022.

[91] A. B. Peter M. Kielar, Daniel H. Biedermann. MomenTUMv2. Technical Report TUM-I1653, 2016.

[92] J. Ondřej, J. Pettré, A.-H. Olivier, and S. Donikian. A synthetic-vision based steering approach for crowd simulation. *ACM Transactions on Graphics (TOG)*, 29:1–9, 2010.

[93] D. Helbing. A Fluid-Dynamic Model for the Movement of Pedestrians. *Complex Systems*, 6:391–415, 1998.

[94] L. Henderson. On the fluid mechanics of human crowd motion. *Transportation Research*, 8:509–515, 1974.

[95] L. Huang, S. Wong, M. Zhang, C.-W. Shu, and W. H. Lam. Revisiting Hughes' dynamic continuum model for pedestrian flow and the development of an efficient solution algorithm. *Transportation Research Part B: Methodological*, 43:127–141, 2009.

[96] C. M. Henein and T. White. Agent-based modelling of forces in crowds. In *International Workshop on Multi-Agent Systems and Agent-Based Simulation*, pages 173–184. Springer, 2004.

[97] R. Hughes. The flow of large crowds of pedestrians. *Mathematics and Computers in Simulation*, 53:367–370, 2000.

[98] R. L. Hughes. A continuum theory for the flow of pedestrians. *Transportation Research Part B: Methodological*, 36:507–535, 2002.

[99] R. L. Hughes. The flow of human crowds. *Annual Review of Fluid Mechanics*, 35:169–182, 2003.

[100] F. S. Hänseler, W. H. Lam, M. Bierlaire, G. Lederrey, and M. Nikolic. A dynamic network loading model for anisotropic and congested pedestrian flows. *Transportation Research Part B: Methodological*, 95:149–168, 2017.

[101] M. Fischer, G. Jankowiak, and M.-T. Wolfram. Micro- and Macroscopic Modeling of Crowding and Pushing in Corridors. *Networks and Heterogeneous Media*, 15:405, 2020.

[102] A. Tordeux, G. Lämmel, F. S. Hänseler, and B. Steffen. A mesoscopic model for large-scale simulation of pedestrian dynamics. *Transportation Research Part C: Emerging Technologies*, 93:128–147, 2018.

[103] H.-h. Tian, Y.-f. Wei, X. Yu, W.-z. Lu, et al. Lattice hydrodynamic model with bidirectional pedestrian flow. *Physica A: Statistical Mechanics and its Applications*, 388:2895–2902, 2009.

[104] K. Hirai and K. Tarui. A simulation of the behavior of a crowd in panic. In *Proceedings of the 1975 International Conference on Cybernetics and Society*, pages 409–411, 1975.

[105] M. Chraibi, A. Seyfried, and A. Schadschneider. Generalized centrifugal-force model for pedestrian dynamics. *Physical Review E*, 82:046111, 2010.

[106] L. A. Pipes. An operational analysis of traffic dynamics. *Journal of Applied Physics*, 24:274–281, 1953.

[107] X. Chen, M. Treiber, V. Kanagaraj, and H. Li. Social Force models for pedestrian traffic – state of the art. *Transport Reviews*, 38:625–653, 2017.

[108] D. R. Parisi, M. Gilman, and H. Moldovan. A modification of the social force model can reproduce experimental data of pedestrian flows in normal conditions. *Physica A: Statistical Mechanics and its Applications*, 388:3600–3608, 2009.

[109] I. M. Sticco, G. A. Frank, F. E. Cornes, and C. O. Dorso. A re-examination of the role of friction in the original Social Force Model. *Safety Science*, 121:42–53, 2020.

[110] A. Portz and A. Seyfried. Modeling Stop-and-Go Waves in Pedestrian Dynamics. *Lecture Notes in Computer Science*, 6068:561–568, 2010.

[111] M. Chraibi and A. Seyfried. Pedestrian dynamics with event-driven simulation. In *Pedestrian and Evacuation Dynamics 2008*, pages 713–718. Springer, 2009.

[112] A. Schadschneider, C. Eilhardt, S. Nowak, and R. Will. Towards a calibration of the floor field cellular automaton. In *Pedestrian and Evacuation Dynamics*, pages 557–566. Springer, 2011.

[113] M. Zhou, H. Dong, F.-Y. Wang, Q. Wang, and X. Yang. Modeling and simulation of pedestrian dynamical behavior based on a fuzzy logic approach. *Information Sciences*, 360:112–130, 2016.

[114] W. Lv, W.-g. Song, J. Ma, and Z.-m. Fang. A two-dimensional optimal velocity model for unidirectional pedestrian flow based on pedestrian's visual hindrance field. *IEEE Transactions on Intelligent Transportation Systems*, 14:1753–1763, 2013.

[115] T. I. Lakoba, D. J. Kaup, and N. M. Finkelstein. Modifications of the Helbing-Molnar-Farkas-Vicsek social force model for pedestrian evolution. *Simulation*, 81:339–352, 2005.

[116] M. Chraibi, A. Schadschneider, and A. Seyfried. On force-based modeling of Pedestrian Dynamics. *Modeling, Simulation and Visual Analysis of Crowds*, page 23–41, 2013.

[117] M. Chraibi. Oscillating behavior within the social force model. *arXiv preprint arXiv:1412.1133*, 2014.

[118] T. Kretz. On oscillations in the social force model. *Physica A: Statistical Mechanics and its Applications*, 438:272–285, 2015.

[119] W. Yu, R. Chen, L.-Y. Dong, and S. Dai. Centrifugal force model for pedestrian dynamics. *Physical Review E*, 72:026112, 2005.

[120] R. Löhner. On the modeling of Pedestrian Motion. *Applied Mathematical Modelling*, 34:366–382, 2010.

[121] M. Chraibi, M. Freialdenhoven, A. Schadschneider, and A. Seyfried. Modeling the desired direction in a force-based model for pedestrian dynamics. In *Traffic and Granular Flow'11*, pages 263–275. Springer, 2013.

[122] G. Köster, F. Treml, and M. Gödel. Avoiding numerical pitfalls in social force models. *Physical Review E*, 87:063305, 2013.

[123] G. B. Ermentrout and L. Edelstein-Keshet. Cellular automata approaches to biological modeling. *Journal of Theoretical Biology*, 160:97–133, 1993.

[124] K. Nagel and M. Schreckenberg. A cellular automaton model for freeway traffic. *Journal de Physique I*, 2:2221–2229, 1992.

[125] V. J. Blue and J. L. Adler. Cellular automata microsimulation of bidirectional pedestrian flows. *Transportation Research Record*, 1678:135–141, 1999.

[126] C. Burstedde, K. Klauck, A. Schadschneider, and J. Zittartz. Simulation of pedestrian dynamics using a two-dimensional cellular automaton. *Physica A: Statistical Mechanics and its Applications*, 295:507–525, 2001.

[127] A. Kirchner and A. Schadschneider. Simulation of evacuation processes using a bionics-inspired cellular automaton model for pedestrian dynamics. *Physica A: Statistical Mechanics and its Applications*, 312:260–276, 2002.

[128] A. Kirchner, K. Nishinari, and A. Schadschneider. Friction effects and clogging in a cellular automaton model for pedestrian dynamics. *Physical Review E*, 67:056122, 2003.

[129] E. Ben-Jacob. From snowflake formation to growth of bacterial colonies II: Cooperative formation of complex colonial patterns. *Contemporary Physics*, 38:205–241, 1997.

[130] S. Bouzat and M. N. Kuperman. Game theory in models of pedestrian room evacuation. *Physical Review E*, 89:032806, 2014.

[131] S. Nowak and A. Schadschneider. Quantitative analysis of pedestrian counterflow in a cellular automaton model. *Physical Review E*, 85:066128, 2012.

[132] L. Luo, Z. Fu, H. Cheng, and L. Yang. Update schemes of multi-velocity floor field cellular automaton for pedestrian dynamics. *Physica A: Statistical Mechanics and its Applications*, 491:946–963, 2018.

[133] M. Schultz and H. Fricke. Stochastic transition model for discrete agent movements. *Lecture Notes in Computer Science*, page 506–512, 2010.

[134] A. Kirchner, A. Namazi, K. Nishinari, and A. Schadschneider. Role of conflicts in the floor field cellular automaton model for pedestrian dynamics. In *2nd International Conference on Pedestrians and Evacuation Dynamics*, pages 51–62, 2003.

[135] B. Maury and J. Venel. A mathematical framework for a crowd motion model. *Comptes Rendus Mathematique*, 346:1245–1250, 2008.

[136] P. Fiorini and Z. Shiller. Motion planning in dynamic environments using velocity obstacles. *The International Journal of Robotics Research*, 17:760–772, 1998.

[137] J. Van den Berg, M. Lin, and D. Manocha. Reciprocal velocity obstacles for real-time multi-agent navigation. In *2008 IEEE international conference on robotics and automation*, pages 1928–1935. Ieee, 2008.

[138] J. van den Berg, S. J. Guy, M. Lin, and D. Manocha. Reciprocal N-body collision avoidance. *Springer Tracts in Advanced Robotics*, page 3–19, 2011.

[139] J. Ondrej, J. Pettre, A.-H. Olivier, and S. Donikian. A synthetic-vision based steering approach for crowd simulation. *ACM SIGGRAPH 2010 papers on - SIGGRAPH '10*, 2010.

[140] Q. Xu, M. Chraibi, and A. Seyfried. Prolonged clogs in bottleneck simulations for pedestrian dynamics. *Physica A: Statistical Mechanics and its Applications*, 573:125934, 2021.

[141] JuPedSim. `https://www.jupedsim.org/`. Accessed: 2020-08-03.

[142] A. Graf. Automated Routing in Pedestrian Dynamics. *Master Thesis (Fachhochschule Aachen, Campus Jülich)*, 2015.

[143] S. Nowak and A. Schadschneider. A cellular automaton approach for lane formation in pedestrian counterflow. In *Traffic and Granular Flow'11*, pages 149–160. Springer, 2013.

[144] J. D. González, M. L. Sandoval, and J. Delgado. Social field model to simulate bidirectional pedestrian flow using cellular automata. In *Traffic and Granular Flow'11*, pages 197–206. Springer, 2013.

[145] R. Bailo, J. A. Carrillo, and P. Degond. Pedestrian models based on rational behaviour. In *Crowd Dynamics, Volume 1*, pages 259–292. Springer, 2018.

[146] Y. Tajima, K. Takimoto, and T. Nagatani. Scaling of pedestrian channel flow with a bottleneck. *Physica A: Statistical Mechanics and its Applications*, 294:257–268, 2001.

[147] M. Chraibi, T. Ezaki, A. Tordeux, K. Nishinari, A. Schadschneider, and A. Seyfried. Jamming transitions in force-based models for pedestrian dynamics. *Physical Review E*, 92:042809, 2015.

[148] A. Tordeux, M. Chraibi, A. Schadschneider, and A. Seyfried. Influence of the number of predecessors in interaction within acceleration-based flow models. *Journal of Physics A: Mathematical and Theoretical*, 50:345102, 2017.

[149] Y. Zhao, T. Lu, M. Li, and L. Tian. The self-slowing behavioral mechanism of pedestrians under normal and emergency conditions. *Physics Letters A*, 381:3149–3160, 2017.

[150] C. Eilhardt and A. Schadschneider. Stochastic headway dependent velocity model for 1d pedestrian dynamics at high densities. *Transportation Research Procedia*, 2:400–405, 2014.

[151] A. Tordeux, A. Schadschneider, and S. Lassarre. Noise-induced stop-and-go dynamics. In *International Conference on Traffic and Granular Flow*, pages 337–345. Springer, 2017.

[152] F. Dietrich, S. Disselnkötter, and G. Köster. How to get a model in pedestrian dynamics to produce stop and go waves. In *Traffic and Granular Flow'15*, pages 161–168. Springer, 2016.

[153] A. Tordeux and A. Schadschneider. White and relaxed noises in optimal velocity models for pedestrian flow with stop-and-go waves. *Journal of Physics A: Mathematical and Theoretical*, 49:185101, 2016.

[154] M. Twarogowska, P. Goatin, and R. Duvigneau. Comparative study of macroscopic pedestrian models. *Transportation Research Procedia*, 2:477–485, 2014.

[155] H. E. Stanley. Freezing by heating. *Nature*, 404:718–719, 2000.

[156] J. Rzezonka, A. Seyfried, B. Hein, M. Chraibi, and A. Schadschneider. Numerical study of bottleneck flow with varying corridor width and motivation using a speed-based model. *Collective Dynamics*, 6:1, 2022.

[157] G. Voronoi. Nouvelles applications des paramètres continus à la théorie des formes quadratiques. premier Mémoire. sur quelques propriétés des formes quadratiques positives parfaites. *Journal für die reine und angewandte Mathematik (Crelles Journal)*, 1908:97–102, 1908.

[158] B. Steffen and A. Seyfried. Methods for measuring pedestrian density, flow, speed and direction with minimal scatter. *Physica A: Statistical Mechanics and its Applications*, 389:1902–1910, 2010.

[159] J. Adrian, A. Seyfried, and A. Sieben. Experimental Data. `http://ped.fz-juelich.de/da/2018crowdqueue`, 2018. Accessed: 2020-09-01.

[160] S. Paetzke, M. Boltes, and A. Seyfried. Influence of individual factors on fundamental diagrams of pedestrians. *Physica A: Statistical Mechanics and its Applications*, 595:127077, 2022.

[161] J. Zhang, S. Cao, D. Salden, and J. Ma. Homogeneity and activeness of crowd on aged pedestrian dynamics. *Procedia Computer Science*, 83:361–368, 2016.

[162] S. Cao, J. Zhang, D. Salden, J. Ma, R. Zhang, et al. Pedestrian dynamics in single-file movement of crowd with different age compositions. *Physical Review E*, 94:012312, 2016.

[163] R. Subaih, M. Maree, M. Chraibi, S. Awad, and T. Zanoon. Experimental Investigation on the Alleged Gender-Differences in Pedestrian Dynamics: A Study Reveals No Gender Differences in Pedestrian Movement Behavior. *IEEE Access*, 8:33748–33757, 2020.

[164] V. Ziemer. *Mikroskopische Fundamentaldiagramme der Fußgängerdynamik - Empirische Untersuchung von Experimenten eindimensionaler Bewegung sowie quantitative Beschreibung von Stau-Charakteristika*. Dissertation, Bergische Universität Wuppertal, 2019.

[165] D. Yanagisawa, A. Tomoeda, and K. Nishinari. Improvement of pedestrian flow by slow rhythm. *Physical Reveiw E*, 85:016111, Jan 2012.

[166] G. Zeng, A. Schadschneider, J. Zhang, S. Wei, W. Song, and R. Ba. Experimental study on the effect of background music on pedestrian movement at high density. *Physics Letters A*, 383:1011–1018, 2019.

[167] S. Cao, P. Wang, M. Yao, and W. Song. Dynamic analysis of pedestrian movement in single-file experiment under limited visibility. *Communications in Nonlinear Science and Numerical Simulation*, 69:329–342, 2019.

[168] S. Buchmueller and U. Weidmann. Parameters of pedestrians, pedestrian traffic and walking facilities. *IVT Schriftenreihe*, 132, 2006.

[169] Pedestrian Data Archive. `https://ped.fz-juelich.de/`. Accessed: 2020-08-11.

[170] R. Hidalgo, D. R. Parisi, and I. Zuriguel. Simulating competitive egress of noncircular pedestrians. *Physical Review E*, 95:042319, 2017.

[171] S. Chen, F. Alonso-Marroquin, J. Busch, R. C. Hidalgo, C. Sathianandan, Á. Ramírez-Gómez, and P. Mora. Scaling laws in granular flow and pedestrian flow. In *AIP Conference Proceedings*, volume 1542, pages 157–160. American Institute of Physics, 2013.

[172] I. M. Sticco, F. E. Cornes, G. A. Frank, and C. O. Dorso. Beyond the faster-is-slower effect. *Physical Review E*, 96:052303, 2017.

[173] K. To, P.-Y. Lai, and H. K. Pak. Jamming of granular flow in a two-dimensional hopper. *Physical Review Letters*, 86:71–74, 2001.

[174] A. Nicolas and I. Touloupas. Origin of the correlations between exit times in pedestrian flows through a bottleneck. *Journal of Statistical Mechanics: Theory and Experiment*, 2018:013402, 2018.

[175] I. M. Sticco, G. A. Frank, and C. O. Dorso. Effects of the body force on the pedestrian and the evacuation dynamics. *Safety science*, 129:104829, 2020.

[176] V. Dossetti, S. Bouzat, and M. Kuperman. Behavioral effects in room evacuation models. *Physica A: Statistical Mechanics and its Applications*, 479:193–202, 2017.

[177] G. A. Patterson, P. Fierens, F. Sangiuliano Jimka, P. Koenig, G. A., I. Zuriguel, L. Pgnaloni, and P. D.R. Clogging transition of vibration-driven vehicles passing through constrictions. *Physical Review Letters*, 119, 2017.

[178] T. Barois, J.-F. Boudet, N. Lanchon, J. S. Lintuvuori, and H. Kellay. Characterization and control of a bottleneck-induced traffic-jam transition for self-propelled particles in a track. *Physical Review E*, 99, 2019.

[179] G. A. Patterson, D. Sornette, and D. R. Parisi. Properties of balanced flows with bottlenecks: Common stylized facts in finance and vibration-driven vehicles. *Physical Review E*, 101:042302, 2020.

[180] D. Parisi and C. Dorso. Microscopic dynamics of pedestrian evacuation. *Physica A: Statistical Mechanics and its Applications*, 354:606–618, 2005.

[181] A. Nicolas, M. Kuperman, S. Ibanez, S. Bouzat, and C. Appert-Rolland. Mechanical response of dense pedestrian crowds to the crossing of intruders. *Scientific Reports*, 9, 2019.

[182] I. Karamouzas, B. Skinner, and S. J. Guy. Universal power law governing pedestrian interactions. *Physical Review Letters*, 113, 2014.

[183] N. Bain and D. Bartolo. Critical mingling and universal correlations in model binary active liquids. *Nature Communications*, 8:15969, 2017.

[184] A. Nicolas. Dense Pedestrian Crowds Versus Granular Packings: An Analogy of Sorts. *Springer Proceedings in Physics Traffic and Granular Flow 2019*, page 411–419, 2020.

[185] C. Kittel. *Introduction to Solid State Physics.* Wiley, 1976.

[186] F. Moučka and I. Nezbeda. Detection and characterization of structural changes in the hard-disk fluid under freezing and melting conditions. *Physical Review Letters*, 94(4):040601, 2005.

[187] K. Binder, S. Sengupta, and P. Nielaba. The liquid-solid transition of hard discs: First-order transition or Kosterlitz-thouless-Halperin-Nelson-young scenario? *Journal of Physics: Condensed Matter*, 14:2323–2333, 2002.

[188] P. M. Reis, R. A. Ingale, and M. D. Shattuck. Crystallization of a quasi-two-dimensional granular fluid. *Physical Review Letters*, 96(25):258001, 2006.

[189] J. Olafsen and J. Urbach. Two-dimensional melting far from equilibrium in a granular monolayer. *Physical Review Letters*, 95(9):098002, 2005.

[190] A. J. Liu and S. R. Nagel. The jamming transition and the marginally jammed solid. *Annual Review of Condensed Matter Physics*, 1:347–369, 2010.

[191] F. Sausset and G. Tarjus. Comment on “correlation between dynamic heterogeneity and medium-range order in two-dimensional glass-forming liquids”. *Physical Review Letters*, 100:099601, 2008.

[192] T. D. Bennett and S. Horike. Liquid, glass and amorphous solid states of coordination polymers and metal–organic frameworks. *Nature Reviews Materials*, 3:431–440, 2018.

[193] A. Bhateja and D. V. Khakhar. Analysis of granular rheology in a quasi-two-dimensional slow flow by means of discrete element method based simulations. *Physics of Fluids*, 32:013301, 2020.

[194] A. Reinmüller, E. Oğuz, R. Messina, H. Löwen, H. Schöpe, and T. Palberg. Colloidal crystallization in the quasi-two-dimensional induced by electrolyte gradients. *The Journal of Chemical Physics*, 136:164505, 2012.

[195] C. R. Berardi, K. Barros, J. F. Douglas, and W. Losert. Direct observation of stringlike collective motion in a two-dimensional driven granular fluid. *Physical Review E*, 81:041301, 2010.

[196] M. G. Clerc, P. Cordero, J. Dunstan, K. Huff, N. Mujica, D. Risso, and G. Varas. Liquid–solid-like transition in quasi-one-dimensional driven granular media. *Nature Physics*, 4:249–254, 2008.

[197] S. Gokhale, K. H. Nagamanasa, R. Ganapathy, and A. K. Sood. Grain growth and grain boundary dynamics in colloidal polycrystals. *Soft Matter*, 9:6634, 2013.

[198] M. Kramár, A. Goullet, L. Kondic, and K. Mischaikow. Persistence of force networks in compressed granular media. *Physical Review E*, 87:042207, 2013.

[199] A. Lobkovsky, F. V. Reyes, and J. Urbach. The effects of forcing and dissipation on phase transitions in thin granular layers. *The European Physical Journal Special Topics*, 179:113–122, 2009.

[200] J. Olafsen and J. Urbach. Two-dimensional melting far from equilibrium in a granular monolayer. *Physical Review Letters*, 95:098002, 2005.

[201] A. Panaitescu, K. A. Reddy, and A. Kudrolli. Nucleation and crystal growth in sheared granular sphere packings. *Physical Review Letters*, 108:108001, 2012.

[202] F. V. Reyes and J. S. Urbach. Effect of inelasticity on the phase transitions of a thin vibrated granular layer. *Physical Review E*, 78:051301, 2008.

[203] V. W. A. D. Villeneuve, L. Derendorp, D. Verboekend, E. C. M. Vermolen, W. K. Kegel, H. N. W. Lekkerkerker, and R. P. A. Dullens. Grain boundary pinning in doped hard sphere crystals. *Soft Matter*, 5:2448, 2009.

[204] S. Ardanza-Trevijano, I. Zuriguel, R. Arévalo, and D. Maza. Topological analysis of tapped granular media using persistent homology. *Physical Reveiw E*, 89:052212, 2014.

[205] M. Guzmán and R. Soto. Critical phenomena in quasi-two-dimensional vibrated granular systems. *Physical Reveiw E*, 97:012907, 2018.

[206] T. Hamanaka, H. Shiba, and A. Onuki. Plastic flow in polycrystal states in a binary mixture. *Physical Reveiw E*, 77:042501, 2008.

[207] J. S. Olafsen and J. S. Urbach. Clustering, Order, and Collapse in a Driven Granular Monolayer. *Physical Review Letters*, 81:4369–4372, 1998.

[208] A. C. Mitus, H. Weber, and D. Marx. Local structure analysis of the hard-disk fluid near melting. *Physical Review E*, 55:6855–6859, 1997.

[209] Persistant Homology. `"https://towardsdatascience.com/persistent-homology-with-examples-1974d4b9c3d0`.

[210] Y. Wang. Granular packing as model glass formers. *Chinese Physics B*, 26:014503, 2017.

[211] C. Tapia-Ignacio, J. Garcia-Serrano, and F. Donado. Nonvibrating granular model for a glass-forming liquid: Equilibration and aging. *Physical Reveiw E*, 94:062902, 2016.

[212] A. J. Liu and S. R. Nagel. Jamming is not just cool any more. *Nature*, 396:21–22, 1998.

[213] T. S. Majmudar, M. Sperl, S. Luding, and R. P. Behringer. Jamming Transition in Granular Systems. *Physical Reveiw Letter*, 98:058001, 2007.

[214] B. Delaunay. Sur la sphère vide. A la mémoire de Georges Voronoï. *Bulletin de l'Académie des Sciences de l'URSS. Classe des sciences mathématiques et na*, pages 793–800, 1934.

[215] J. M. Kosterlitz and D. J. Thouless. Long range order and metastability in two dimensional solids and superfluids. (Application of dislocation theory). *Journal of Physics C: Solid State Physics*, 5:L124, 1972.

[216] J. M. Kosterlitz and D. J. Thouless. Ordering, metastability and phase transitions in two-dimensional systems. *Journal of Physics C: Solid State Physics*, 6:1181–1203, 1973.

[217] B. I. Halperin and D. R. Nelson. Theory of two-dimensional melting. *Physical Review Letters*, 41:121–124, 1978.

[218] A. Baskaran and M. C. Marchetti. Enhanced Diffusion and Ordering of Self-Propelled Rods. *Physical Reveiw Letter*, 101:268101, 2008.

[219] J. Jones. On the determination of molecular fields.—i. from the variation of the viscosity of a gas with temperature. *Proceedings of the Royal Society of London. Series A, Containing Papers of a Mathematical and Physical Character*, 106:441–462, 1924.

[220] Lennard-Jones liquid simulation. `https://www.triplespark.net/sim/ljfluid/`. Accessed: 2022-09-30.

[221] A. L. Thorneywork, J. L. Abbott, D. G. Aarts, P. Keim, and R. P. Dullens. Bond-orientational order and Frank's constant in two-dimensional colloidal hard spheres. *Journal of Physics: Condensed Matter*, 30:104003, 2018.

[222] J. Hoshen and R. Kopelman. Percolation and cluster distribution. I. Cluster multiple labeling technique and critical concentration algorithm. *Physical Review B*, 14:3438–3445, 1976.

[223] T. Frühwirth. *Constraint Handling Rules.* Cambridge University Press, 2009.

[224] Union and find examples. `https://en.wikipedia.org/wiki/Disjoint-set_data_structure`. Accessed: 2022-09-30.

[225] A. Garcimartín, I. Zuriguel, D. Maza, J. Pastor, D. Parisi, and C. Martín-Gómez. Pedestrian Data Archive. `http://ped.fz-juelich.de/extda/garcimartin2017`, 2017. Accessed: 2022-09-05.

[226] Supplemantery videos. `https://fz-juelich.sciebo.de/s/1IyTdgpyIkwWSI1`. Accessed: 2022-27-10.

[227] E. L. Kaplan and P. Meier. Nonparametric estimation from incomplete observations. *Journal of the American Statistical Association*, 53:457–481, 1958.

[228] J. W. Vaupel, K. G. Manton, and E. Stallard. The impact of heterogeneity in individual frailty on the dynamics of mortality. *Demography*, 16:439–454, 1979.

[229] M. A. McDowell, C. D. Fryar, and C. L. Ogden. Anthropometric reference data for children and adults: United States, 1988-1994. *Vital and Health Statistics. Series 11, Data from the national health survey*, pages 1–68, 2009.

[230] M. Boltes and A. Seyfried. Collecting pedestrian trajectories. *Neurocomputing*, 100:127–133, 2013.

[231] R. M. Nedderman et al. *Statics and Kinematics of Granular Materials*, volume 352. Cambridge University Press Cambridge, 1992.

[232] F. Alonso-Marroquin and P. Mora. Beverloo law for hopper flow derived from self-similar profiles. *Granular Matter*, 23:1–8, 2021.

[233] E. A. Lazar, J. Lu, and C. H. Rycroft. Voronoi cell analysis: The shapes of particle systems. *American Journal of Physics*, 90:469–480, 2022.

[234] D. Helbing, I. J. Farkas, and T. Vicsek. Freezing by heating in a driven mesoscopic system. *Physical Review Letters*, 84:1240, 2000.

Appendix A

Appendix

A.1 Supplement Section 3

Estimation of agent diameter

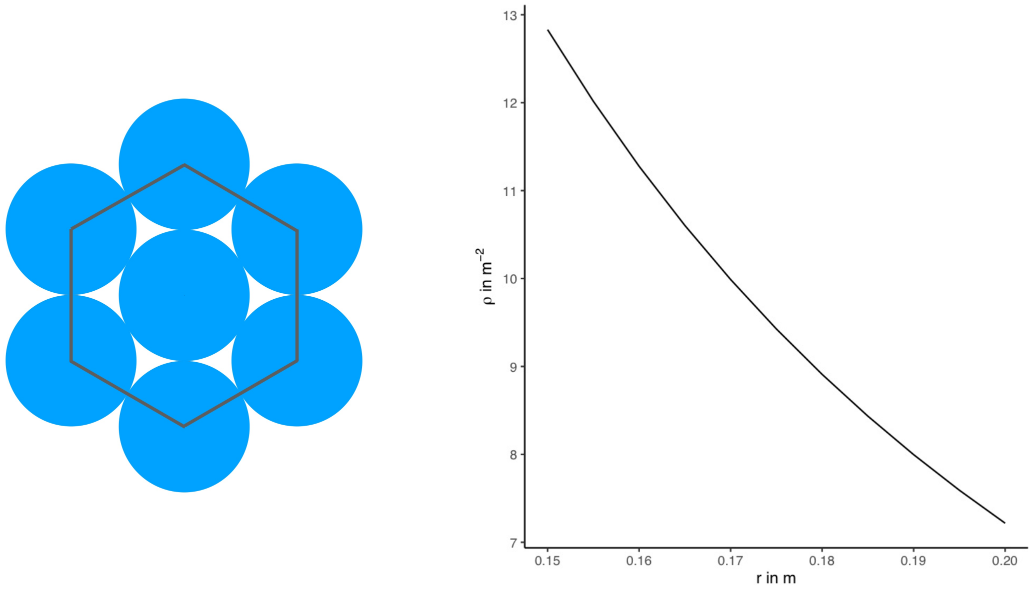

Figure S1: Circle packing left: Circles in hexagonal packing. The area inside the grey hexagon is used to determine the packing density in (A.1). **Right** The hexagonal packing density in respect to the radius r of a disc.

In 2d, the maximal packing fraction that can be achieved (by a hexagonal packing) of identical disks with radius $r = l/2$ is $\eta = \frac{\pi}{\sqrt{12}} \approx 0.9069$ (Figure S1 left). This provides an estimate for the upper bound of the density

$$\rho_{max} = \frac{\eta}{r^2 \pi}. \tag{A.1}$$

Figure S1 right illustrates equation (A.1). The maximal experimental density ρ is slightly above 9 m^{-2} (see Figure 3.4). For the simulations a value of $r_a = 0.175$ m is chosen, which corresponds to a maximal density of about 9.4 m^{-2}, as this yields good results. The agent size chosen corresponds to a rather small shoulder width, since e.g. [5] gives an approximate adult shoulder width of $l = 0.46$ m. However, the circle diameter of 0.35 m could be seen as a contracted pedestrian.

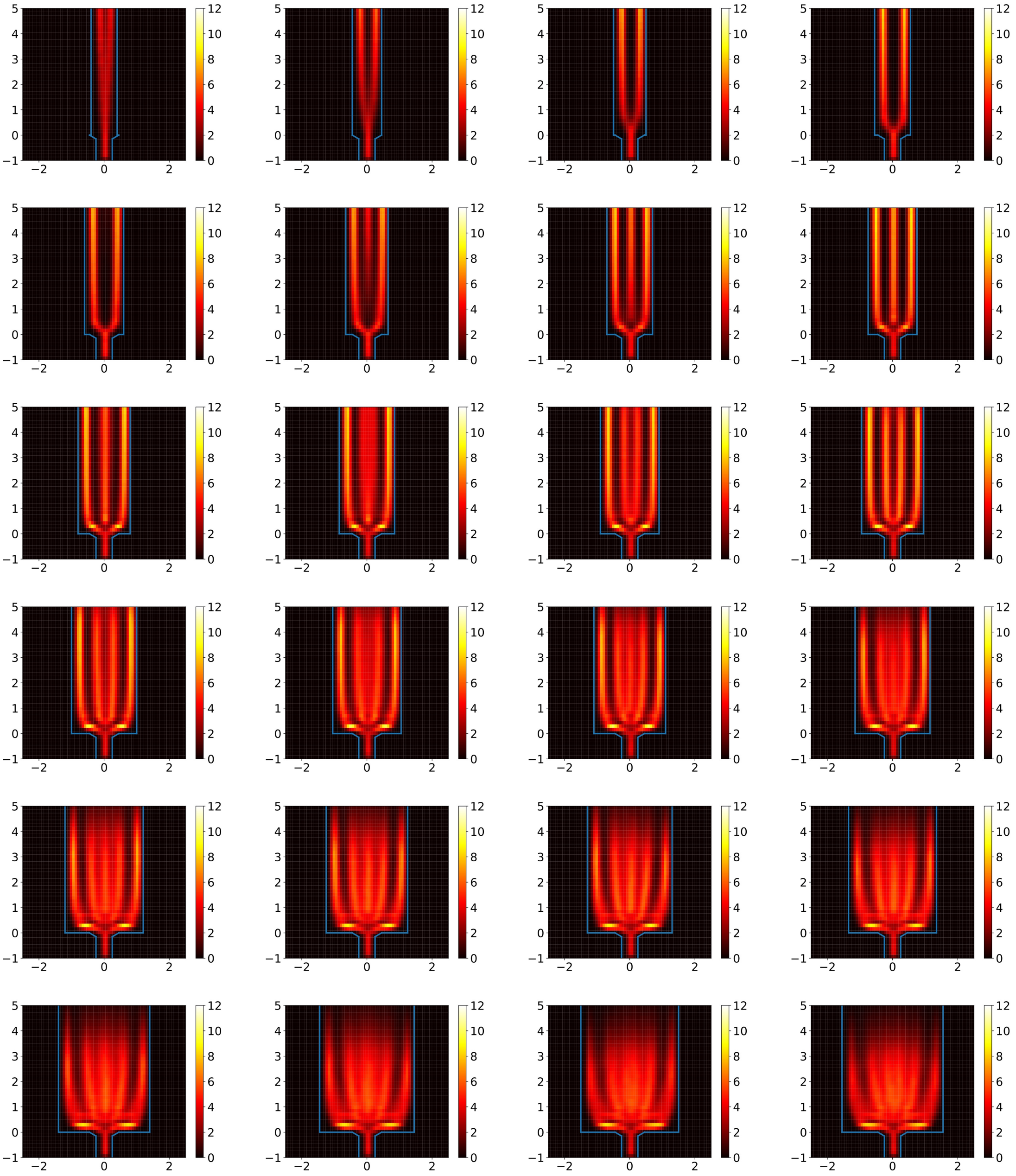

Figure S2: Mean density fields for all 500 runs from 10 to 30 s for $T = 1.3$ s for $b = 0.8$ m to $b = 3.1$ m in 0.1 m steps.

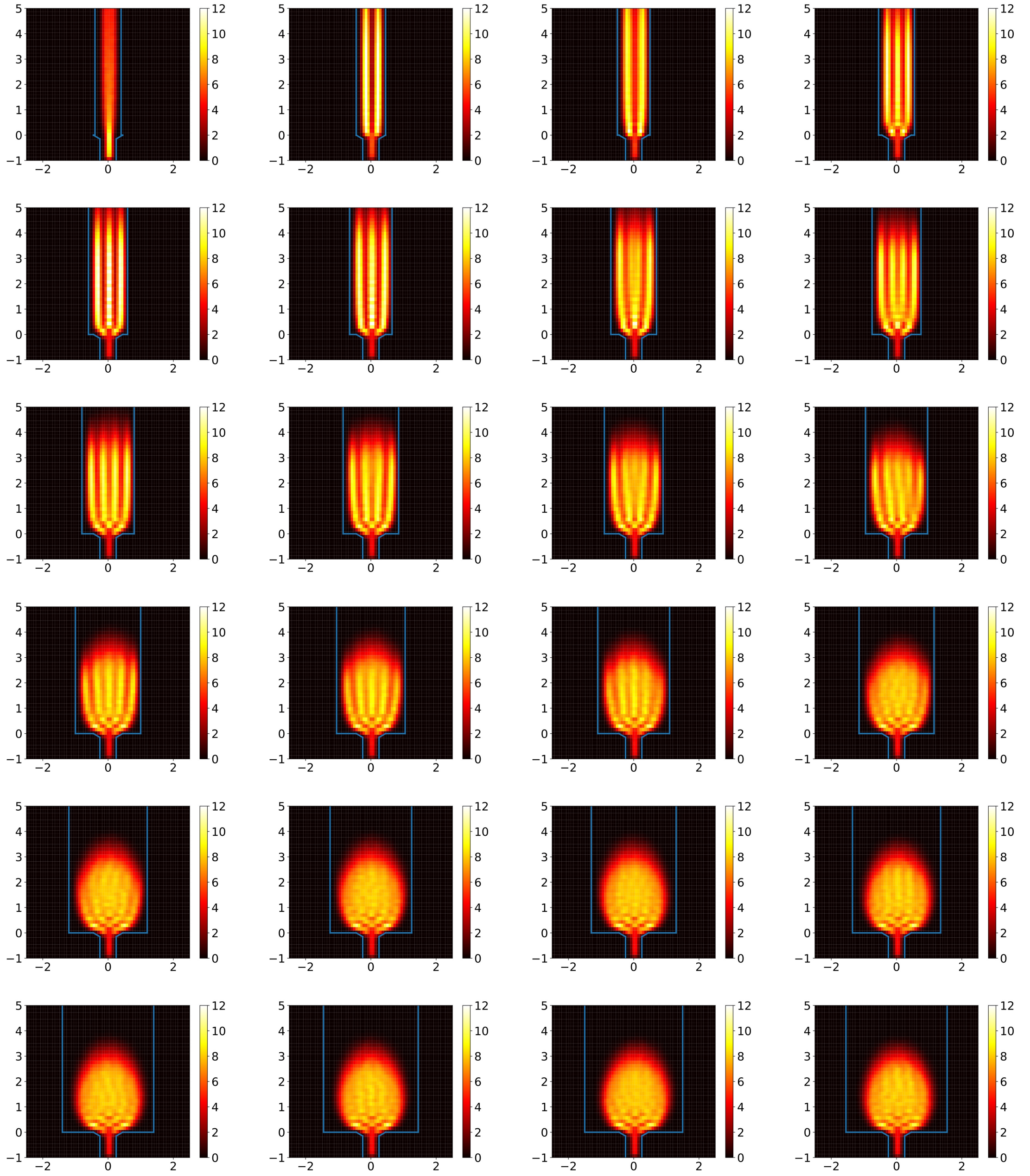

Figure S3: Mean density fields for all 500 runs from 10 to 30 s for $T = 0.1$ s for $b = 0.8$ m to $b = 3.1$ m in 0.1 m steps.

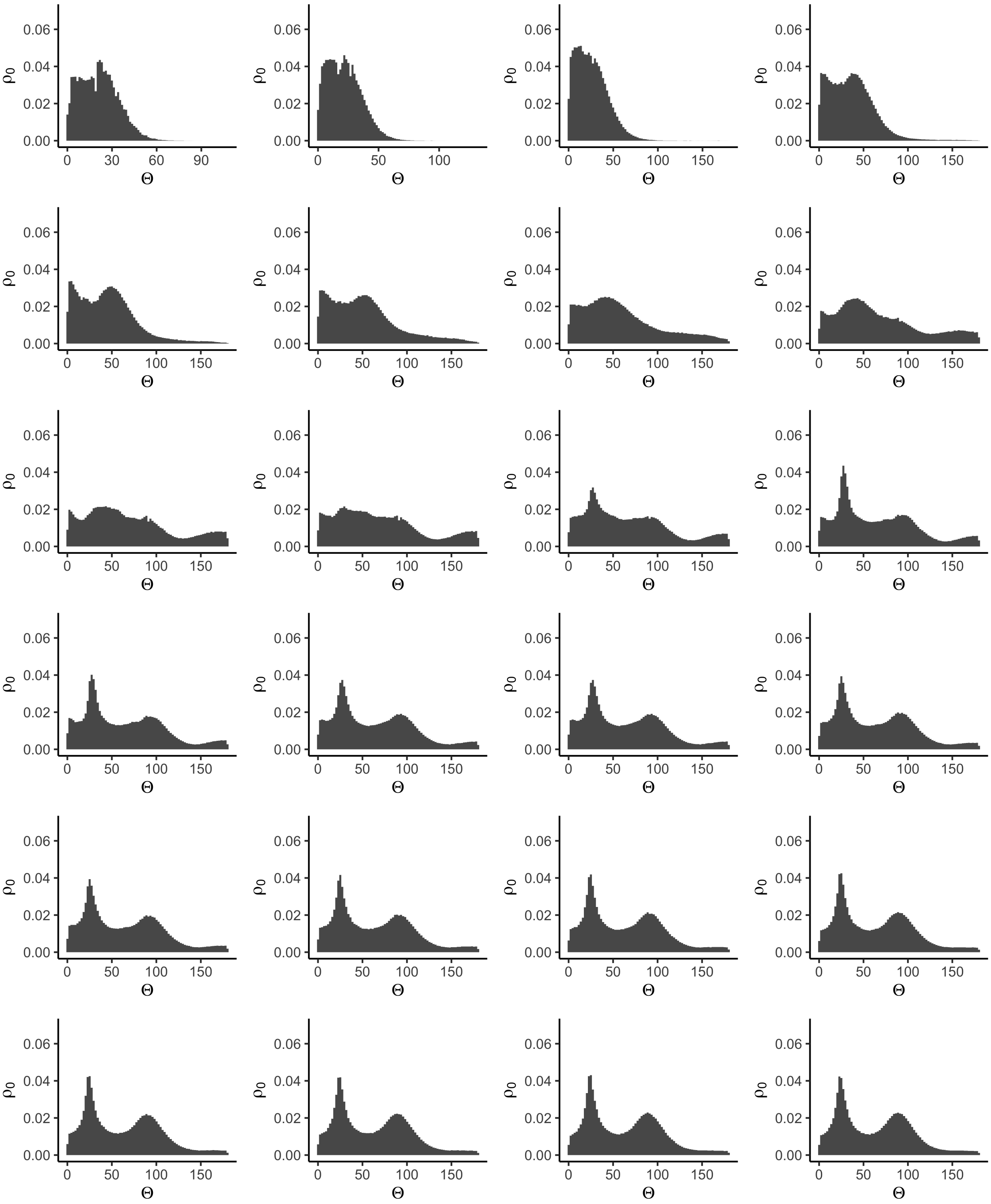

Figure S4: Interaction angle distribution for all 500 simulations from 10 s for $T = 1.3\,\mathrm{s}$. The corridor width starts at $b = 0.8\,\mathrm{m}$ and increases in 0.1 m steps to $b = 2.9\,\mathrm{m}$.

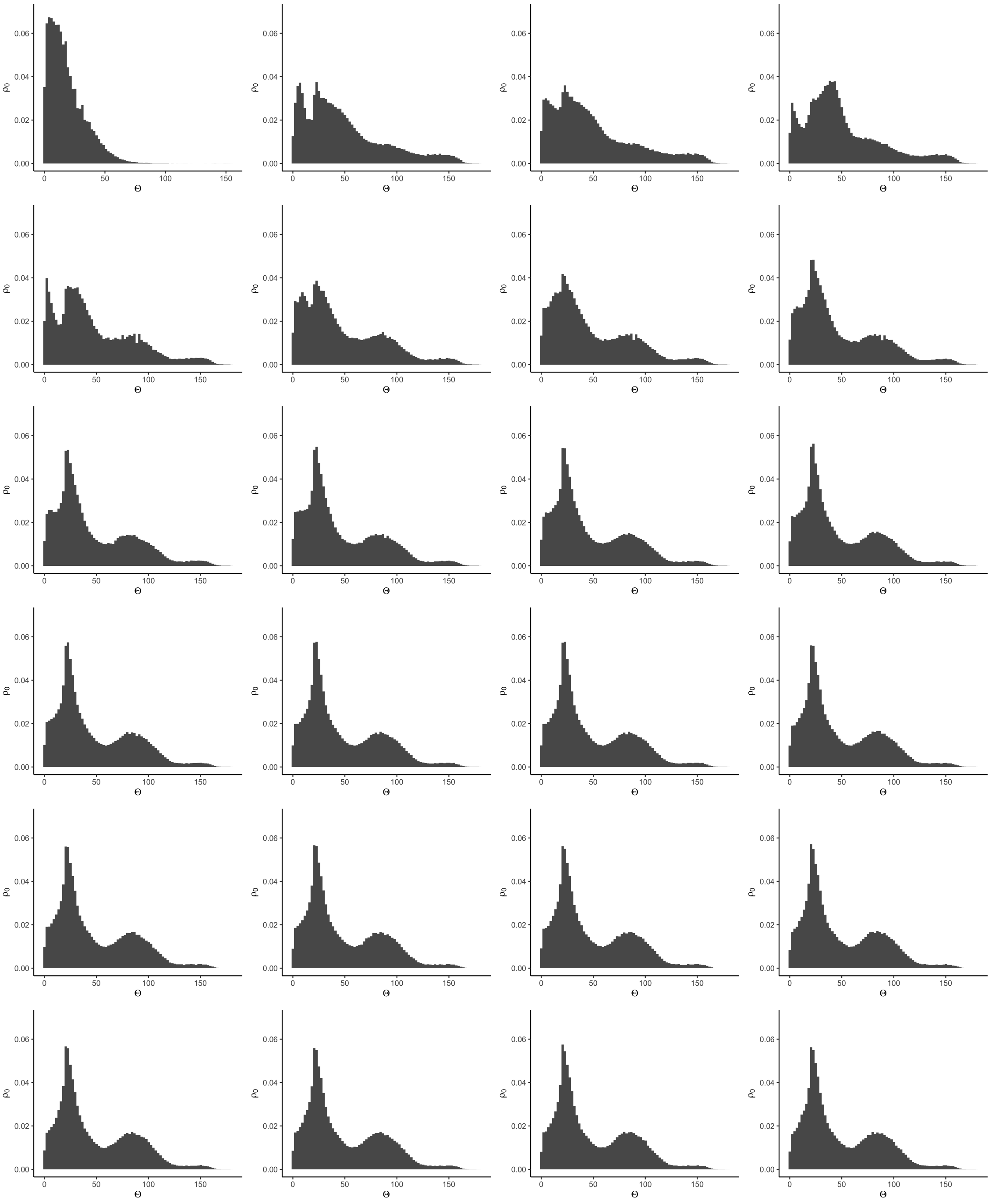

Figure S5: Interaction angle distribution for all 500 simulations from 10 s for $T = 0.1\,\mathrm{s}$. The corridor width starts at $b = 0.8\,\mathrm{m}$ and increases in 0.1 m steps to $b = 2.9\,\mathrm{m}$.

A.2 Supplemantery figures Section 5

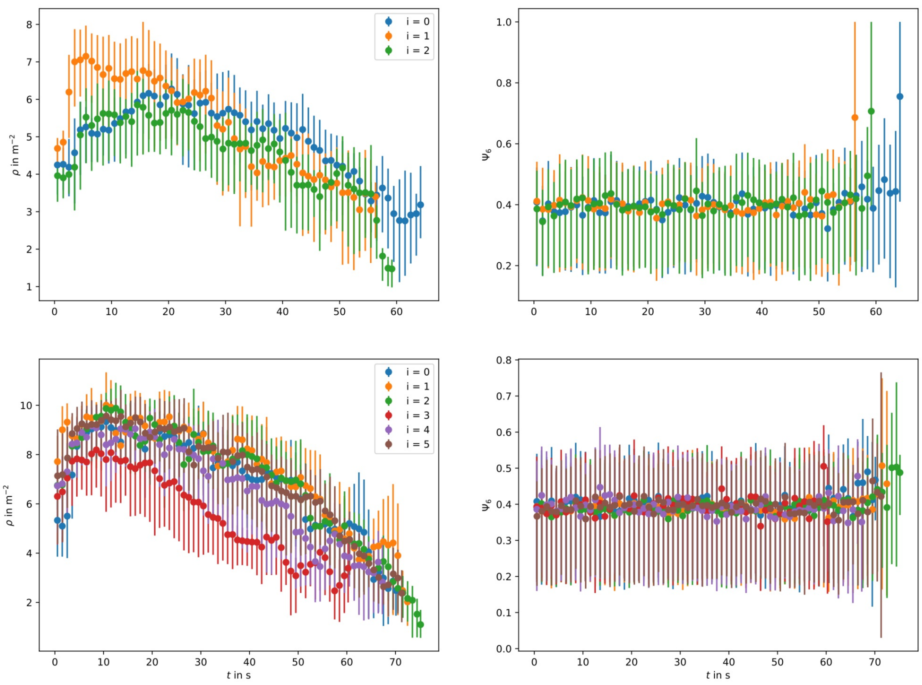

Figure S6: (Left): Density time series for the experimental runs i for low motivation (top) and high motivation *bottom*. **Right:** Analogous to left for the orientational order Ψ_6.

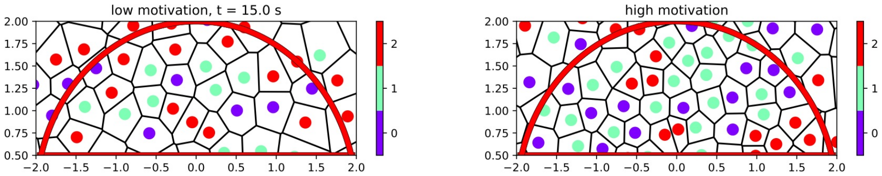

Figure S7: (Left): Density time series for the experimental runs i for low motivation (top) and high motivation *bottom*. **Right:** Analogous to left for the orientational order Ψ_6.

A.3 Supplemantery figures Section 5.1

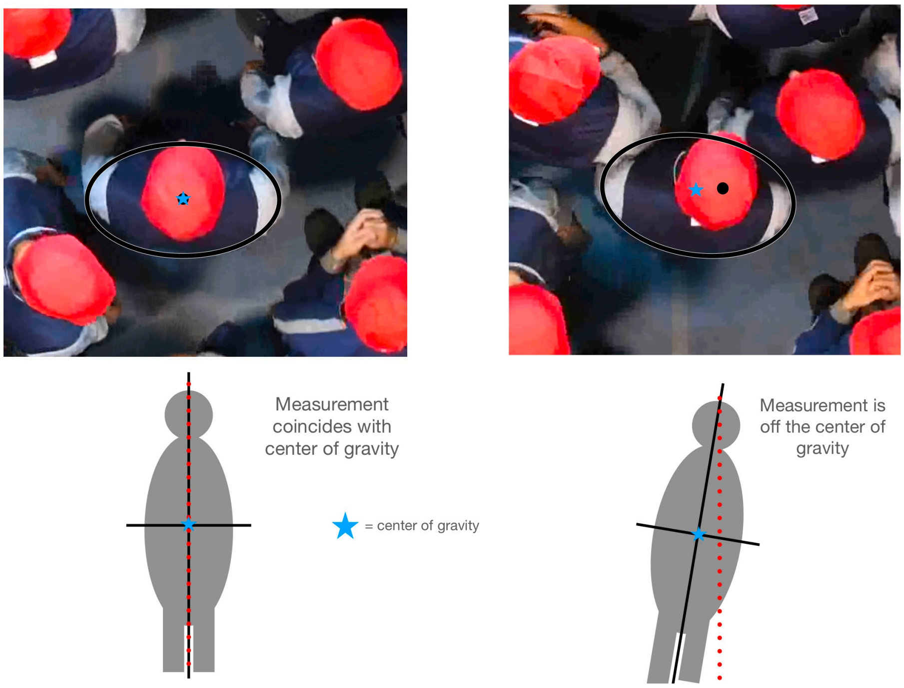

Figure S8: Illustration of body sway in the experimental trajectories and a simplified illustration of the difference in measuring the head position and the center of gravity. The red dots show the mapping of the position measures by the head position (black dots on the snapshot of the experiment). The blue star shows the position of the center of gravity.

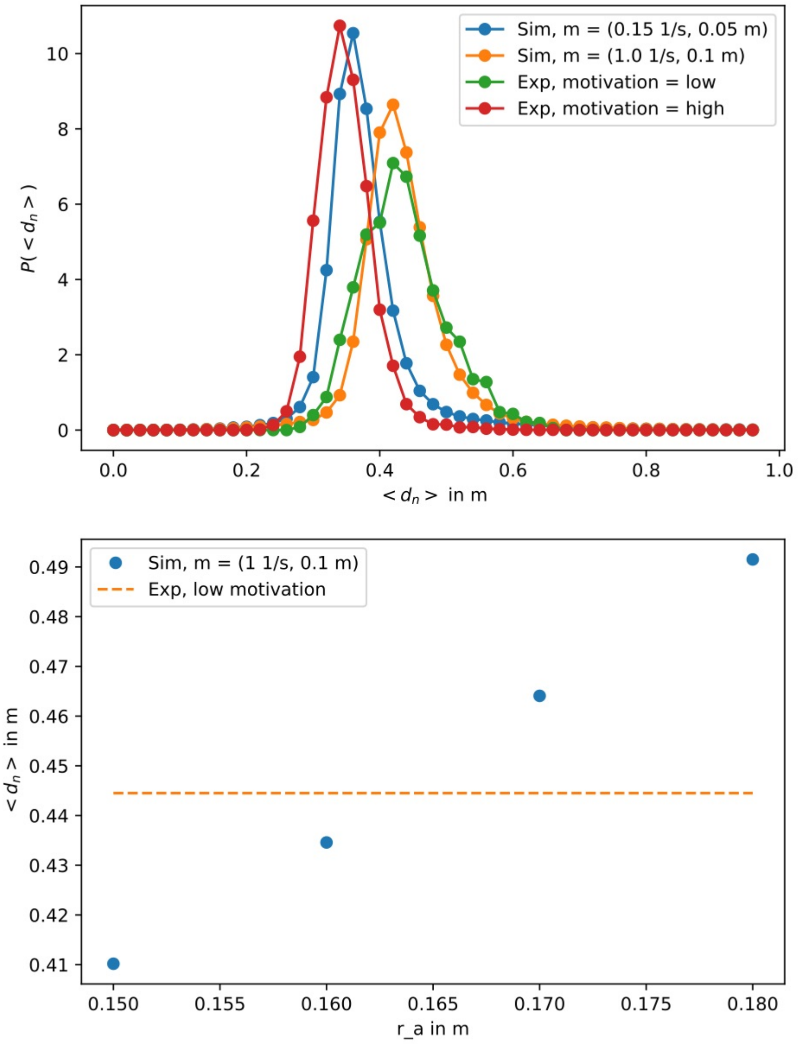

Figure S9: Top: Comparison of the distribution of the mean-neighbor-distance $\langle d_n \rangle$ between the simulations and the experiments for high motivation ($m = (0.15\text{ s}, 0.05\text{ m})$) and low motivation ($m = (1\text{ s}, 0.1\text{ m})$). **Bottom:** Comparison of the mean mean-neighbor-distance $\langle\langle d_n \rangle\rangle$ in respect to the agent radius r_a in the simulation with $m = (1\text{ s}, 0.1\text{ m})$, compared to the value of low motivation experiment (dashed line) .

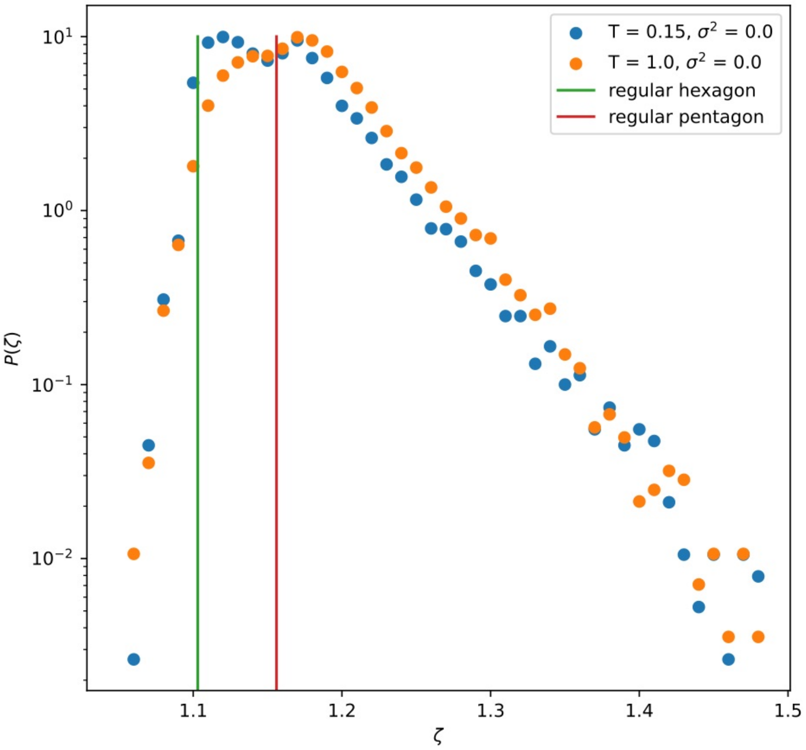

Figure S10: Log-plot of the shape-factor distribution in Figure 5.9.

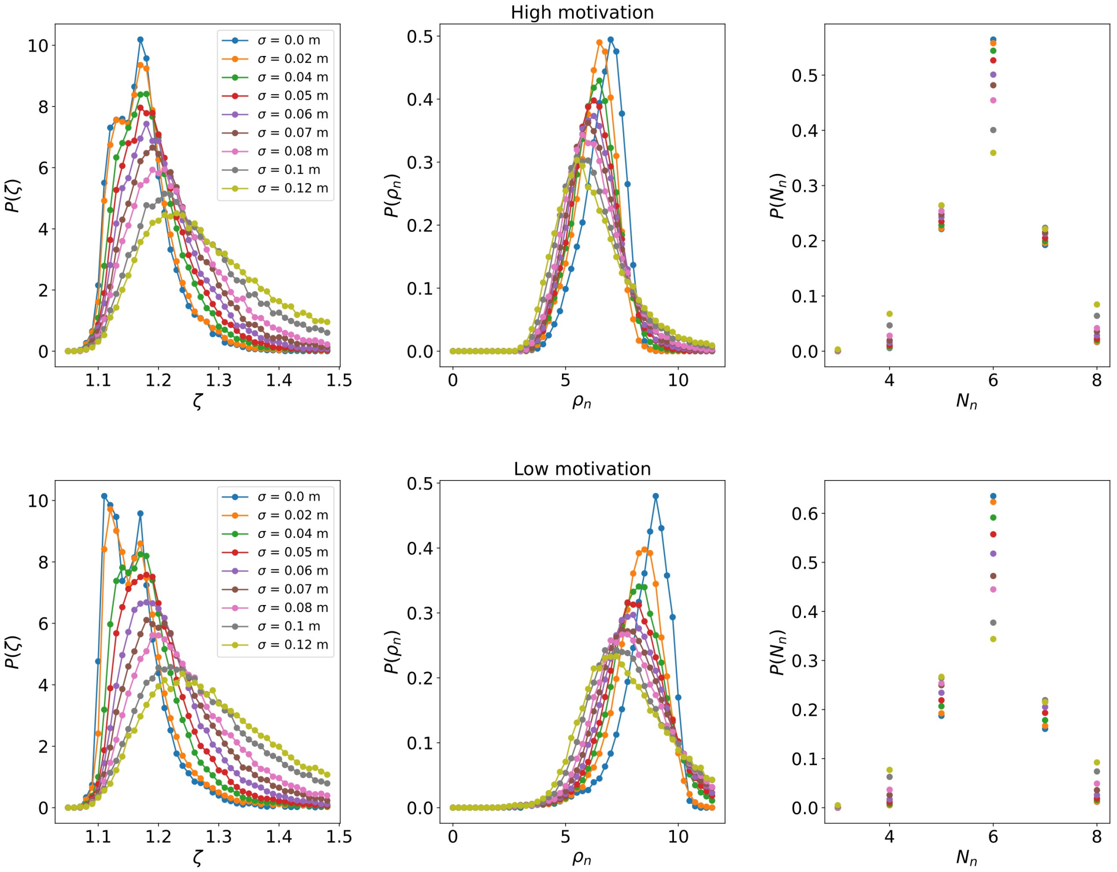

Figure S11: Distribution of the shape factor ζ, neighbor density ρ_n and coordination number N_n for the CSM simulations (dots) and the experiments (crosses).

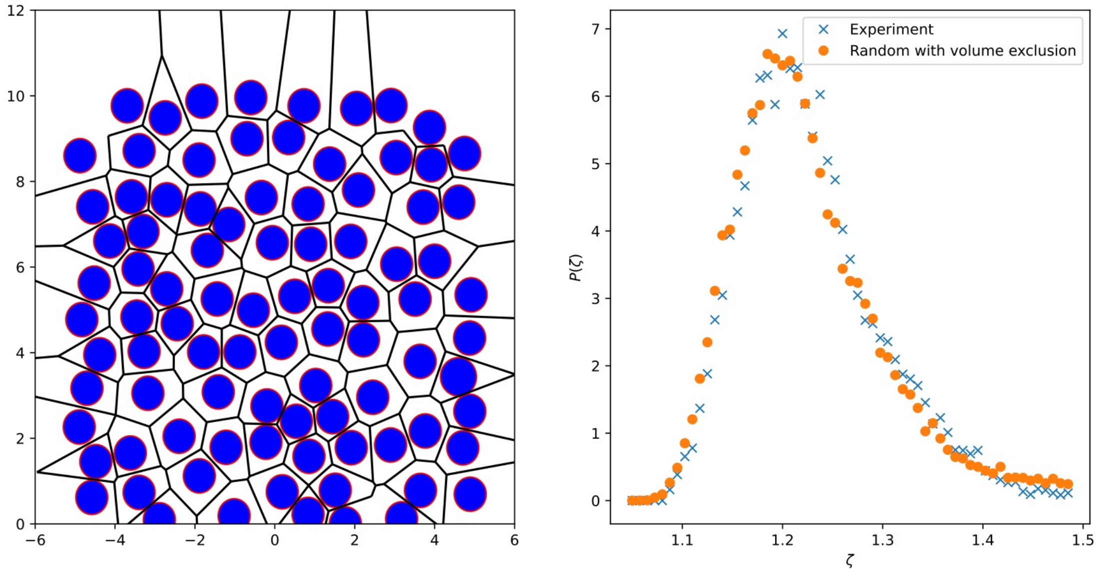

Figure S12: Left: Example scatter-plot with Voronoi cells of randomly distributed particles with volume exclusion. **Right** Distribution of the shape-factor $P(\zeta)$ of 500 systems with $N = 90$ particles distributed in a 10×10 m space with $l = 0.4$ m (orange dots) and the experiments with low motivation (blue crosses).

A.4 Social force model simulations

Parameter	Variable	Value
Corridor width	b	8 m
Desired velocity	v_0	1.0 m/s
Acceleration time	τ	0.5 s
Agent size	l	0.32 m
Interaction strength	A	2000 N
Interaction range	d	0.08 m
Population	N	190
Elasticity	K	1.2×10^5 kg s^{-2}
Friction	κ	2.4×10^5 kg (m s)$^{-1}$
Floor field resolution	Δh	0.01 m
Wall avoidance distance	d_w	0.25 m
Time step in simulation	Δt	0.0005 s
Agent mass	m_a	80 kg

Table A.1: Summary of model parameters and their values

Simulations of the experiment [1] with low motivation using the social force model (SFM) [23] with monodisperse agents analogous to the simulations described in section 5.1. The parameters of the model used in the simulation are summarized in table A.1. The system was simulated 20 times with random initial conditions. Analogous to section 5.3 noise is added onto the simulated trajectories. Figure S13 depicts the time series of the mean neighbor-density $\langle \rho_n \rangle$ and the orientational order parameter $\langle \Psi_6 \rangle$. Similarly to the CSM simulations, the mean neighbor-density $\langle \rho_n \rangle$ fits closely to the experimental data but the $\langle \Psi_6 \rangle$ is much larger close to about $\langle \Psi_6 \rangle \approx 0.8$ for $t \geq 3$ s which is a significant hexagonal order in the system and significantly higher than in the CSM with $\langle \Psi_6 \rangle \approx 0.5$. Figure S15 A shows analogous to Figure S11 the distributions of the measures for ζ, ρ_n and N_n. The SFM displays a closed back hexagonal order. The shape factor is sharply peaked near the value for the regular hexagon and the coordination number has a sharp peak at $N_n = 6$ with $P(N_n) \approx 0.7$. The neighbor density is also sharply peaked around its mean value. The system is hexagonally structured which can also be well illustrated in the snapshot at $t = 15\,\mathrm{s}$ in Figure S13. Adding noise to the system analogous to the procedure described in section 5.3 has a similar effect compared to the CSM. The mean and SFM of the different measures are shown in Figure S15 B, analogous to Figure 5.18. The minimum of the mse for the different measures is around $0.09 \leq \sigma \leq 0.1$ m. The noise has very minor effects on the mean value $\langle \rho_n \rangle$ and $\langle N_n \rangle$ but decrease the hexagonal-order significantly. The mean hexagonal order $< \Psi_6 >$ intersects with the experimental value at $\sigma \approx 0.06$ m but the value around $\sigma = 0.1$ m is still close to the experiments. In conclusion this shows that even a highly ordered system cannot be detected properly with reasonable ammount of error in the trajectory measurement considering the estimated $\Delta x \approx 0.1\,\mathrm{m}$ in [1].

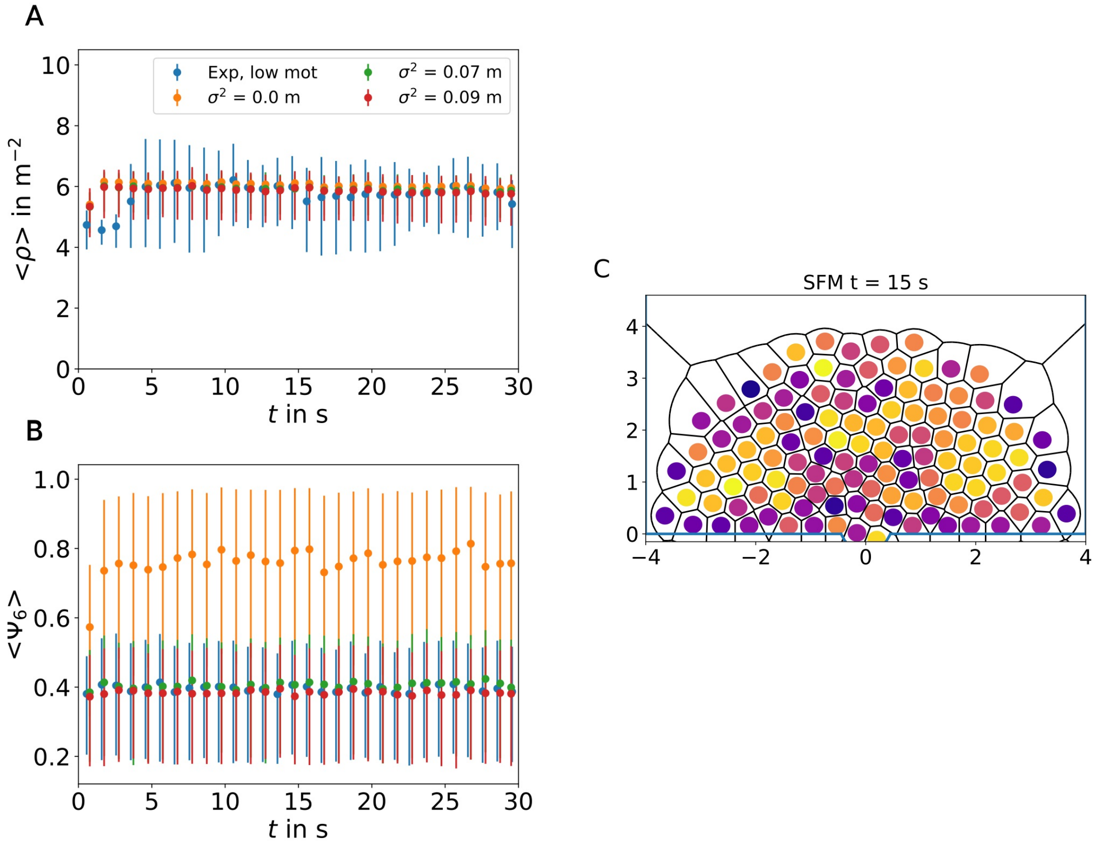

Figure S13: Left: Time series of the SFM analogous to Figure 5.16 showing the effect of noise on the mean neighbor density $\langle \rho_n \rangle$ and the orientational order parameter $\langle \Psi_6 \rangle$. The error bars show where 95% of the data for every individual are. **Right:** Snapshot of a simulation with the SFM at $t = 15\,\mathrm{s}$. Purple is a low value of Ψ_6, while yellow is a high value of Ψ_6.

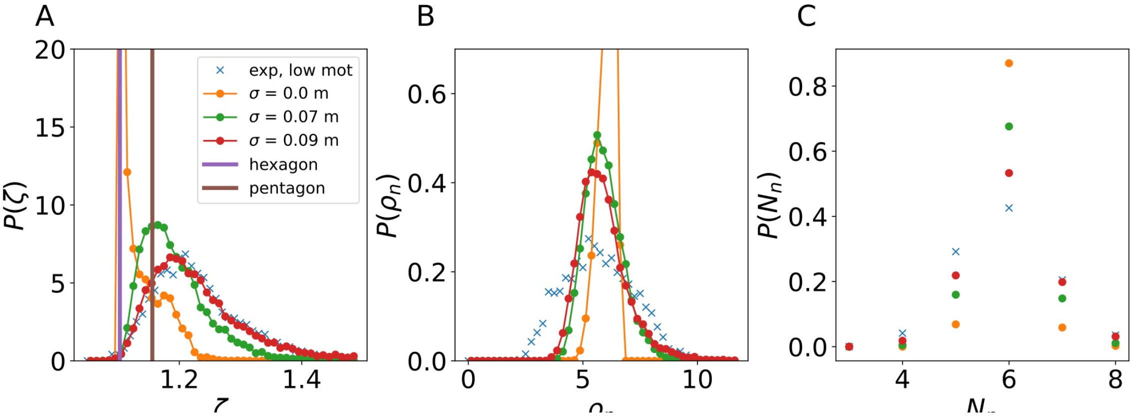

Figure S14: Distribution of the shape factor ζ (**A**), neighbor density ρ_n (**B**) and coordination number N_n (**C**) analogous to Figure S11.

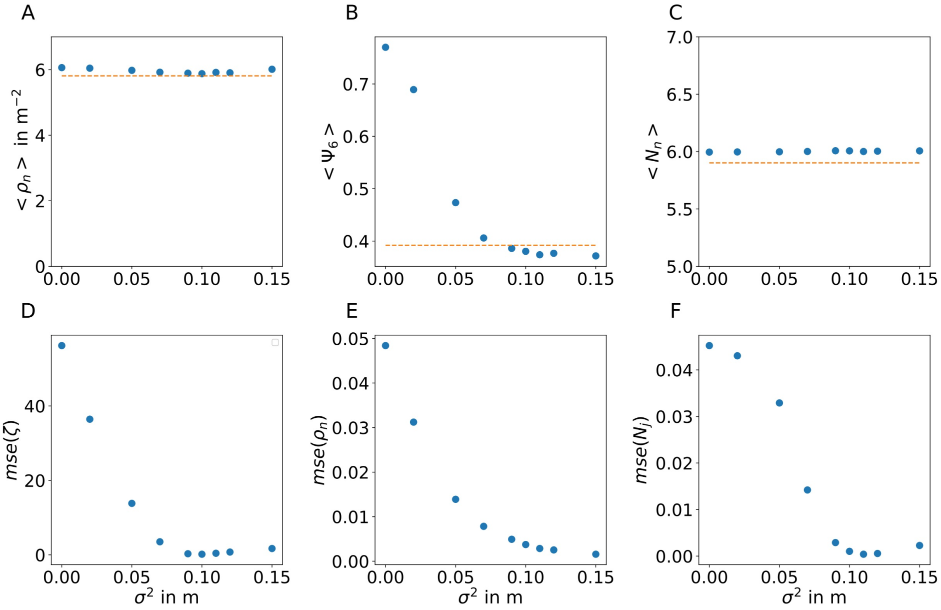

Figure S15: Plot analogous to Figure 5.18. Top row: mean value of $\langle\rho_n\rangle$, $\langle\Psi_6\rangle$ and N_n in the time interval of $10\,\mathrm{s} < t < 20\,\mathrm{s}$. Bottom row: the mse of the simulated distributions and the experimental distributions in respect to the addes noise to the trajectory for the measures as mentioned above.

A.5 Supplementary figures and tables Section 6

Run	t_{max}
1	5000
2	5000
3	3200
4	3250
5	1100
6	5000
7	5000
8	5000
9	5000
10	5000
11	5000
12	5000
13	4550
14	5000
15	4250
16	4000
17	3250
18	4450
19	1550
20	5000
21	400
22	5000
23	5000
24	5000
25	1900

Table A.2: Maximal time of the simulation until it either clogs or reaches the maximal simulation time of $t = 5000\,\mathrm{s}$

A.6 Supplementary figures section 6.1

Figure S17 depicts the shape factor distribution $P(\zeta)$ at different distances in A and continuous over the space in B for different distances r to the bottleneck with $a = 10$, $\Delta r = 1$ m and the other parameters as in Table 6.1. The plot is analogous to Figure 6.3 for $a = 2.5$. The shape of the distribution for $r < 21$ m is similar to the case where $a = 2.5$, as discussed in section 6.1. For $r > 21$ m, the distribution

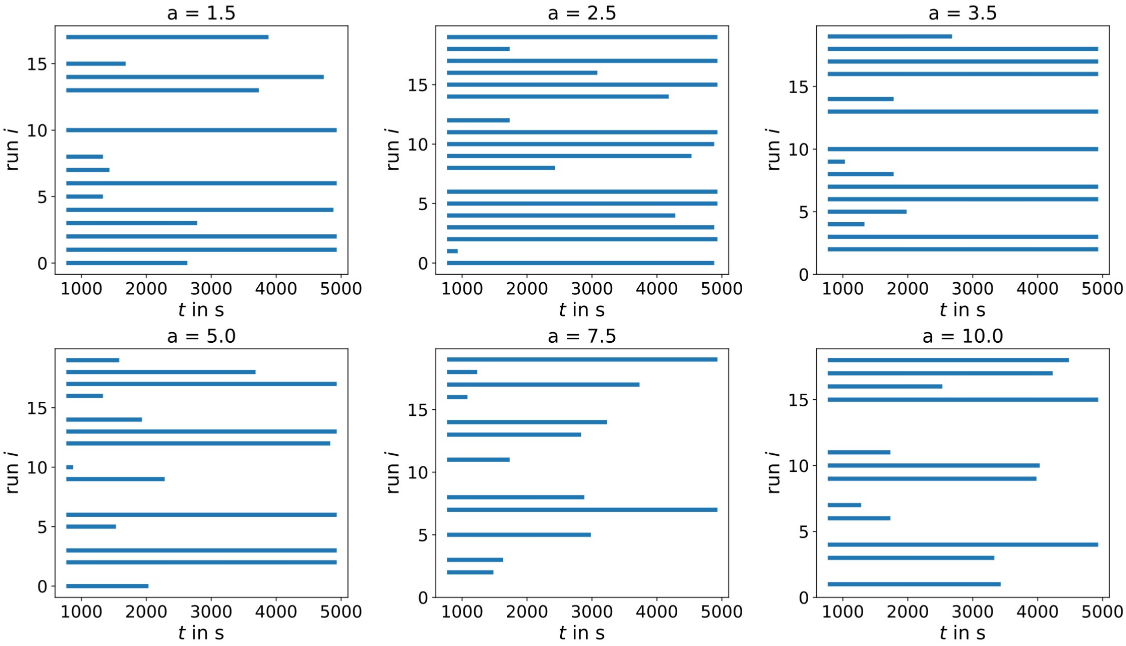

Figure S16: Time T_c until the simulations clog for different values of a.

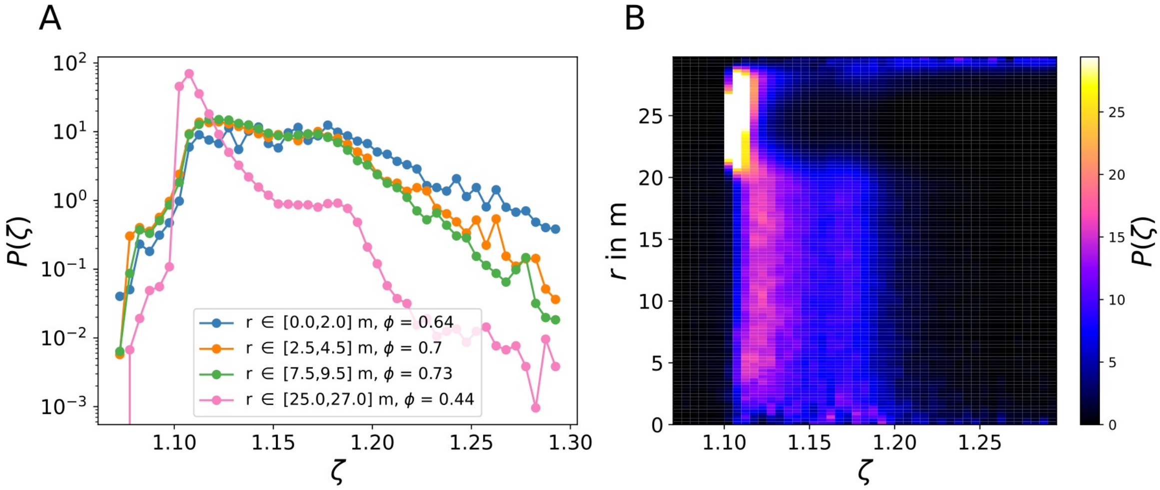

Figure S17: (**A**) Distribution of the shape factor at different distances for the simulation with the repulsion strength $a = 10$ and other variables as in Table 6.1. (**B**) Heat map of the shape factor distribution in respect to the distance from the bottleneck r.

changes its shape to a mono-modal distribution with its peak very close to the value of $\zeta = 1.101$, which is the hexagonal shape. Larger ζ decay exponentially, and there is a plateau around the pentagonal shape at $\zeta = 1.15$, which shows the defects in the crystal structure. The heat map of the shape factor distribution in panel B shows the sharp transition between the bi-modal and mono-modal regime, with a distinct interface.

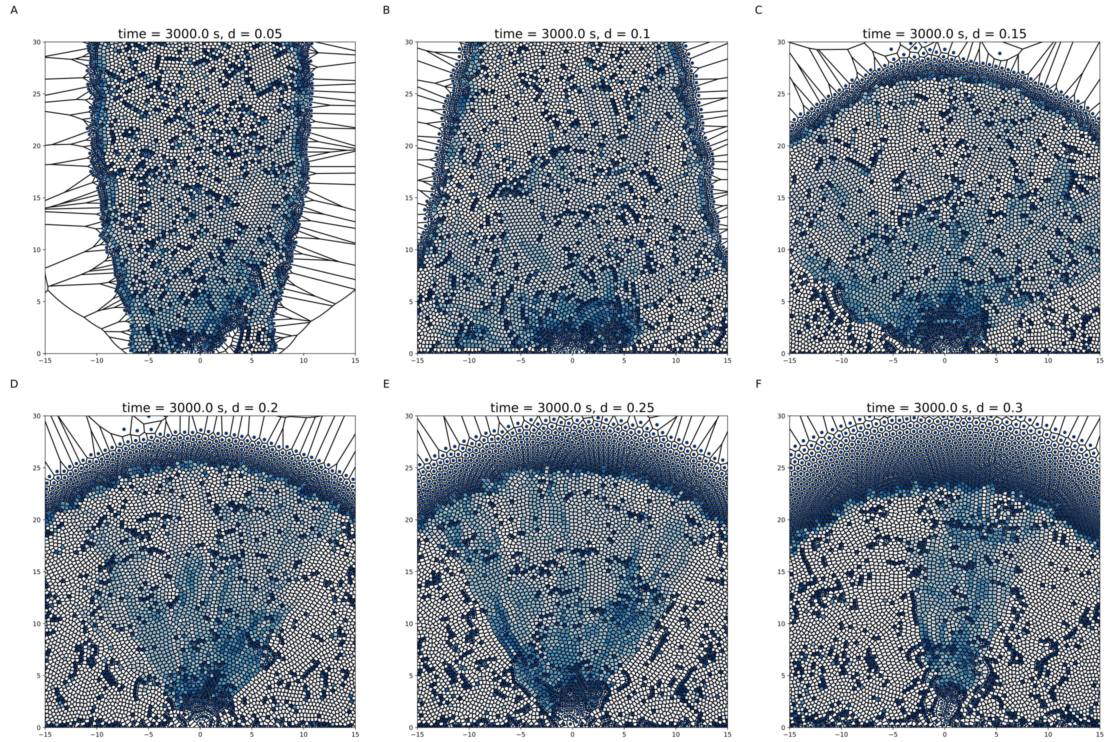

Figure S18: Illustration of the value of the speed function V(s) of the agents for different d in [m] analogous to Figure 6.18 at $t = 3000\,\mathrm{s}$. Agents coloured in white are stationary $V(s) = 0\,\mathrm{m/s}$, while bluer agents are faster $V(s) > 0$.

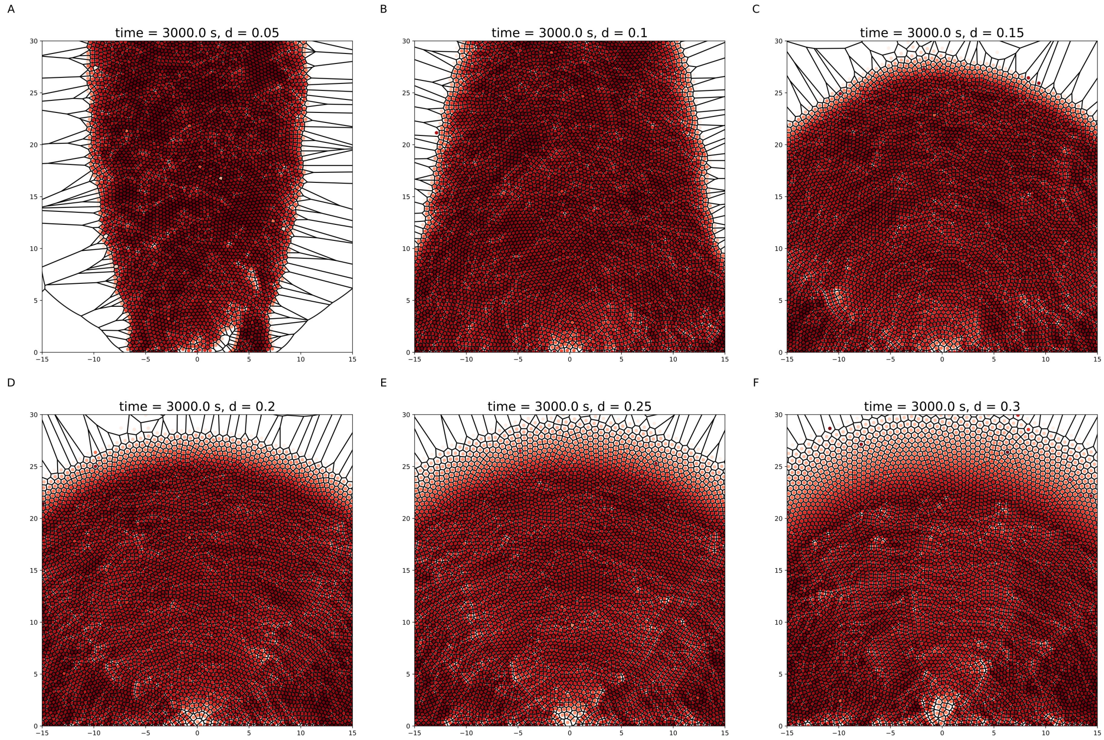
time = 3000.0 s, d = 0.05

time = 3000.0 s, d = 0.1

time = 3000.0 s, d = 0.15

time = 3000.0 s, d = 0.2

time = 3000.0 s, d = 0.25

time = 3000.0 s, d = 0.3

Figure S19: Illustration of the value of the packing fraction of the agents for different d in [m] analogous to Figure 6.18 at $t = 3000\,\mathrm{s}$. Darker red marks higher packing fraction ϕ.

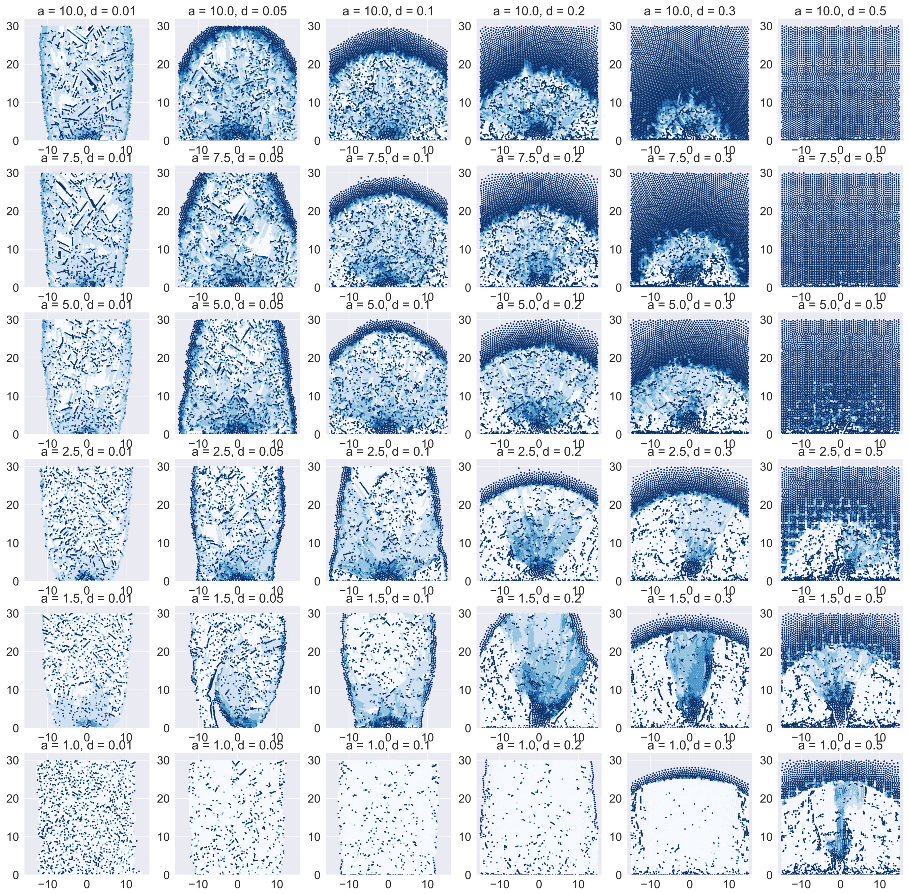

Figure S20: Illustration of the value of the packing fraction of the agents for different d analogous to Figure 6.18 at $t = 2000\,\mathrm{s}$. Darker red marks higher packing fraction ϕ.

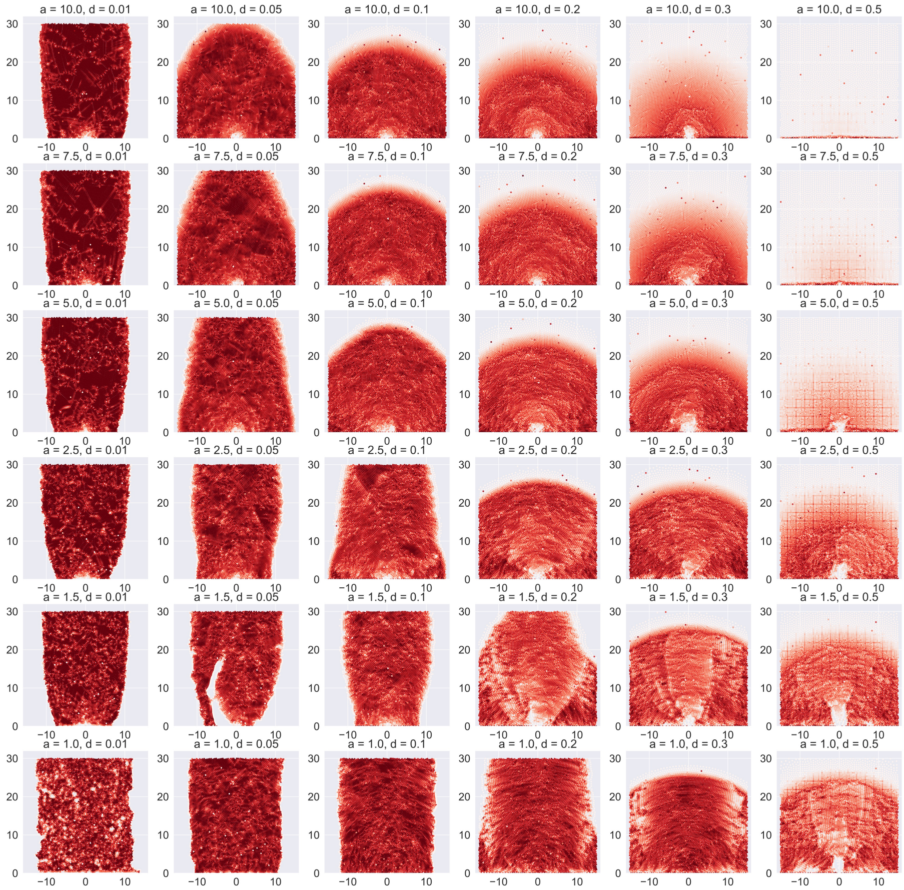

Figure S21: Illustration of the value of the packing fraction of the agents for different d analogous to Figure 6.18 at $t = 2000\,\mathrm{s}$. Darker blue marks faster agents, while white agents sopped.

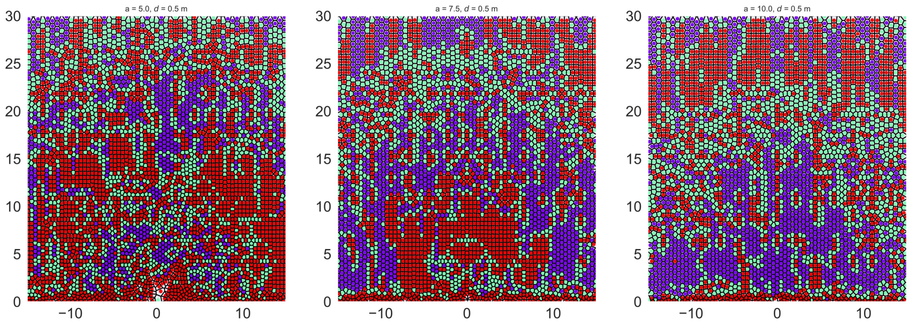

Figure S22: Shape factor classes analogous to Figure 6.17 for $a \in \{5.0, 7.5, 10.0\}$ and $d = 0.5\,\text{m}$. The purple agents have a high hexagonal order. Red agents in these systems tend to be in a square order.

A.7 Supplementary figures section 6.2

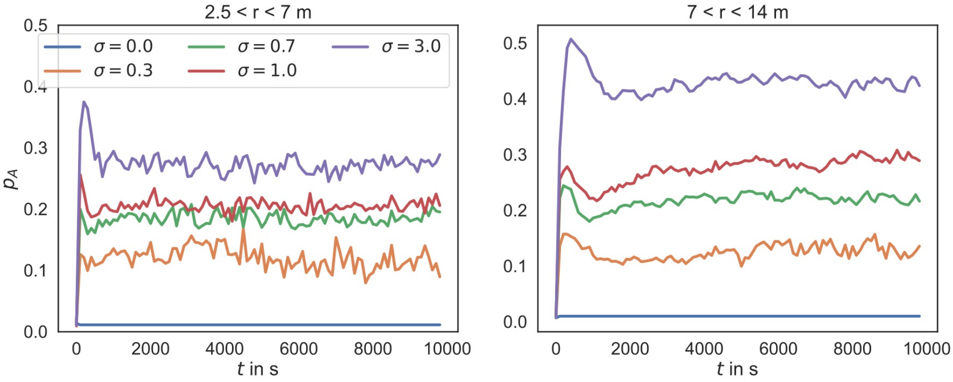

Figure S24: Time series of the fraction of agents in shape class A p_A in respect to the time t in seconds for different values of σ.

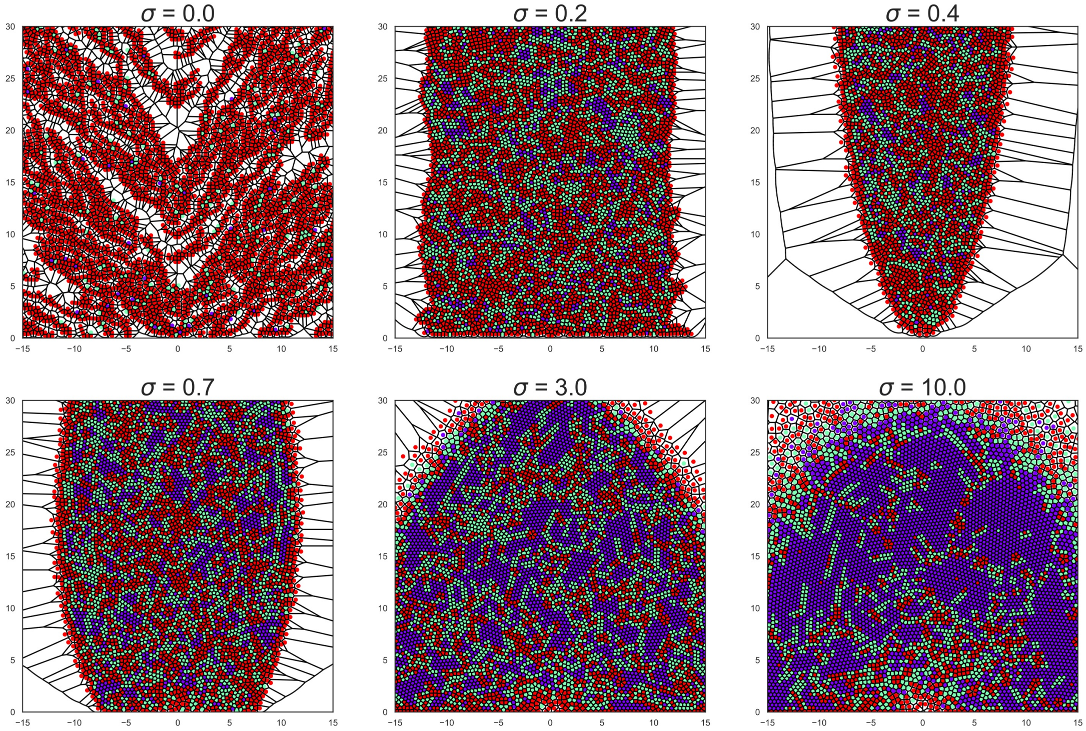

Figure S23: A snapshot of the simulations at $t = 9000\,\mathrm{s}$ with different σ specified in the title of the panels. The colors represent the shape classes analogous to Figure 6.4, with purple representing class A, green class B and red class C.

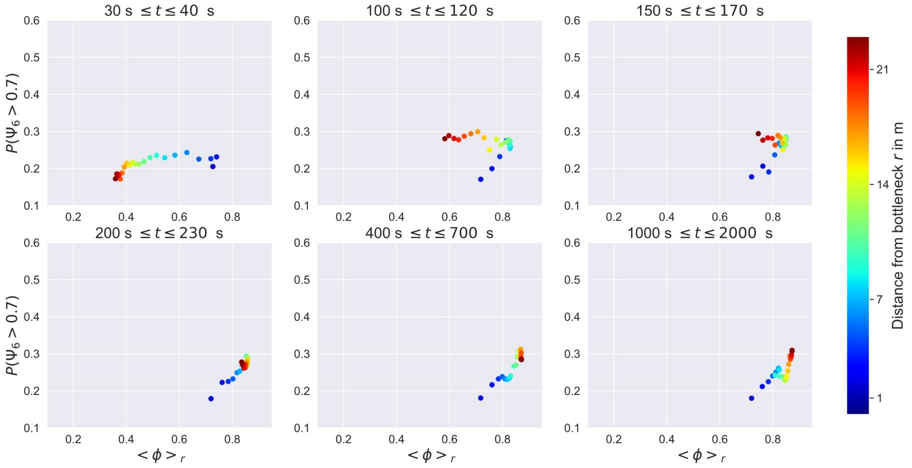

Figure S25: Plot of the hexagonal order in the system in respect to the packing fraction at different times of the simulation and different distance intervals $r + \Delta r$ from the bottleneck indicated by the colour. The noise is $\sigma = 0.7$. The value of $\Delta r = 1$ and the time intervals are indicated in the title.

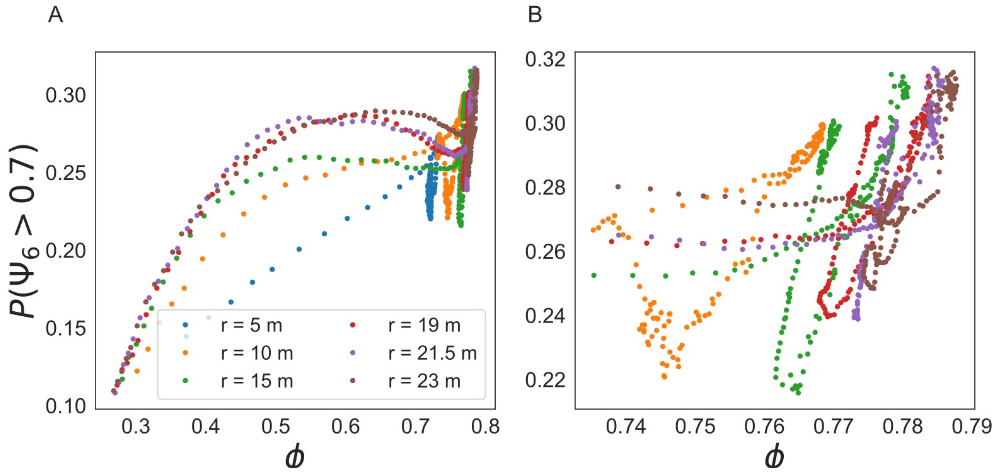

Figure S26: The hexagonal order $P(\Psi_6 > 0.7)$ in respect to the packing fraction ϕ at different distances r from the bottleneck with $\sigma = 0.7$. The dots show the time evolution of the system, where each dot is one point in time on the space. (**A**) shows the entire trajectory and (**B**) shows the interval $\phi > 0.74$.

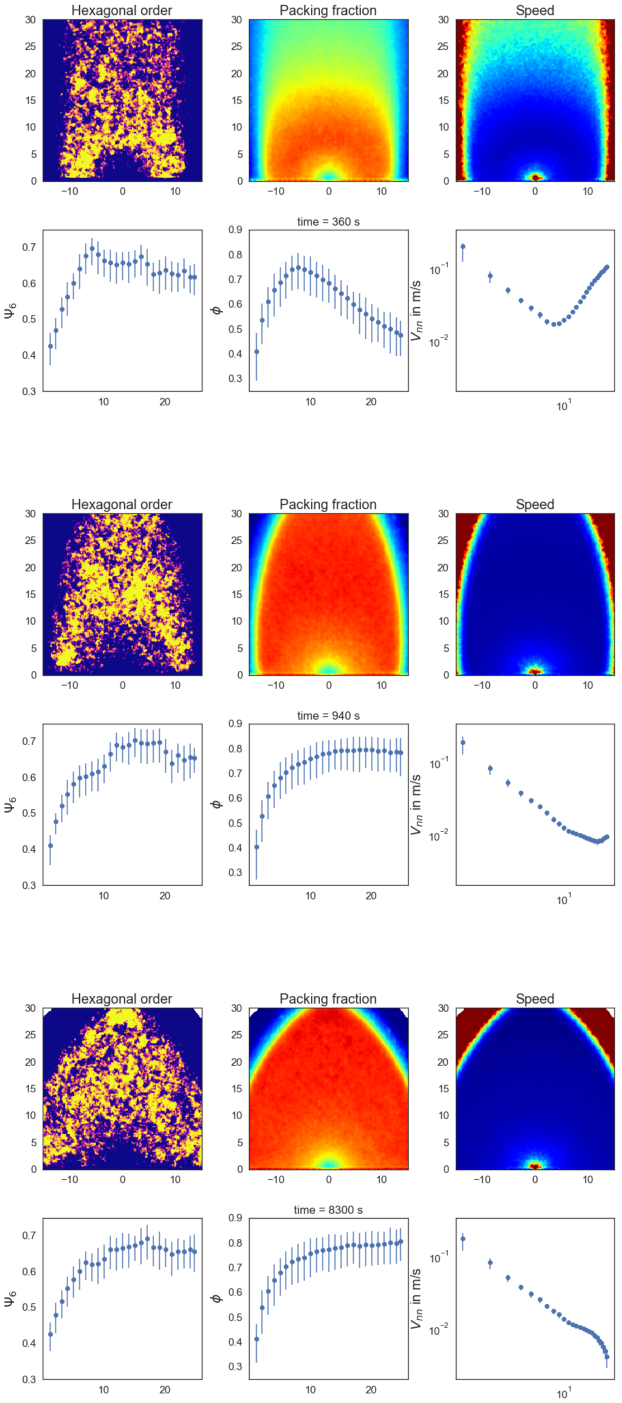

Figure S27: Snapshots of the hexagonal order field $\Psi_6(\mathbf{r})$, density field $\rho(\mathbf{r})$ and speed field $V_{nn}(\mathbf{r})$ at three different times $t \in \{140, 1120, 7500\}$s and the corresponding measure averaged over the distance to the bottleneck r in the panel underneath.

A.8 Supplementary figures section 6.4

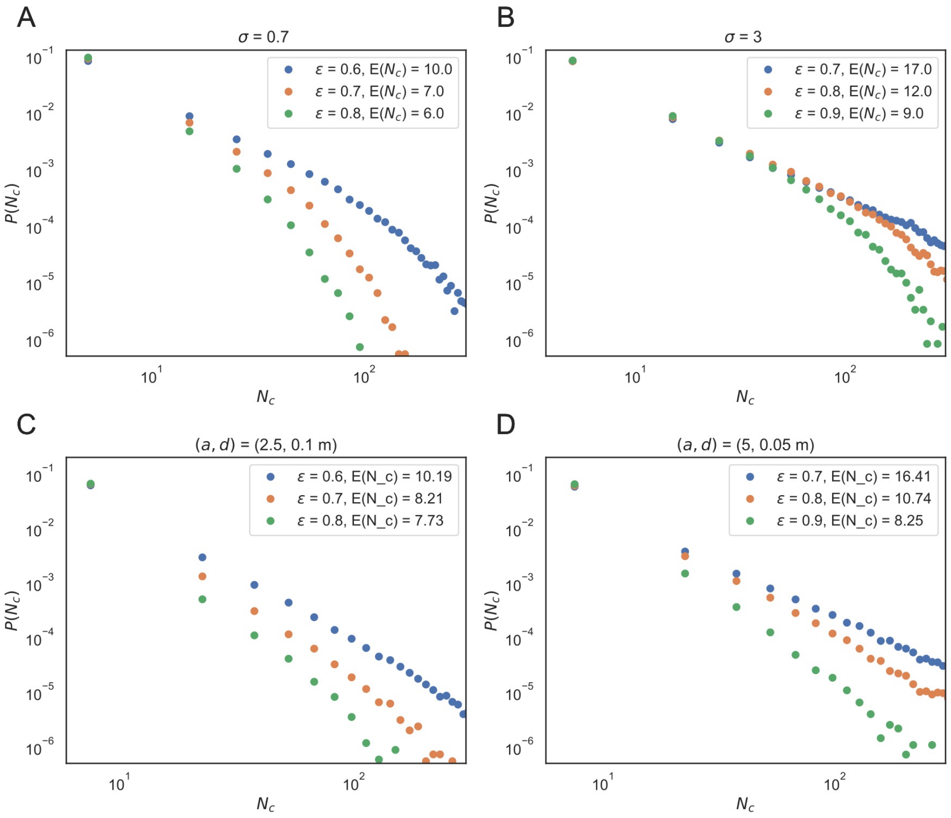

Figure S28: Log-log-plot of the cluster size distribution defined by the hexagonal order of the system $\Psi_6 > \epsilon$ analogous to Figure 6.55.

Acknowledgment

Finally, I want to thank all the people that helped me with this achievement. First, I would like to thank my supervisor Andreas Schadschneider for allowing me to conduct research in the fascinating field of pedestrian dynamics and guiding me throughout my research endeavor. Further, I want to thank Armin Seyfried and Mohcine Charibi, who gave me the opportunity to conduct my research at the Institute for Advanced Simulation of the Forschungszentrum Jülich and provided further guidance within the thesis advisory committee. I am thankful for the opportunities I gained during my work at the Forschungszentrum Jülich, like visiting a summer school in France and giving presentations at conferences. I want to thank Joachim Krug for reviewing this dissertation and Jan Jolie for taking over as the thesis committee chair. I want to thank my colleagues from the Forschungszentrum Jülich and the University of Cologne, with whom I had interesting discussions and amusing conversations about scientific and nonscientific topics. I am especially thankful for our virtual coffee breaks during the Corona lockdowns. Further, I want to thank the JSC for providing the computational resources on the JURECA cluster on which part of the research was conducted. I am thankful to Maria, Micha, and Marieke for proofreading parts of the thesis. I want to thank my fellow students and friends Alex, Hannes, Marc, and Phillipp, with whom I had a great time, good discussions, and much fun at the university. I want to thank Moni for the good times and beautiful vacations we went on. Furthermore, I want to thank my cat Nala for the company during the long work hours.

Zu guter Letzt möchte ich meiner Familie danken die mich so lange unterstützt hat. Vor allen meinen Eltern die mir immer zur Seite standen.

Eidesstattliche Versicherung

Hiermit versichere ich an Eides statt, dass ich die vorliegende Dissertation selbstständig und ohne die Benutzung anderer als der angegebenen Hilfsmittel und Literatur angefertigt habe. Alle Stellen, die wörtlich oder sinngemäß aus veröffentlichten und nicht veröffentlichten Werken dem Wortlaut oder dem Sinn nach entnommen wurden, sind als solche kenntlich gemacht. Ich versichere an Eides statt, dass diese Dissertation noch keiner anderen Fakultät oder Universität zur Prüfung vorgelegen hat; dass sie - abgesehen von unten angegebenen Teilpublikationen und eingebundenen Artikeln und Manuskripten - noch nicht veröffentlicht worden ist sowie, dass ich eine Veröffentlichung der Dissertation vor Abschluss der Promotion nicht ohne Genehmigung des Promotionsausschusses vornehmen werde. Die Bestimmungen dieser Ordnung sind mir bekannt. Darüber hinaus erkläre ich hiermit, dass ich die Ordnung zur Sicherung guter wissenschaftlicher Praxis und zum Umgang mit wissenschaftlichem Fehlverhalten der Universität zu Köln gelesen und sie bei der Durchführung der Dissertation zugrundeliegenden Arbeiten und der schriftlich verfassten Dissertation beachtet habe und verpflichte mich hiermit, die dort genannten Vorgaben bei allen wissenschaftlichen Tätigkeiten zu beachten und umzusetzen. Ich versichere, dass die eingereichte elektronische Fassung der eingereichten Druckfassung vollständig entspricht.

Teilpublikation:

Rzezonka, J., Chraibi, M., Seyfried, A., Hein, B., and Schadschneider, A. (2022). An attempt to distinguish physical and socio-psychological influences on pedestrian bottleneck. Royal Society Open Science, 9(6), 211822.

Rzezonka, J., Seyfried, A., Hein, B., Chraibi, M., and Schadschneider, A. (2021). Numerical Study of Bottleneck Flow with Varying Corridor Width and Motivation Using a Speed-Based Model. Collective Dynamics, 6, 1-13.

Jonas Rzezonka

Köln, den 06.11.2022